D-Q Frame Impedance Based Small-signal Stability Analysis of PV Inverters in Distribution Grids

Ye Tang

Dissertation submitted to the faculty of the Virginia Polytechnic Institute and State University in partial fulfillment of the requirements for the degree of

Doctor of Philosophy
In
Electrical Engineering

Rolando Burgos, Chair
Dushan Boroyevich
Jih-Sheng (Jason) Lai
Lamine Mili
Ranga Pitchumani

December 14th, 2020
Blacksburg, Virginia

Keywords: PV generator, distribution system, small-signal stability, impedance-based stability criterion

D-Q Frame Impedance Based Small-signal Stability Analysis of PV Inverters in Distribution Grids

Ye Tang

With development of renewable energies worldwide, power system is seeing higher penetration of Utility-scale photovoltaic (PV) farms at distributed level as well as transmission level. Power electronics converters present negative incremental impedance characteristics at their input while under regulated output control, which brings in the possibility of system instability. Recent evidence suggests that large-scale penetration of PV inverters increases the probability of instability. While IEEE standard 1547 newest version requires PV inverters to have reactive power control, there have been few investigations into the small-signal stability impact of PV inverters on distribution systems especially with reactive power control.

In addition, the existing studies either use the conventional way of state space equations and eigenvalues or use time-domain simulation methodology, which are based on the assumptions that detailed models of the grid and the PV inverters are accessible. Different from the previous literatures, this research employs Generalized Nyquist Criterion (GNC) method based on measured impedances in *d-q* frames at connection interfaces. GNC method has the advantage that interconnection stability can be judged without knowing the grid and PV generator model details. This work first demonstrates the advantage of volt-var droop mode control among all different local reactive power control modes for PV inverters in the aspects of static impact on grid voltage profiles and

power loss in a 12kV test-bed distribution system. Then it is discovered that *d-q* frame impedance of PV inverter under volt-var droop mode control shows a significant difference from other reactive power control modes. The *d-q* frame impedance derived from the small-signal model of PV generator is validated by both MATLAB simulation results and hardware experiments. Based on the *d-q* frame impedances, GNC is utilized to analyze the stability connection of a single PV farm and multiple PVs into the grid. GNC stability assessment results match with time-domain simulations and reveal the stability problem related to volt-var droop mode control. Furthermore, considering the unbalance of the distribution system, a new impedance model in *d-q* frame is proposed to capture both the dynamics of PV inverter operating in unbalanced points and the dynamics of three-phase unbalanced grid. The new impedance model is a combination of positive-negative sequence impedance and conventional *d-q* frame impedance. A procedure is designed for the measurement of the extended *d-q* frame impedance and the GNC application to predict small-signal stability of the unbalanced grid, which are justified by both time domain simulation and hardware experiments.

D-Q Frame Impedance Based Small-signal Stability Analysis of PV Inverters in Distribution Grids

Ye Tang

GENERAL AUDIENCE ABSTRACT

To overcome the limited fossil fuel reserve on the earth and global warming, renewable energies become more and more popular worldwide. Centralized thermal power generators in the transmission system are gradually being replaced by distributed energy resources (DER) which are connection to the distribution system, bringing more challenges to the safe and stable operation of the power system. This work focuses on the small-signal stability impact of photovoltaic (PV) generators in the distribution system, which basically analyzes into whether the connection of PV generator to the distribution system will end up in an expected steady operation state with high resistance to any relatively small disturbances. The stability assessment tool is based on impedance measurement which treats both sides as black boxes and bridges the information gap between Utility operators and PV generator vendors. A major finding of this work is that while PV generators in the distribution system help to provide grid-support functions of voltage regulation, they may cause voltage small-signal stability problems due to the high grid impedance, which is worse if more PV inverters are put in parallel. Even PV farms connected to different branches of the complicated radial distribution system may have interactions with each other. So the design of control strategy and parameters of PV generator should consider the impact of other PV generators. GNC method based on

impedances measurement is feasible and accurate for stability assessment of a distribution system with multiple PV farms. The impedance based method is upgraded and extended to be applied for the connection of power electronics devices to the three-phase unbalanced distribution systems.

ACKNOWLEDGEMENTS

First, I would like to express my sincere gratitude to my advisor, Dr. Rolando Burgos, for his advices, help and guidance. I will not be able to accomplish these without his patience in giving me time and the encouragement to learn in the initial period. I am really impressed by his research enthusiasm and brainstorming capabilities, which motivates me to face the well-known challenges and to explore the unknown part of our knowledge map.

I would also like to thank Dr. Dushan Boroyevich, whose foresight often inspires me to think deeper and further rather than being confined to a specific technical issue. His challenging questions can always pinpoint the bottleneck of my work and his recognition is always a huge inspiration to me.

I would very like to show my gratitude to the rest of my committee, Dr. Jih-Sheng (Jason) Lai, Dr. Lamine Mili and Dr. Ranga Pitchumani, for giving me valuable advices and insightful suggestions from scientific perspectives and reality experiences. It has been wonderful to have them on my advisory committee.

I would like to thank the support from the Center for Power Electronics Systems (CPES) Wide Bandgap High Power Converters and Systems (WBG-HPCS) Mini-consortium and Dominion Energy.

The great CPES staffs have made it easy for me to focus on my progress and I would like to thank them all: Ms. Marianne Hawthorne, Ms. Teresa Shaw, Ms. Teresa Rose, Ms. Linda Long, Mr. David Gilham, Mr. Matthew Scanland, Ms. Audri Cunningham, Ms. Na Ren, Ms. Yan Sun, Mr. Dennis Grove, and Mr. Neil Croy.

Many senior students and postdocs have offered me great help during these years, especially Dr. Chi Li, for his help in guidance in experiments, Mr. Slavko Mocevic for his advice in debugging my hardware, Dr. Zeng Liu and Dr. Igor Cvetkovic for the cooperation and work on experimental set-ups and Dr. Bo Wen for his enlightenment for some breakthroughs in my research.

It is a pleasure to work with the talented colleagues in the Wide Bandgap High Power Converters and Systems (WBG-HPCS) mini-consortium who offered me help and support. I would like to thank Dr. Yang Jiao, Dr. Jun Wang, Mr. Wei Zhang, Dr. Fang Chen, Mr. Shishuo Zhao, Mr. Yadong Lv, Dr. Zhengrong Huang, Mr. Zheqing Li, Dr. Yi-Hsun Hsieh, Ms. Yu Rong, Ms. Lakshmi Ravi, Mr. Xiang Lin, Mr. Jian Liu, Mr. Yuliang Cao, Ms. Tianyu Zhao, Ms. Qing Lin, Ms. Biqi Wang, Ms. Ning Yan and Mr. Minh Ngo.

I also would like to thank all my friends at CPES who made my life enjoyable and beautiful: Mr. Keyao Sun, Ms. Le Wang, Ms. Qian Li, Ms. Virginia Li, Dr. Qiong Wang, Dr. Bingyao Sun, Dr. Ming Lv, Dr. Chao Fei, Dr, Yincan Mao, Dr. Lingxiao Xue, Dr. Han Cui, Dr. Shuilin Tian, Dr. Xiucheng Huang, Dr. Zhemin Zhang, Dr. Zhengyang Liu, Dr. Yuchen Yang, Dr. Junjie Feng, Dr. Lujie Zhang, Dr. Dongbin Hou, Mr. Vahid Najmi, Mr. Ruiyang Qin, Mr. Chen Li, Mr. Alex Chu, Dr. Syed Bari, Dr. Niloofar Rashidi, Dr. Chien-An Chen, Ms. Emma Raszmann, Ms. Rebecca Rye, Dr. Ting Ge, Ms. Jiewen Hu, Mr. Joseph Kozak, Mr. Ripun Phukan, Dr. Bin Li, Mr. Bo Li, Dr. Zichen Miao, Mr. Victor Turriate, Ms. Grace Watt, Dr. Christina DiMarino, Dr. Sungjae Ohn, Mr. Feng Jin, Mr. Shuo Wang, Mr. Tam K.T. Nguyen, Mr. Yue Xu and Ms. Luxing Wang.

Finally but most importantly, I would like to give some special thanks to my family members, my parents, Mr. Haiqing Tang and Ms. Xia Wu, my parents in law, Dr. Ao Yu and Dr. Yongjian Wang, my husband Mr. Jianghui Yu and my daughter Hanwei Yu for their love, encouragement and support from all respects.

TABLE OF CONTENTS

Chapter 1. Introduction 1

1.1 Small-Signal impact of PV generation in distribution system 1

1.2 Small-Signal stability assessment approach 4

1.2.1 State space modeling 4

1.2.2 GNC based on *d-q* frame impedances 5

1.3 Single-Phase *d-q* frame impedance method 10

1.4 Motivation and objectives 11

1.5 Dissertation outline 12

Chapter 2. Impact of PV Inverter Penetration on Voltage Profile and Power Loss 14

2.1 Introduction 14

2.2 Test-Bed medium voltage power system 16

2.3 Impact on voltage profile 17

2.3.1 Sensitivity analysis about impact on voltage profile 18

2.3.2 PV under unity power factor 23

2.3.4 PV under different reactive power control 26

2.3.5 Conclusions about impact on voltage profile 31

2.4 Impact on system power loss 32

2.4.1 PV under unity power factor 32

2.4.2 PV under different reactive power control 33

2.4.3 Conclusions about impact on power loss 35

2.5 Conclusions 36

Chapter 3. PV Inverter Impedances in D-Q Frame under Different Q Control Modes 38

3.1 Introduction 38

3.2 Derivation of *d-q* frame impedance of PV generator 39

3.2.1 Open loop power stage model 40

3.2.2 Effect of PLL 43

3.2.3 Effect of current controller 45

3.2.4 Effect of DC voltage controller 47

3.2.5 Effects of digital delay 49

3.2.6 Effects of reactive power control 51

3.3 Validation through simulation 61

3.4 Small-Signal model validation through hardware 65

3.5 Conclusions about comparison between different reactive power modes 68

Chapter 4. GNC for the Connection of PV Inverters to the Distribution System 70

4.1 Introduction of test-bed distribution system parameters and modeling tool 71

4.2 Small-Signal stability assessment of the system with a single PV farm..... 73

4.2.1 Different Q control modes 73

4.2.2 Different PV locations 82

4.2.3 Different PV capacities 83

4.2.4 Different irradiances 84

4.2.5 Solutions for the instability 86

4.3 Small-signal stability assessment of the system with two PV farms 87

4.3.1 Different Q control 87

4.3.2 Second PV farm connected to different locations 92

4.3.3 Different capacities of PV penetration 93

4.3.4 Different irradiances 95

4.4 Experimental verification on the scaled-down test-bed 96

4.4.1 One PV Inverter 96

4.4.2 Two PV Inverter 101

4.5 Summary and conclusions 105

Chapter 5. Stability Assessment of Three Phase Unbalanced Distribution System 107

5.1 Introduction and state of art 107

5.2 D-Q frame impedance modeling of three-phase unbalanced system 109

5.2.1 Modeling of the three-phase converter in the unbalanced system 109

5.2.2 Modeling of the unbalanced three-phase lines 115

5.2.3 Modeling of the unbalanced three single-phase loads 118

5.3 D-Q frame impedance measurement and application in three-phase unbalanced system 121

5.3.1 Impedance measurement for the unbalanced system 121

5.3.2 GNC application based on the measured *d-q* frame impedances 126

5.4 Simulation results of the proposed *d-q* frame impedance based small-signal stability assessment in the unbalanced system..... 128

5.5.1 Unbalance comes from source voltages 129

5.5.2 Unbalance comes from loads.....133

5.5 Experimental verification..... 135

5.5.1 Unbalance comes from source voltages 135

5.5.2 Unbalance comes from load 139

5.6 Summary and conclusions 141

Chapter 6. Conclusions and Future Work 143

References 150

LIST OF FIGURES

Figure 1-1 Watt-var control curve 4

Figure 1-2 Volt-var doop control curve 4

Figure 1-3 Impedance model of DC circuit 6

Figure 1-4 D-Q frame average model a three-phase PV inverter 7

Figure 1-5 Impedance model of a three-phase balanced system 7

Figure 1-6 Excitation and response sequence components of power electronics device that is unsymmetrical in d axis and q axis 9

Figure 2-1 One-line diagram of the distribution system 16

Figure 2-2 Voltage contouring of the distribution system..... 17

Figure 2-3 56 bus system voltage profile with PV at bus 45..... 18

Figure 2-4 System voltage profile with different capacities of PV at bus 45. 24

Figure 2-5 Eligible allocations for different PV capacities in 56 bus system..... 26

Figure 2-6 (a) Watt-var mode curve (b) Volt-var Q= f(V) mode droop curve.. 27

Figure 2-7 Voltage of PV injection bus under different Q control..... 28

Figure 2-8 Voltage magnitude setting point acquisition..... 29

Figure 2-9 Bus 45 voltage with PV under different Q modes 30

Figure 2-10 System eligible allocations for 5 MW of PV under mode 3,4 or 5 . 30

Figure 2-11 System loss when PV generator is connected to different buses 32

Figure 2-12 System loss in terms of P and Q injected to bus 45 34

Figure 2-13 System power loss comparison of different Q modes..... 35

Figure 3-1 Switching model of the PV generator..... 39

Figure 3-2 Average model of the PV generator power stage 40

Figure 3-3 Small-signal model of the PV generator power stage 41

Figure 3-4 Transfer function diagram of PV inverter power stage dynamics .. 42

Figure 3-5 Bode plots of PV inverter terminal impedance with constant duty ratio control 43

Figure 3-6 Transfer function diagram of PV inverter with constant duty cycle and PLL control 44

Figure 3-7 Comparison of PV inverter terminal impedance with and without PLL 45

Figure 3-8 Transfer function diagram of PV inverter with closed current loop control 46

Figure 3-9 Bode plot of terminal impedances with and without current loop controller 46

Figure 3-10 Transfer function diagram of PV inverter with dual loop control 48

Figure 3-11 Bode plot of terminal impedances with and without DC voltage loop controller 48

Figure 3-12 Transfer function diagram of PV inverter with dual loop control and digital delay 50

Figure 3-13 Bode plot of terminal impedances with and without digital delay 50

Figure 3-14 Transfer function diagram of PV inverter with reactive power control 51

Figure 3-15 (a) mode 4 Watt-var mode curve (b) mode 5 Volt-var droop mode curve 53

Figure 3-16 Bode plot of terminal impedances under mode 1 – mode 4..... 54

Figure 3-17 Bode plot of terminal impedances under mode 1, mode 2 and mode 5 55

Figure 3-18 Phasor diagram under unity power factor mode (a) current response at d axis (b) current response at q axis 57

Figure 3-19 Phasor diagram under mode 2- mode 4 (a) current response at d axis (b) current response at q axis..... 58

Figure 3-20 Phasor diagram of volt-var mode (a) K_v =0, (b)0 < K_v< -I_q, (c) -I_q < K_v < -(I_d^2+ I_q^2)/I_q, (d) K_v > -(I_d^2+ I_q^2)/I_q..... 61

Figure 3-21 PV *d-q* frame impedance under mode 1 unity power factor 62

Figure 3-22 PV *d-q* frame impedance under mode 2 constant Q 63

Figure 3-23 PV *d-q* frame impedance under mode 3 constant PF..... 63

Figure 3-24 PV *d-q* frame impedance under mode 4 Watt-var mode..... 64

Figure 3-25 PV *d-q* frame impedance under mode 5 volt-var mode 64

Figure 3-26 Impedance measurement hardware circuit diagram..... 65

Figure 3-27 PV *d-q* frame impedance under mode 1 unity power factor 66

Figure 3-28 PV *d-q* frame impedance under mode 2 Q constant 67

Figure 3-29 PV *d-q* frame impedance under mode 3 PF constant..... 67

Figure 3-30 PV *d-q* frame impedance under mode 4 Watt - var mode..... 68

Figure 3-31 PV *d-q* frame impedance under mode 5 Volt - var..... 68

Figure 4-1 D-Q frame impedance model of grid with PV 70

Figure 4-2 One-line diagram of the distribution system 72

Figure 4-3 Grid impedance in *d-q* frame 73

Figure 4-4 (a) mode 4 Watt-var mode curve (b) mode 5 Volt-var droop mode curve 74

Figure 4-5 Bode plots of PV impedance under mode 1- mode 4 and the grid impedance 75

Figure 4-6 Comparison of characteristic loci when PV impedance is under mode 1- mode 4 75

Figure 4-7 Bode plots of PV impedance under mode 1, mod 2 and mode 5 and the grid impedance 76

Figure 4-8 Characteristic Loci under different Q control modes 77

Figure 4-9 Time domain simulation of PV output currents in *d-q* frame under droop mode 77

Figure 4-10 Time domain simulation of PV output currents in abc frame under droop mode 78

Figure 4-11 Time domain simulation of PV output currents in abc frame under droop mode 79

Figure 4-12 Time domain simulation of PV output currents in abc frame under droop mode 79

Figure 4-13 Magnitude comparison of four elements of PV admittance matrix 80

Figure 4-14 Bode plot comparison of λ_1 and L_{11} 81

Figure 4-15 Bode plot comparison of estimated and accurate Y_{dd} and Y_{qd} 82

Figure 4-16 Connection stability in terms of electrical distance 83

Figure 4-17 Characteristic loci when PV capacity increases (under mode 5) ... 84

Figure 4-18 Characteristic loci with different irradiances (under mode 5) 85

Figure 4-19 Zoomed in characteristic loci with different irradiances (under mode 5)..... 85

Figure 4-20 Proof of solution of the unstable case 87

Figure 4-21 D-Q frame impedances of the PV and the grid, case 1: Unity power factor, case 2: Q constant, Case 3: Droop mode..... 88

Figure 4-22 Characteristic loci for multiple PVs under different Q control..... 89

Figure 4-23 Three-phase currents of first PV farm under Q control under mode 1 or mode 2 89

Figure 4-24 Three-phase currents of first PV farm under Q control mode 5 ... 90

Figure 4-25 PV and grid impedances in *d-q* frame. Case 1: inductive zone, case 2: capacitive zone 91

Figure 4-26 Characteristic loci when multiple PVs are at different zones of droop curve..... 91

Figure 4-27 PV and grid impedances in *d-q* frame, Case 1: second PV at bus 56, case 2: second PV at bus 41, Case 3: second PV at bus 19. 92

Figure 4-28 Characteristic loci with different allocation for the second PV farm 93

Figure 4-29 PV and grid impedances in *d-q* frame Case 1: 1MW, case 2: 2MW, Case 3: 3MW. 94

Figure 4-30 Characteristic loci when total PV capacity increases 94

Figure 4-31 PV and grid impedances in *d-q* frame Case 1: 100% iradiance, case 2: 80% irradaince, Case 3: 60% irradiance. 95

Figure 4-32 Characteristic loci when irradiance changes 96

Figure 4-33 Hardware experiment circuit of a single PV inverter case..... 97

Figure 4-34 Picture of the hardware components..... 97

Figure 4-35 Recorded waveform of PV inverter transients on the scope 98

Figure 4-36 PV inverter Vab and Ia waveform on the scope for the stable and unstable cases 98

Figure 4-37 Characteristic loci for the Q constant control 99

Figure 4-38 Characteristic loci for volt-var droop control 100

Figure 4-39 Circuit of the two PV inverter hardware experiment..... 101

Figure 4-40 Picture of the hardware components of two PV inverter test 102

Figure 4-41 Recorded waveform of PV inverter transients on the scope 103

Figure 4-42 Characteristic loci for the stable case of Q constant control..... 104

Figure 4-43 Characteristic loci for the unstable case of volt-var control 104

Figure 5-1 Three-phase converter in unbalanced system. 110

Figure 5-2: The modeling of PV inverter..... 110

Figure 5-3: The modeling of PV inverter..... 112

Figure 5-4: The current responses of PV inverter in ABC frame 113

Figure 5-5: Unbalanced lines in ABC frame 116

Figure 5-6: D-Q frame model for three-phase unbalanced lines..... 117

Figure 5-7: Unbalanced loads in ABC frame 119

Figure 5-8: Unbalanced loads in *d-q* frame 120

Figure 5-9: Unbalanced loads in *d-q* frame 120

Figure 5-10: Flow chart of single-phase measurement..... 122

Figure 5-11 Basic algorithm of single-phase measurement method..... 123

Figure 5-12 Flow char of the impedance measurement for three-phase unbalanced system 126

Figure 5-13 Small-signal representation of the three-phase unbalanced system in *d-q* frame..... 127

Figure 5-14 Small-signal representation of the three-phase unbalanced system in *d-q* frame..... 128

Figure 5-15 Four characteristic loci for the stable case when substation voltage is unbalanced 129

Figure 5-16 PV output currents for the stable case when substation voltage is unbalanced..... 130

Figure 5-17 Four characteristic loci for the unstable case when substation voltage is unbalanced..... 131

Figure 5-18 PV output currents for the unstable case when substation voltage is unbalanced 131

Figure 5-19 Two characteristic loci for the unstable case when substation voltage is unbalanced..... 132

Figure 5-20 Four characteristic loci for the stable case when load is unbalanced 133

Figure 5-21 PV output currents for the stable case when system load is unbalanced..... 134

Figure 5-22 Four characteristic loci for the unstable case when load is unbalanced..... 134

Figure 5-23 PV output currents for the unstable case when system load is unbalanced 135

Figure 5-24 Hardware experiment main circuit when the unbalance comes from AC source 136

Figure 5-25 Picutre of the hardware circuit 136

Figure 5-26 Recorded waveform of PV inverter on the scope 137

Figure 5-27 Four characteristic loci for the stable case when AC voltage is unbalanced 138

Figure 5-28 Four characteristic loci for the unstable case when AC voltage is unbalanced 138

Figure 5-29 Hardware experiment main circuit when the unbalance comes from line-to-line load 139

Figure 5-30 Recorded waveform of PV inverter on the scope 140

Figure 5-31 Four characteristic loci for the stable case when the loads are unbalanced 140

Figure 5-32 Four characteristic loci for the stable case when the loads are unbalanced 141

LIST OF TABLES

Table 2-1 Elements of sensitivity matrix VP of 56 bus system 24

Table 2-2 Optimal allocation for different PV capacity 33

Table 3-1 Meaning of each block in the transfer function diagram..... 52

Table 3-2 Impedance polarity in terms of droop slope..... 60

Table 3-3 Parameters of the PV impedance measurement hardware circuits.. 66

Table 4-1 Parameters of the first PV generator 101

Table 4-2 Parameters of the second PV generator 102

Table 5-1 Parameters of the hardware circuits with unbalanced source 137

Table 5-2 Parameters of the hardware circuits with unbalanced load..... 139

Chapter 1. INTRODUCTION

1.1 Small-Signal impact of PV generation in distribution system

Due to the global warming caused by carbon dioxide and the limited stock of fossil fuels, solar energy generators are developing rapidly worldwide. The solar PV deployment was boosted up more than 10 times in United States from 2010 to 2020, showing the increasing trend of PV generators over the years 150[1].

PV generators are divided into three categories according to the power rating, namely residential PV, non-residential PV and Utility PV farms. Residential PV systems are generally 2–10 kW and installed on sloped roofs, while commercial (non-residential) systems may be between 10 kW and multi-megawatts and are most often installed on flat or low-slope roofs. Utility PV farms are usually bigger than 1MW.

According to the data from U.S Energy Informaiton Adminstration (EIA), most of these Utility PV plants are relatively small and are between 1 MW and 5 MW. Of 2,500 utility-scale solar photovoltaic (PV) facilities in Unites States, about 80% of them are below 5 MW based on data through November 2018 [2].

The utility PV farms of 5 MW or even smaller size are mostly likely to be connected to the distribution system, which is considered to be weaker than the transmission system because of the high impedance. In other words, the distribution system is seeing higher and higher penetration of utility PV as well as the transmission system, a fact that makes the impact of PV generation on the distribution system non-negligible. Besides the power quality issues of voltage flicker and voltage profile as a result of irradiance inconsistency and harmonics problems as PV inverter is a switching power electronics device, there's

concern that the dynamic control of PV generator will influence the power system small-signal stability significantly. Large-scale penetration of PV inverters increases the probability of instability [3]-[11]. N. Pogaku first pointed out that the detail dual loop control modeling of power inverters is necessary in the power systems small-signal stability analysis to capture the several hundred Hz of oscillation modes caused by the interactions between the converter close loop control and the grid [1]. J. L. Agorreta found a resonant mode of 2.6 kHz because the multiple grid-tied PV inverters are coupled due to the grid connection, and the design of the multiple PV inverters need to a full small-signal model of all converters and the grid to get rid of the oscillation [4] . [5] found that the voltage stability can be affected by the PV inverters and their allocations (whether scattered or centralized). In [6] and [7], it was found that the PV penetration can have a detrimental effect on small signal stability of the power system because of lack of inertia. [8] showed the possibility of some low-frequency oscillations when PV inverter is connected to a weak 0.4 kV system. [9] not only admitted the possibility of instability of PV connection to the distribution system, but also proved that the control parameters of PV inverter influence the possibility of instability a lot using the damping ratio of eigenvalues. [10] emphasized the importance of detailed modeling of DC side components of Utility PV when doing small-signal stability analysis of distribution system. [11] confirmed that low-frequency eigenvalues are introduced by considering PV primary DC side dynamics and the dual loop controllers, and that interconnecting PV may lead to system interactions and instability.

Another reason to pay close attention to the small-signal stability impact of PV to the power system is the increase of control complexity in PV inverters in the distribution

system. Originally PV inverter only needs to meet the goal of maximum solar power or active power harvesting by controlling the DC side voltage to be the maximum power point. But as PV capacities increase, the maleficent impact on distribution system voltage profile urges the grid to negotiate with PV farms to help resolve this problem. The incremental requirement of providing grid support functionalities is revealed by recent updates of IEEE standard 1547. In the 2003 version, it was written that the distributed resources (DR) shall not actively regulate the voltage at the point of common coupling (PCC). In the 2014 version, it was updated as coordination with and approval of the area power system, DR operators shall be required to actively participate to regulate the voltage by changes of reactive power. While in the latest version published in 2018, the DR shall be capable of injecting reactive power and absorbing reactive power with a reactive power capability of 44% of nameplate active power. The utility PV inverter should offer the local reactive power control modes of (1) Unity Power Factor (2) Constant Reactive Power (3) Constant Power Factor (4) Watt-var Mode and (5) Volt-var Droop Mode. The mode 4 Watt-var mode is illustrated by Fig.1-1 that reactive power is a function of active power, the curve of which is defined by agreement of PV farm and the Utility. The mode 5 Volt-var droop mode is exhibited by Fig. 1-2 that reactive power is a droop function of PCC voltage magnitude. The execution of reactive power control will change the dynamics of PV generators, especially under the mode 5 that the PV generator is regulating its terminal AC voltage directly and acting more like a voltage source instead of a current source. The different reactive power control modes will be modeled in detail and compared in this work.

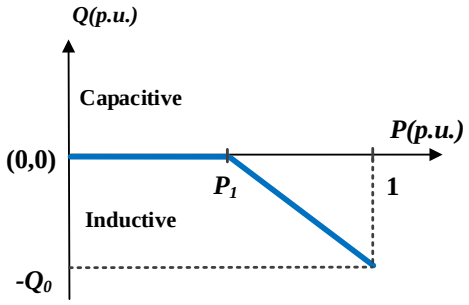

Figure 1-1 Watt-var control curve

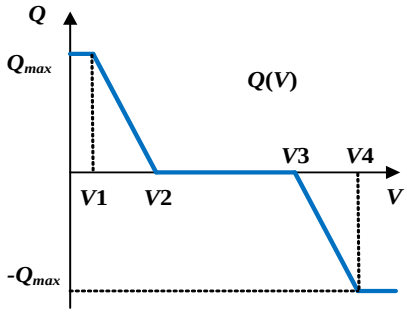

Figure 1-2 Volt-var doop control curve

1.2 Small-Signal stability assessment approach

1.2.1 State space modeling

The most widely used method to assess the power system small-signal stability is the state space modeling [12]. The dynamic analysis of a balanced three-phase electrical power system comprised of a finite set of synchronous generators, inductors, capacitors and so on, which are analyzed by use of the state variable approach. Each component is described by its own state model. These state models for all the components are then interconnected according to the topology of the power system to form a full state model for the total system. And linearization around a balanced steady state operation point yields a linear time invariant (LTI) system as below:

$$\begin{cases} \Delta\dot{\mathbf{x}}(t) = \mathbf{A}\cdot\Delta\mathbf{x}(t) + \mathbf{B}\cdot\Delta\mathbf{u}(t) \\ \Delta\mathbf{y}(t) = \mathbf{C}\cdot\Delta\mathbf{x}(t) + \mathbf{D}\cdot\Delta\mathbf{u}(t) \end{cases} \tag{1-1}$$

in which $\Delta\mathbf{x}$ is the state vector, $\Delta\mathbf{y}$ is the output vector , $\Delta\mathbf{u}$ is the input vector and **A** is the state matrix. Then the small-signal stability can be studied by observing the eigenvalues of the state matrix **A**. The real and imaginary parts of the eigenvalues can provide the damping ratio and oscillation frequency information of all the oscillation modes during small disturbances. There have been some literature papers utilizing this approach for small-signal stability impact of PV inverters on the power system.

The limitation of the state space representation is that the size of the state matrix gets much bigger with the increasing number of components in the power system. And more importantly, this method requires the full knowledge of state space equations and models of every component in the system. In reality, most of the grid-connected power electronics devices are working as black boxes. The Utility users don't have access to the detailed information of the converters including hardware design and controller principles and parameters, nor do the power electronics vendors know the power system information. Both sides don't have a full model of the whole complete system.

1.2.2 GNC based on *d-q* frame impedances

As a more practical alternative compared to the state space modeling, impedance-based stability analysis has been a very useful tool in DC systems for a long time [13], where the stability is assessed by Nyquist stability criterion based on the measured impedances on both sides of the connection interface. Fig 1-3 is the small-signal representation of a DC system. The small-signal dynamics are represented by impedances

of both sides Z_s and Z_l. The load voltage is related to the source voltage by the equation below of (1-2).

$$v_l = (1 + Z_l / Z_s) v_s \tag{1-2}$$

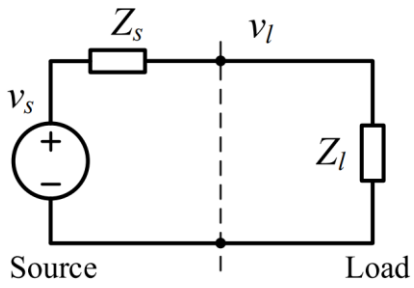

Figure 1-3 Impedance model of DC circuit

Then the system stability can be predicted by applying Nyquist stability criteria to the minor loop-gain ($L = Z_l/Z_s$). The main advantage of this approach is that no model is needed from either side, while the measured impedances intrinsically model all the dynamics within frequency of interest, including circuit components in the power stage and all the controllers. Stability criteria guidelines can be formulated then by establishing requirement of phase margin or gain margin on the bode plots of minor loop-gain to ensure a stable operation [14]-[16]. This allows for new devices to be added to the system easily as black boxes while making sure that system is still stable after the connection.

Different from a DC system, a three-phase AC system's operation point is a trigonometric function in terms of time, so the linearization cannot be done directly in the stationary (*abc*) frame. But after the Park transformation from *abc* frame to *d-q* frame, three phase time variant systems become two coupled DC systems, namely the d-axis circuit and q-circuit, as shown in the example of Fig.1-4. All the variables in the figure are DC values, so that small-signal model can be obtained very easily after linearization

around the steady state. But different from the DC system, the impedance looking from AC side is a 2 by 2 matrix as in (1-3) instead a scalar in a DC circuit.

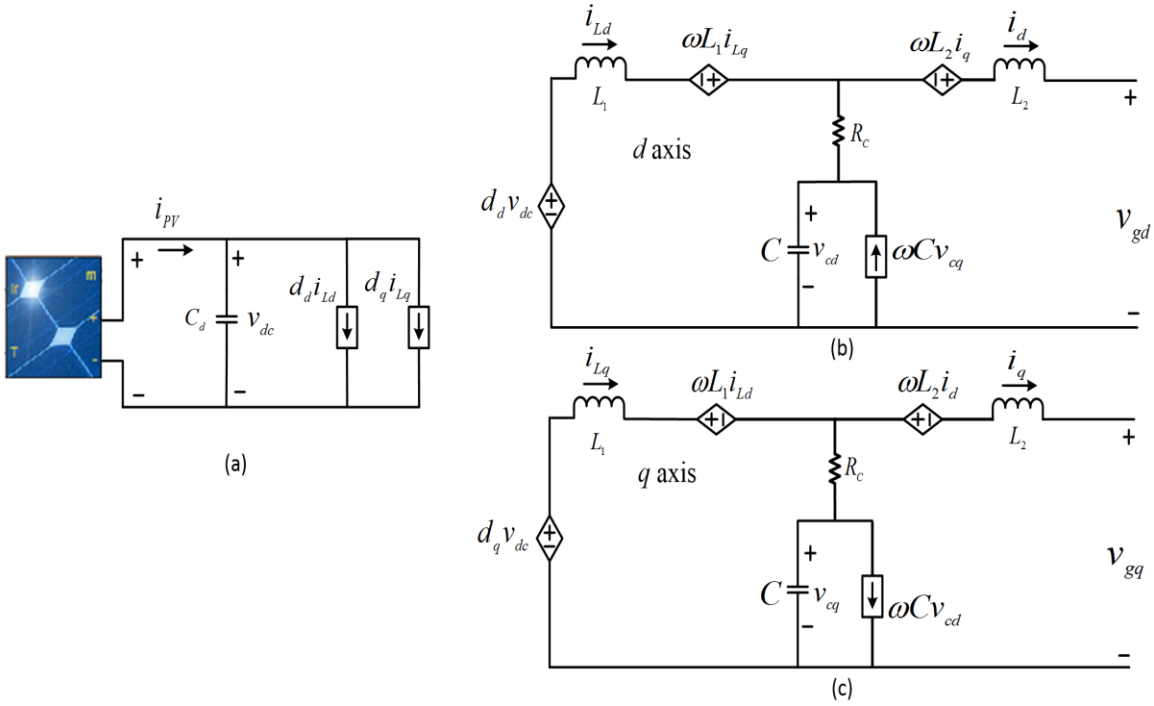

Figure 1-4 D-Q frame average model a three-phase PV inverter

$$\mathbf{Z_{dq}}(s)=\begin{bmatrix} Z_{dd}(s) & Z_{dq}(s) \\ Z_{qd}(s) & Z_{qq}(s) \end{bmatrix} \tag{1-3}$$

Similar to a DC system which can be represented by Fig.1-3, the small-signal model of a balanced three-phase AC system can also be transformed to the impedance model in Fig. 1-5.

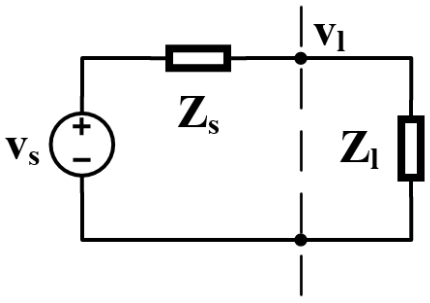

Figure 1-5 Impedance model of a three-phase balanced system

In which

$$\mathbf{v_s}(s)=\begin{bmatrix} v_{sd}(s) \\ v_{sq}(s) \end{bmatrix}, \mathbf{v_I}=\begin{bmatrix} v_{ld}(s) \\ v_{lq}(s) \end{bmatrix} \tag{1-4}$$

$$\mathbf{Z_s}(s)=\begin{bmatrix} Z_{sdd}(s) & Z_{sdq}(s) \\ Z_{sqd}(s) & Z_{sqq}(s) \end{bmatrix}, \mathbf{Z_I}(s)=\begin{bmatrix} Z_{ldd}(s) & Z_{ldq}(s) \\ Z_{lqd}(s) & Z_{lqq}(s) \end{bmatrix} \tag{1-5}$$

The interface voltage vector is related to the source voltage by

$$\mathbf{V_I}(s)=[\mathbf{I}+\mathbf{Z_S}(s)\cdot\mathbf{Y_I}(s)]^{-1}\cdot\mathbf{V_s}(s) \tag{1-6}$$

Minor loop-gain is defined as Eq. (1-6), which is the product of the source impedance matrix and the load admittance matrix in *d-q* frame.

$$\mathbf{L}(s)=\mathbf{Z_s}(s)\cdot\mathbf{Y_I}(s) \tag{1-7}$$

As discovered by Ref. [17], the small-signal stability for a balanced three-phase ac system stability can be predicted by applying Generalized Nyquist Criterion (GNC) [18] to the minor loop-gain **L**(s). Here the dimension of **L**(s) is two by two, so for each frequency **L**(s) has two eigenvalues. Let {*l1*(s), *l2*(s)} be the set of frequency-dependent eigenvalues of **L**(s). These traces of the two eigenvalue in the complex plane form characteristic loci of matrix **L**(s) as the variable *s* traverses the standard Nyquist contour in the clockwise direction. Then the Generalized Nyquist Criterion can be formulated as below:

"Let the multivariable system shown in Fig. 1-5 have no open-loop unobservable or uncontrollable modes whose corresponding characteristic frequencies lie in the right-half plane. Then the system will be closed-loop stable if and only if the net sum of anticlockwise encirclements of the critical point (–1+j0) by the set of characteristic loci of **L**(s) is equal to the total number of right-half plane poles of $\mathbf{Z_{sdq}}$(s)and $\mathbf{Y_{ldq}}$(s)."

Compared to the positive sequence impedance method used in [19]-[22], *d-q* frame impedance matrix method is more accurate for stability assessment of system with power electronics devices with unsymmetrical control on the *d-q* frame [23]. For example, PV inverter that has non-symmetrical control in *d-q* frame because of the DC voltage loop and phase locked loop (PLL). For this type of converters, one positive sequence frequency f_p of perturbation may result in not only the same frequency f_p of response but also another frequency of $|2f_1-f_p|$, where f_1 is the line frequency .This frequency coupling effect is shown in Fig.1-6, which is due to the different dynamics in d-axis and q-axis in the synchronous reference frame, which is mentioned in [24]-[26] and mathematically proved in [27].

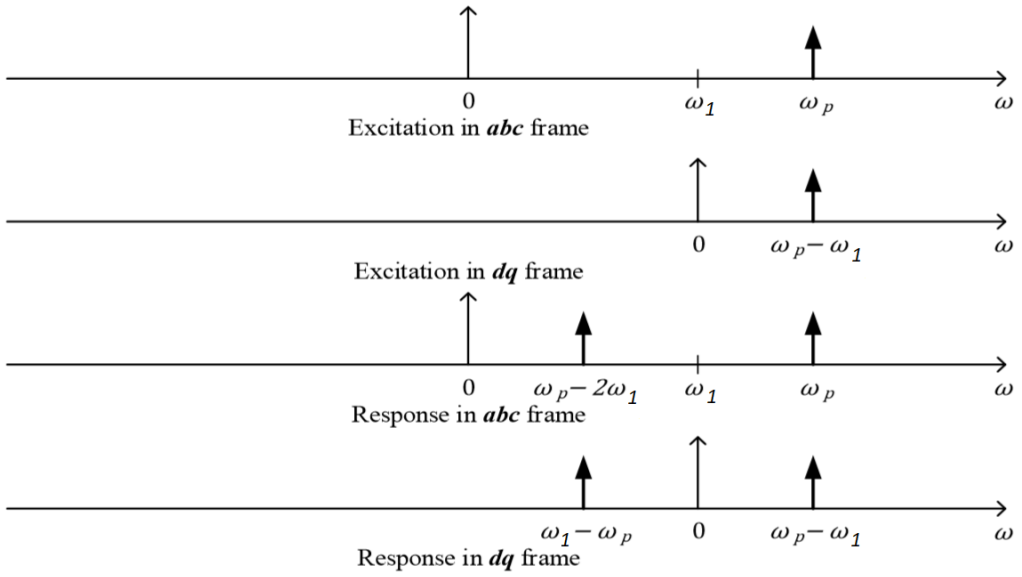

Figure 1-6 Excitation and response sequence components of power electronics device that is unsymmetrical in d axis and q axis

Ever since the creation of the GNC method based on *d-q* frame impedances in the electrical system, it is being used a lot for small-signal assessment of connection to power electronics devices to the electrical systems. B. Wen discovered the negative incremental

resistance in grid-tied inverters because of grid synchronization and current injection based on phase-locked loop (PLL). The frequency range of the negative incremental resistance behavior is determined by the bandwidth of PLL, and the magnitude of the resistance can be calculated by the power rating of the inverter, thus forming some design oriented guideline to avoid this type of instability [28]-[39]. This same type of problem caused by grid-synchronization was further explored by *d-q* frame impedances method in the later papers of [40],[41]. C. Li found the stability interactions of multiple STATCOMs which are very close in the power system and used the GNC method to pinpoint that the ac voltage regulation was the main reason of instability [42]-[48]. The interactions between power grid and HVDC were brought into attention by [49]-[56] using GNC based on *d-q* frame impedances. And the stability problem of wind farm connected through HVDC was covered in [57]-[60]. While [61]-[66] covered the stability connection problem to the grid of VSC three-phase converters including electric vehicles.

1.3 Single-Phase *d-q* frame impedance method

The aforesaid frequency coupling effect not only exists in three-phase balanced system but also appears in single-phase circuit under *d-q* frame control. One example is the single-phase railway AC/DC converter with DC voltage loop based on synchronous reference frame [67] and another example is the single-phase PFC load also with DC voltage loop [68]. But for a single-phase circuit, the operation point is time variant and only single phase information is available. To solve this modeling problem, the single-phase *d-q* frame impedance modeling and measurement method is recently created for stability assessment of such kind of single-phase circuit [69]-[70]. In this kind of approach, a fictitious balanced three-phase is constructed. Single phase sinusoidal

variables are regarded as α axis component, on which 90 degree of delay is added to form a fictitious β axis. After α-β to *d*-*q* transformation, a DC operation point is formed for system steady state, based on which perturbation is introduced and measured to get the *d*-*q* frame impedances. Basically speaking, the single-phase impedance measurement method builds a three phase balanced system based on the original system. The original system is the Phase A system, based on which virtual circuits of phase B and phase C are created by adding 120 and 240 degree of delay. The single-phase circuit is the simplest unbalanced three-phase circuit, and its *d*-*q* impedance model and measurement method gives some hints about the impedance modeling of three-phase unbalanced systems.

1.4 Motivation and objectives

As mentioned forehead, little work was done to fully understand what impact the high penetration of Utility PV will bring to the distribution system in the aspect of small-signal stability, and the approach in the previous literature papers is state-space model which requires the full models of the PV farms and the grid.

This research researches into the small-signal stability impact of PV of very high penetration level, at the distribution system level, and using *d*-*q* frame impedance based GNC method. The impedances of the Utility PV farms under analysis include all details of the generator, so as the DC and AC sides power stage, the inner-current loops, the outer-DC voltage loop and the reactive power control. All local reactive power control modes mentioned in most updated IEEE 1547 will be compared about the potential detrimental influence on the whole system stability. Furthermore, the case of multiple PV farms will be looked into thoroughly to explore the possible interactions between multiple PV farms in the same distribution system.

In addition, as the three-phase loads and voltages may be unbalanced in the distribution system where the three-phase Utility PV farms are connected, the previous *d-q* frame impedance based GNC methods is no longer applicable. To solve this problem, this work will upgrade the *d-q* frame impedance matrix to make the GNC method applicable to the three-phase unbalanced distribution system.

1.5 Dissertation outline

The dissertation is organized as follows:

Chapter 2 compares different local reactive power control modes for PV inverters in the aspects of static impact on grid voltage profiles and power loss in a 12kV test-bed distribution system. It is discovered that the impact of active power or reactive power on the voltage magnitude is almost linear, thus the rate by which the voltage increases at different geographical locations can be estimated accurately by the proposed sensitivity matrix, which was shown to be related to the system impedances. Volt-var droop mode is preferred compared to other reactive power control in aspects of voltage profile and system power loss.

In chapter 3, the terminal impedances in *d-q* frame are derived of utility-scale PV farm based on small signal model of PV inverters. It is discovered that *d-q* frame impedance of PV inverter under volt-var droop mode control shows a significant difference from other reactive power control modes. The PV terminal impedance matrix model derived from small-signal model is proved by MATLAB time domain simulation and validated by scaled-down hardware experiments.

In chapter 4, GNC is utilized to analyze the stability connection of a single PV farm and multiple PVs into the grid based on the *d-q* frame impedances. The reactive power control of volt-var droop mode is the first mode to cause instable connection as the number of PV inverters increases. For the instability problem caused by volt-var droop mode control, comparison is done for different PV allocations, different PV capacities (different number of PV inverters) and different irradiance condition. GNC stability assessment results match with time-domain simulations and reveal the stability problem related to volt-var droop mode control.

And in chapter 5, considering the unbalance of the distribution system, a new impedance model in *d-q* frame is proposed to capture both the dynamics of PV inverter operating in unbalanced points and the dynamics of three-phase unbalanced grid. The new impedance model is a combination of positive-negative sequence impedance and conventional *d-q* frame impedance. A procedure is designed for the measurement o extended *d-q* frame impedance and the GNC application to predict small-signal stability of the unbalanced grid.

Finally, Chapter 6 concludes the whole dissertation and discuss about the possible future work to be explored.

Chapter 2. IMPACT OF PV INVERTER PENETRATION ON VOLTAGE PROFILE AND POWER LOSS*

2.1 Introduction

Due to environment problems caused by fossil fuels, installation of photovoltaic (PV) systems is increasing rapidly worldwide. The impact on voltage profile is the most commonly recognized problem caused by high PV inverter penetration in distribution systems. Accordingly, a significant effort has been devoted to assess the static problems produced in distribution systems. The impact on voltage profile is bigger as the PV capacity increases, which has a limit in the amount of PV power to be installed with respect to the over-voltage problem [71]-[76]. Actually, the PV inverter penetration limit is influenced by the system original voltage profile, where for instance a lightly loaded case has the least PV penetration limit. The penetration threshold also depends on how PV inverters are located. The threshold decreases as the distance from the feeder source to the PV system increases, or the feeder impedance increases [72][75][76]. But so far no comparison has been made between busses of different branches of the radial system, or busses of a meshed system. After the release of the revised IEEE 1547 standard [77], different local reactive power control strategies have been designed and compared for PV inverters to regulate the system voltage [76]-[77], but similarly, the voltage impact and

penetration limit of PV inverters with reactive power control has not been fully analyzed yet.

The uncertain variables in PV impact analysis include PV location, PV capacity and reactive power control strategies, which yield numerous cases to be analyzed and compared. In this paper, a voltage sensitivity analysis is conducted to prove that the voltage variation is almost proportional to the PV capacity, analyzing voltage impact quantitatively without solving power flow equations. Sensitivity matrices are used to compare PV inverters connected at different locations. Different from the sensitivity matrices in [80]-[81], which are dependent on the system operating state, and the matrices in [82], which are only valid for radial systems, the matrices in this paper are shown to be only related to the system topology and its impedance, being also valid for meshed systems. Finally, from the sensitivity analysis conducted, guidelines are formulated for PV inverters in terms of location and reactive power control.

Further, contrary to the PV impact on voltage profile, system power loss forms a U-shape trajectory as the PV inverter capacity increases [83]. Accordingly, the optimal PV size differs for different systems [77],[84],[85]. Regarding the comparison of different local reactive power control strategies, [86] and [87] did not consider the impact on power loss, and [76] took the network power loss into consideration but neglected the reactive power control. Alternatively, centralized reactive power control has been shown to reduce network power losses the most [88]-[90], at a cost in communications that however is not practical.

This chapter analyzes the impact of PV generators on the voltage profile and power loss in distribution systems, taking into considerations PV inverters of different

capacities, installed at different locations, and with different local reactive power control strategies. For voltage impact, sensitivity matrices are used to compare PV generators connected at different locations. After some approximations, is shown how these matrices are only related to the system topology and impedances, results that are also valid to meshed systems. Guidelines are formulated for PV inverters in terms of geographical location and reactive power control scheme.

2.2 Test-Bed medium voltage power system

One of Southern California Edison (SCE)'s distribution feeders with very high penetration of photovoltaics is chosen as the test bed. It's a 12kV and very lightly loaded rural distribution feeder, with a radial topology and a PV integration that can be as high as 5MW. This paper assumes that the PV generator can be injected at any bus of the system. The circuit diagram of the distribution system is shown by Fig.2-1, and parameters for the system are given in [91], a typical day time loading of 20% of the peak

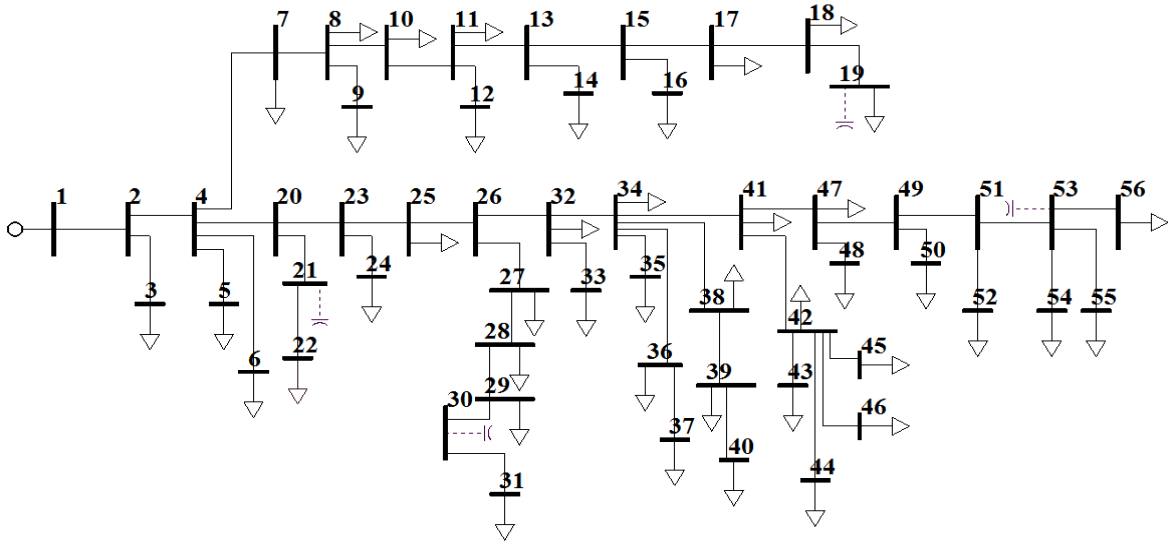

Figure 2-1 One-line diagram of the distribution system

with power factor 0.9 is chosen as the base operation point [91]. The system has 56 buses, and bus 1 is the slack bus with voltage of 1.0 p.u. , all the other buses are load buses when PV generators are not connected. The base capacity for the system is 1 MVA.

2.3 Impact on voltage profile

Voltage contouring function of PSS/E is utilized to visibly analyze the impact of PV injection on voltage profile. The color of the buses and surrounding area is determined by the voltage magnitude of the power flow calculation results. Fig.2-2 is the voltage contouring results along with the color setting when active power injected from PV farm varies because of the irradiance change. The color is warmer when the voltage is higher. Blue corresponds to voltage magnitude of 0.975 p.u., which is the lower limit by the standard. In the other hand, yellow corresponds to voltage magnitude of 1.05 p.u., which is the upper limit. And dark red corresponds to voltage magnitude even higher than the upper limit.

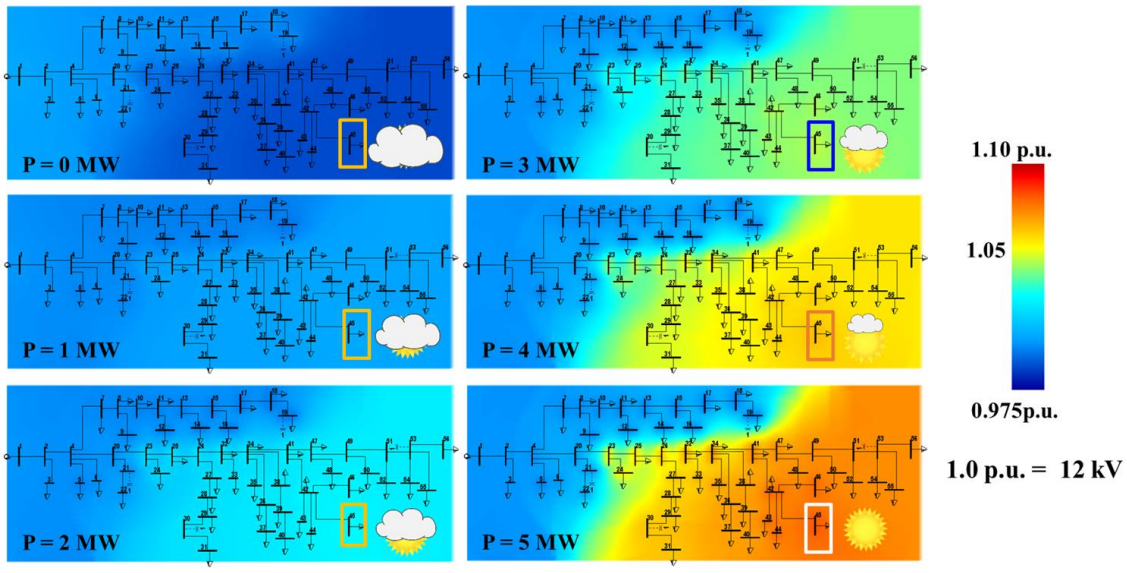

Figure 2-2 Voltage contouring of the distribution system

As the irradiance increases from 0% to 100% with the step of 20%, the active power injected adds up by 1 MW from case to case. It can be observed clearly that the active power injected boosts up the voltage profile of the whole distribution system, and higher the capacities, bigger the impact on the voltage profile.

2.3.1 Sensitivity analysis about impact on voltage profile

As mentioned before handed that the voltage impact is higher as PV capacity increases. Actually the voltage boost and the active power injected are linearly related illustrated by the curve of Fig.2-3, which is the voltage curve of several typical buses in the system in terms of active power injected from PV farm on bus 45. All the voltage curves are almost straight lines with different slope rates, which induces the interest of sensitivity analysis about voltage increase over active power injection. Through the results of sensitivity analysis, the impact of one PV farm on all buses in the same distribution system can be compared very easily as well as the cases of different PV connection locations.

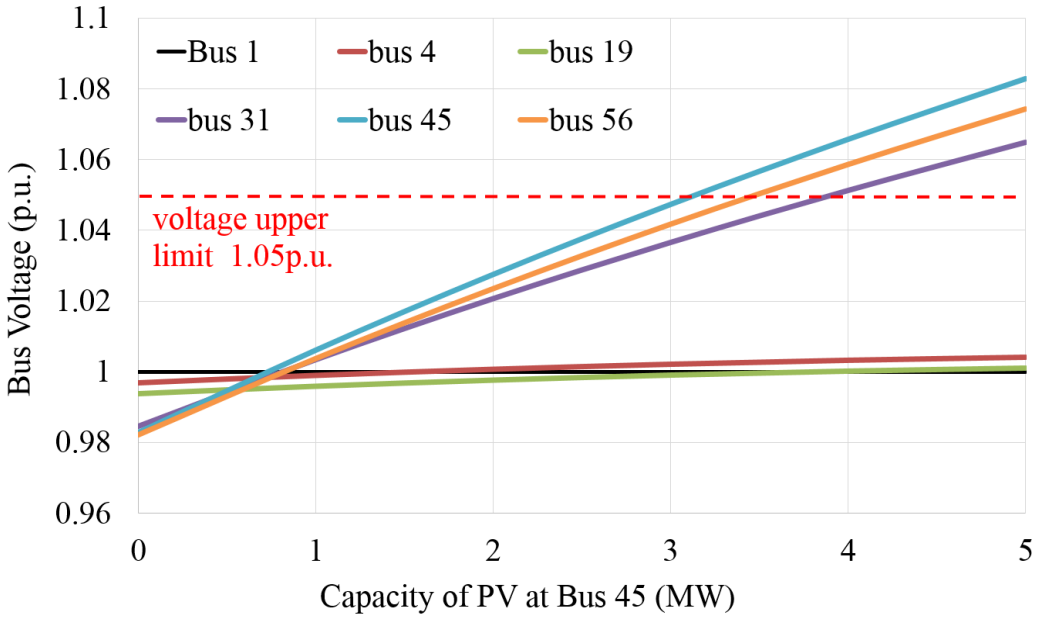

Figure 2-3 56 bus system voltage profile with PV at bus 45

The system voltage profile variation due to PV injection is determined by nonlinear power flow equations. Sensitivity analysis is the linearization of these power flow equations, which seeks to exchange solution accuracy for efficiency. The linearization process is described below:

There are *n* busses in the system, in which there are *m* load busses. The power flow equations are

$$\begin{cases} P_i = V_i \sum_{j=1}^{n} V_j (G_{ij} \cdot \cos\theta_{ij} + B_{ij} \cdot \sin\theta_{ij}) \\ Q_i = V_i \sum_{j=1}^{n} V_j (G_{ij} \cdot \sin\theta_{ij} - B_{ij} \cdot \cos\theta_{ij}) \end{cases} \tag{2-1}$$

where P_i and Q_i are the injected active and reactive power at bus *i*, G_{ij} and B_{ij} are real and reactive components of system admittance matrix $\mathbf{Y} = \mathbf{G} + j\,\mathbf{B}$. Linearization of (2-1) is

$$\begin{bmatrix} \mathbf{\Delta P} \\ \mathbf{\Delta Q} \end{bmatrix} = \begin{bmatrix} \partial\mathbf{P}/\partial\boldsymbol{\theta} & \partial\mathbf{P}/\partial\mathbf{V} \\ \partial\mathbf{Q}/\partial\boldsymbol{\theta} & \partial\mathbf{Q}/\partial\mathbf{V} \end{bmatrix} \begin{bmatrix} \mathbf{\Delta\theta} \\ \mathbf{\Delta V} \end{bmatrix} = \begin{bmatrix} \mathbf{H} & \mathbf{N} \\ \mathbf{M} & \mathbf{L} \end{bmatrix} \begin{bmatrix} \mathbf{\Delta\theta} \\ \mathbf{\Delta V} \end{bmatrix} = \mathbf{J} \begin{bmatrix} \mathbf{\Delta\theta} \\ \mathbf{\Delta V} \end{bmatrix} \tag{2-2}$$

in which

$$\begin{cases} H_{ii} = -Q_i - V_i^2 B_{ii}, H_{ij} = V_i V_j (G_{ij} \cdot \sin\theta_{ij} - B_{ij} \cdot \cos\theta_{ij}) \\ N_{ii} = P_i / V_i + V_i G_{ii}, N_{ij} = V_i (G_{ij} \cdot \cos\theta_{ij} + B_{ij} \cdot \sin\theta_{ij}) \\ M_{ii} = P_i - V_i^2 G_{ii}, M_{ij} = -V_i V_j (G_{ij} \cdot \cos\theta_{ij} + B_{ij} \cdot \sin\theta_{ij}) \\ L_{ii} = Q_i / V - V_i B_{ii}, L_{ij} = V_i (G_{ij} \cdot \sin\theta_{ij} - B_{ij} \cdot \cos\theta_{ij}) \end{cases} \tag{2-3}$$

Once **J** is known, the variation of voltage can be estimated by

$$\begin{bmatrix} \mathbf{\Delta\theta} \\ \mathbf{\Delta V} \end{bmatrix} = \mathbf{J}^{-1} \begin{bmatrix} \mathbf{\Delta P} \\ \mathbf{\Delta Q} \end{bmatrix} \tag{2-4}$$

In medium voltage distribution systems, bus voltages are within [0.975 p.u., 1.05 p.u.]

according to standard [92], so $V_i \approx 1$ p.u. For any line in the system, the angular difference between two busses θ_{ij} is very small, so $sin\ \theta_{ij} \approx 0$, $cos\ \theta_{ij} \approx 1$. In addition, $P_i << G_{ii}$ and $Q_i << B_{ii}$, so $H_{ii} \approx -B_{ii}$, $N_{ii} \approx -G_{ii}$, $M_{ii} \approx G_{ii}$, $L_{ii} \approx -B_{ii}$. After this approximation, (2-3) is transformed to

$$\begin{cases} H_{ii} = -B_{ii}, H_{ij} = -B_{ij} \\ N_{ii} = G_{ii}, N_{ij} = G_{ij} \\ M_{ii} = -G_{ii}, M_{ij} = -G_{ij} \\ L_{ii} = -B_{ii}, L_{ij} = -B_{ij} \end{cases} \tag{2-5}$$

which is equal to

$$\mathbf{J} = \begin{bmatrix} \mathbf{H} & \mathbf{N} \\ \mathbf{M} & \mathbf{L} \end{bmatrix} = \begin{bmatrix} -\mathbf{B_1} & \mathbf{G_1} \\ -\mathbf{G_2} & -\mathbf{B_2} \end{bmatrix} \tag{2-6}$$

In (2-6), $\mathbf{B_1}$ and $\mathbf{B_2}$ are formed by elements of **B**, and $\mathbf{G_1}$ and $\mathbf{G_2}$ are formed by elements of **G**. The dimension of $\mathbf{B_1}$, $\mathbf{B_2}$, $\mathbf{G_1}$ and $\mathbf{G_2}$ is *(n-1)×(n-1)*, *m×m*, *(n-1)×m*, and *m×(n-1)* respectively. It can be concluded from (2-6) that

$$\mathbf{J}^{-1} = \begin{bmatrix} -(\mathbf{B_1} + \mathbf{G_1}\mathbf{B_2^{-1}}\mathbf{G_2})^{-1} & (\mathbf{B_1} + \mathbf{G_1}\mathbf{B_2^{-1}}\mathbf{G_2})^{-1}\mathbf{G_2}\mathbf{B_2^{-1}} \\ (\mathbf{B_2} + \mathbf{G_2}\mathbf{B_1^{-1}}\mathbf{G_1})^{-1}\mathbf{G_2}\mathbf{B_1^{-1}} & -(\mathbf{B_2} + \mathbf{G_2}\mathbf{B_1^{-1}}\mathbf{G_1})^{-1} \end{bmatrix} \tag{2-7}$$

such that

$$\mathbf{\Delta V} = \mathbf{VP} \cdot \mathbf{\Delta P} + \mathbf{VQ} \cdot \mathbf{\Delta Q} \tag{2-8}$$

in which

$$\begin{cases} \mathbf{VP} = (\mathbf{B_2} + \mathbf{G_2}\mathbf{B_1^{-1}}\mathbf{G_1})^{-1}\mathbf{G_2}\mathbf{B_1^{-1}} \\ \mathbf{VQ} = -(\mathbf{B_2} + \mathbf{G_2}\mathbf{B_1^{-1}}\mathbf{G_1})^{-1} \end{cases} \tag{2-9}$$

The sensitivity matrices in (2-9) can be used to estimate voltage impact of PV active and reactive power injection. For a radial distribution system without shunt devices, including fixed or switched capacitors, it can be proved that the sensitivity matrices in (2-9) match the sensitivity matrices in [82], which were obtained from radial power flow models, with the advantage that the elements of the matrices in (2-9) are directly related to line impedances. Additionally, whereas the sensitivity matrices in [82] are only applicable to radial systems, the matrices in (2-9) also apply to meshed distribution systems.

For a radial system, there is one slack bus at the substation which can be set as bus 1, the other busses are treated as load busses (constant active power and reactive power injection), which means $m = n - 1$, $\mathbf{B_1} = \mathbf{B_2} = \mathbf{B}(2{:}n, 2{:}n)$, $\mathbf{G_1} = \mathbf{G_2} = \mathbf{G}(2{:}n, 2{:}n)$, where the bus number is based on its respective distance to bus 1. Further, when there are n branches between the busses, set the bus with smaller number as the starting bus for each branch, and number the branches based on their starting bus number. Set $\mathbf{Y_L}$ as a $n \times n$ diagonal matrix formed by the admittances of all branches, $\mathbf{Y_L} = \mathbf{Y_G} + j\,\mathbf{Y_B}$. Set $\mathbf{Y_Z}$ as a $n \times n$ diagonal matrix formed by impedances of all branches, $\mathbf{Y_Z} = \mathbf{Y_R} + \mathrm{j}\,\mathbf{Y_X}$

$$\begin{cases} \mathbf{Y_L} = diag(g_1 + jb_1, g_2 + jb_2, \cdots, g_n + jb_n) \\ \mathbf{Y_G} = diag(g_1, g_2, \cdots, g_n), \mathbf{Y_B} = diag(b_1, b_2, \cdots, b_n) \\ \mathbf{Y_Z} = diag(r_1 + jx_1, r_2 + jx_2, \cdots, r_n + jx_n) \\ \mathbf{Y_R} = diag(r_1, r_2, \cdots, r_n), \mathbf{Y_X} = diag(x_1, x_2, \cdots, x_n) \end{cases} \tag{2-10}$$

$g_k + j\,b_k$ and $r_k + j\,x_k$ is the admittance and impedance of branch k, and $g_k + j\,b_k = 1/(r_k + \mathrm{j}\,x_k)$.

The node-branch incidence matrix [93] is defined below to keep track of the way

branches and nodes are connected, for a radial system without shunt devices, the dimension of **A** is $n \times n$. In consequence of the way the busses and branches are numbered, **A** is a lower triangular matrix and

$$\mathbf{A} = \begin{bmatrix} \mathbf{A_b} \\ \mathbf{A_l} \end{bmatrix} = \begin{array}{c} \text{branches connected} \\ \text{to bus 1} \\ \hline \text{the other branches} \end{array} \begin{bmatrix} 1 & 0 & \cdots & 0 \\ 0 & 1 & \cdots & 0 \\ \vdots & \vdots & \ddots & \vdots \\ \hline 1 & -1 & \cdots & 0 \\ 1 & 0 & \cdots & 0 \\ \vdots & \vdots & \ddots & \vdots \end{bmatrix} \tag{2-11}$$

$$\begin{cases} \mathbf{B_1} = \mathbf{B_2} = \mathbf{A}^{\mathbf{T}} \mathbf{Y_B} \mathbf{A} \\ \mathbf{G_1} = \mathbf{G_2} = \mathbf{A}^{\mathbf{T}} \mathbf{Y_G} \mathbf{A} \end{cases} \tag{2-12}$$

Substituting (2-12) to (2-9) yields,

$$\begin{cases} (\mathbf{B_2} + \mathbf{G_2} \mathbf{B_1^{-1}} \mathbf{G_1})^{-1} \mathbf{G_2} \mathbf{B_1^{-1}} = \mathbf{A}^{-1} \mathbf{Y_R} (\mathbf{A}^{\mathbf{T}})^{-1} \\ -(\mathbf{B_2} + \mathbf{G_2} \mathbf{B_1^{-1}} \mathbf{G_1})^{-1} = \mathbf{A}^{-1} \mathbf{Y_X} (\mathbf{A}^{\mathbf{T}})^{-1} \end{cases} \tag{2-13}$$

so that the voltage sensitivity matrices in terms of active power and reactive power are

$$\begin{bmatrix} \Delta V_1 \\ \Delta V_2 \\ \vdots \\ \Delta V_n \end{bmatrix} = \begin{bmatrix} 0 & 0 \\ 0 & \mathbf{A}^{-1} \mathbf{Y_R} (\mathbf{A}^{\mathbf{T}})^{-1} \end{bmatrix} \begin{bmatrix} \Delta P_1 \\ \Delta P_2 \\ \vdots \\ \Delta P_n \end{bmatrix} + \begin{bmatrix} 0 & 0 \\ 0 & \mathbf{A}^{-1} \mathbf{Y_X} (\mathbf{A}^{\mathbf{T}})^{-1} \end{bmatrix} \begin{bmatrix} \Delta Q_1 \\ \Delta Q_2 \\ \vdots \\ \Delta Q_n \end{bmatrix} \tag{2-14}$$

The voltage sensitivity matrices in terms of active power and reactive power are

$$\begin{cases} \mathbf{VP} = \begin{bmatrix} 0 & 0 \\ 0 & \mathbf{A}^{-1} \mathbf{Y_R} (\mathbf{A}^{\mathbf{T}})^{-1} \end{bmatrix} \\ \mathbf{VQ} = \begin{bmatrix} 0 & 0 \\ 0 & \mathbf{A}^{-1} \mathbf{Y_X} (\mathbf{A}^{\mathbf{T}})^{-1} \end{bmatrix} \end{cases} \tag{2-15}$$

The sensitivity matrices of (2-15) match with sensitivity matrices in [82], which are **R** = $[R_{ij}]_{n \times n}$ = **VP** and **X** = $[X_{ij}]_{n \times n}$ = **VQ**

$$\begin{cases} R_{ij} := \sum_{(h,k)\in\zeta_i\cap\zeta_j} r_{hk} \\ X_{ij} := \sum_{(h,k)\in\zeta_i\cap\zeta_j} x_{hk} \end{cases} \tag{2-16}$$

Here ζ_i is the set of lines on the unique path from bus 1 to bus i, $\zeta_i \cap \zeta_j$ is the set of lines which are both in the unique path from bus 1 to bus i and the unique path from bus 1 to bus j. $r_{hk} + j\, x_{hk}$ is the impedance of the line from bus h to bus k. The results of (2-8), (2-15) and (2-16) can be used to study the impact of active power and reactive power produced or consumed on voltage magnitude of the whole system.

For meshed system, (2-16) is no longer applicable as there is no unique path from bus 1 to bus i. But $\mathbf{Y} = \mathbf{G} + j\,\mathbf{B}$ can still be obtained from the system topology and impedances to be substituted to (2-9) to obtain the sensitivity matrices.

The sensitivity matrix of **VP** is composed by the resistive part of the lines while the sensitivity matrix of **VQ** is composed by the inductive part of the lines. One big advantage of the sensitivity matrices is that their values are only related to the line impedances and independent of the load status or operation points of the system.

2.3.2 PV under unity power factor

To test the feasibility of linearizing the impact on voltage profile and accuracy of the sensitivity matrices, voltage profile change of the several typical buses is estimated using the increasing ratios of (15) and (16) and compared with accurate power flow results from PSS/E in Fig.2-4. The solid curves are from PSS/E power flow calculation which is accurate and the dashed lines are linear estimation based on the original voltage profile without PV injection added by the increasing rates from (15) and (16) times the PV active power injection. It can be observed that the estimation results match with accurate results

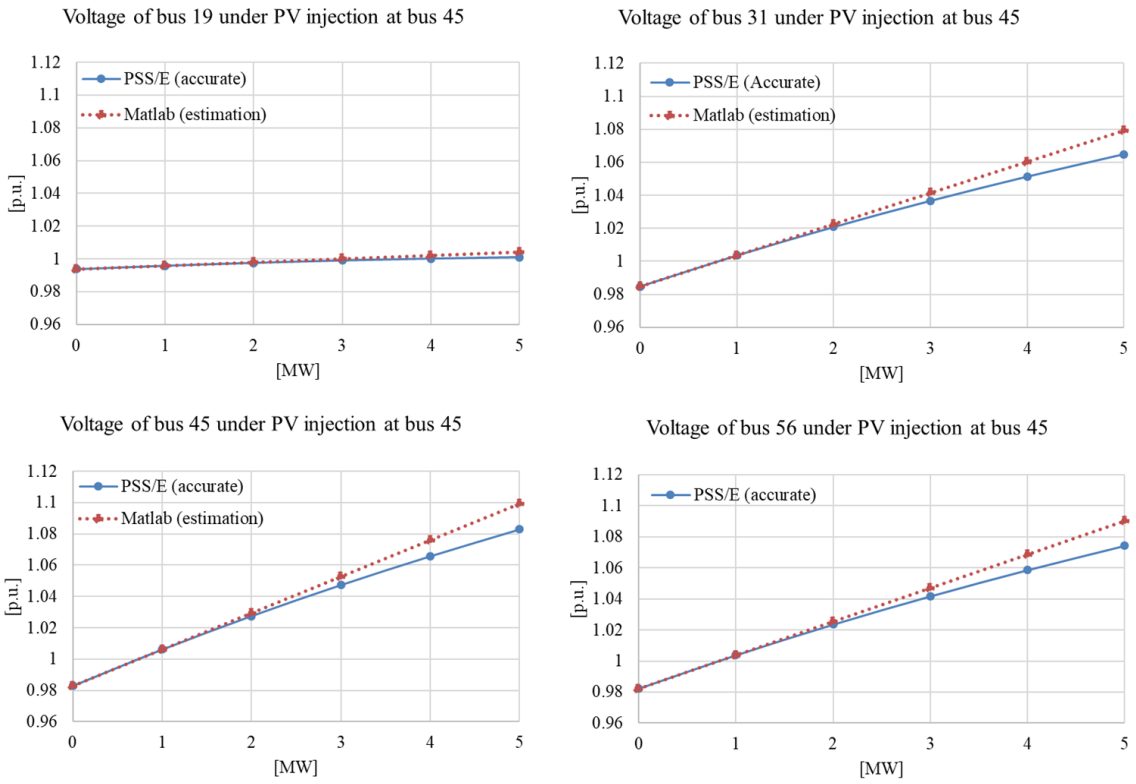

Figure 2-4 System voltage profile with different capacities of PV at bus 45.

very well, proving that the sensitivity ratios are reliable and useful as an index for voltage profile impact.

Part of the sensitivity matrix **VP** which is the sensitivity index of voltage increase over active power injection for 56 bus is shown in Table 2-1.

Table 2-1 Elements of sensitivity matrix VP of 56 bus system

VP_{ij} i \ j	19	31	41	45	56
19	0.0414	0.0021	0.0021	0.0021	0.0021
31	0.0021	0.0296	0.0189	0.0189	0.0189
41	0.0021	0.0189	0.0216	0.0216	0.0216
45	0.0021	0.0189	0.0216	0.0233	0.0216
56	0.0021	0.0189	0.0216	0.0216	0.0255

It can be concluded that:

(1) The sensitivity matrices of has the highest value in diagonal elements, which means that the highest voltage impact is at the injection location. For example, the same injection capacity at bus 45 will cause biggest voltage raise at bus 45 than other buses in the test-bed system as shown in Fig.3. This is because that the increasing rate in the diagonal elements of **VP** is the added resistors along the path all the way from bus 1 to bus 45 (The path is bus 1-2-4-20-23-25-26-32-34-41-42-45). While the increasing rate at other buses, bus 56 for example, is the added resistors of path (the path of bus 1-2-4-20-23-25-26-32-34-41**)** which are both in the unique path from bus 1 to bus 45 *i* and the unique path from bus 1 to bus 56. Unity power factor PV generators will increase all bus voltages. The highest impact is at the injection bus.

(2) The sensitivity matrix VP is symmetrical. For radial 56 bus system, define bus j as behind bus i when bus i is on the unique path from bus 1 to bus j. Voltage increasing rates are the same at bus i and buses behind bus i, but higher than increasing rates of other buses, because the intersection part of ζi and ζj has more lines when j = i or bus j is behind bus i.

(3) To avoid system under-voltage and overvoltage profile, PV generator should be connected as close to the substation as possible. Sensitivity matrix element serves as the electrical distance, which is dominated by active part of line. The impact on voltage profile is more severe if PV farm is connected to the grid with further electrical distance from the substation. In the case of connection to bus 45, 5 MW of PV will cause the connection bus voltage to exceed the upper limit as shown in Fig.3. Bus 45 is an eligible location for 3 MW of PV, but not for 4 MW or 5 MW

of PV. The eligible maps for different capacities of PV are shown by Fig.2-5. Buses eligible for 5 MW of PV are labeled with red flags, buses eligible for 3 MW but not for 5 MW are labeled with yellow flags, and buses eligible for 1 MW but for 3 MW or above are labeled with green flags. As the PV capacity increases, more and more buses are excluded from eligible locations. When PV capacity increases to 5 MW, PV generators can only be connected to buses very close to the substation to avoid overvoltage problems. So to reduce the impact of voltage profile, the PV farm is better to be connected to the substation as close as possible.

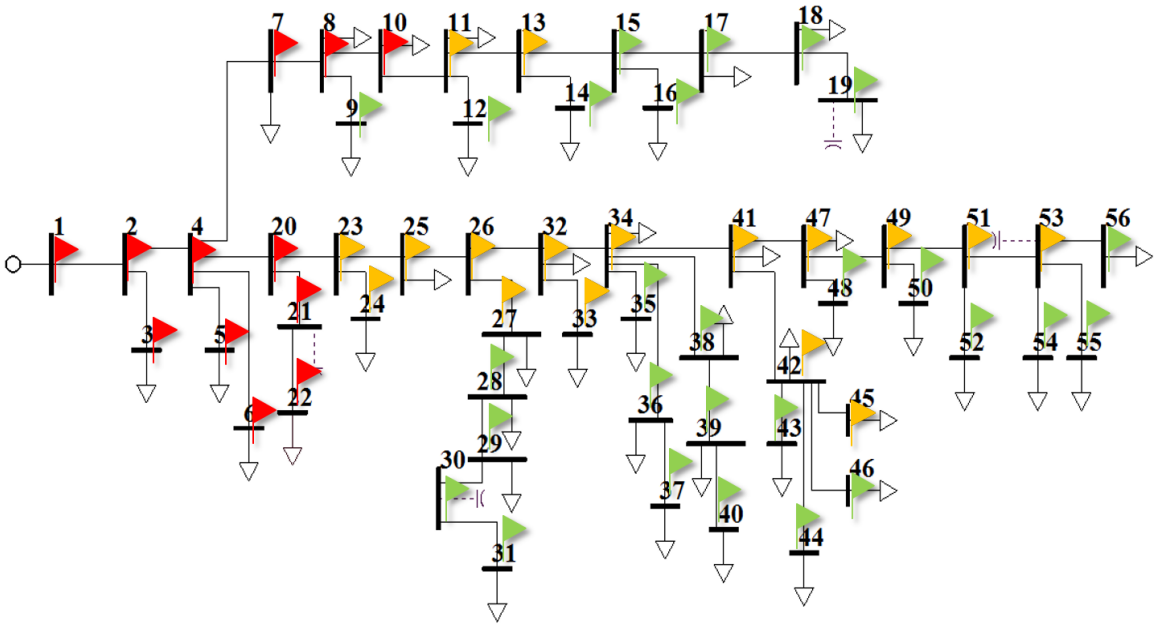

Figure 2-5 Eligible allocations for different PV capacities in 56 bus system

2.3.4 PV under different reactive power control

With rapid development of PV penetration, the impact on voltage profile is not ignorable as confirmed by last section when PV connection bus voltage exceeds the upper limit. Consequently, the IEEE 1547 standard has been updated which requires the

PV in the distribution system to help regulate voltage by utilizing its reactive power capability.

The commonly used photovoltaic generator local reactive power control modes include mode 1 unity power factor, mode 2 fixed reactive power, mode 3 fixed power factor, mode 4 reactive power as a function of active power (Watt-var mode) and mode 5 reactive power as a function of bus voltage (Volt-var mode) [78],[94]. Mode 4 and mode 5 are illustrated by Fig.2-6.

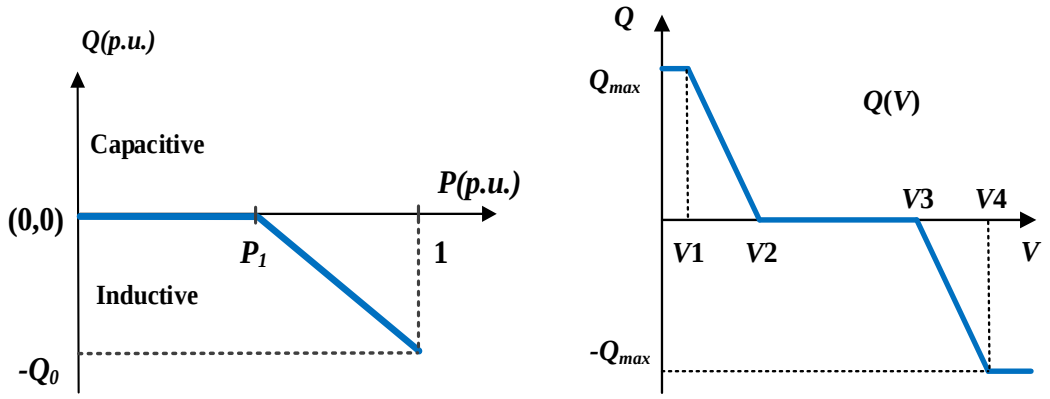

Figure 2-6 (a) Watt-var mode curve (b) Volt-var Q= f(V) mode droop curve

All five modes are applied on the PV farm connected to bus 45. Fig.2-7 is the voltage profile of PV farm terminal bus 45 when the PV active power increases from 0 to full power in correspond to irradiance variation. In mode 2, reactive power reference is set to be 1.5 MVar inductive to compensate the voltage boost caused by active power injection shown by mode 1 curve, but this setting has the problem of under-voltage when irradiance is low, showing that this mode is lack of flexibility for voltage regulation as a local control strategy. In mode 3, power factor is set to be 0.91 lagging. In mode 4, P_1 = 3.5 MW and the slope is -1 in the curve in Fig.2-6(a). In mode 5, V_1 = 0.975 p.u., V_2 = 1.00 p.u., V_3 = 1.025 p.u., V_4 = 1.05 p.u. and Q_{max} = 2.5 MVar. Mode 3 to mode 5 are all

able to regulate the PV bus voltage within the limit of ASIC standard [92]. While Mode 1 unity power factor and mode 2 constant Q are not able to regulate the voltage within range.

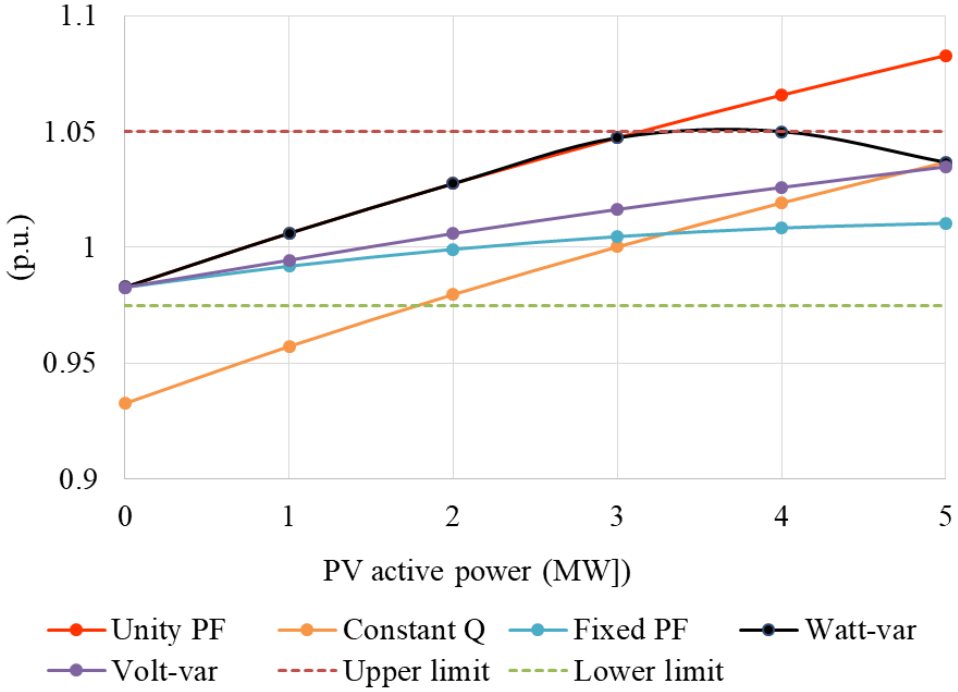

Figure 2-7 Voltage of PV injection bus under different Q control

When PV generator is working on mode 2-mode 4, voltage variation of all the load buses because of PV power injection can be estimated by (2-8). When PV generator is working on mode 5, reactive power injected by PV is the function of $Q = f(V)$ shown below

$$Q=\begin{cases} Q_{\max} & V<V1 \\ Q_{\max}\cdot\dfrac{V-V1}{V1-V2}+Q_{\max} & V1\le V\le V2 \\ 0 & V2\le V\le V3 \\ Q_{\max}\cdot\dfrac{V-V3}{V3-V4} & V3\le V\le V4 \\ -Q_{\max,} & V>V4 \end{cases} \tag{2-17}$$

The ratio of ΔQ/ΔV is a discrete function as in (2-17). There are two steps to estimate the voltage variation.

Step 1 apply $Q = f(V)$ control assuming no active power injection. Before $Q = f(V)$ control the voltage of bus i is V_0, if $V_0 \leq V2$ or $V_0 \geq V3$, $\Delta Q = f(V_0) \neq 0$, illustrated by the black curve in Fig.2-8.

Step 2 Looking from PV inverter to the grid, bus i voltage variation ΔV in terms of reactive power injection ΔQ also follow the yellow lines in Fig.2-8 according to the sensitivity analysis in section II, so the new operation point V_0' for bus i is the cross point of the yellow curve and the black curve. Without irradiance, $Q = f(V)$ control moves bus i voltage from V_0 to V_0', which helps prevent voltage to exceed upper and lower limit.

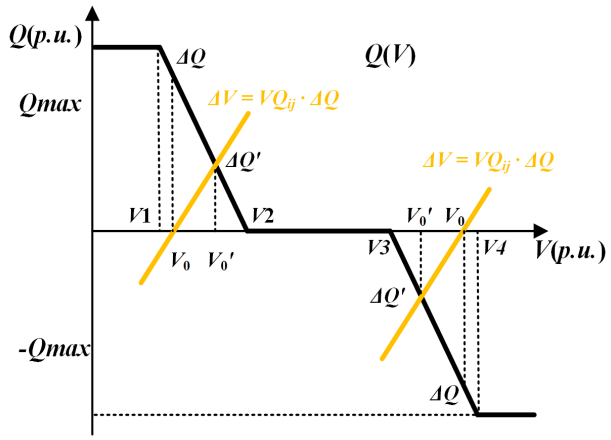

Figure 2-8 Voltage magnitude setting point acquisition

The voltage impact of PV generator working on mode 5 is estimated by step one illustrated by Fig.2-8. Fig.2-9 shows voltage of bus 45 in terms of active power injected by PV after reactive power control is applied on PV generator, which reveals that these reactive power control strategies are effective to prevent overvoltage problems. The accuracy of voltage sensitivity analysis in last section about different Q modes is proved

by comparison in Fig.2-9 as well, in which accurate full power flow results (solid lines) are from PSS/E and estimated results (dotted lines) are from MATLAB using sensitivity analysis. Fig.2-10 of eligible map of 5 MW of PV under reactive power control further confirms overvoltage relief due to reactive power control.

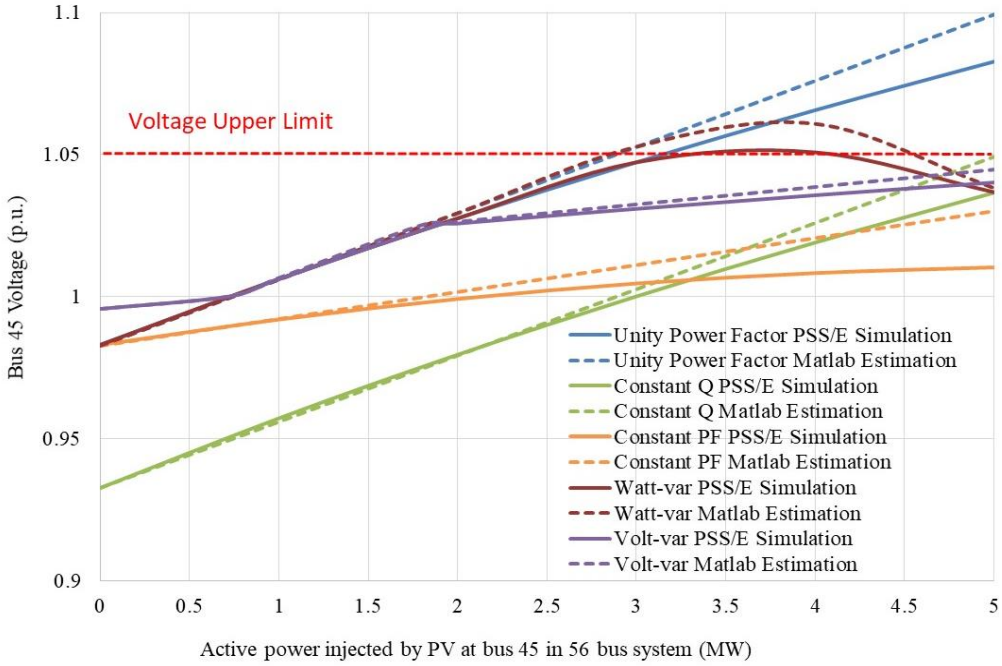

Figure 2-9 Bus 45 voltage with PV under different Q modes

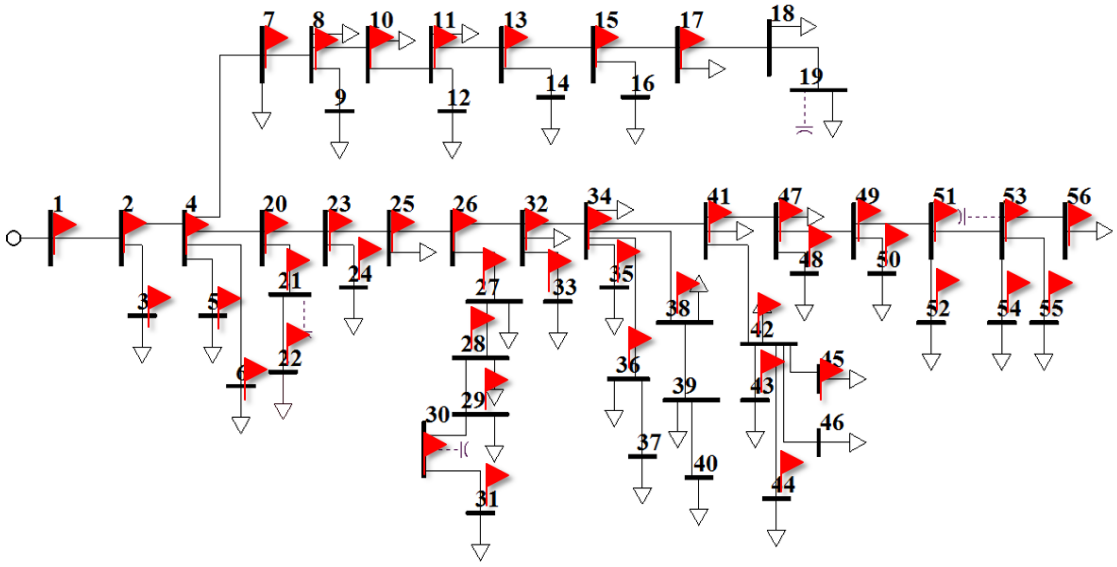

Figure 2-10 System eligible allocations for 5 MW of PV under mode 3,4 or 5

In Fig.2-10, bus 18 and bus 19 are still not eligible locations even after making use of full reactive power capability because these two buses have high R/X ratio, the voltage increase caused by active power can be not compensated enough by PV generator reactive power, other voltage regulation devices needed to be involved including OLTC and SVC.

2.3.5 Conclusions about impact on voltage profile

A known broad statement is that active power injected by PV inverters increases the system voltage. This paper showed that the rate by which the voltage increases at different geographical locations can be estimated accurately by the proposed sensitivity matrix, which was shown to be related to the line impedances. The diagonal elements are the resisters of the path from substation bus to the connection bus. And the sensitivity is diagonal dominant and symmetrical. The highest increasing rate is at the injection bus, which means that voltage variation caused by active power injection is biggest at the connection point compared to impact on other buses. To reduce the impact on voltage profile, connect PV as close to the substation as possible and make use of the reactive power capacity of the PV inverters. Further, in what regards the reactive power compensation capability of PV inverters, this paper showed that the reactive power control mode Q = f (V) is preferred over power factor control modes because Q = f (V) provides voltage regulation service when there's no sun, and Q = f (V) is effective to mitigate overvoltage and under voltage whereas power factor control cannot achieve at the same time. Nonetheless, there still will be a PV penetration limit even under reactive power control since PV inverters have a limited reactive power control capability at full active power, which is also limited by applicable standards and grid codes.

2.4 Impact on system power loss

2.4.1 PV under unity power factor

In Fig.2-11, as the capacity of PV generator at bus 19 in 56 bus system increases, system power loss trajectory forms a U-shape curve. The explanation is that when PV injection is very small, power flow of all lines is reduced, resulting in power loss decrease, as PV injection increases, reversed power flow in certain lines will increase system power flow instead.

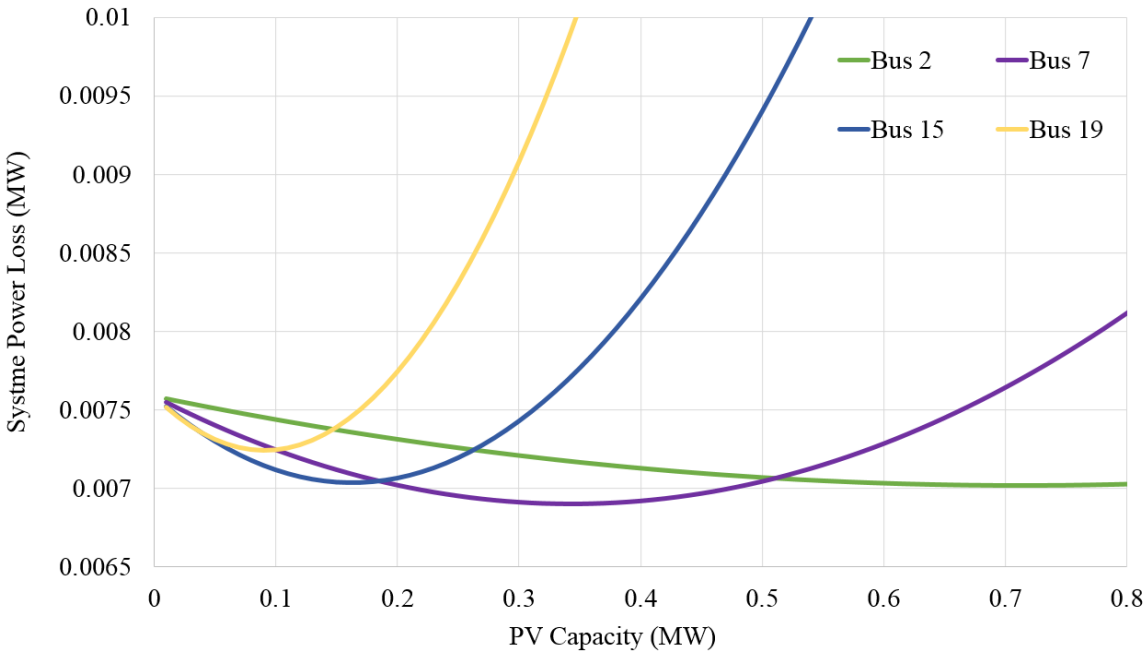

Figure 2-11 System loss when PV generator is connected to different buses

It also shows that the U shape curves of different injection locations have different optimal PV percentage, because threshold to cause reverse power flow is different for different buses as the load upstream and downstream is different for each bus, the optimal PV injection location which causes least system power loss is different. Comparison of power loss of cases in which PV is connected each case provides the optimal allocation.

The optimal allocation for PV capacity of 0-1MW in 56 bus system is listed in Table 2-2. For a fixed amount of active power injection by PV generator, the optimal location is the bus which has half of the PV capacity of load downstream.

Table 2-2 Optimal allocation for different PV capacity

PV capacity (MW)	0.2	0.4	0.6	0.8	1
Load behind optimal bus (MW)	0.1032	0.2248	0.375	0.4386	0.4907
Optimal location Under mode 1	Bus 51	Bus 41	Bus 34	Bus 32	Bus 23

2.4.2 PV under different reactive power control

The impact on the power loss in terms of reactive power injected is also a U-shape curve (system only has inductive load). Comparison of different reactive power control shows that mode 4 and mode 5 only become inductive when voltage is boosted by the active power from solar power, so is preferred to reduce the impact on power loss.

Different amount of active power and reactive power is injected to bus 45 in 56 bus system, System power loss is plotted in Fig.2-12, which reveals that for the typical load condition of 56 bus system, optimal P is not dependent on Q, and optimal Q is not dependent on P. Optimal P and optimal Q are positive, which means certain amount of active power and reactive power should be injected to achieve minimum power loss.

To analyze the impact on system power loss, different amount of active power and reactive power is injected to bus 45 in 56 bus system. System power loss is plotted in Fig.2-13, Fig.2-13 reveals that for the typical load condition of 56 bus system, system power loss forms a U shape curve both for active power injection and reactive power injection, optimal P is not dependent on Q, and optimal Q is not dependent on P.

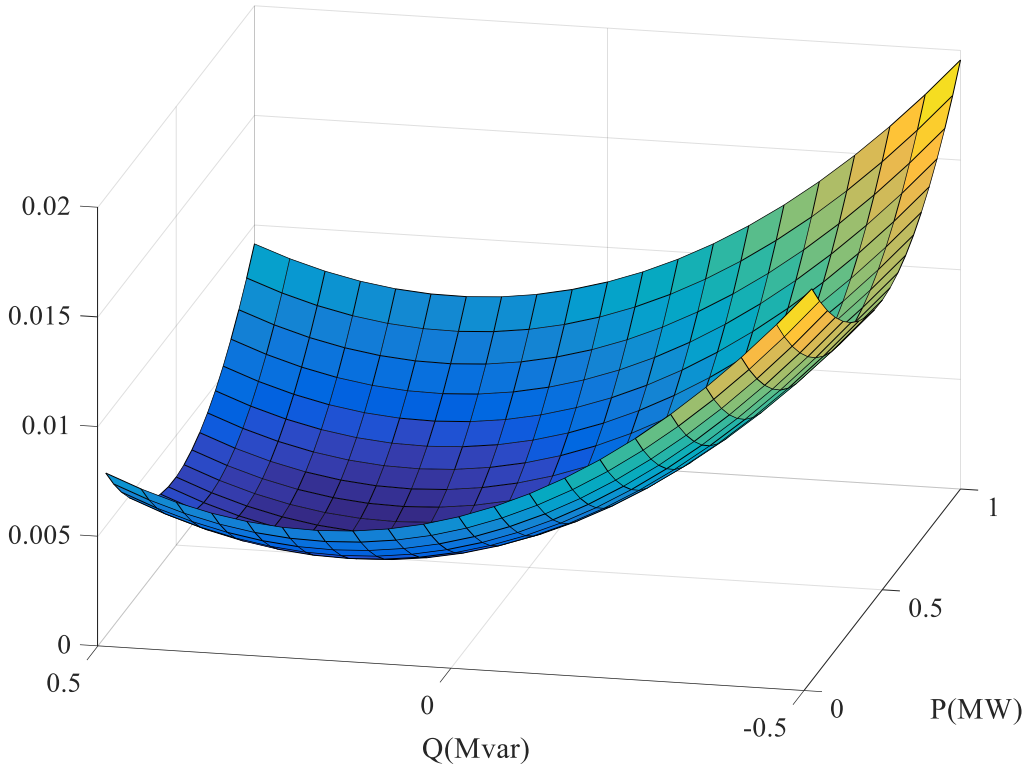

Figure 2-12 System loss in terms of P and Q injected to bus 45

Optimal P and optimal Q are positive, which means certain amount of active power and reactive power should be injected to achieve minimum power loss and help to understand the comparison of impact on system power loss of different reactive power control modes in Fig.2-13. Power loss under unity power factor is set as base value of 100% in each set of bar curves. Mode 2 and 3 cause higher power loss than other options because PV inverter in mode 2 and 3 is consuming reactive power all the way. In contrast, PV under mode 4 and mode 5 is only inductive when needed (the active power injected exceeds P_1 or PV terminal voltage is over the threshold of V_3). In addition, when irradiance is zero, mode 5 injects reactive power because voltage bus 45 is below V_2=1.00p.u., which reduces system power loss compared to other modes.

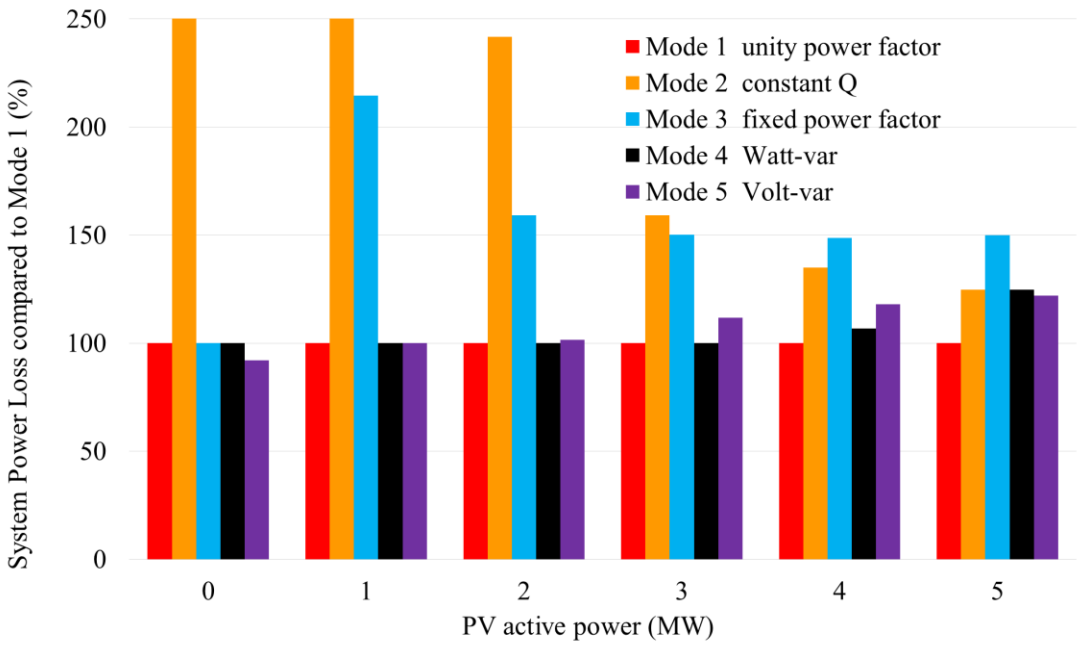

Figure 2-13 System power loss comparison of different Q modes

In sum, mode 5 volt-var mode is the best option considering voltage regulation and system power loss because

(1) Mode 1 unity power factor and mode 2 constant Q are not able to regulate the voltage within range.

(2) Mode 3 costs more system power loss than mode 4 and mode 5.

(3) Mode 5 is only inductive when needed and is able to deal with both overvoltage and under voltage.

2.4.3 Conclusions about impact on power loss

As PV capacity increases, system power loss forms a U shape curve, which indicates that the impact on power loss is nonlinear and cannot be studied by using sensitivity analysis as in section 1.3. A certain amount of active power and reactive power should be injected to reduce system power loss. The optimal values of injection depends on injection buses and the optimal active power is independent of reactive power. Optimal

location of PV connection for minimum system power loss depends on load distribution. And the comparison of different reactive power control modes shows that reactive power control of mode 4 voltage-var or Q =f(V) and mode 5 watt-var P = f(Q) are preferred to reduce the impair on power loss because of inductive reactive power.

2.5 Conclusions

A static analysis based on distribution system power flow regarding PV as a load bus is done to research into the impact of PV on system voltage profile and power loss. Comparison is done between PV farm of different capacities, different locations and different reactive power control modes.

A broad known statement is that active power injected by PV inverters increases the system voltage. It is discovered that the impact of active power or reactive power on the voltage magnitude is almost linear, thus the rate by which the voltage increases at different geographical locations can be estimated accurately by the proposed sensitivity matrix, which was shown to be related to the system impedances. The biggest voltage influence is at the injection bus, the increasing ratio of which is dominated by the resistors between the substation and the PV bus. The voltage boost because of active power injection will cause a limitation of maximum PV capacity, which can be mitigated by connecting PV to a bus as close to the substation as possible or making use of the reactive power capability of PV. Further, in what regards the reactive power compensation capability of PV inverters, this paper showed that the reactive power control mode Q = f (V) is preferred over power factor control modes because Q = f (V) provides voltage regulation service when there's no sun, and Q = f (V) is effective to mitigate overvoltage and under voltage whereas power factor control cannot achieve at

the same time. Nonetheless, there will be a PV penetration limit even under reactive power control because PV has limited reactive power control capability at full active power and the high R/X ratio in the distribution system.

Furthermore, it is shown that as the capacity of PV inverters increases, the system power loss will find an optimum operating point that will vary both with the physical location of the PV inverter unit and with the amount of power injected, and that the use of reactive power compensation to mitigate the impact on the system voltage profile will detrimentally affect the system power loss, in what is then an operational tradeoff. Accordingly, and in what could be considered a guideline for PV inverter allocation, to reduce the impact on voltage profile PV these units should be connected as close to the substation as possible (electrical distance indicated by sensitivity matrix), where the optimal allocation to reduce network power loss will depend on the distribution of load. Q =f(V) is preferred compared to other reactive power control in both aspects.

Chapter 3. PV Inverter Impedances in D-Q Frame under Different Q Control Modes*

3.1 Introduction

With development of renewable energies worldwide, power system is seeing higher penetration at distributed level as well as transmission level. In addition, IEEE 1547 newest version requires PV inverters to have reactive power control, thus increasing inverter control complexity .As negative incremental resistance caused by constant power behavior of power converters may bring stability problem, stability of PV integration to distributed system attracts more and more attention. Different from real-time simulation or character root method, which require full models of all components in distributed system, the generalized Nyquist stability criterion (GNC) for stability analysis of three-phase AC power system only uses measured *d-q* Frame impedances. Compared to the positive sequence impedance method used previously, *d-q* frame impedance matrix method is more accurate for stability assessment of system with PV inverter that has non-symmetrical control in *d-q* frame including DC voltage loop and phase locked loop (PLL).

The goal of this chapter is to observe how the *d-q* frame impedance of utility-scale PV inverters is shaped by the power stage and the controllers. For the purpose of the

impact study, the *d-q* frame impedance model is derived from small-signal model of the PV generator, which is validated by MATLAB simulation and hardware experiments as well.

3.2 Derivation of *d-q* frame impedance of PV generator

The configuration of a utility PV generator testbed is shown in Fig.3-1. The switching model is built in Simulink with switching frequency set to be 3 kHz. The rated capacity is 250 kW. The topology contains PV arrays, a DC capacitor, a single stage DC/AC inverter, a three phase LCL filter and a step up transformer. The PV arrays have 29 PV panels in series in each string and 40 strings in parallel. The rated DC voltage is 870 V, which is also the MPPT point of PV arrays under standard weather condition (1000 W/m2 and 25 ℃). The DC capacitor is chosen to be 8.2 mF to keep DV voltage ripple under ±5%. Parameters of LCL filter with resistor in series with cap are L_1 = 0.32 mH, L_2=0.32 mH,

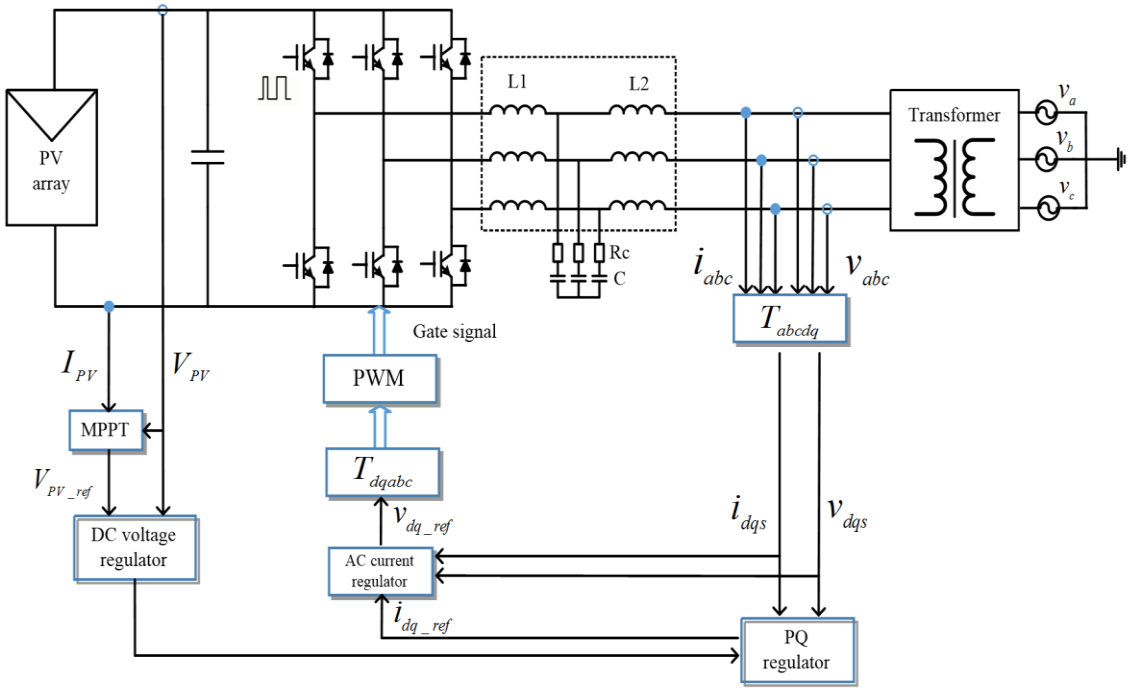

Figure 3-1 Switching model of the PV generator

C=70.3 μF, Rc = 0.50 Ω. The parameters of LCL filter are set to make sure that PV inverter output voltage and current harmonics are within standard limit. For three phase step up transformer, the rms values of line to line voltages of primary and secondary side are 330 V and 12 kV separately. Dual loop control strategy is applied in which inner current loops regulate output current in *d-q* axis separately and outer DC voltage loop regulates DC voltage. Reactive power can be regulated based on reactive current loop. The controller may have an outer AC voltage loop or reactive power loop according to different reactive power control strategies.

3.2.1 Open loop power stage model

With switching ripple ignored, average model of the PV generator in *d-q* axis is formed in Fig.3-2. Fig.3-2(a) is average model of DC side, while Fig.3-2(b) and Fig.3-2(c) are average models of AC side in *d-q* axis separately based on primary side voltage of step up transformer.

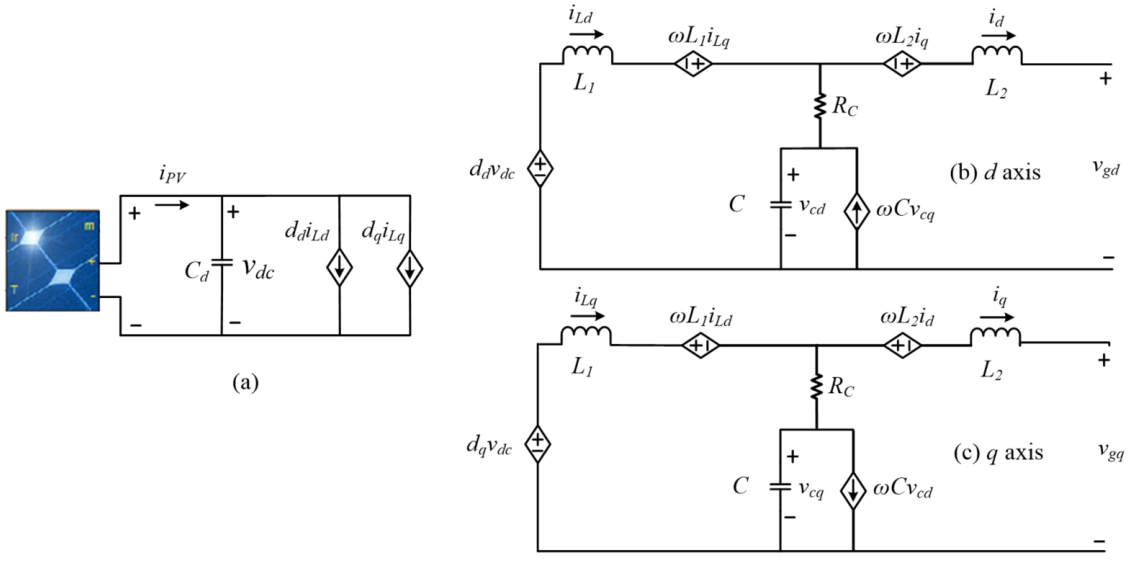

Figure 3-2 Average model of the PV generator power stage

Based on the average model of PV generator power stage of Fig.3-2, linearization can be made around the DC operation steady state. In small signal perturbation model of Fig.3-3, PV arrays can be equivalent to a voltage source with a resistor, while resistor and voltage source values are dependent on PV panel operation point [95].

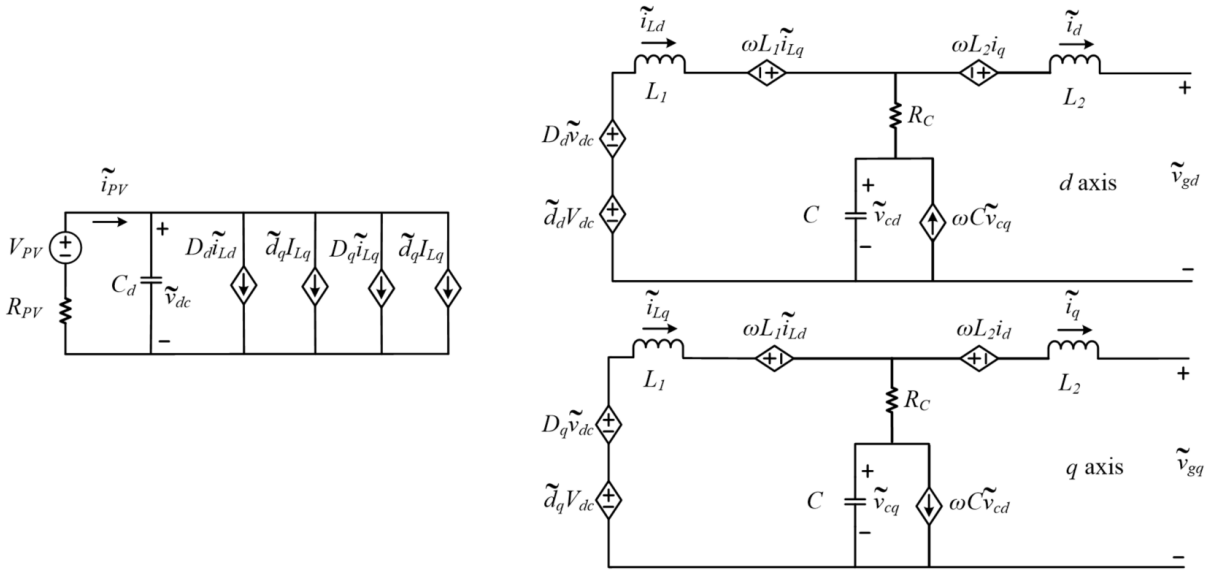

Figure 3-3 Small-signal model of the PV generator power stage

The I-V curve of the PV array is defined by the four parameters of V_{oc} = 36.3 V, V_{mpp} = 30 V, I_{sc} = 7.1839 A and I_{mpp} = 7.84A. For maximum power point, the small-sginal equivalent resistor R_{PV}=3.0269 Ω and V_{PV} = 7140 V. After PV array is represented by a voltage source with a resistor, seven order state space equations can be formed for power stage in Fig.3-3, while the state vector is

$$\vec{\mathbf{x}} = [\tilde{v}_{dc}, \tilde{i}_{Ld}, \tilde{i}_{Lq}, \tilde{v}_{cd}, \tilde{v}_{cq}, \tilde{i}_d, \tilde{i}_q]^T \tag{3-1}$$

the input vector is

$$\vec{\mathbf{u}} = [\tilde{d}_d, \tilde{d}_q, \tilde{v}_{gd}, \tilde{v}_{gq}]^T \tag{3-2}$$

and the output measurement is

$$\vec{\mathbf{y}} = [\tilde{v}_{dc}, \tilde{i}_d, \tilde{i}_q]^T \tag{3-3}$$

Solving the state space equations yields

$$\vec{\tilde{\mathbf{i}}}^{s} = \mathbf{G_{id}} \cdot \vec{\tilde{\mathbf{d}}}^{s} + \mathbf{G_{iv}} \cdot \vec{\tilde{\mathbf{v}}}^{s} \tag{3-4}$$

$$\tilde{V}_{DC} = \mathbf{G_{Dd}} \cdot \vec{\tilde{\mathbf{d}}}^{s} + \mathbf{G_{Dv}} \cdot \vec{\tilde{\mathbf{v}}}^{s} \tag{3-5}$$

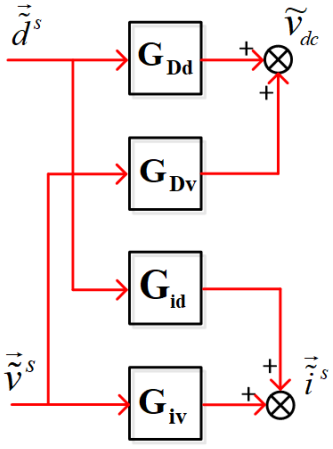

Figure 3-4 Transfer function diagram of PV inverter power stage dynamics

Equation (3-4)-(3-5) related to power stage dynamics are shown by red arrows and blocks in Fig.3-4,which is the diagram of small-signal model of PV inverter if only the dynamics of the power stage is considered and the output impedance is

$$\mathbf{Z} = \mathbf{G_{iv}}^{-1} \tag{3-6}$$

The impedance matrix of open loop power stage is a seven-order transfer function which includes the dynamics of DC capacitor and AC side LCL filter. The bode plots are shown in Fig.3-5.

At high frequencies (kHz), the bode plots are showing pure inductor dynamics, which is the AC side inductors. The resonant frequency of LCL filter is 1.5kHz. And there is a resonance at 10-100 Hz which is caused by DC side capacitor and AC side inductors and also influenced by the duty ratio as well. The dynamics change from capacitive to inductive at this resonant frequency. And below this frequency it's more impacted by DC

side capacitor and PV array equivalent resistance in small-signal model. The dynamics below100 Hz will be shadowed by the current controllers discussed in section 3.2.3.

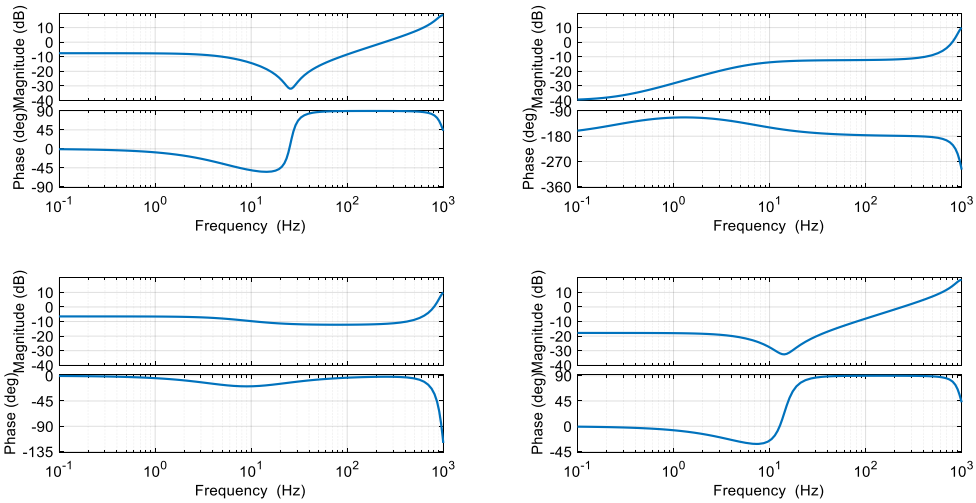

Figure 3-5 Bode plots of PV inverter terminal impedance with constant duty ratio control

3.2.2 Effect of PLL

Phase Lock Loop (PLL) track grid voltage phases to do transformation between *d-q* axis and *abc* axis. PLL bandwidth is set to be 6 Hz with PI block parameter to be k_{p_pll}=0.1, k_{i_pll} =1.

As mentioned by [35], the dynamics of PLL causes phase difference between grid d-q axis and controller *d-q* axis. $\tilde{\vec{\mathbf{d}}}^{s}, \tilde{\vec{\mathbf{v}}}^{s}, \tilde{\vec{\mathbf{i}}}^{s}, \tilde{\vec{\mathbf{i}}}_{\mathbf{L}}$ are variables in grid *d-q* axis while $\tilde{\vec{\mathbf{d}}}^{c}$, $\tilde{\vec{\mathbf{v}}}^{c}, \tilde{\vec{\mathbf{i}}}^{c}$, $\tilde{\vec{\mathbf{i}}}_{\mathbf{ref}}$ are the variables in converter *d-q* axis. (3-7)-(3-9) are the conversion between $\tilde{\vec{\mathbf{d}}}^{s}$, $\tilde{\vec{\mathbf{v}}}^{s}, \tilde{\vec{\mathbf{i}}}^{s}$ and $\tilde{\vec{\mathbf{d}}}^{c}$, $\tilde{\vec{\mathbf{v}}}^{c}, \tilde{\vec{\mathbf{i}}}^{c}$, $\tilde{\vec{\mathbf{i}}}_{\mathbf{ref}}$, which is shown by blue in Fig.3-6

$$\tilde{\vec{\mathbf{v}}}^{c} = \mathbf{G}_{\mathbf{PLL}}^{\mathbf{V}} \cdot \tilde{\vec{\mathbf{v}}}^{s} \tag{3-7}$$

$$\tilde{\vec{\mathbf{i}}}^{c} = \mathbf{G}_{\mathbf{PLL}}^{\mathbf{i}} \cdot \tilde{\vec{\mathbf{v}}}^{s} + \tilde{\vec{\mathbf{i}}}^{s} \tag{3-8}$$

$$\tilde{\vec{\mathbf{d}}}^{s} = \mathbf{G}_{\mathbf{del}} \cdot (\mathbf{G}_{\mathbf{PLL}}^{\mathbf{d}} \cdot \tilde{\vec{\mathbf{v}}}^{\mathbf{s}} + \tilde{\vec{\mathbf{d}}}^{\mathbf{c}}) \tag{3-9}$$

In which

$$tf_{PLL} = k_{ppll} + k_{ipll} \cdot \frac{1}{s} \tag{3-10}$$

$$G_{PLL} = \frac{tf_{PLL}}{s + V_d^s \cdot tf_{PLL}} \tag{3-11}$$

$$\mathbf{G_{PLL}^{V}} = \begin{bmatrix} 1 & V_q^s \cdot G_{PLL} \\ 0 & 1 - V_d^s \cdot G_{PLL} \end{bmatrix} \tag{3-12}$$

$$\mathbf{G_{PLL}^{d}} = \begin{bmatrix} 0 & -D_q^s \cdot G_{PLL} \\ 0 & D_d^s \cdot G_{PLL} \end{bmatrix} \tag{3-13}$$

$$\mathbf{G_{PLL}^{i}} = \begin{bmatrix} 0 & I_q^s \cdot G_{PLL} \\ 0 & -I_d^s \cdot G_{PLL} \end{bmatrix} \tag{3-14}$$

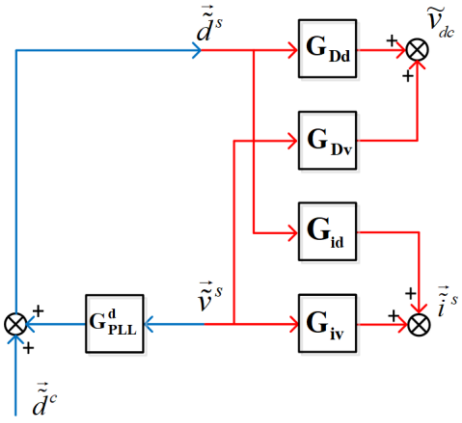

Figure 3-6 Transfer function diagram of PV inverter with constant duty cycle and PLL control

The loop in Fig.3-6 is solved to get PV impedance so that

$$\tilde{\vec{\mathbf{v}}}^{\mathbf{s}} = \mathbf{Z} \cdot \tilde{\vec{\mathbf{i}}}^{\mathbf{s}} \tag{3-15}$$

$$\mathbf{Z} = \left(\mathbf{G_{iv}} + \mathbf{G_{id}} \mathbf{G_{PLL}^{d}} \right)^{-1} \tag{3-16}$$

Fig. 3-7 shows how the PV inverter *d-q* frame impedance is influenced by PLL control. The bode plots have a clear difference below the PLL Bandwidth of 6 Hz. And negative sign of Z_{qq} is observed because of PLL synchronization.

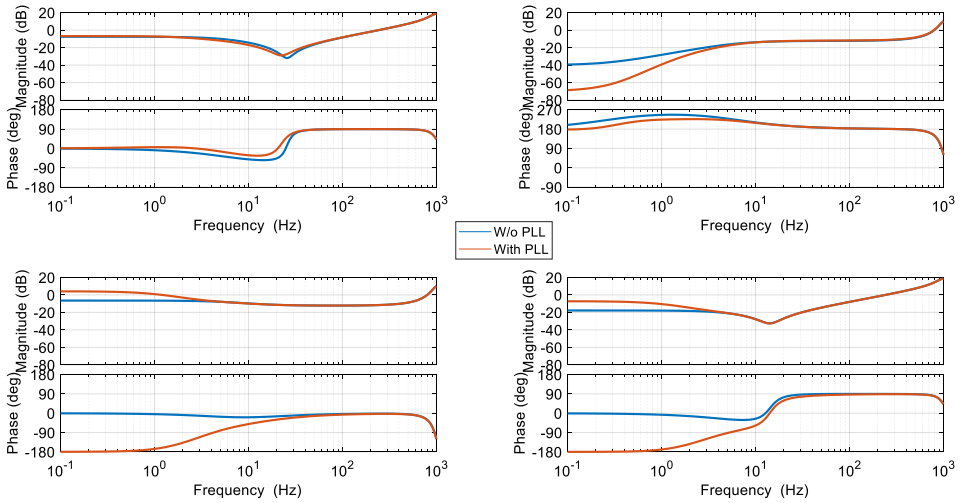

Figure 3-7 Comparison of PV inverter terminal impedance with and without PLL

3.2.3 Effect of current controller

For PV controller in Fig.3-1, AC current regulator is a PI controller with parameter of k_{pi}= 0.0011 and k_{ii}=0.33, making the current control bandwidth to be 250 Hz. The measured output of power stage $\vec{\mathbf{y}} = \left[\tilde{i}_d, \tilde{i}_q\right]^T$ goes through current regulator as shown by black lines and blocks in Fig.3-8. For controller related blocks,

$$\tilde{\vec{\mathbf{d}}}^c = \mathbf{G_{dei}} \cdot \tilde{\vec{\mathbf{i}}}^c + \mathbf{G_{ci}}(\tilde{\vec{\mathbf{i}}}_{\mathbf{ref}} - \tilde{\vec{\mathbf{i}}}^c) \tag{3-17}$$

in which $\mathbf{G_{dei}} = \begin{bmatrix} 0 & -\dfrac{\omega L}{V_{dc}} \\ \dfrac{\omega L}{V_{dc}} & 0 \end{bmatrix}$, $\mathbf{G_{ci}} = \begin{bmatrix} k_{pi} + \dfrac{k_{ii}}{s} & 0 \\ 0 & k_{pi} + \dfrac{k_{ii}}{s} \end{bmatrix}$.

Solving the transfer loop yields

$$\mathbf{Z} = \left\{\mathbf{G_{iv}} + \mathbf{G_{id}}\left[\mathbf{G^d_{PLL}} + \left(\mathbf{G_{dei}} - \mathbf{G_{ci}}\right) \cdot \mathbf{G^i_{PLL}}\right]\right\}^{-1} \cdot \left[\mathbf{I} - \mathbf{G_{id}}\left(\mathbf{G_{dei}} - \mathbf{G_{ci}}\right)\right] \tag{3-18}$$

Fig.3-9 is the comparison of impedances with and without current controller. It can be observed that with the current loop bandwidth of 250 Hz , the inverter is regulated as a constant current source, so the terminal impedance magnitude is boosted up a lot by the current controller by its control bandwidth. The non-diagonal elements of Zdq and Zqd represent the coupling between the d axis and q axis. The decoupling block $\mathbf{G_{dei}}$ of current controller is able to reduce the magnitude of Zdq and Zqd compared to open loop

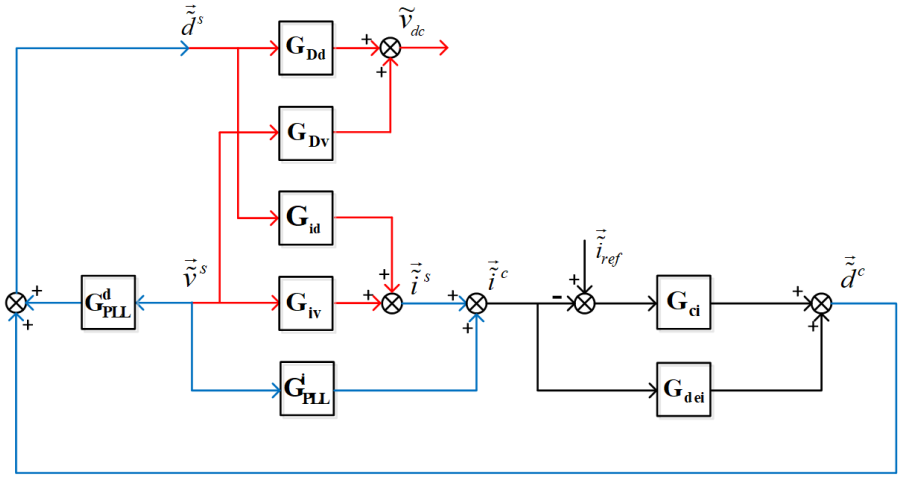

Figure 3-8 Transfer function diagram of PV inverter with closed current loop control

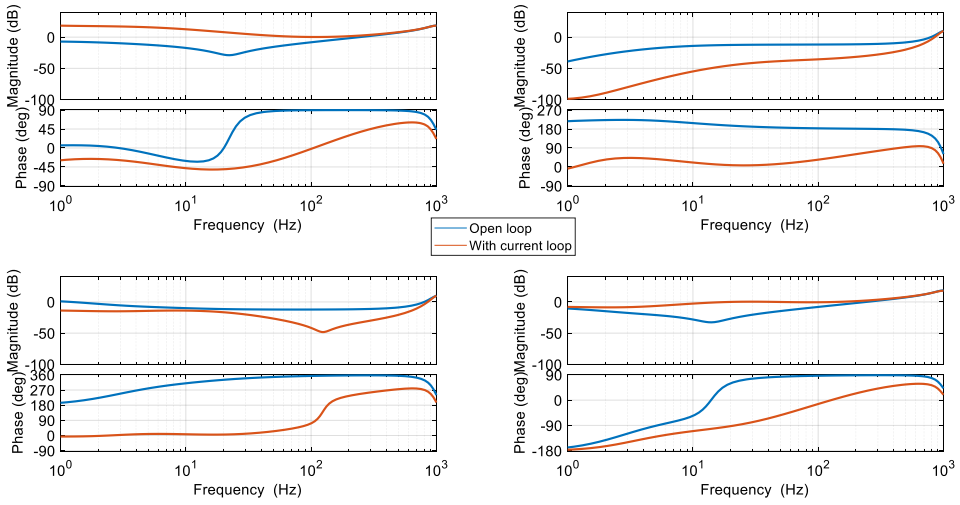

Figure 3-9 Bode plot of terminal impedances with and without current loop controller

case. As the LCL type of filter is used here and the measured and controlled currents are located at the grid side inductor, so the decoupling block $\mathbf{G_{dei}}$ of current controller is not able to completely remove the interactions of the d channel and q channel.

3.2.4 Effect of DC voltage controller

For PV controller in Fig.3-1, DC voltage regulator is a PI controller with parameter of k_{pv}=-3, k_{iv}=-30, making the DC voltage control loop bandwidth to be 22.2 Hz. V_{dc_ref} is the DC voltage reference given by maximum power point tracking (MPPT) block. The most widely used MPPT principle is perturb and observe (P&O), which perturbs PV array voltage to find the right direction of adjusting DC voltage to increase PV array output power . For utility scale single stage PV inverter, the frequency of MPPT block to change V_{dc_ref} is smaller than DC voltage loop bandwidth. The time interval to perturb PV array voltage is less than 1 second as environmental condition changes not very fast in PV farms. So in this paper, V_{dc_ref} is considered to be constant, which means that impedance derived is only valid above MPPT perturb frequency which is less than 1 Hz.

The measured output of power stage $\vec{\mathbf{y}} = \left[\tilde{v}_{dc}, \tilde{i}_d, \tilde{i}_q\right]^T$ goes through current regulator and voltage regulator blocks as shown by black lines and blocks in Fig.3-10. For controller related blocks,

$$\vec{\tilde{\mathbf{i}}}_{ref} = -\mathbf{G_{cvd}} \cdot \tilde{v}_{dc} \tag{3-19}$$

in which $\mathbf{G_{cvd}} = \begin{bmatrix} k_{pv} + \dfrac{k_{iv}}{s} \\ 0 \end{bmatrix}$.

Solving the transfer loop yields

$$\mathbf{Z}=\left\{\mathbf{G}_{\mathbf{iv}}+\mathbf{G}_{\mathbf{id}}\left(\mathbf{G}_{\mathbf{del}}\mathbf{G}_{\mathbf{ci}}\mathbf{G}_{\mathbf{cvd}}\mathbf{G}_{\mathbf{Dd}}+\mathbf{I}\right)^{-1}\left[\mathbf{G}_{\mathbf{PLL}}^{\mathbf{d}}+\left(\mathbf{G}_{\mathbf{dei}}-\mathbf{G}_{\mathbf{ci}}\right)\cdot\mathbf{G}_{\mathbf{PLL}}^{\mathbf{i}}-\mathbf{G}_{\mathbf{ci}}\mathbf{G}_{\mathbf{cvd}}\mathbf{G}_{\mathbf{Dv}}\right]\right\}^{-1} \cdot\left[\mathbf{I}-\mathbf{G}_{\mathbf{id}}\left(\mathbf{G}_{\mathbf{del}}\mathbf{G}_{\mathbf{ci}}\mathbf{G}_{\mathbf{cvd}}\mathbf{G}_{\mathbf{Dd}}+\mathbf{I}\right)^{-1}\left(\mathbf{G}_{\mathbf{dei}}-\mathbf{G}_{\mathbf{ci}}\right)\right] \tag{3-20}$$

Fig.3-10 is the comparison of impedances with and without DC voltage controller. It can be observed that with the current loop bandwidth of 22 Hz , the inverter is regulated as a

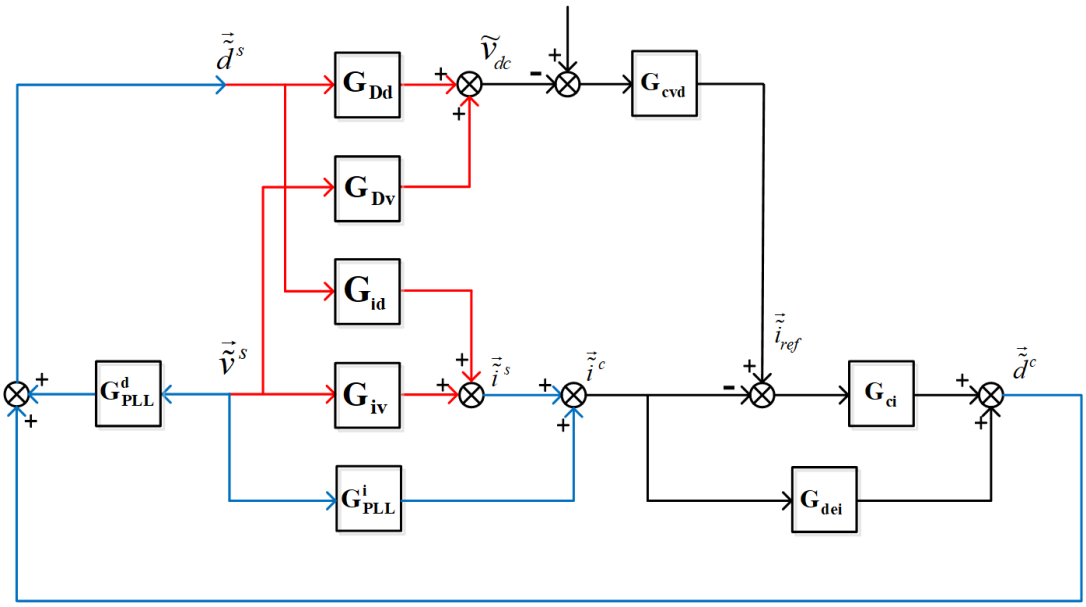

Figure 3-10 Transfer function diagram of PV inverter with dual loop control

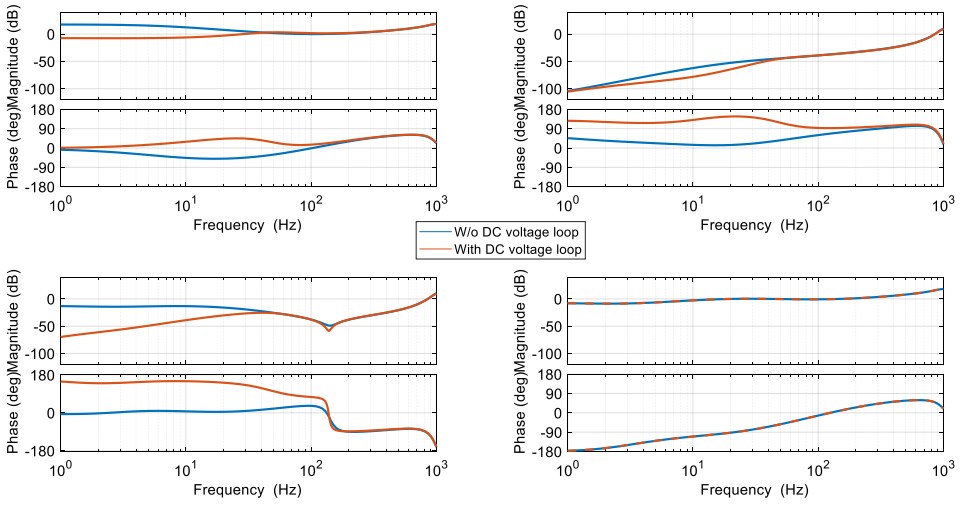

Figure 3-11 Bode plot of terminal impedances with and without DC voltage loop controller

constant power source (as the active power output stays the same as DC voltage stays the same), the terminal impedance magnitude is reduced a lot by the DC voltage controller within its control bandwidth. And the at very low frequencies, the magnitudes of Z_{dd} and Z_{qq} are the same, both are equal to V_d/I_d, but Z_{dd} has a positive sign and Z_{qq} has a negative sign because of PLL effect.

3.2.5 Effects of digital delay

The switching frequency is f_{sw} . The measurement and duty cycle update is done every switching period and executed next switching period. And the PWM modulation will also add some time delay which is averaged to be half the switching period. So the overall digital delay is 1.5 switching period and can be model as below

$$\mathbf{G_{del}} = \begin{bmatrix} \dfrac{1-0.5T_{del}\cdot s}{1+0.5T_{del}\cdot s} & 0 \\ 0 & \dfrac{1-0.5T_{del}\cdot s}{1+0.5T_{del}\cdot s} \end{bmatrix} \tag{3-21}$$

In which $T_{del} = 1.5T_{sw} = 1.5/f_{sw}$

Fig.3-12 is close-loop transfer function diagram of the PV inverter with digital delay. Solving the close loop yields

$$\begin{aligned} \mathbf{Z} = \Big\{ & \mathbf{G_{iv}} + \mathbf{G_{id}}(\mathbf{G_{del}}\mathbf{G_{ci}}\mathbf{G_{cvd}}\mathbf{G_{Dd}} + \mathbf{I})^{-1}\mathbf{G_{del}}\left[\mathbf{G^{d}_{PLL}} + \left(\mathbf{G_{dei}} - \mathbf{G_{ci}}\right)\cdot\mathbf{G^{i}_{PLL}} - \mathbf{G_{ci}}\mathbf{G_{cvd}}\mathbf{G_{Dv}}\right]\Big\}^{-1} \\ & \cdot\left[\mathbf{I} - \mathbf{G_{id}}(\mathbf{G_{del}}\mathbf{G_{ci}}\mathbf{G_{cvd}}\mathbf{G_{Dd}} + \mathbf{I})^{-1}\mathbf{G_{del}}\left(\mathbf{G_{dei}} - \mathbf{G_{ci}}\right)\right] \end{aligned} \tag{3-22}$$

And Fig.3-13 is the bode plot of the terminal impedances with and without digital delay.

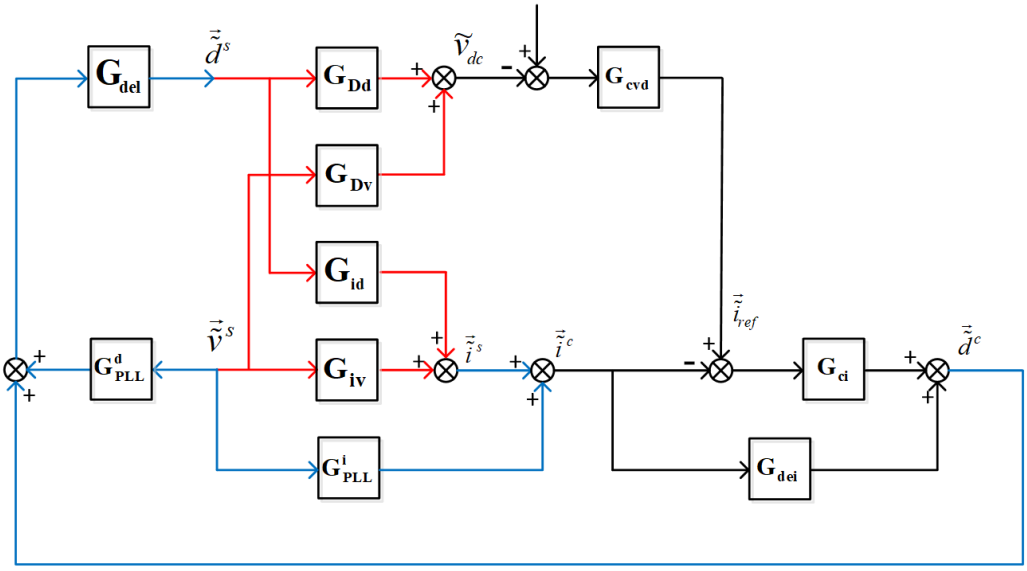

Figure 3-12 Transfer function diagram of PV inverter with dual loop control and digital delay

It can be observed that the impact is within 30 Hz to around 2kHz. The bigger change is the phase not the magnitude, because the digital delay transfer function doesn't change the magnitude but the phase.

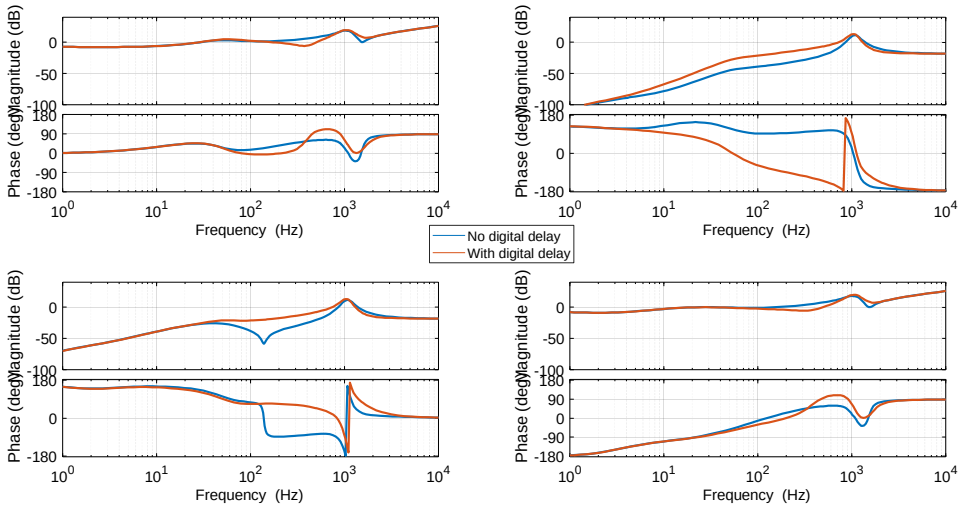

Figure 3-13 Bode plot of terminal impedances with and without digital delay

3.2.6 Effects of reactive power control

Reactive power control is achieved by an outer reactive power control loop that the error of reactive power goes through a PI controller (k_{pq}=-6.6×10^{-5}, k_{iq}=-0.66) to generate i_{qref}. So the current reference dynamics are not only related to DC voltage control but also influenced by reactive power control. The current reference vector dynamics are represented by

$$\tilde{\vec{\mathbf{i}}}_{ref} = -\mathbf{G}_{\mathbf{cvd}} \cdot \tilde{v}_{dc} + \mathbf{G}_{\mathbf{cvq}} \cdot \tilde{\vec{\mathbf{v}}}^{c} + \mathbf{G}_{\mathbf{qi}} \cdot \tilde{\vec{\mathbf{i}}}^{c} \tag{3-23}$$

Considering the dynamics brought by the reactive power control, the transfer function diagram of PV inverter is updated as Fig. 3-14.Table 3-1 lists meanings of all the transfer functions in Fig.3-3 and the corresponding dynamics.

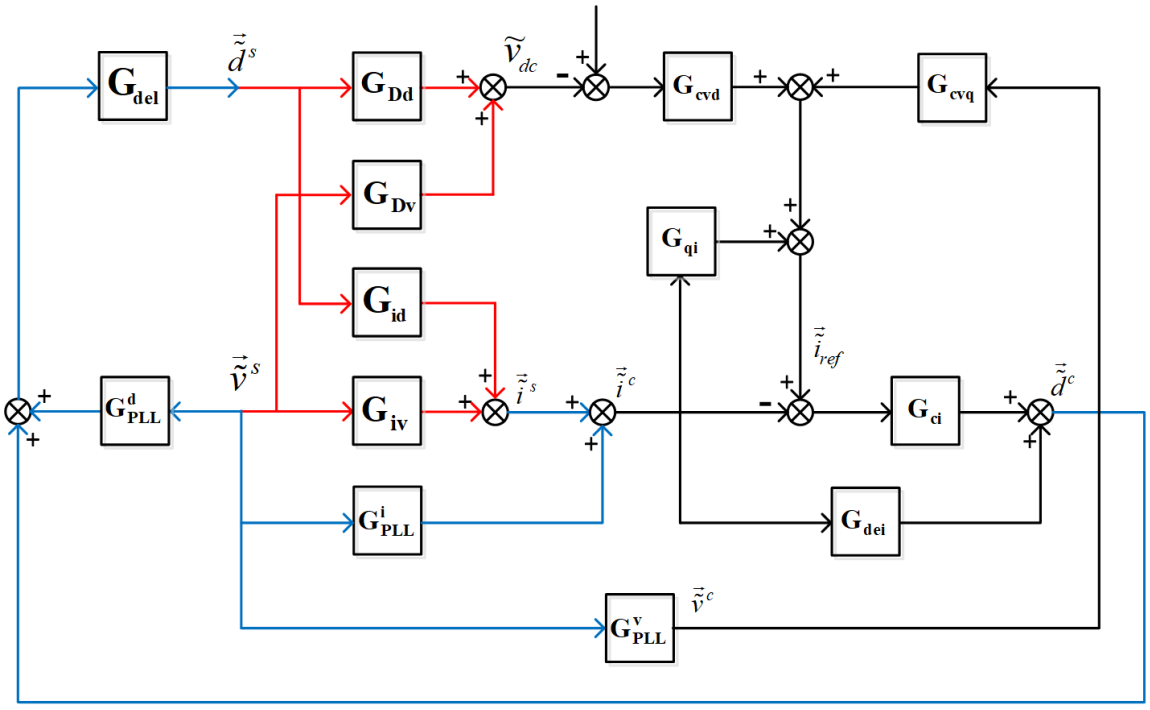

Figure 3-14 Transfer function diagram of PV inverter with reactive power control

Table 3-1 Meaning of each block in the transfer function diagram

Transfer function	Meaning of transfer function	Dynamics for
$\mathbf{G_{id}}$	$\tilde{\vec{\mathbf{i}}}^{s}$ over $\tilde{\vec{\mathbf{d}}}^{s}$	Power stage
$\mathbf{G_{iv}}$	$\tilde{\vec{\mathbf{i}}}^{s}$ over $\tilde{\vec{\mathbf{v}}}^{s}$	
$\mathbf{G_{Dd}}$	$\tilde{V}_{DC}$ over $\tilde{\vec{\mathbf{d}}}^{s}$	
$\mathbf{G_{Dv}}$	$\tilde{V}_{DC}$ over $\tilde{\vec{\mathbf{v}}}^{s}$	
$\mathbf{G_{cvd}}$	$\tilde{\vec{\mathbf{i}}}_{\mathbf{ref}}$ over $-\tilde{v}_{DC}$	DC voltage controller
$\mathbf{G_{cvq}}$	$\tilde{\vec{\mathbf{i}}}_{\mathbf{ref}}$ over $\tilde{\vec{\mathbf{v}}}^{c}$	Reactive power control
$\mathbf{G_{qi}}$	$\tilde{\vec{\mathbf{i}}}_{\mathbf{ref}}$ over $\tilde{\vec{\mathbf{I}}}^{c}$	
$\mathbf{G_{dei}}$	$\tilde{\vec{\mathbf{d}}}^{c}$ over $\tilde{\vec{\mathbf{i}}}^{c}$	Decoupling of current controller
$\mathbf{G_{ci}}$	$\tilde{\vec{\mathbf{d}}}^{c}$ over $\tilde{\vec{\mathbf{i}}}_{\mathbf{ref}} - \tilde{\vec{\mathbf{i}}}^{c}$	Current controller
$\mathbf{G}_{\mathbf{PLL}}^{\mathbf{V}}$	$\tilde{\vec{\mathbf{v}}}^{c}$ over $\tilde{\vec{\mathbf{v}}}^{s}$	PLL effect and Digital control delay
$\mathbf{G}_{\mathbf{PLL}}^{\mathbf{i}}$	$\tilde{\vec{\mathbf{i}}}^{c}$ over $\tilde{\vec{\mathbf{v}}}^{s}$	
$\mathbf{G}_{\mathbf{PLL}}^{\mathbf{d}}$	$\tilde{\vec{\mathbf{d}}}^{s}$ over $\tilde{\vec{\mathbf{v}}}^{s}$	
$\mathbf{G_{del}}$	$\tilde{\vec{\mathbf{d}}}^{s}$ over $\tilde{\vec{\mathbf{d}}}^{c}$	

The loop in Fig.3 is solved to get PV impedance so that $\tilde{\vec{v}}^{s} = \mathbf{Z_{PV}} \cdot \tilde{\vec{i}}^{s}$. The terminal impedance is updated as

$$\mathbf{Z} = \left\{ \begin{array}{l} \mathbf{G_{iv}} + \mathbf{G_{id}}(\mathbf{G_{del}}\mathbf{G_{ci}}\mathbf{G_{cvd}}\mathbf{G_{Dd}} + \mathbf{I})^{-1}\mathbf{G_{del}} \cdot \\ \left[\mathbf{G}_{\mathbf{PLL}}^{\mathbf{d}} + \left(\mathbf{G_{dei}} - \mathbf{G_{ci}} + \mathbf{G_{ci}} \cdot \mathbf{G_{qi}}\right) \cdot \mathbf{G}_{\mathbf{PLL}}^{\mathbf{i}} + \mathbf{G_{ci}} \cdot \mathbf{G_{cvq}} \cdot \mathbf{G}_{\mathbf{PLL}}^{\mathbf{v}} - \mathbf{G_{ci}}\mathbf{G_{cvd}}\mathbf{G_{Dv}} \right] \end{array} \right\}^{-1} \cdot \left[\mathbf{I} - \mathbf{G_{id}}(\mathbf{G_{del}}\mathbf{G_{ci}}\mathbf{G_{cvd}}\mathbf{G_{Dd}} + \mathbf{I})^{-1}\mathbf{G_{del}} \left(\mathbf{G_{dei}} - \mathbf{G_{ci}} + \mathbf{G_{ci}} \cdot \mathbf{G_{qi}}\right) \right] \quad (3\text{-}24)$$

For mode 1 unity power factor or mode 2 Q constant

$$\mathbf{G_{qi}} = \begin{bmatrix} 0 & 0 \\ 0 & (k_{pq} + \dfrac{k_{iq}}{s})V_d \end{bmatrix} \quad (3\text{-}25)$$

$$\mathbf{G_{cvq}} = \begin{bmatrix} 0 & 0 \\ (k_{pq} + \dfrac{k_{iq}}{s})I_q & (k_{pq} + \dfrac{k_{iq}}{s})(-I_d) \end{bmatrix} \quad (3\text{-}26)$$

For mode 3 constant power factor or mode 4 Watt-var mode shown in Fig.3-15 (a), the ratio of reactive power over active power is

$$k_{P2Q} = -\frac{\tilde{Q}}{\tilde{P}} \tag{3-27}$$

$$\mathbf{G_{qi}} = \begin{bmatrix} 0 & 0 \\ (k_{pq} + \frac{k_{iq}}{s})(k_{P2Q}V_d - V_q) & (k_{pq} + \frac{k_{iq}}{s})(k_{P2Q}V_q + V_d) \end{bmatrix} \tag{3-28}$$

$$\mathbf{G_{cvq}} = \begin{bmatrix} 0 & 0 \\ (k_{pq} + \frac{k_{iq}}{s})(k_{P2Q}I_d + I_q) & (k_{pq} + \frac{k_{iq}}{s})(k_{P2Q}I_q - I_d) \end{bmatrix} \tag{3-29}$$

For mode 5 droop mode control shown in Fig. 3-15 (b)

$$k_V = -\frac{\tilde{Q}}{\tilde{V}} \tag{3-30}$$

$$\mathbf{G_{qi}} = \begin{bmatrix} 0 & 0 \\ 0 & (k_{pq} + \frac{k_{iq}}{s})V_d \end{bmatrix} \tag{3-31}$$

$$\mathbf{G_{cvq}} = \begin{bmatrix} 0 & 0 \\ (k_{pq} + \frac{k_{iq}}{s})(k_V + I_q) & (k_{pq} + \frac{k_{iq}}{s})(-I_d) \end{bmatrix} \tag{3-32}$$

The four *d*-*q* frame impedances in Fig.3-15 are PV impedances under mode (1)-mode (4). In mode (2-4), PV inverter is inductive in steady state. PV farm is composed of 12 inverter modules. For each module, P = 250 kW, Q = –75 kVar (Generator convention,

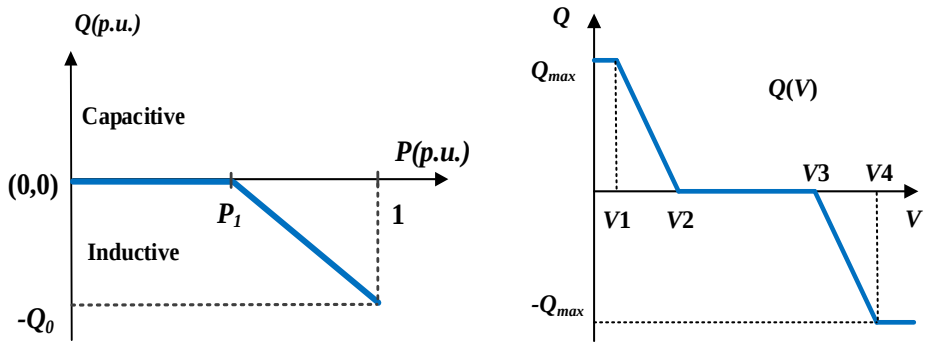

Figure 3-15 (a) mode 4 Watt-var mode curve (b) mode 5 Volt-var droop mode curve

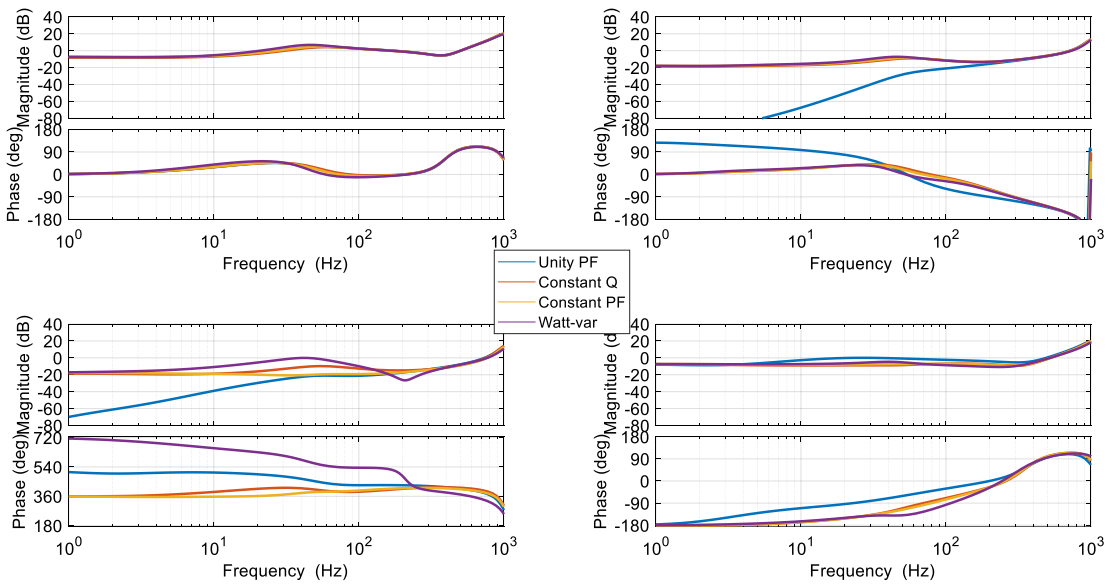

Figure 3-16 Bode plot of terminal impedances under mode 1 – mode 4

output as positive direction). In mode 4, P_1= 200 kW (0.8 p.u.), ratio of slope is –1.5 in Fig.3-15 (a).

In all four curves, PV impedances in *d-q* frame are diagonal dominant, which means Z_{dd} and Z_{qq} are much bigger than Z_{dq} and Z_{qd} in magnitude. And all four curves are almost the same at high frequencies over 200 Hz. At lower frequency, blue curve of unity power factor is different from other curves, Z_{dq} and Z_{qd} are zero in magnitude as Q is zero, while the other three curves are almost the same. So mode (2-4) can be represented by mode 2 in dynamics.

Fig.3-16 is the impedance of PV inverter under mode 1, mode 2 (as it can represent mode 2, mode 3, and mode 4) and mode 5. In mode 5, the steady state operation point is the same as other modes, P = 250 kW, Q = –75 kVar (Generator convention, Output as positive direction). V_1 = 0.0975 p.u., V_2 = 1.0 p.u., V_3 = 1.025 p.u., V_4=1.05 p.u., *Qmax*= 110 kVar in Fig.3-15(b). Compared to mode 1 and mode 2, one obvious difference of mode 5 is that signs of Z_{dd} and Z_{qq} in zero frequency are inverted in mode 5. The

magnitude of Z_{dd} is decreased, while the magnitude of Z_{qd} is increased obviously. This will cause unstable PV integration case, which can be proved in chapter IV.

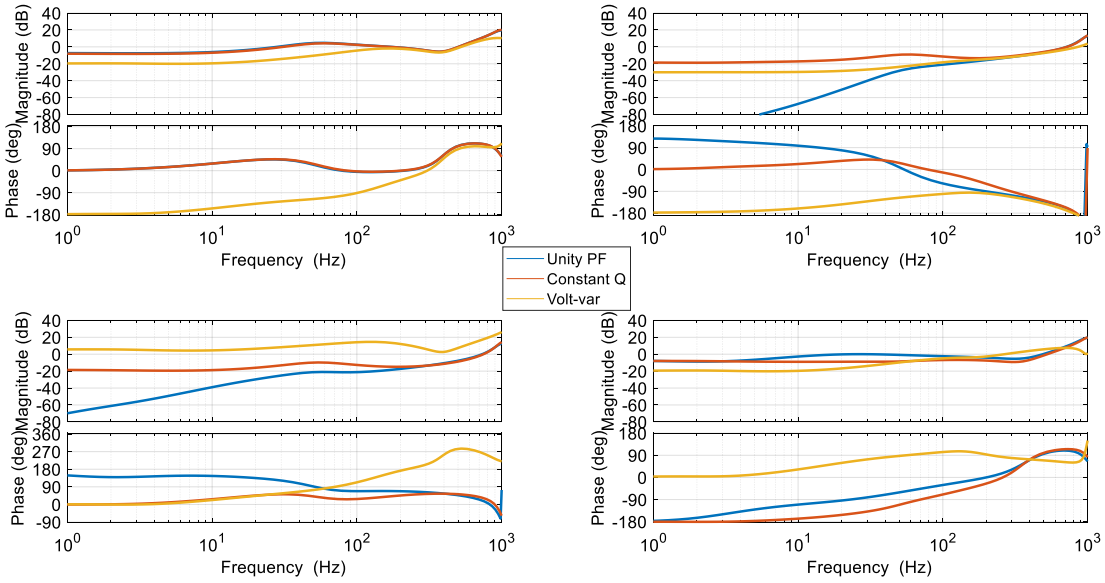

Figure 3-17 Bode plot of terminal impedances under mode 1, mode 2 and mode 5

To double check and also understand how the reactive power control change the signs of impedances and the diagonal dominance at very low frequencies, two approaches are utilized to compare the five control modes. First approach is to substitute frequency of zero to the small-signal model and the second approach is the phasor diagram illustration.

In the first approach, active power and reactive power equations can be expressed in terms of PV interface voltage and current in *d-q* frame. Linearization of the equations yields the PV impedances at very low frequency, the polarity of which can be validated by phasor diagrams of the second approach.

When deriving the impedance of a PV inverter, motor convention is used (injection is defined to be positive direction). At very low frequency, the difference between *d-q* frame of converter controller and *d-q* frame of the grid can be ignored. $\tilde{\vec{v}}^c$ is equal to $\tilde{\vec{v}}^s$ and $\tilde{\vec{i}}^c$ is equal to $\tilde{\vec{i}}^s$. The active power and reactive power can be expressed in terms of

terminal voltage and current as

$$\begin{cases} v_d i_d + v_q i_q = P \\ -v_d i_q + v_q i_d = Q \end{cases} \tag{3-33}$$

At low frequency, DC voltage of the inverter keeps the same, so does active power output. At unity power factor mode, linearization of equation (3-33) yields

$$\begin{cases} V_d \tilde{i}_d + \tilde{v}_d I_d + V_q \tilde{i}_q + \tilde{v}_q I_q = \tilde{P} = 0 \\ -V_d \tilde{i}_q + \tilde{v}_d I_q + V_q \tilde{i}_d + \tilde{v}_q I_d = \tilde{Q} = 0 \end{cases} \tag{3-34}$$

Substitute $V_q = 0$ to (3-34) to get

$$\begin{bmatrix} \tilde{v}_d \\ \tilde{v}_q \end{bmatrix} = \frac{V_d}{-(I_d^2 + I_q^2)} \begin{bmatrix} Id & Iq \\ Iq & -Id \end{bmatrix} \begin{bmatrix} \tilde{i}_d \\ \tilde{i}_q \end{bmatrix} \tag{3-35}$$

$$\mathbf{Z}(s)\big|_{s=j0} = \frac{V_d}{-(I_d^2 + I_q^2)} \begin{bmatrix} Id & Iq \\ Iq & -Id \end{bmatrix} \tag{3-36}$$

At unity power factor, $I_q = 0$. And $I_d < 0$, so

$$\begin{cases} Z_{dd} = \dfrac{V_d}{I_d} > 0 \\ Z_{qq} = \dfrac{V_d}{I_d} < 0 \end{cases} \tag{3-37}$$

The phasor diagram can be used to analyze the polarity of the impedances at low frequency. As PV inverter is basically a current source, so the perturbation is on voltage phasor and the response is on current phasor. For example, Fig. 3-17(a) shows how much voltage perturbation (from $\vec{v}$ to $\vec{v}'$) is needed to change current vector by $\tilde{i}_d$ only at d axis. Under unity power factor, originally $\vec{v}$ and $\vec{i}$ align with each other but have different polarity as injection is defined to be positive direction of current. The reactive power stays zero, so $\vec{v}'$ still lies on d axis. At low frequency, DC voltage of the inverter keeps the same, so does active power output.

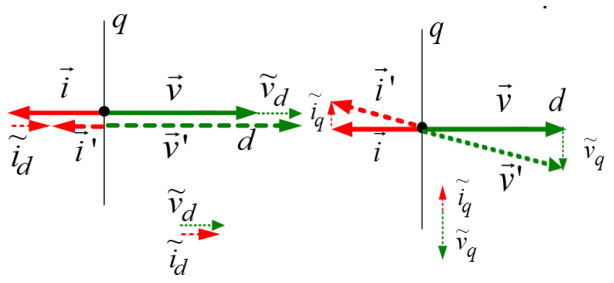

Figure 3-18 Phasor diagram under unity power factor mode (a) current response at d axis (b) current response at q axis

$$|\vec{v}|\cdot|\vec{i}|=|\vec{v}\,'|\cdot|\vec{i}\,'| \tag{3-38}$$

It can be concluded from (3-38) that $|\vec{v}\,'|<|\vec{v}|$ and $\tilde{v}_d>0$. To cause current response of $\tilde{i}_d>0$, the voltage perturbation $\tilde{v}_d>0$ and $\tilde{v}_q=0$, so $Z_{dd}=\tilde{v}_d/\tilde{i}_d>0$, $Z_{qd}=\tilde{v}_q/\tilde{i}_d=0$. For q axis, Fig.3-17 (b) illustrates voltage perturbation from $\vec{v}$ to $\vec{v}\,'$ to get current response of $\tilde{i}_q$ at q axis (from $\vec{i}$ to $\vec{i}\,'$). Under unity power factor with the effect of PLL, $\vec{v}\,'$ will align with $\vec{i}\,'$ so that $\tilde{v}_q<0$, $Z_{qq}=\tilde{v}_q/\tilde{i}_q<0$ causing negative impedance at q channel. The polarity analysis from phasor diagram matches with results from (3-37).

If PV inverter is under Q constant, PF constant and watt-var control modes, similar analysis can be done as well. At very low frequency perturbation, DC voltage can be considered to be constant, so active power output is constant, reactive power is constant too under mode 2 Q constant, mode 3 constant power factor and mode 4 watt-var control. Equation (3-35)-(3-36) can be applied in these three modes to get the results of

$$Z_{dd}=\frac{V_d I_d}{-(I_d^2+I_q^2)}>0 \tag{3-39}$$

$$Z_{qq}=\frac{-V_d I_d}{-(I_d^2+I_q^2)}<0 \tag{3-40}$$

If original operation steady state is inductive, $Q>0$, $I_q<0$,

$$Z_{qd} = \frac{V_d I_q}{-(I_d^2 + I_q^2)} > 0 \tag{3-41}$$

$$Z_{dq} = \frac{V_d I_q}{-(I_d^2 + I_q^2)} > 0 \tag{3-42}$$

Phasor diagrams of Fig.3-18 can be used to look into polarity of impedances under these three modes of control. In Fig.3-18, the original operating point of PV inverter is inductive (Q > 0, injection to PV inverter is defined to be positive). As active power and

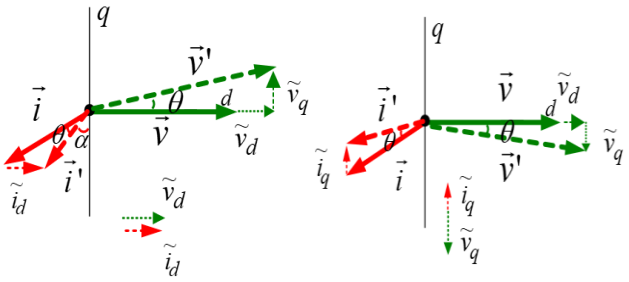

Figure 3-19 Phasor diagram under mode 2- mode 4 (a) current response at d axis (b) current response at q axis

reactive power stay the same before and after perturbation, the phase difference of voltage phasor $\vec{v}$ and current phasor $\vec{i}$ stays the same. In Fig.3-18 (a), $\vec{i}'$ leads $\vec{i}$ by θ, so $\vec{v}'$ leads $\vec{v}$ by θ too, so $\tilde{v}_q > 0$,

$$Z_{qd} = \tilde{v}_q / \tilde{i}_d > 0 \tag{3-43}$$

In addition,

$$|\vec{v}| \cdot |\vec{i}| = |\vec{v}'| \cdot |\vec{i}'| \tag{3-44}$$

So

$$\frac{|\vec{v}|}{|\vec{v}'|} = \frac{|\vec{i}'|}{|\vec{i}|} = \frac{\cos(\theta + \alpha)}{\cos\alpha} = \cos\theta - \sin\theta \tan\alpha < \cos\theta \tag{3-45}$$

$$|\vec{v}| < |\vec{v}'| \cos\theta \tag{3-46}$$

Then $\tilde{v}_d > 0$,

$$Z_{dd} = \tilde{v}_d / \tilde{i}_d > 0 \tag{3-47}$$

For *q* axis impedances showed in Fig.3-18(b), it is similar that phasor angle difference and multiply of magnitude phasors keep unchanged, so $\tilde{v}_d > 0$, $\tilde{v}_q < 0$,

$$Z_{dq} = \tilde{v}_d / \tilde{i}_q > 0 \tag{3-48}$$

$$Z_{qq} = \tilde{v}_q / \tilde{i}_q < 0 \tag{3-49}$$

The polarity results from phasor diagrams match with results from equation (3-43), (3-47) - (3-49) when PV inverter is working in inductive zone. When PV inverter is working in capacitive zone, similar phasor diagram as Fig.3-18 can be drawn to predict impedance polarity. The only big difference is the initial angle between voltage phasor and current phasor.

From equation (3-43), (3-47) - (3-49) it can be concluded that impedance matrix is diagonal dominant at low frequencies, Z_{dd} is always positive, Z_{qq} is always negative, and the polarity of non-diagonal elements is dependent on original operating state (inductive or capacitive).

If PV is working under volt-var mode in the droop curve of Fig.3-15(b), (3-34) and (3-36) should be changed to

$$\begin{cases} V_d \tilde{i}_d + \tilde{v}_d I_d + V_q \tilde{i}_q + \tilde{v}_q I_q = \tilde{P} = 0 \\ -V_d \tilde{i}_q + \tilde{v}_d I_q + V_q \tilde{i}_d + \tilde{v}_q I_d = \tilde{Q} = k_v \tilde{v}_d \end{cases} \tag{3-50}$$

$$\mathbf{Z}(s)\big|_{s=j0} = \frac{V_d}{-I_d^2 - (K_v + I_q) I_q} \begin{bmatrix} Id & Iq \\ K_v + Iq & -Id \end{bmatrix} \tag{3-51}$$

The polarity of impedance matrix is related to the absolute value of the droop slope k_v, as listed in Table 3-2.

Table 3-2 Impedance polarity in terms of droop slope

	$0 \leqslant K_v < -I_q$	$-I_q < K_v < -(I_d^2 + I_q^2)/I_q$	$K_v > -(I_d^2 + I_q^2)/I_q$
Z_{dd}	+	+	-
Z_{qd}	+	-	+
Z_{dq}	+	+	-
Z_{qq}	-	-	+

The polarity change in Table 3-2 can be illustrated by Fig.3-19. As shown in Fig.3-19(a), if droop control curve ratio is zero, then it is the same case as Fig.3-18 Q constant control. $\vec{v}'$ is at point A. No matter how K_v changes, the end of phasor $\vec{v}'$ will lie on the line L, which crosses point A and is perpendicular to the reverse extension of $\vec{i}'$. This is because that active power output stays unchanged, so the projection of $\vec{v}'$ along $\vec{i}'$ keeps unchanged compared to point A. When K_v starts to increase, $\vec{v}'$ will end at point A' which is at right hand of point A because $\Delta|\vec{v}| > 0$, $\Delta Q > 0$. After K_v increases to the threshold of $-I_q$, point A' is below d axis, making $\tilde{v}_q$ negative, and Z_{qd} to be negative. If K_v is bigger than $-(I_d^2 + I_q^2)/I_q$, $\vec{v}'$ will end at point A' which is at left hand of point A. In this case, $\Delta|\vec{v}| < 0$, $\Delta Q < 0$, making $\tilde{v}_d$ negative, Z_{dd} negative, $\tilde{v}_q$ positive and Z_{qd} positive. Similar methods can be used in the phasor diagram of current response in q axis for polarity of Z_{dq} and Z_{qq}. The analysis from phasor diagram match with results in Table 3-2 when PV is working in inductive zone (PV terminal AC voltage is within *V3* and *V4* in Fig.3-15(b)).

When AC voltage is within *V1* and *V2* in Fig.3-15(b), PV is working in capacitive zone, (3-50)-(3-51) are still valid. $I_q > 0$, so it can be observed from (51) that impedance polarity is not affected by value of droop slope K_v, $Z_{dd}>0$, $Z_{dq}<0$, $Z_{dq}<0$, $Z_{qq}<0$.

In conclusion, at very low frequencies, PV impedance is seeing negative polarity only at Z_{qq} element because of PLL effect under unity power factor. The polarity of

impedances under Q constant, power factor constant or watt-var mode are the same, Z_{dd} is positive, Z_{qq} is negative and Z_{dq} and Z_{qd} are dependent on whether PV is capacitive and inductive. In addition impedance matrices are diagonal dominant under these mode 1-mode 4. While PV impedance in DQ frame under mode 5 Volt-var control may change

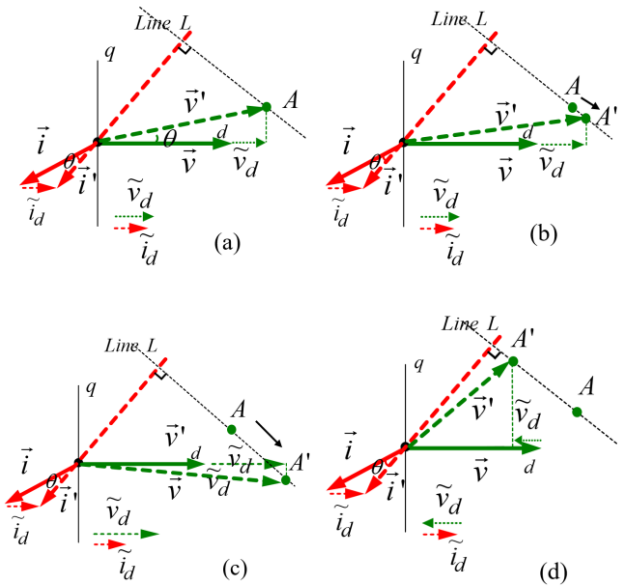

Figure 3-20 Phasor diagram of volt-var mode (a) K_v =0, (b)0 < K_v< -I_q, (c) -I_q < K_v < -(I_d^2+ I_q^2)/I_q, (d) K_v > -(I_d^2+ I_q^2)/I_q

polarity according the magnitude of droop curve slope K_v when PV is in inductive zone, the threshold of which are expressed as a function of PV inverter steady state operation point.

3.3 Validation through simulation

Average model shown in Fig.3-2 is built in Simulink with PV controller shown in Fig.3-1 including a PLL. With PV arrays running under standard weather condition and MPPT state. The output impedance of PV generator is obtained by two approaches. One approach is using linearization function of Simulink. After adding grid voltage perturbation and setting PV output current to be measurement, PV output impedance

under steady state is achieved by simulation. The other approach is to calculate the terminal impedances according to the closed-loop expression (3-24). If the PV terminal impedances obtained through the two approach match very well, it is proved that the derivation process for (3-24) is mathematically correct.

The impedance check is done for PV local reactive power control modes of

(1) Unity power factor. Impedance matrix plotted in Fig.3-21.

(2) Constant reactive power. Impedance matrix plotted in Fig.3-22.

(3) Constant power factor. Impedance matrix plotted in Fig.3-23.

(4) Watt-var mode, or Q as a function of P. Impedance matrix plotted in Fig.3-24.

(5) Volt-var mode, or Q as a droop function of AC voltage. Impedance matrix plotted in Fig.3-25.

The impedances calculated by using (3-24) for unity power factor is plotted as blue curve in Fig.3-21. And the orange curve in the Fig.3-21 is the simulation results using

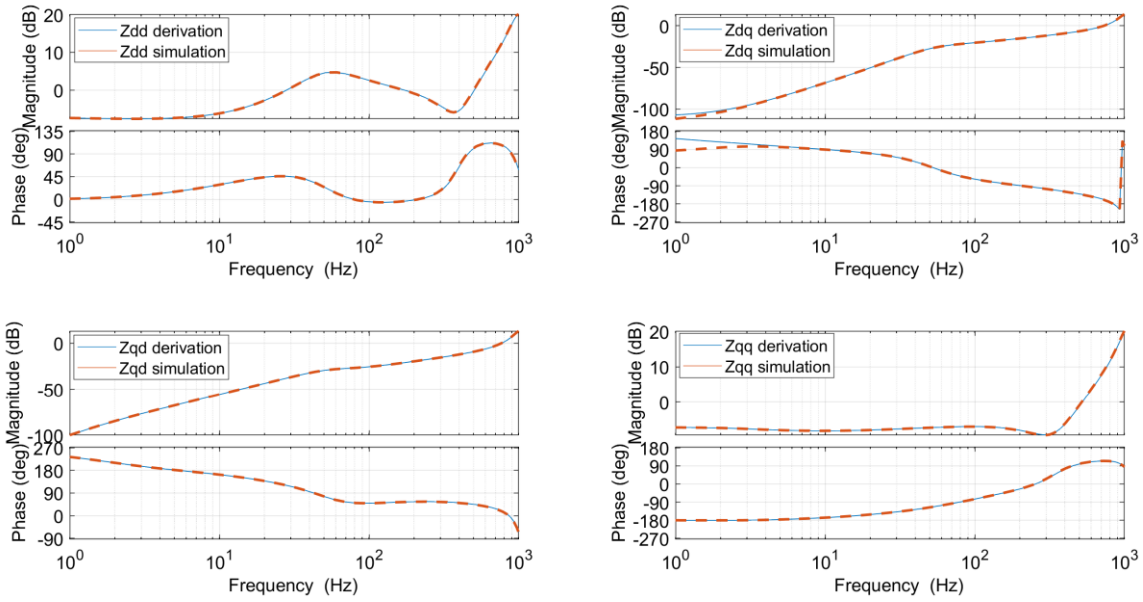

Figure 3-21 PV *d-q* frame impedance under mode 1 unity power factor

linearization function of MATLAB. It's clear that simulation results match with derivation results. There is some mismatch in the phase Zdq below 10 Hz. That can be ignored because the magnitude of Zdq below 10 Hz is very small, under -60 dB.

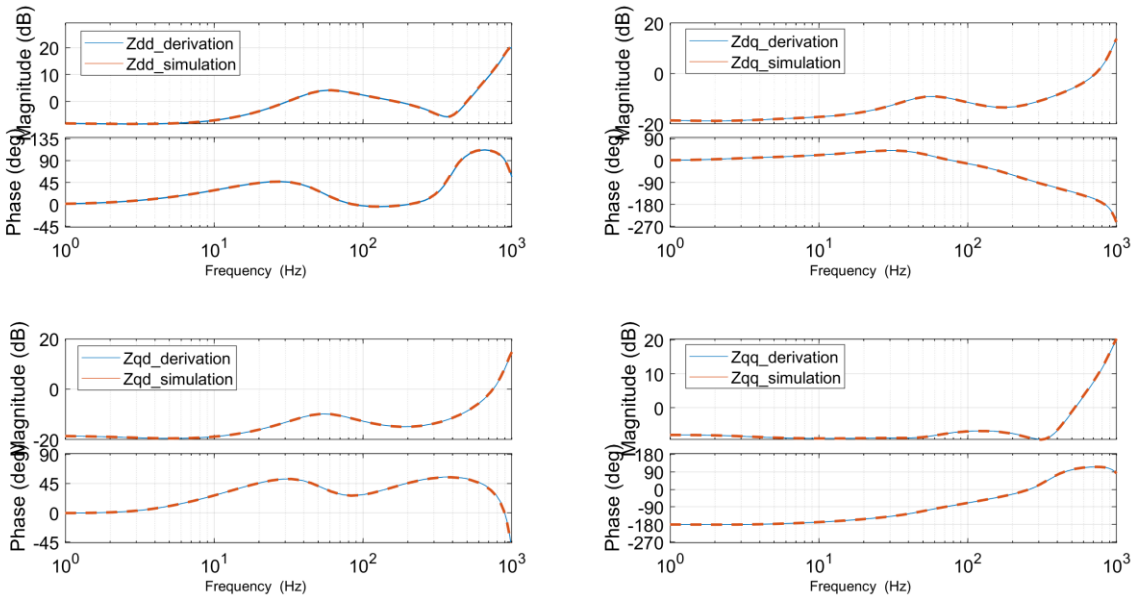

Figure 3-22 PV *d-q* frame impedance under mode 2 constant Q

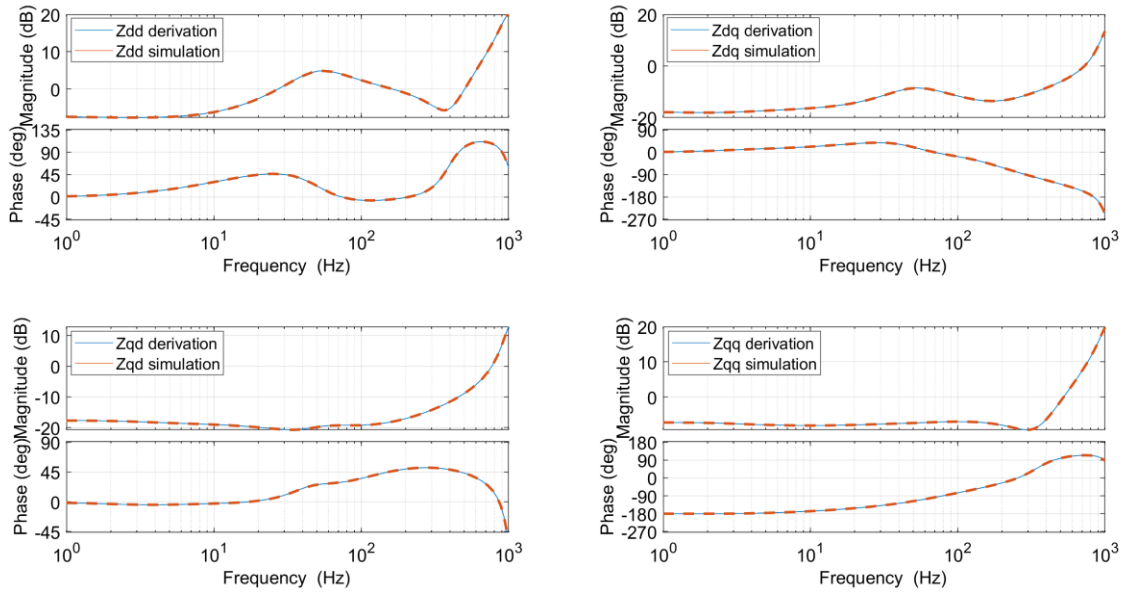

Figure 3-23 PV *d-q* frame impedance under mode 3 constant PF

In mode 2-mode 5, the power outputs are the same, P = 250 kW, Q = - 75 kVar. In mode 4 shown by Fig.3-24, P_1= 200 kW (0.8 p.u.), ratio of slope is –1.5 in Fig.3-15 (a).

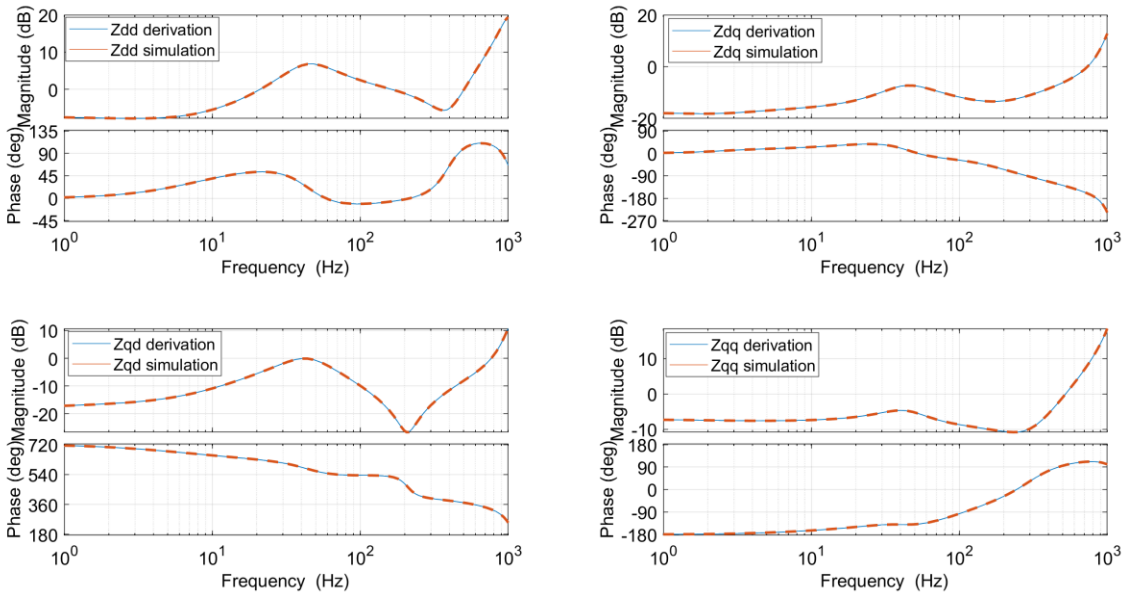

Figure 3-24 PV *d-q* frame impedance under mode 4 Watt-var mode

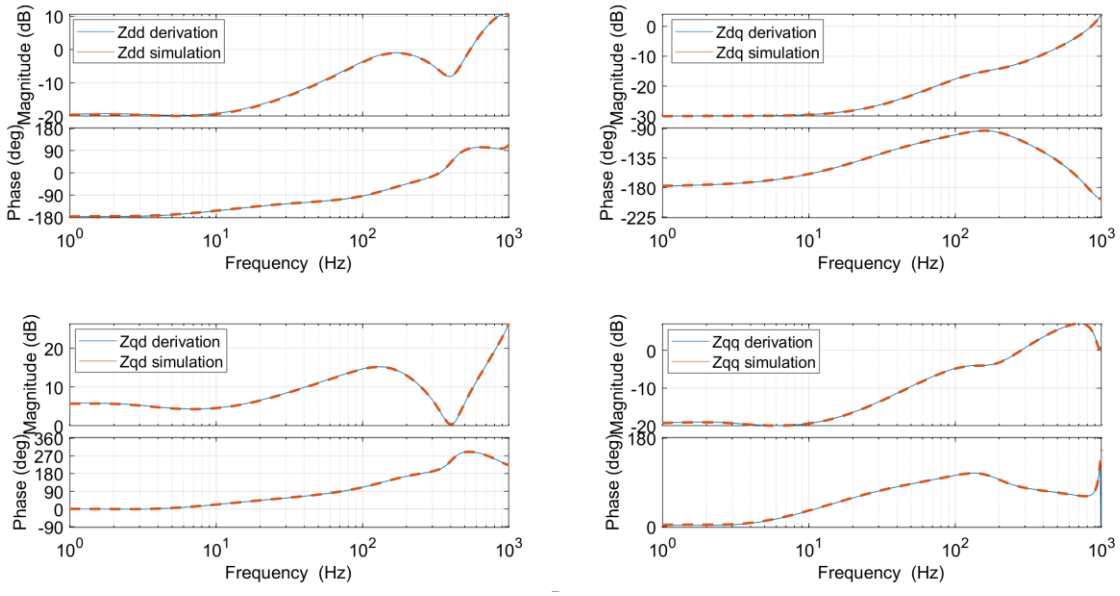

Figure 3-25 PV *d-q* frame impedance under mode 5 volt-var mode

In mode 5, the steady state operation point is the same as other modes, P = 250 kW, Q = –75 kVar (Generator convention, Output as positive direction). *V1* = 0.0975 p.u., *V2* = 1.0 p.u., *V3* = 1.025 p.u., *V4*=1.05 p.u., *Qmax*= 110 kVar in Fig.3-15(b).

For all five reactive power control modes, the derived impedance plots match with the simulation results very well, which means that our impedance model is true in the aspect of including all the dynamics of the power stage and the controllers.

3.4 Small-Signal model validation through hardware

Hardware experiments are done to measure the PV inverter impedance. The main circuit is shown in Fig. 3-26. A single stage DC-AC inverter is built to deliver active power from PV emulator to AC grid. Agilent E4360A PV emulators working as PV array is connected to the DC side of the inverter. And an Impedance measurement unit (IMU) introduced by [95-101] is used to inject perturbation and obtain response. The parameters of the circuit is listed in Table 3-3.

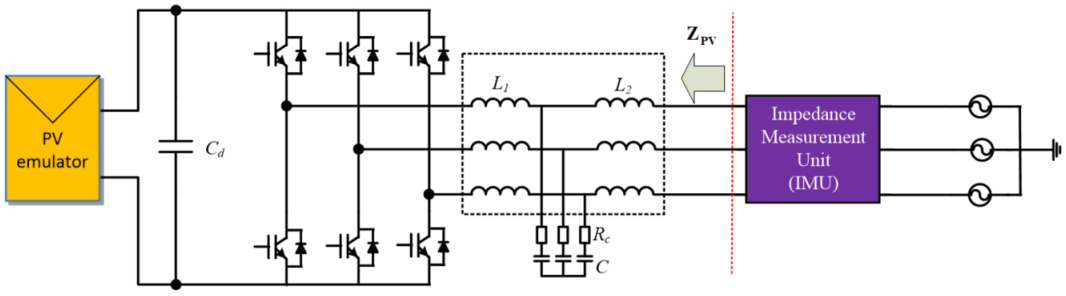

Figure 3-26 Impedance measurement hardware circuit diagram.

The bode plots of Fig.3-27 to Fig.3-31 are PV terminal impedances from derivation (solid lines) and measurement (star lines) under different Q control modes. For all modes, P= 2640 W. For other mode, the steady state Q = –800 Var (Inductive). In volt-var control, droop slope K_v =160 and Q = - K_v (V-125). It is observed that the derivation

Table 3-3 Parameters of the PV impedance measurement hardware circuits

Parameter		Value
PV array	V_{oc}	55 V
	V_{mpp}	50 V
	I_{sc}	4.5 A
	I_{mpp}	3.6 A
DC voltage		250 V
DC capacitor		600 μF
LCL filter	L_1	250 μH
	L_2	250 μH
	R_c	1 Ω
	C	35 μF
Switching frequency		20 kHz
Line frequency		60 Hz
AC line-to-line rms voltage		130 V

results and measurement match very well in Z_{dd} and Z_{qq}, but there is some mismatch at Z_{qd} and Z_{dq} when Z_{qd} and Z_{dq} are much smaller than Z_{dd} and Z_{qq} in Fig.3-27, which is due to measurement error and may be resolved later. For mode 5 in Fig.3-31, the signs of Z_{dd} and Z_{qq} are really flipped, and the impedance matrix is no longer diagonal dominant compared to other control modes as predicted by derivation results.

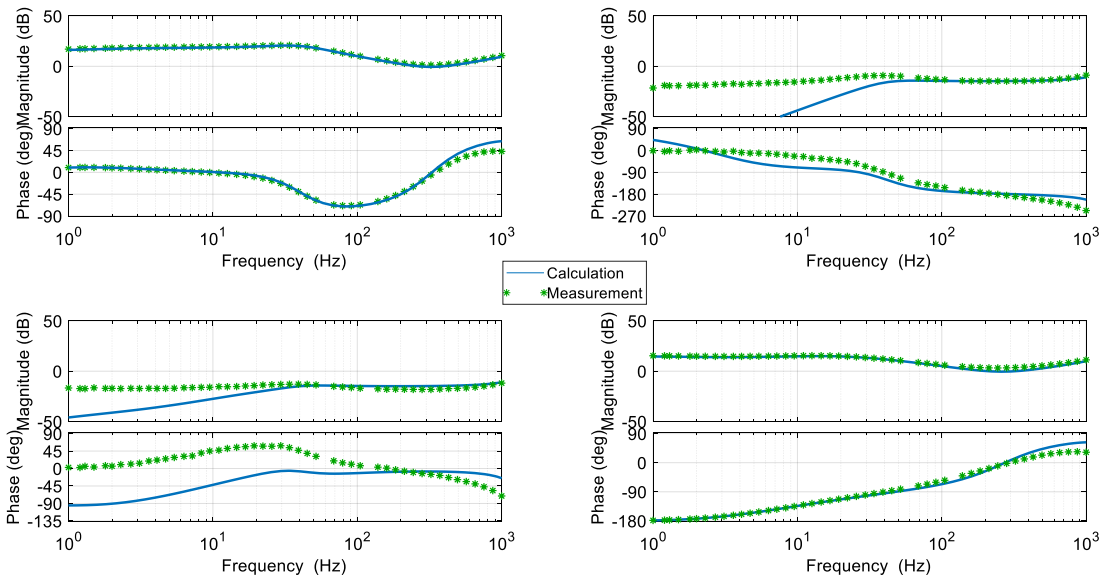

Figure 3-27 PV *d-q* frame impedance under mode 1 unity power factor

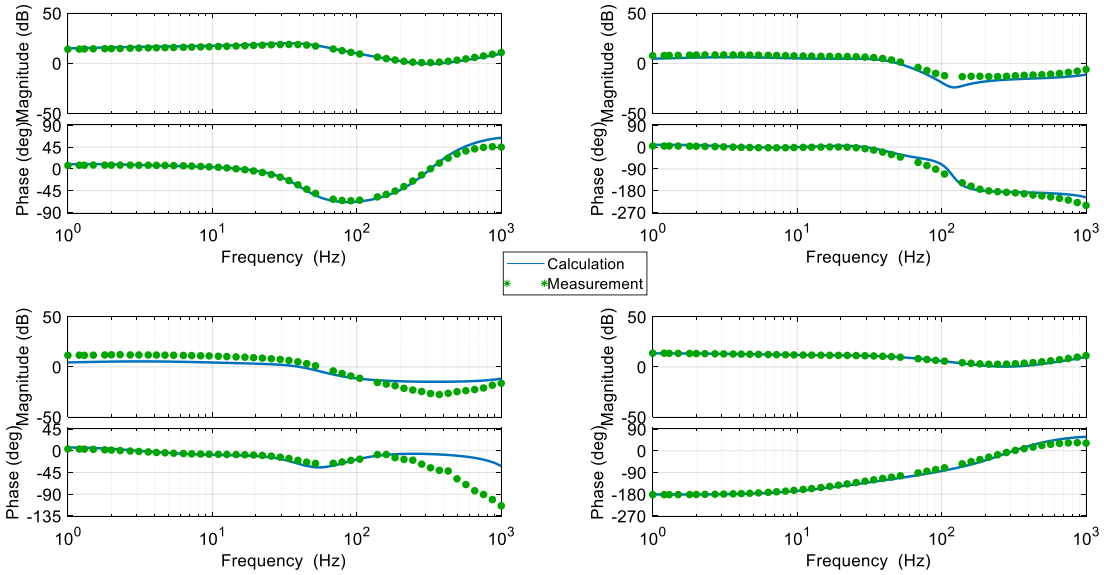

Figure 3-28 PV *d-q* frame impedance under mode 2 Q constant

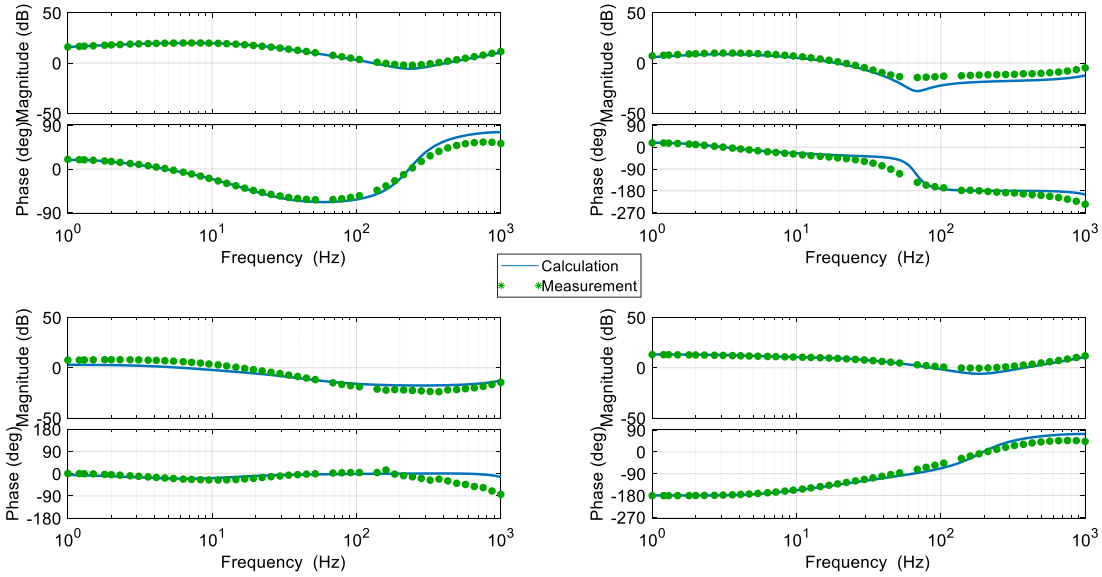

Figure 3-29 PV *d-q* frame impedance under mode 3 PF constant

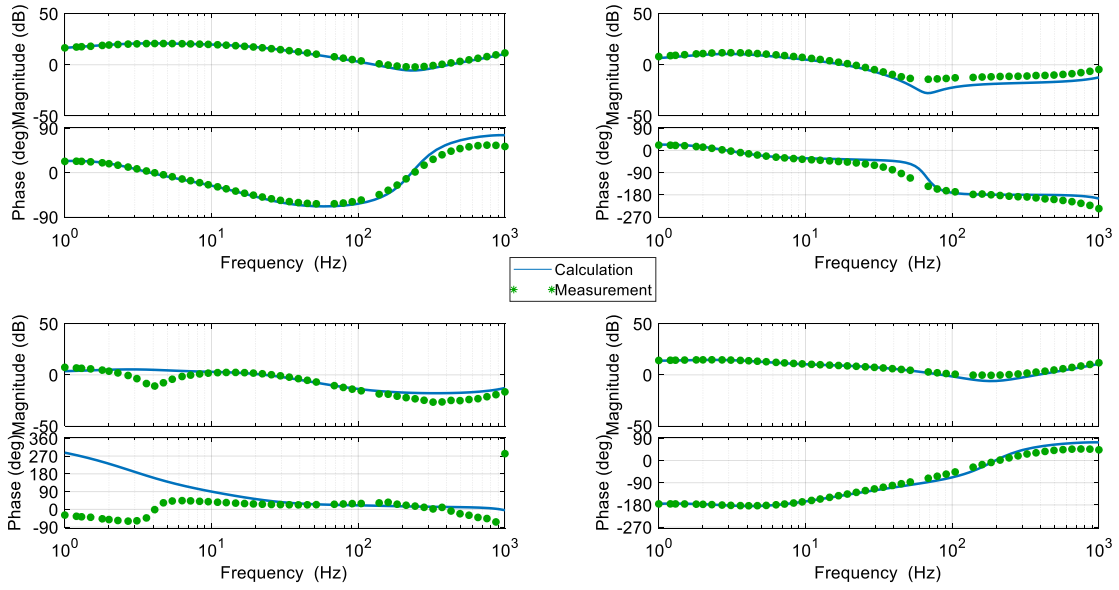

Figure 3-30 PV *d-q* frame impedance under mode 4 Watt - var mode

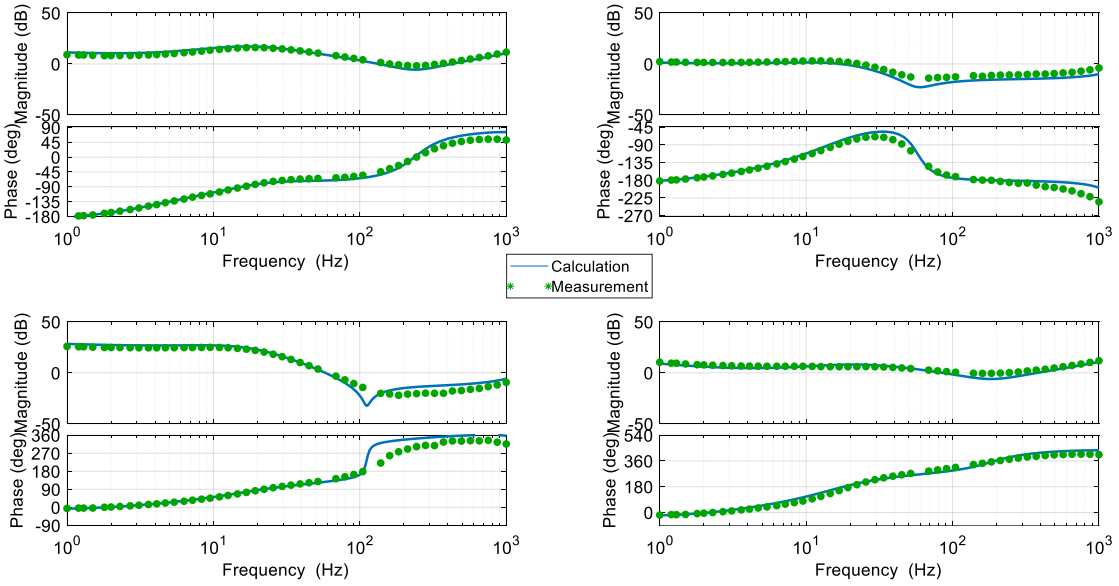

Figure 3-31 PV *d-q* frame impedance under mode 5 Volt - var

3.5 Conclusions about comparison between different reactive power modes

A switching model and its corresponding average model are built for Utility PV farm generators. The terminal impedances in *d-q* frame are derived of utility-scale PV farm

based on small signal model of the PV generator, which include the dynamics from the PV array, the power stage and the controllers in the synchronous reference frame. The PV terminal impedance matrix model derived from small-signal model is proved by time domain simulation and validated by scaled-down hardware experiments.

A comparison is done among impedances of PV inverters under 5 different reactive power control modes. The terminal *d-q* frame impedance matrix shows least coupling between d axis and q axis at unity power factor control compared to other modes. The sign of Zdd is positive at low frequencies because of constant active power output. The sign of Zqq is negative at low frequencies because of PLL synchronization. And the constant Q mode, constant power factor mode and watt-var control mode add some *d-q* coupling compared to unity power factor due to the non-zero reactive power at steady state. These three modes have similar *d-q* frame impedances. While the volt-var control mode changes PV terminal impedance signs and magnitudes significantly. The signs of Zdd and Zqq are flipped compared to other modes and the magnitude of Zqd is much higher than other three elements. As the *d-q* frame impedance matrix turn non-diagonal dormant, it's impossible to judge the system stability by purely looking at the impedances of the PV farm and the grid. The application of GNC is need to predict connection stability.

Chapter 4. GNC for the Connection of PV Inverters to the Distribution System

As introduced in chapter 1, the small-signal stability for a balanced three-phase ac system stability can be predicted by using GNC to the minor loop-gain **L**(s). Here the dimension of **L**(s) is two by two, so for each frequency **L**(s) has two eigenvalues. Let {*l1*(s), *l2*(s)} be the set of frequency-dependent eigenvalues of L(s). These traces of the two eigenvalue in the complex plane form characteristic loci of matrix L(s) as the variable *s* traverses the standard Nyquist contour in the clockwise direction.

For the specific case of this work, the power system with PV generator can be modeled as Fig.4-1 for small-signal stability analysis: $\mathbf{Z_{grid}}$ and $\mathbf{Y_{PV}}$ are the grid *d-q* frame impedance and PV generator admittance separately and neither of the two has any right-half plane poles. Accordingly, PV terminal *d-q* frame voltage is related to grid source voltage by

$$\mathbf{v_{PV}}(s) = [\mathbf{I} + \mathbf{Z_{grid}}(s) \cdot \mathbf{Y_{PV}}(s)]^{-1} \mathbf{v_{grid}}(s) \tag{4-1}$$

And the return ratio matrix is

$$\mathbf{L}(s) = \mathbf{Z_{grid}}(s) \cdot \mathbf{Y_{PV}}(s) \tag{4-2}$$

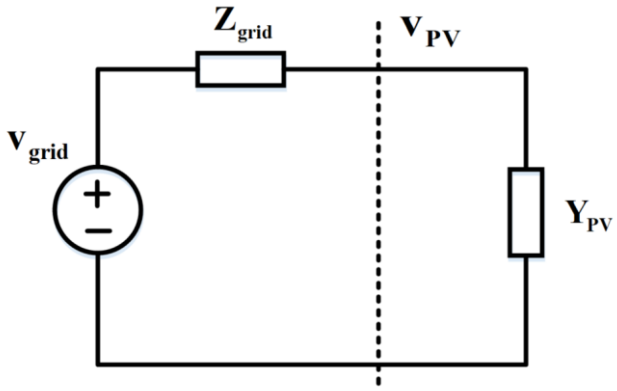

Figure 4-1 D-Q frame impedance model of grid with PV

The total number of right-half plane poles of $\mathbf{Z}_{\mathbf{sdq}}(s)$and $\mathbf{Y}_{\mathbf{ldq}}(s)$ is zero. Then the system will be closed-loop stable if and only if the net sum of anticlockwise encirclements of the critical point (–1+j0) by the set of characteristic loci of $\mathbf{L}(s)$ is equal to zero. This chapter applies GNC on the *d-q* frame impedances of the grid side and the PV farm side at point of common coupling (PCC) to assess the interface small-signal stability.

4.1 Introduction of test-bed distribution system parameters and modeling tool

To make use of the GNC method, the first step is to acquire impedances of grid side and PV generator side at the power common coupling (PCC) point. Grid test-bed is shown in Fig.4-2, which is a rural lightly loaded radial 12kV distribution system that has 56 buses. The parameters are included in [91]. An average model in *d-q* frame is built in Simulink to do time domain simulation and impedance measurement using linearization function. The load is modeled as passive constant impedance load in the model. It is known that impedance for a single line in *d-q* frames is

$$\mathbf{Z}_{\text{line}} = \begin{bmatrix} LineR + LineL \cdot s & -\omega_0 \cdot LineL \\ \omega_0 \cdot LineL & LineR + LineL \cdot s \end{bmatrix} \tag{4-3}$$

In which LineR and LineL are the resistor and the inductance of the line. For a complicated system in Fig.4-2, the impedance measured in *d-q* frames at one bus can be estimated by

$$\mathbf{Z}_{\text{grid}} = \begin{bmatrix} PathR + PathL \cdot s & -\omega_0 \cdot PathL \\ \omega_0 \cdot PathL & PathR + PathL \cdot s \end{bmatrix} \tag{4-4}$$

In which PathR and PathL are sum of resistors and inductances of all lines along the path from substation to measured bus.

This grid *d-q* frame impedance estimation is validated by Fig.4-3. The red curves are from estimation using equation (4-4) at bus 45, the path goes along bus 1 – bus 2 – bus 4 – bus 20 – bus 23 – bus 25 – bus 26 – bus 32 – bus 34 – bus 41 – bus 42 – bus 45. And blue curves are from linearization function of Simulink based on the *d-q* frame model.

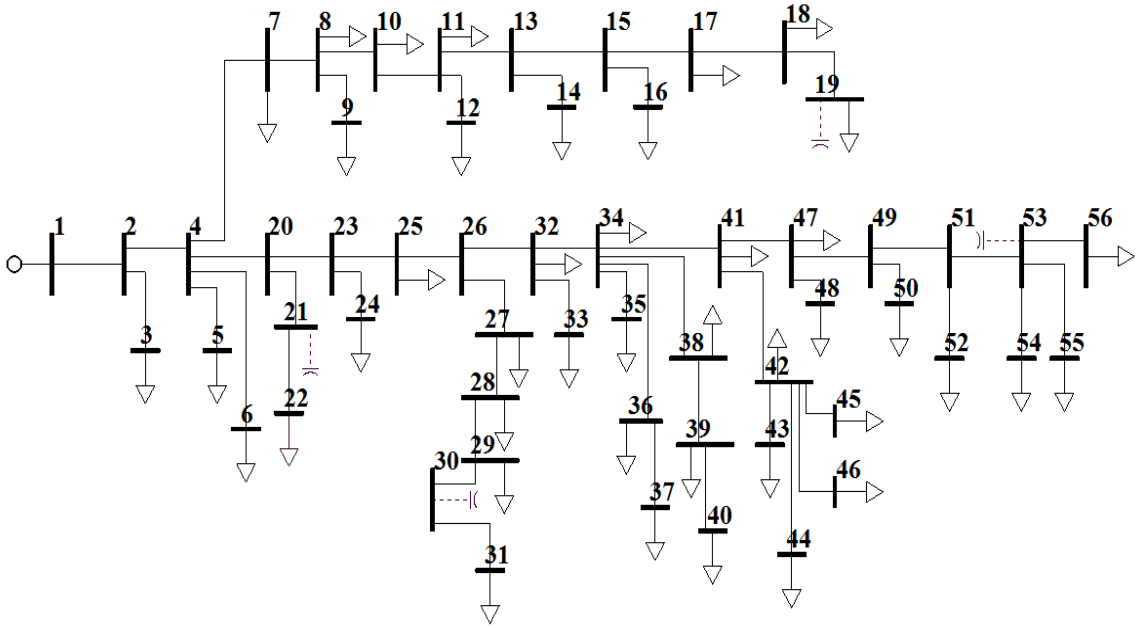

Figure 4-2 One-line diagram of the distribution system

It can be observed from Fig.4-3 that the estimated *d-q* frame impedance from path impedance of the orange curve match the accurate linearization terminal impedance of the blue curve. The accuracy of estimation of (4-4) means that the impedances of the grid side is dominated by the lines on the path of the measured bus to the substation, the lines on other branches and all the loads can be ignored in the test-bed.

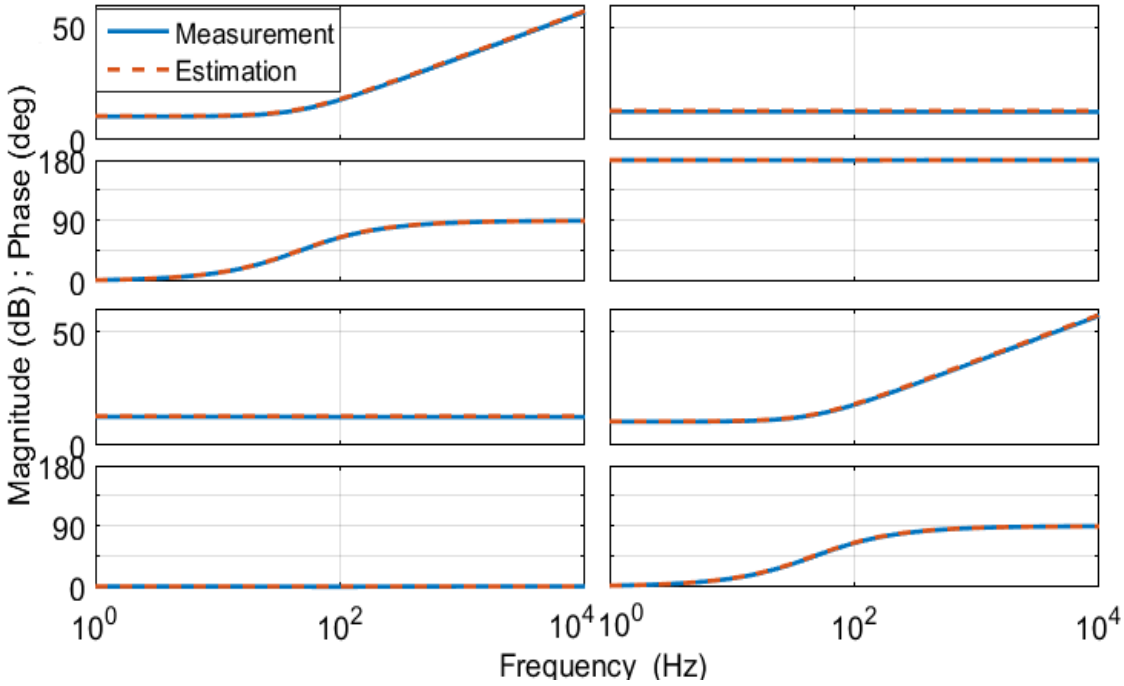

Figure 4-3 Grid impedance in *d-q* frame

4.2 Small-Signal stability assessment of the system with a single PV farm

4.2.1 Different Q control modes

PV generator impedances in *d-q* frame can be derived from small signal model of PV modules that considers dynamics of power stage, digital controllers and PLL effects. The five modes in comparison are

(1) unity power factor,

(2)constant reactive power,

(3) constant power factor,

(4) Watt-var mode shown in Fig.4-4 (a) .

(5) Volt-var droop modes shown in Fig.4-4 (b).

In mode 2 to mode 5, PV inverter is inductive in steady state. PV farm is composed of 12 inverter modules. For each module, P = 250 kW, Q = –75 kVar (Generator convention, Output as positive direction). In mode 4, P_1= 200 kW (0.8 p.u.), ratio of slope is –1.5 in Fig.4-4 (a). In mode 5. V_1 = 0.975 p.u., V_2 = 1.00 p.u., V_3= 1.025 p.u., V_4 = 1.05 p.u.in Fig.4-4 (b).

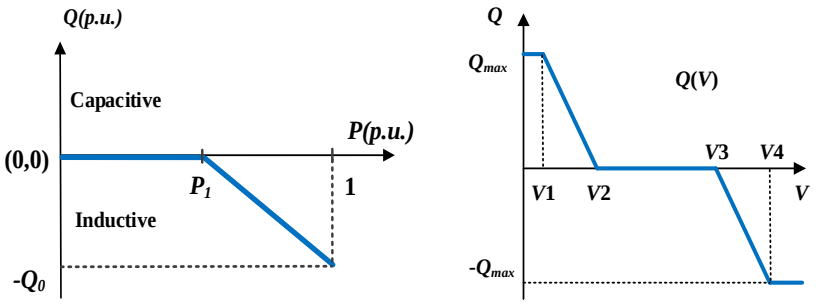

Figure 4-4 (a) mode 4 Watt-var mode curve (b) mode 5 Volt-var droop mode curve

Fig.4-5 shows PV terminal impedances of the mode 1 to mode 4 for 3MW PV farm (twelve 250 kW power modules in parallel) and the impedance of the grid. For these four modes, PV impedance matrices are diagonal dominant and have almost same values in diagonal elements. And PV impedance under mode 2- mode 4 have very similar values in the non-diagonal elements of Z_{dq} and Z_{qd} as well. GNC is applied based on the grid impedance and PV impedance. Fig.4-6 is the Nyquist plots of eigenvalues of return ratio matrix calculated from (4-2). It can be seen that PV connection is stable under these four modes. The small-signal dynamics of mode 2 to mode 4 are almost identical, so mode 3

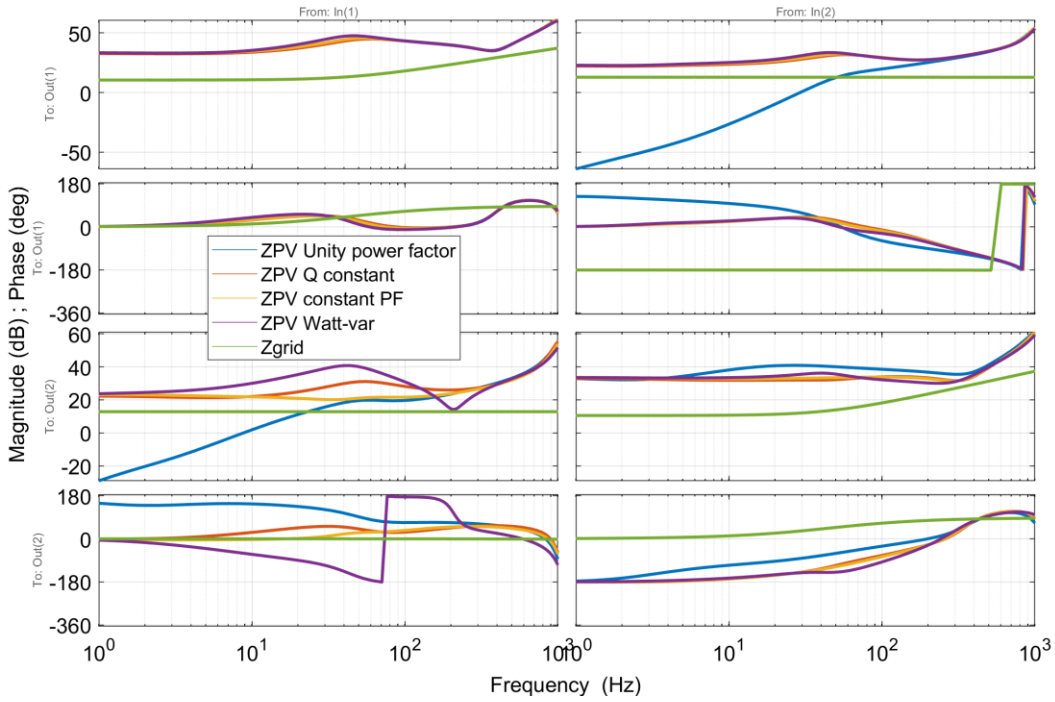

Figure 4-5 Bode plots of PV impedance under mode 1- mode 4 and the grid impedance

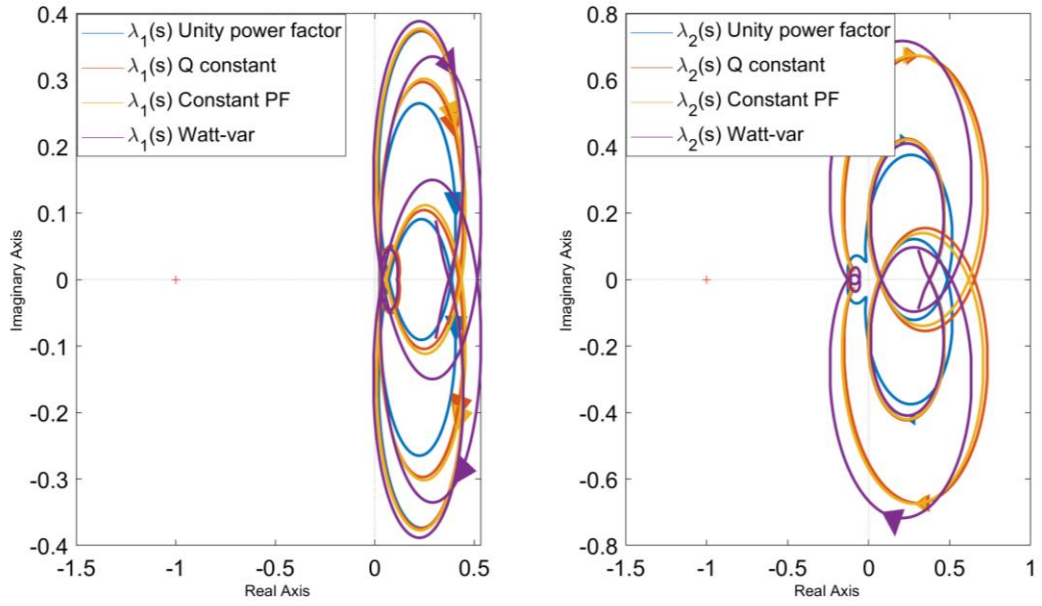

Figure 4-6 Comparison of characteristic loci when PV impedance is under mode 1- mode 4

and mode 4 can be represented by mode 2.So in the later comparison, only mode 1 unity power factor, mode 2 Q constant mode and mode 5 Volt-var droop mode are compared. Fig. 4-7 is bode plot of the PV impedances and grid impedance. Volt-var

droop mode control of Q = f(V) flips the signs of PV impedance elements of Z_{dd}, Z_{dq}, Z_{qq} and increases the value of Z_{qd} so that impedance matrix becomes non-diagonal dominant. Because the matrices are not diagonal dominant, so it's not possible to predict small-signal stabiltiy, GNC needs to applied to get the Nyquist plots of the two eigenvalues. Fig.4-8 is the Nyquist plots of eigenvalues of return ratio matrix calculated from (4-2) for the three modes. From Fig.4-8 it can be seen that different from mode 1 and mode 2, when PV inverter is under volt-var droop mode, one of the eigenvalues encircles (-1,0) two times clock wise. Combined with the known fact that grid impedance and PV admittance don't have RHP pole, the small-signal stability assessment for the interconnection is unstable according to GNC.

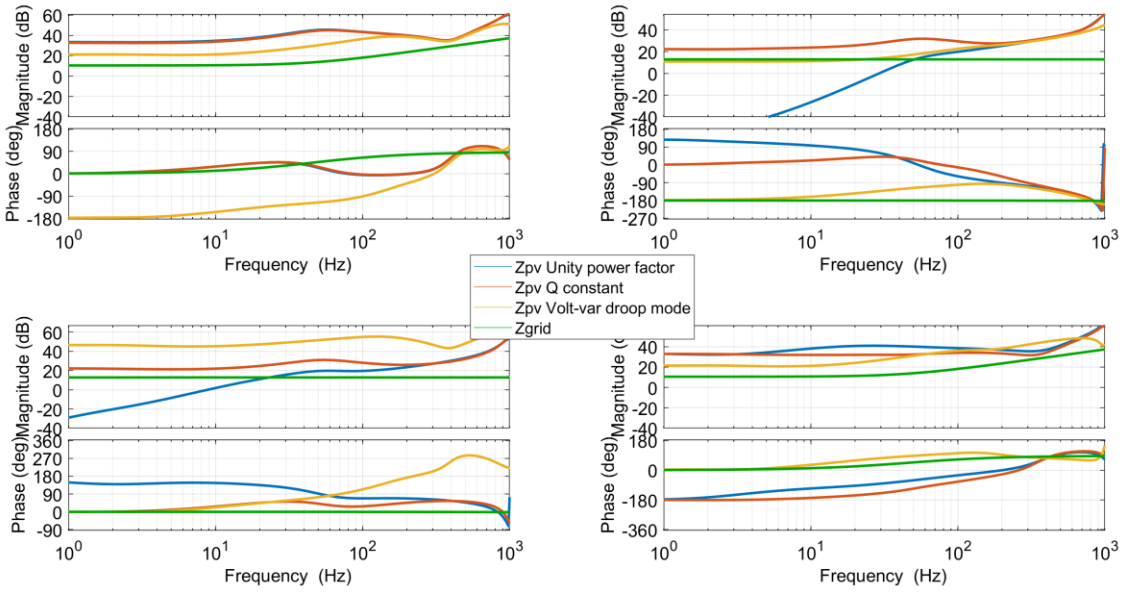

Figure 4-7 Bode plots of PV impedance under mode 1, mod 2 and mode 5 and the grid impedance

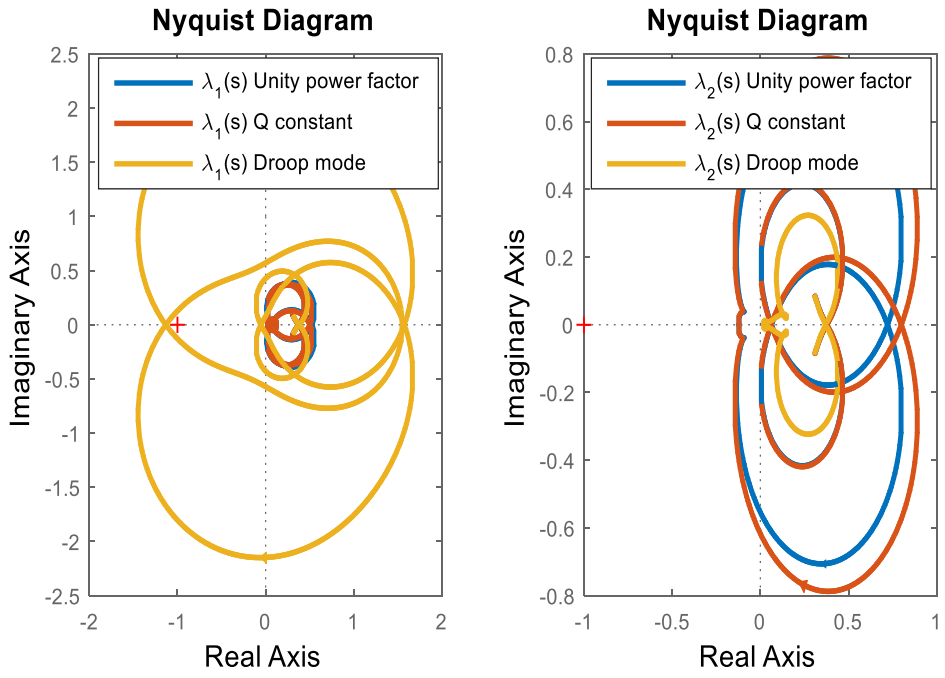

Figure 4-8 Characteristic Loci under different Q control modes

The stability assessment is validated by time domain simulation results in Fig.4-9. which is output current of 3 MW PV farm (12 modules) under droop mode in *d-q* frame.

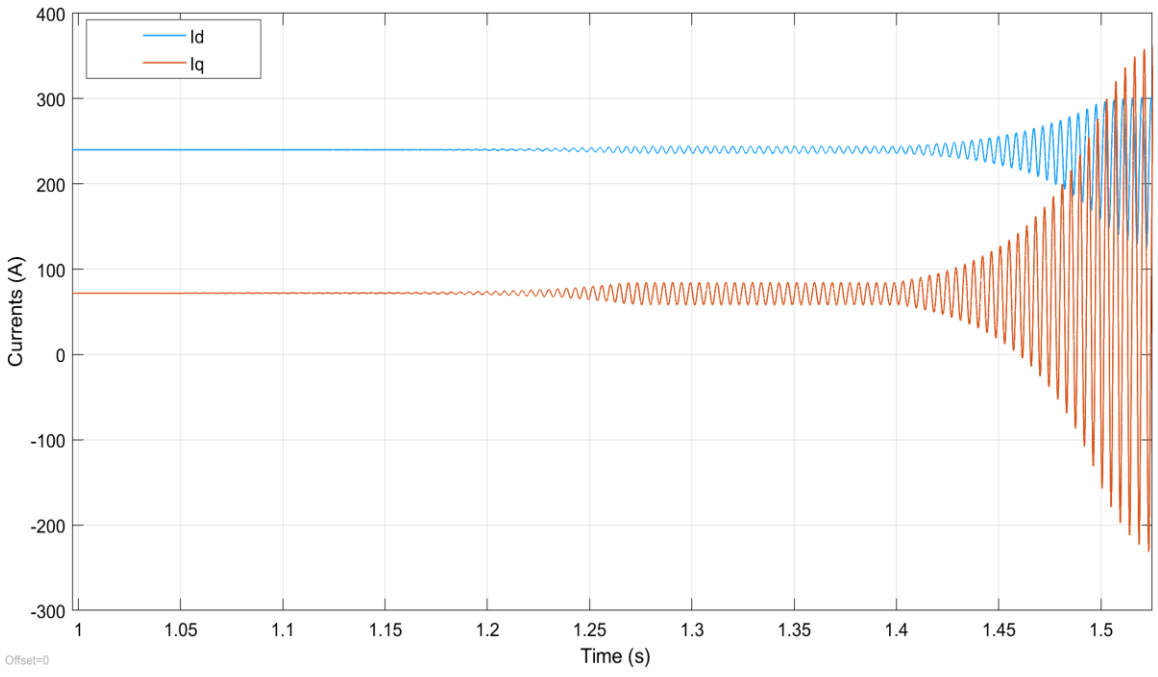

Figure 4-9 Time domain simulation of PV output currents in *d-q* frame under droop mode

At the time of 1 second, PV inverter is shifted from mode 2 to mode 5 and the current outputs start to oscillate. The oscillation frequency is 260 Hz. Oscillation magnitude is limited by Q magnitude – Q_{max} in droop mode curve in Fig.3 before 1.4 s. To further prove the instability problem, the Q_{max} limiter is removed at 1.4s and the oscillation of current starts to increase exponentially.

Fig. 4-10 to Fig. 4-12 are the PV curents in abc frame to show the instaibity from another aspect. Fig.4-10 is the three-phase currents when PV is under mode 2 constant reactive power. Fig 4-11 is the three-phase currents when PV is under mode 5 with a Q limiter, while Fig. 4-12 is the three-phase currents when the Q limiter is removed.

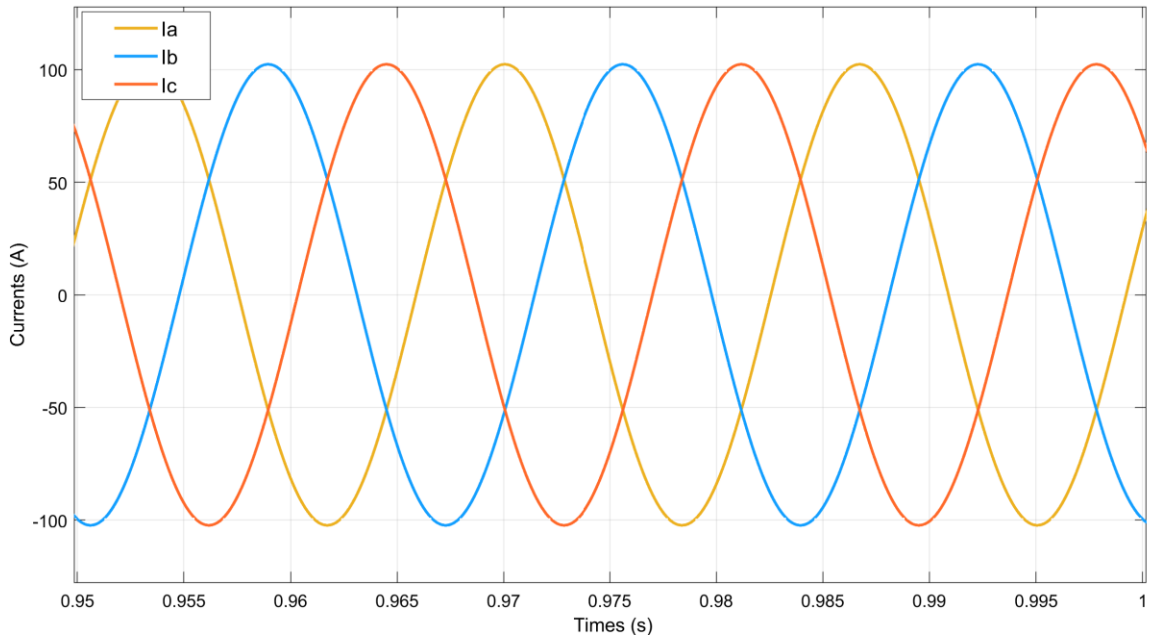

Figure 4-10 Time domain simulation of PV output currents in abc frame under droop mode

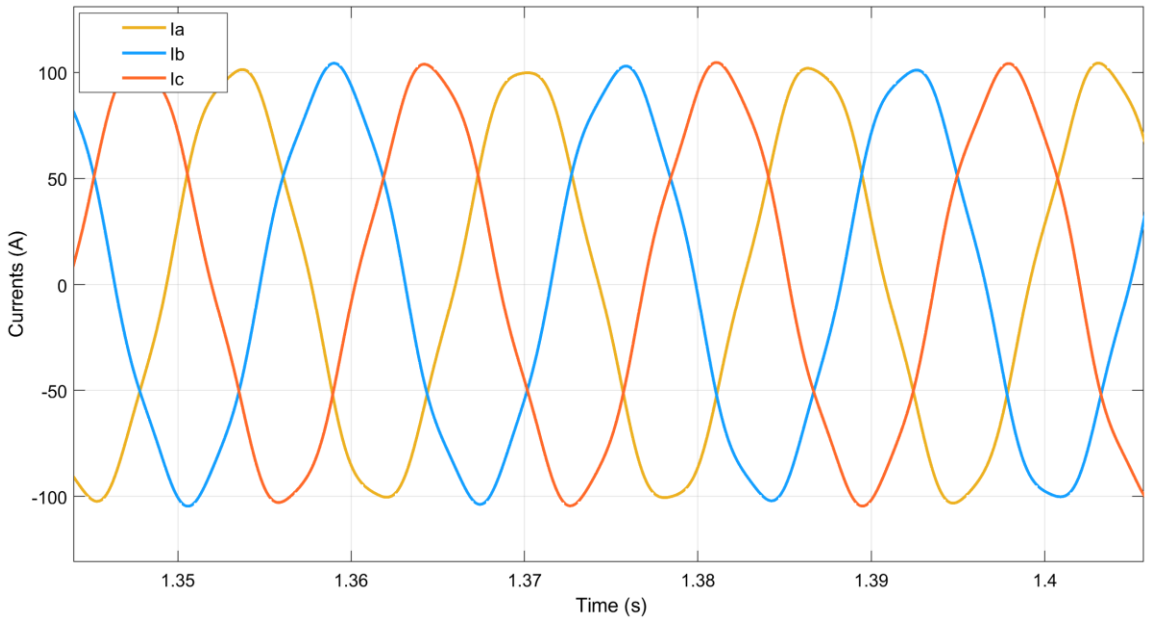

Figure 4-11 Time domain simulation of PV output currents in abc frame under droop mode

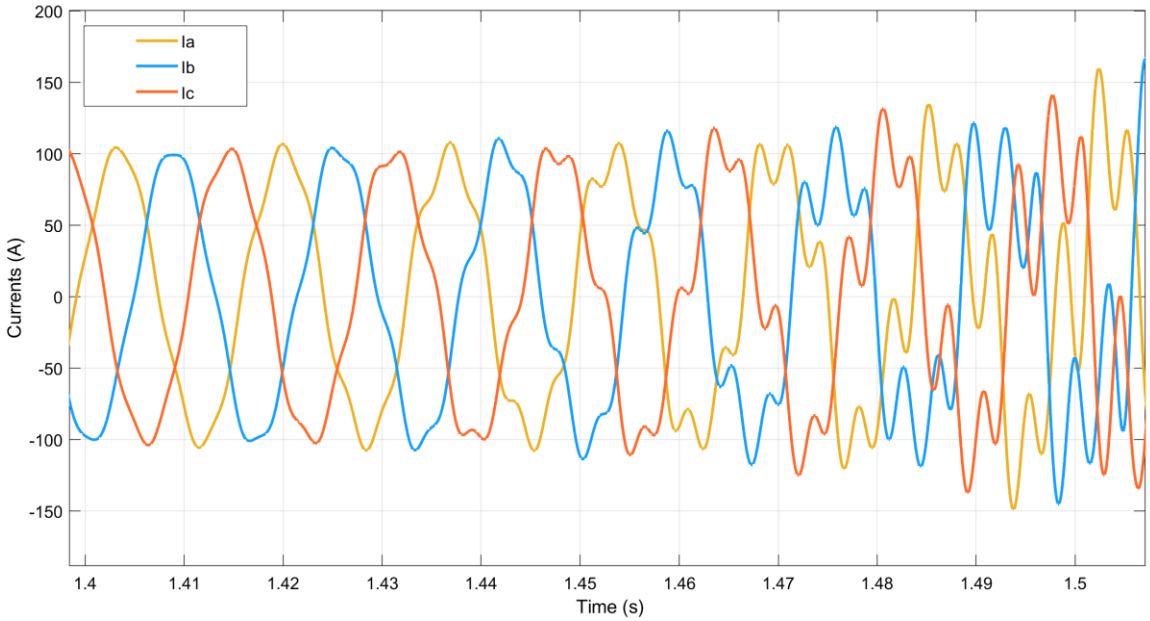

Figure 4-12 Time domain simulation of PV output currents in abc frame under droop mode

The comparison of all the modes leads to the conclusion that with the PV capacity of 3MW, only the mode 5 volt-var droop mode control will cause connection instability. To pinpoint the main dynamics that affect this instability problem, further mathematical

analysis is done to dig out what transfer functions in the diagram of Fig.3-14 causes the eigenvalue λ_1 to encircles (-1,0).

Set the name of elements of grid impedance matrix and PV admittance matrix as $\mathbf{Z_{grid}} = \begin{bmatrix} Z_{dd} & Z_{dq} \\ Z_{qd} & Z_{qq} \end{bmatrix}$, $\mathbf{Y_{PV}} = \begin{bmatrix} Y_{dd} & Y_{dq} \\ Y_{qd} & Y_{qq} \end{bmatrix}$.According to the magnitude comparison in Fig.4-13, $Y_{dd}>>Y_{dq}$ and $Y_{qd}>>Y_{qq}$, so $L_{11}>>L_{12}$ in the return ratio matrix **L** in (4-6).

$$\begin{bmatrix} L_{11} & L_{12} \\ L_{21} & L_{22} \end{bmatrix} = \begin{bmatrix} Z_{dd} & Z_{dq} \\ Z_{qd} & Z_{qq} \end{bmatrix} \cdot \begin{bmatrix} Y_{dd} & Y_{dq} \\ Y_{qd} & Y_{qq} \end{bmatrix} = \begin{bmatrix} Z_{dd} \cdot Y_{dd} + Z_{dq} \cdot Y_{qd} & Z_{dd} \cdot Y_{dq} + Z_{dq} \cdot Y_{qq} \\ Z_{qd} \cdot Y_{dd} + Z_{qq} \cdot Y_{qd} & Z_{qd} \cdot Y_{dq} + Z_{qq} \cdot Y_{qq} \end{bmatrix} \quad (4\text{-}5)$$

Then the first eigenvalue of **L** can be estimated by $\lambda_1=L_{11}$, as shown in Fig. 4-14. The reason is because the two eigenvalues of **L** are basically the solutions of equation (4-6)

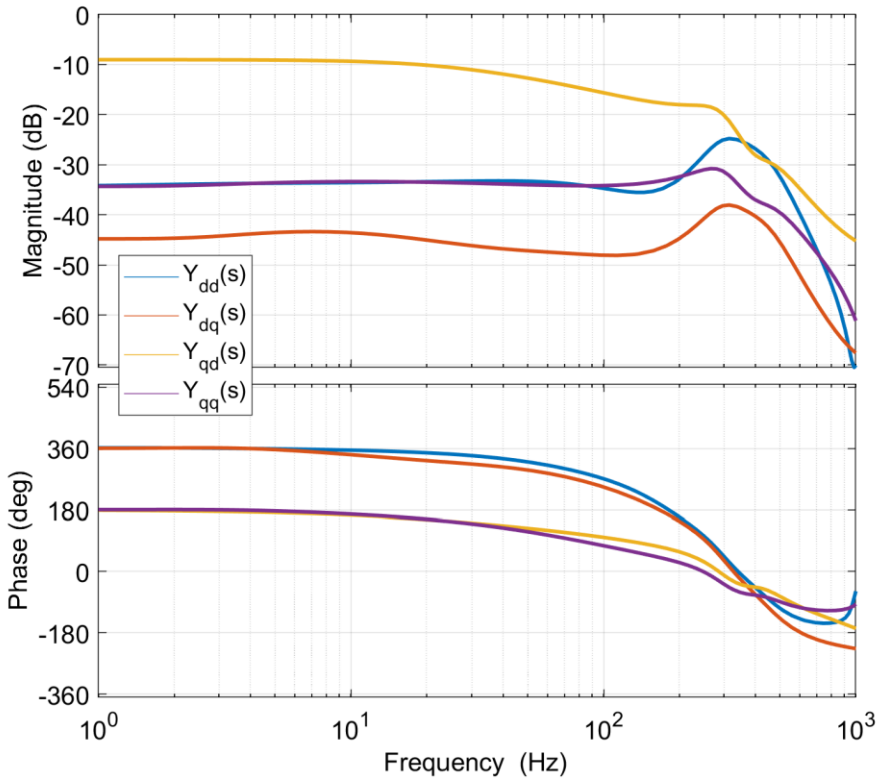

Figure 4-13 Magnitude comparison of four elements of PV admittance matrix

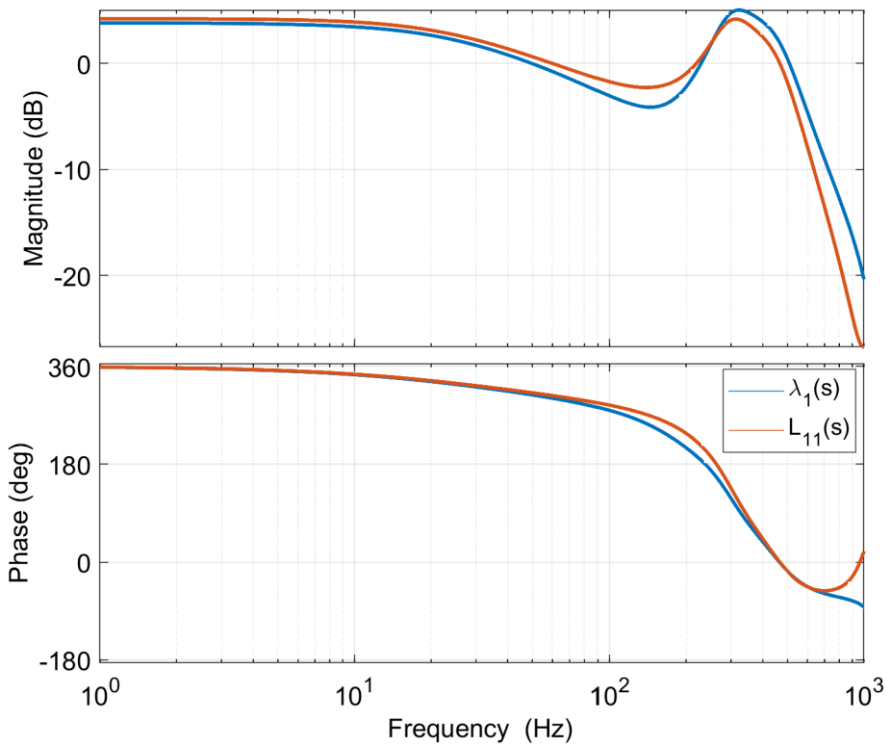

Figure 4-14 Bode plot comparison of λ_1 and L_{11}

$$\begin{vmatrix} L_{11}-\lambda & L_{12} \\ L_{21} & L_{22}-\lambda \end{vmatrix} = 0 \tag{4-6}$$

And because $L_{11} >> L_{12}$ and L_{11} is comparable to L_{21} , the eigenvalue λ_1 which is more related to the d axis or first row elements of **L** can be estimated to be L_{11}. L_{11} is related to grid impedance and PV admittance by

$$L_{11} = Z_{dd} \cdot Y_{dd} + Z_{dq} \cdot Y_{qd} \tag{4-7}$$

The oscillation frequency is between 200 Hz and 300Hz, which is much higher than the DC voltage loop control bandwidth and the PLL loop control bandwidth. If the dynamics of DC voltage loop and PLL are igored, then the admittance of PV can be estimated by

$$\mathbf{Y} = \left[\mathbf{I} - \mathbf{G_{id}} \mathbf{G_{del}} \left(\mathbf{G_{dei}} - \mathbf{G_{ci}} + \mathbf{G_{ci}} \cdot \mathbf{G_{qi}}\right)\right]^{-1} \cdot \left(\mathbf{G_{iv}} + \mathbf{G_{id}} \mathbf{G_{del}} \cdot \mathbf{G_{ci}} \cdot \mathbf{G_{cvq}}\right) \tag{4-8}$$

Fig.4-15 is the comparison of estimation from (4-8) and accuate result from (3-24) between 100 Hz to 1000Hz for each module. It is observed that the esimtation result is

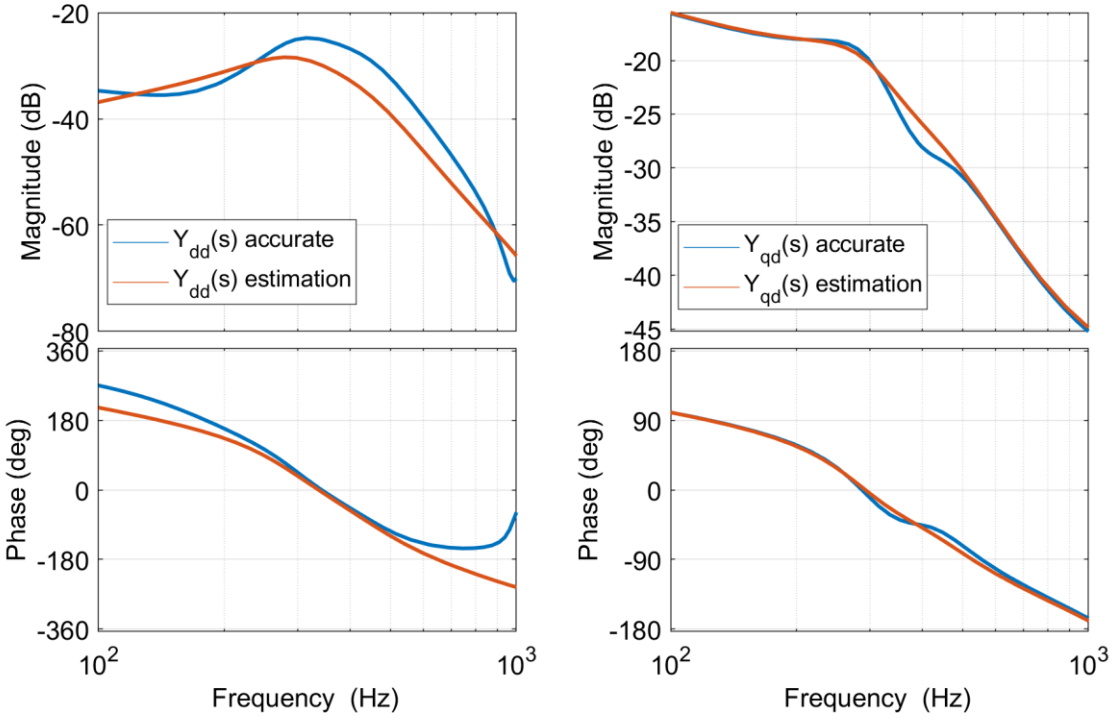

Figure 4-15 Bode plot comparison of estimated and accurate Y_{dd} and Y_{qd}

very close to the accurate model. So between this range of frequency interest, the first row of PV admittance is mostly influenced by the power stage, the inner current controller, the digital delay and the reacitve power controller, which are the main dynamics involved in the stability problem discovered.

4.2.2 Different PV locations

If the location of the single PV farm changes from bus 45 to other locations within the grid, the stability results of connection are different. Fig.4-16 shows the scatter diagram of connection stability of all buses for all buses in the system while PV inverter is under reactive power control mode 5. The horizontal axis is PathR and the vertical axis is PathL.

It can be concluded that bigger the electrical distance from the substation, it's more likely for PV connection to be unstable. It's because that higher grid impedance will increase the grid impedance matrix elements of Z_{dd} and Z_{dq} in (4-7).

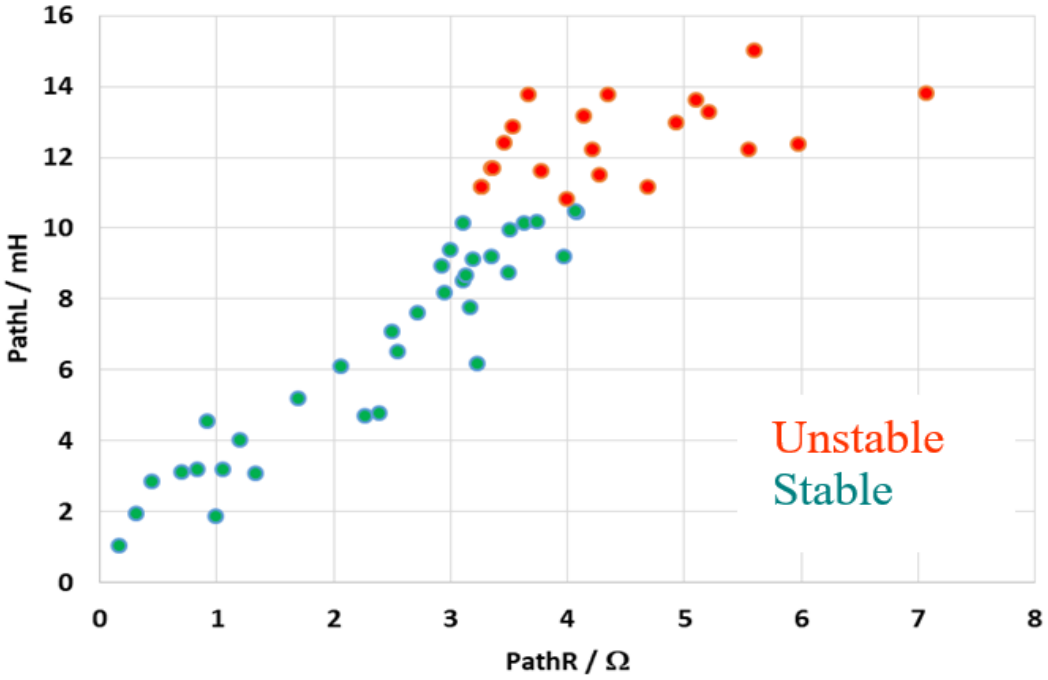

Figure 4-16 Connection stability in terms of electrical distance

4.2.3 Different PV capacities

The PV capacity or the number of PV module in parallel is also a very important factor in the integration stability. Fig.4-17 shows characteristic loci of L(s) when number of PV modules changes, as PV capacity increase from 1 MW to 3 MW, PV integration becomes unstable. In Fig.8, all the PV modules are under Q control mode 5 of volt-var droop mode with Q loop.

As PV capacity increases, it's more likely to cause system instability. The first reason is that as more PV inverters are connected, the voltage magnitude of PCC point is boosted up more so that it's more likely to settle down in the inductive zone of the droop

curve instead of the dead band. And the second reason is that as the number of PV inverters increase, more PV inverters are working in parallel, which increase the ratio of the equivalent admittance of the PV farm over one PV module. And higher PV admittance will positively affect the magnitude of **L** and its eigenvalues.

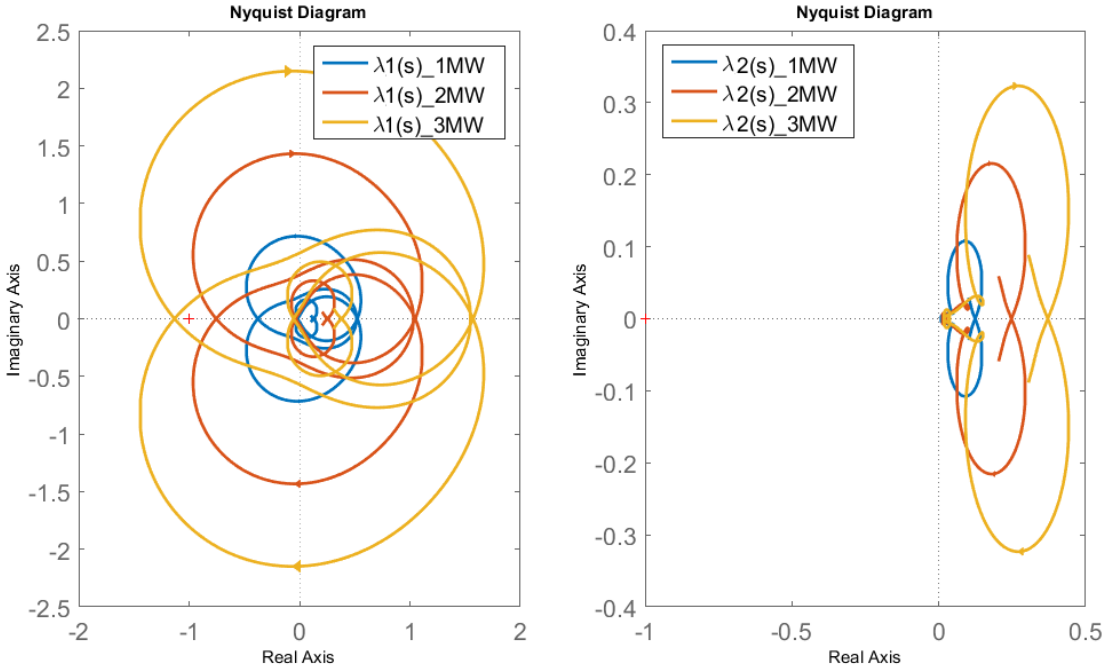

Figure 4-17 Characteristic loci when PV capacity increases (under mode 5)

4.2.4 Different irradiances

In all the previous results shown, PV generators are running at rated power, which is under 100% irradiance. Fig.4-18 shows the characteristic loci of L(s) when irradiance reduces from 100% to 80% then to 60%. Fig.4-19 is the zoomed in view of Fig.4-18 around the critical point of (-1,0).

In three cases, PV is running at MPPT and at Q mode 5 volt-var droop mode for each inverter. 12 inverters are connected in parallel. At full irradiance, P = 250 kW. At 80% irradiance, P = 200 kW. At 60% irradiance, P = 150 kW.

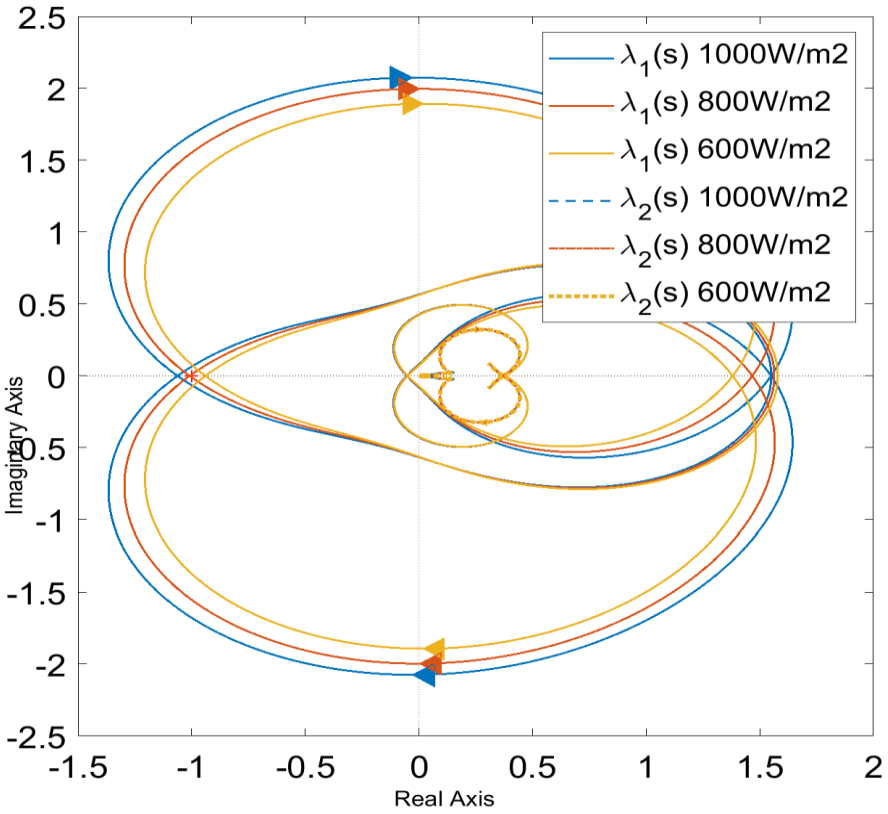

Figure 4-18 Characteristic loci with different irradiances (under mode 5)

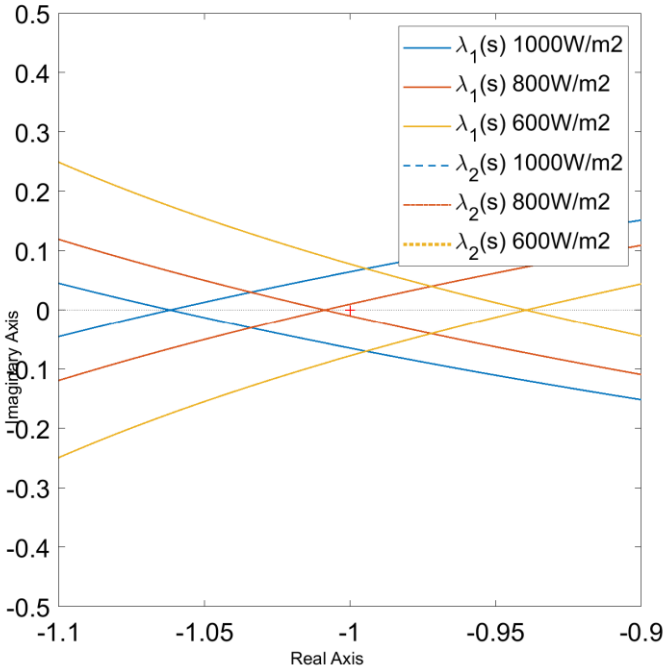

Figure 4-19 Zoomed in characteristic loci with different irradiances (under mode 5)

It is shown in Fig.4-19, in the cases of 100% irradiance and 80% irradiance, characteristic locus of λ_1 encircles (-1,0) , but for the irradiance of 60%, λ_1 no longer encircles (-1,0). In other words, as the irradiance reduces, the characteristic locus of λ_1 is shrunk and finally no longer encircles (-1,0). The trend is the same as the last section of reducing the PV capacity or the number of PV inverters, even though the number of PV inverters in this section keeps the same. It means that as long as the total active power and reactive power and Q control of the PV farm keep the same, the terminal impedance keeps the same even though the numbers of PV inverters are not the same.

4.2.5 Solutions for the instability

The instability is due to interaction of multiple inverters. If the number of PV inverters in parallel reduces, the unstable case becomes stable. And the instability will only happen when PV inverter is working in inductive zone of droop curve. If PV is working in capacitive zone, the connection of PV inverter and the grid is stable.

Modifications can be made on the PV inverter controllers to solve the stability problem under the control mode of volt-war. The solutions include reducing current loop bandwidth, reducing reactive power loop bandwidth and reducing controller delay by increasing switching frequency.

Fig. 4-20 shows the Nyquist diagrams of eigenvalues if one of the solutions is applied. Compared to the blue curves of original Q= f(V) droop control, $\lambda_1(s)$ doesn't encircles (-1,0) in red, yellow and purple curves, which shows that the system is stable after the modifications.

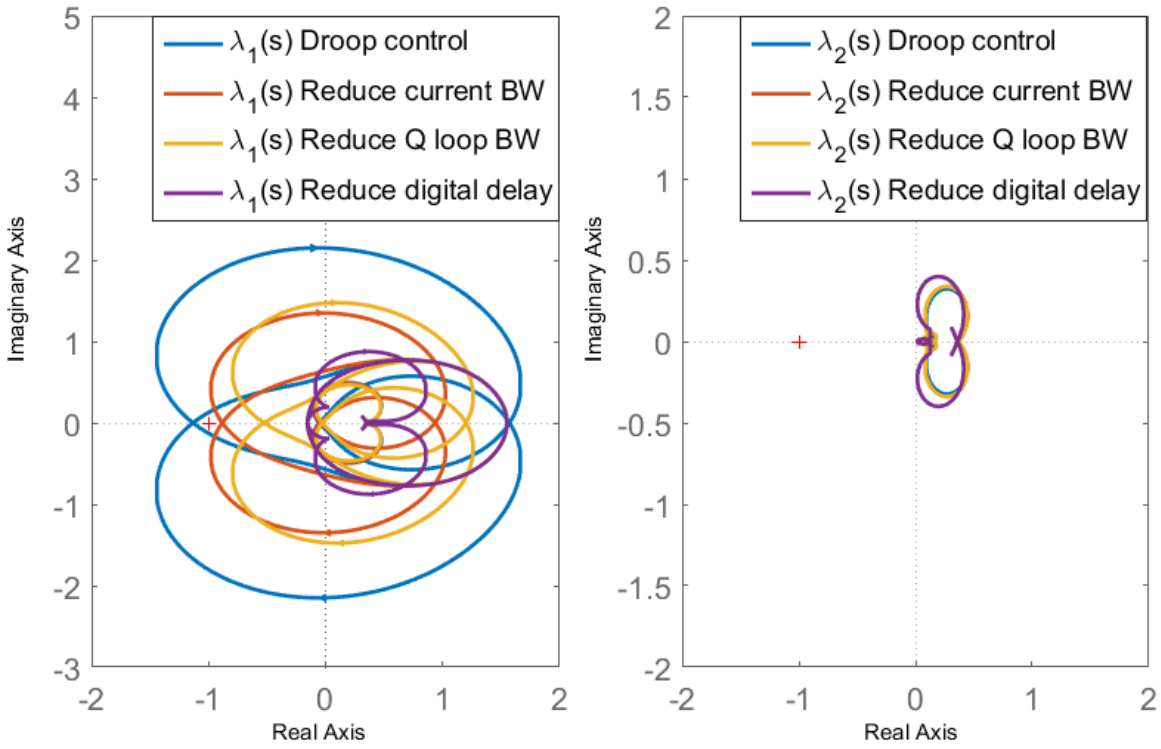

Figure 4-20 Proof of solution of the unstable case

4.3 Small-signal stability assessment of the system with two PV farms

In this section, 3MW of PV generator is split evenly into two PV farms to analyze the stability of multiple PV connection. One PV farm is at bus 45, and the other PV farm may be connected to any bus of the system. For all the grid side and PV side impedances shown below, they are measured at PCC point of bus 45, so the grid side impedance includes dynamics of the second PV farm.

4.3.1 Different Q control

To compare the interactions of two PV generators under different Q control modes, three cases are compared in which both PV farms are under mode 1 unity power factor, mode 2 Q constant and mode 5 volt-var droop mode separately. Mode 3 and mode 4 can be represented by mode 2 as shown in section 4.3.1. For all three cases, the two PV farms

are connected to bus 45 and bus 56. And when PV are under Q constant mode, the Q reference is set to be the same value as droop mode. As the system is under light load condition (20% of the peak load) and PV generator is at full active power harvest, PV generators are inductive at bus 45 and bus 56.

GNC based on *d-q* frame impedances is applied at the first PV farm terminal of bus 45. Impedances of grid side and PV side are shown in Fig.4-21. So the PV impedance only contain the dynamics of the first farm and the grid side impedance includes the dynamics of the lines and the second PV farm as well.

Fig. 4-22 shows Nyquist plots of eigenvalues of return ration matrix of three cases. Only λ_1 of case three encircles (-1,0) which indicates unstable of system operation of these two PV generators under mode 5 volt-var droop control.

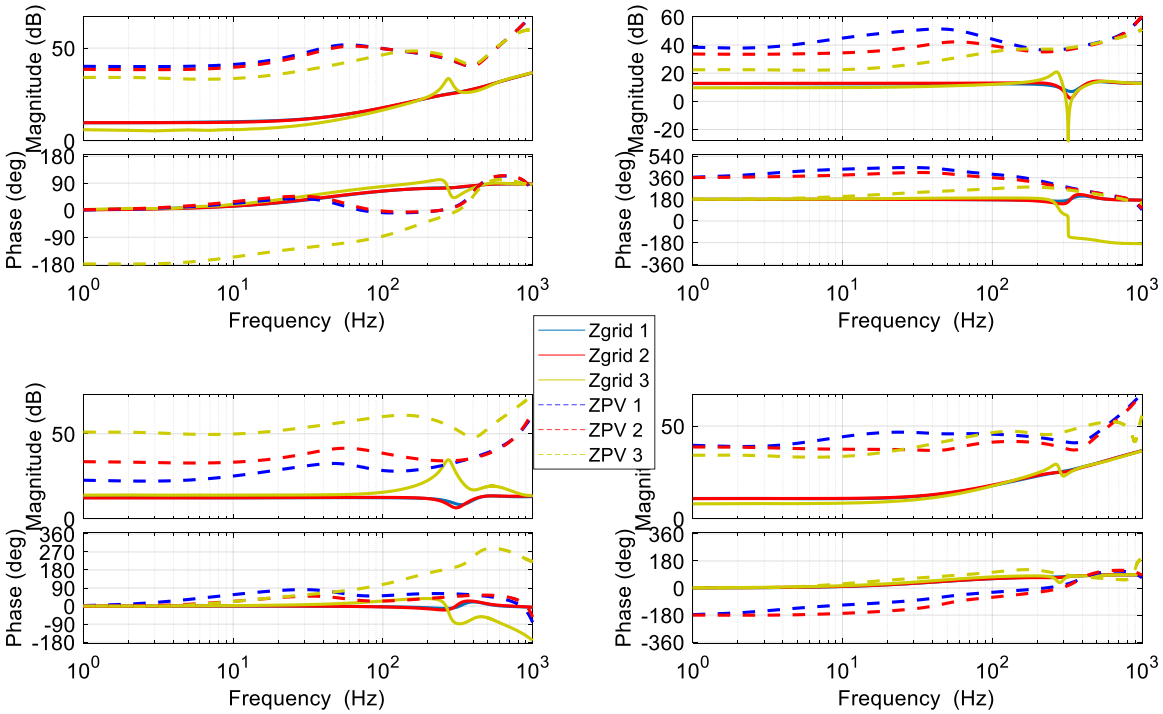

Figure 4-21 *d-q* frame impedances of the PV and the grid, case 1: Unity power factor, case 2: Q constant, Case 3: Droop mode.

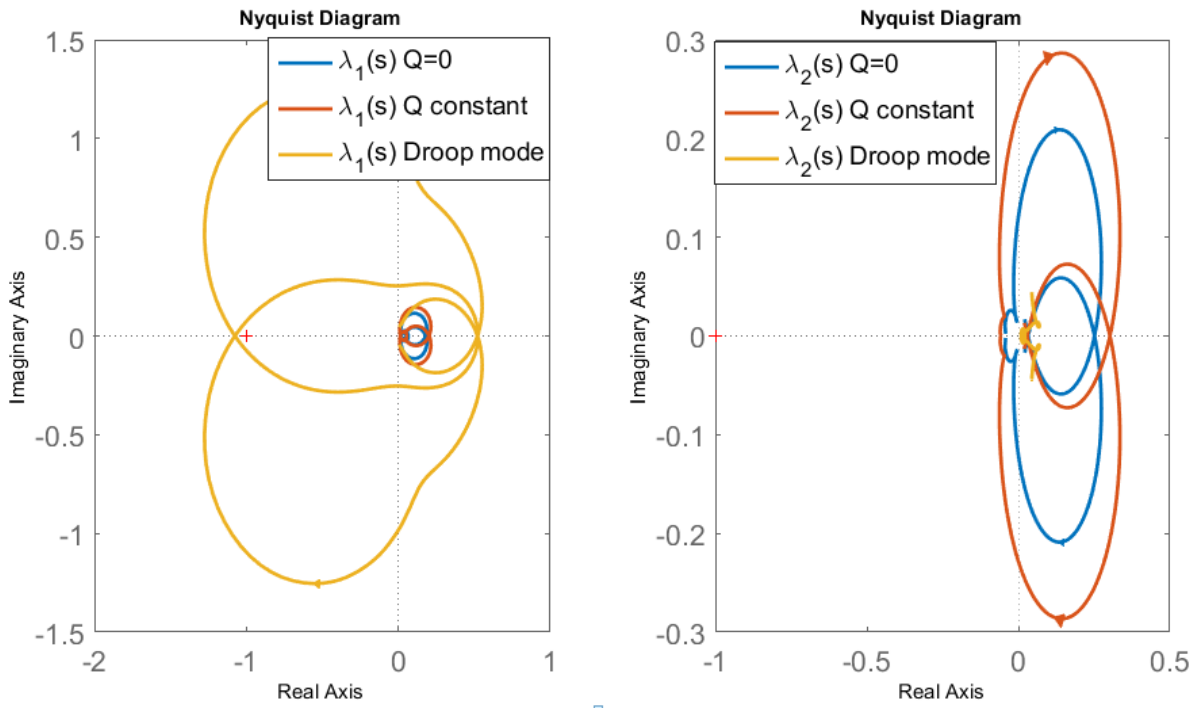

Figure 4-22 Characteristic loci for multiple PVs under different Q control

And the GNC application result is validated by the time domain waveforms of Fig.4-23 and Fig.4-24. At mode 1 or mode 2, the three-phase currents of first PV farm terminal are of pure sinusoidal shapes while the currents are distorted and twisted because of system oscillations when PV is under mode 5 control

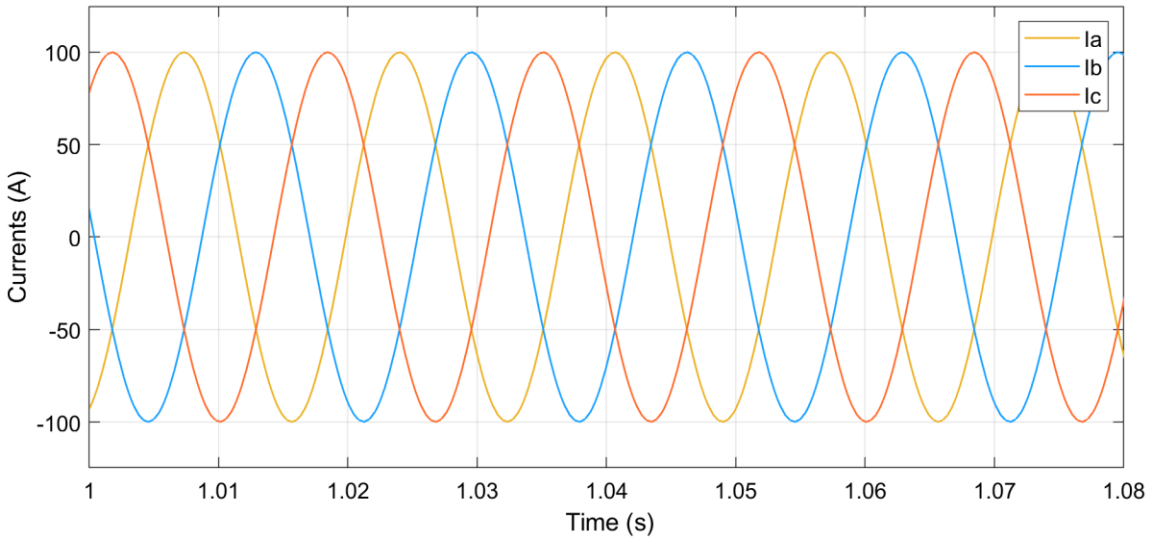

Figure 4-23 Three-phase currents of first PV farm under Q control under mode 1 or mode 2

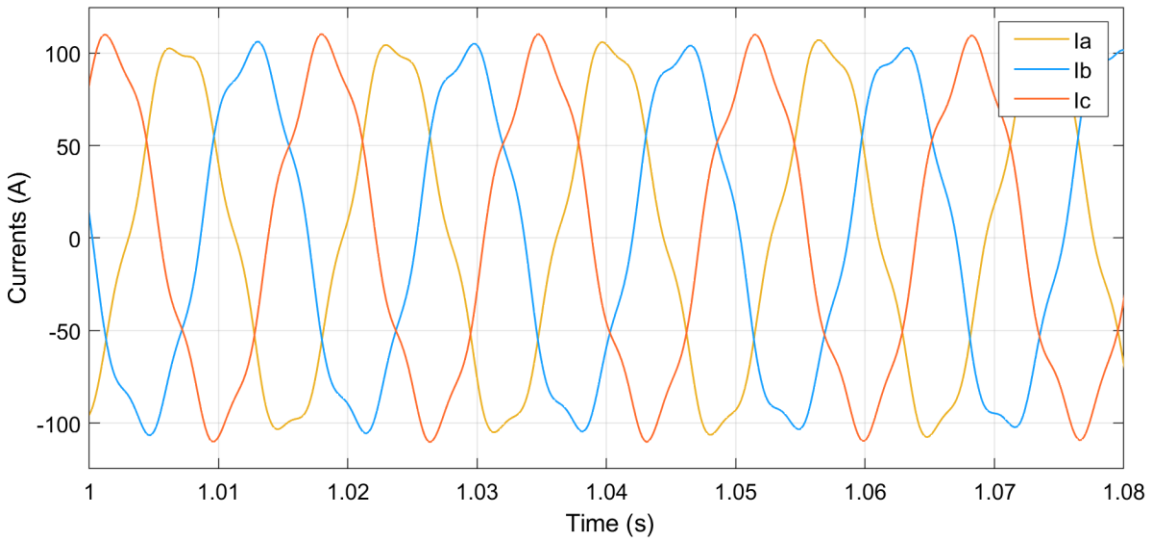

Figure 4-24 Three-phase currents of first PV farm under Q control mode 5

Fig. 4-4(b) is the droop control curve Q = f(V) that is applied on PV generators under droop mode. For previous cases of droop mode, PV generator terminal voltages are above V3 (1.025 p.u.), so the generators are working in inductive zone. In another case, system load increases to peak load, system voltage profile is at low level, the two PV farms terminal voltage drop below V2 (1.0 p.u.), so the PV generators work in capacitive zone.

Fig.4-25 is the impedances of grid and PV generator for the inductive case and the capacitive case. And Fig.4-26 is the corresponding Nyquist plots of eigenvalues of return ratio matrix. The inductive case is unstable because λ_1 encircles (-1,0), while the capacitive case is stable.

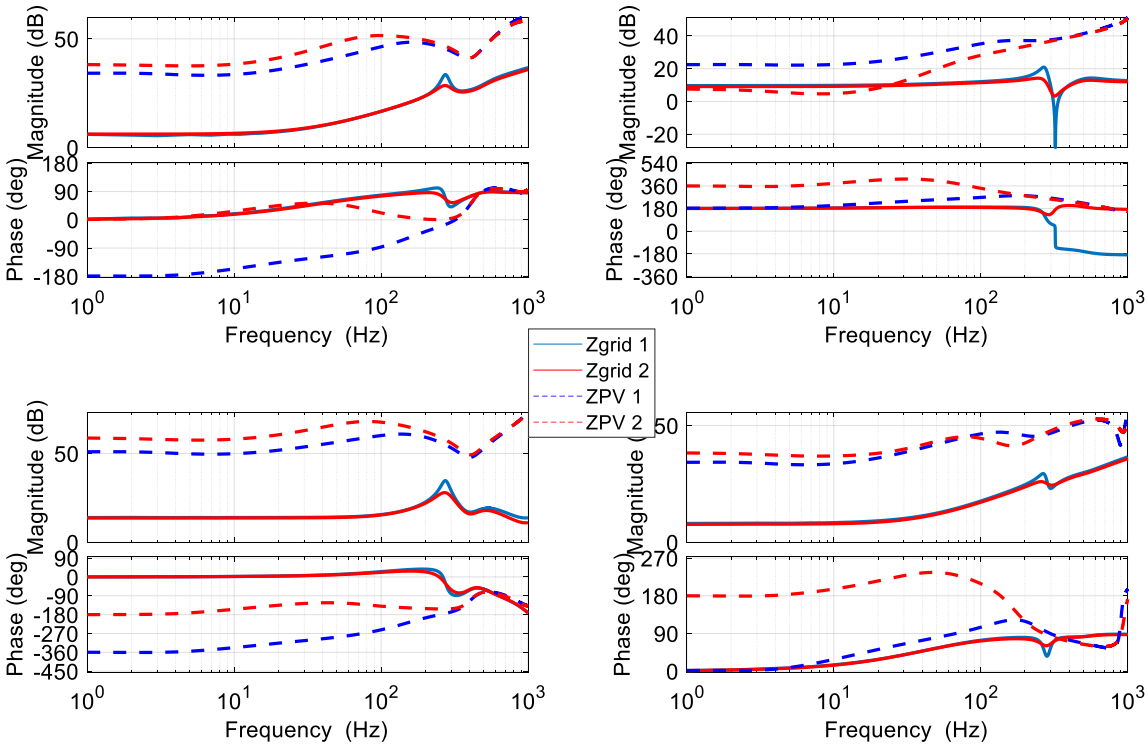

Figure 4-25 PV and grid impedances in *d-q* frame. Case 1: inductive zone, case 2: capacitive zone

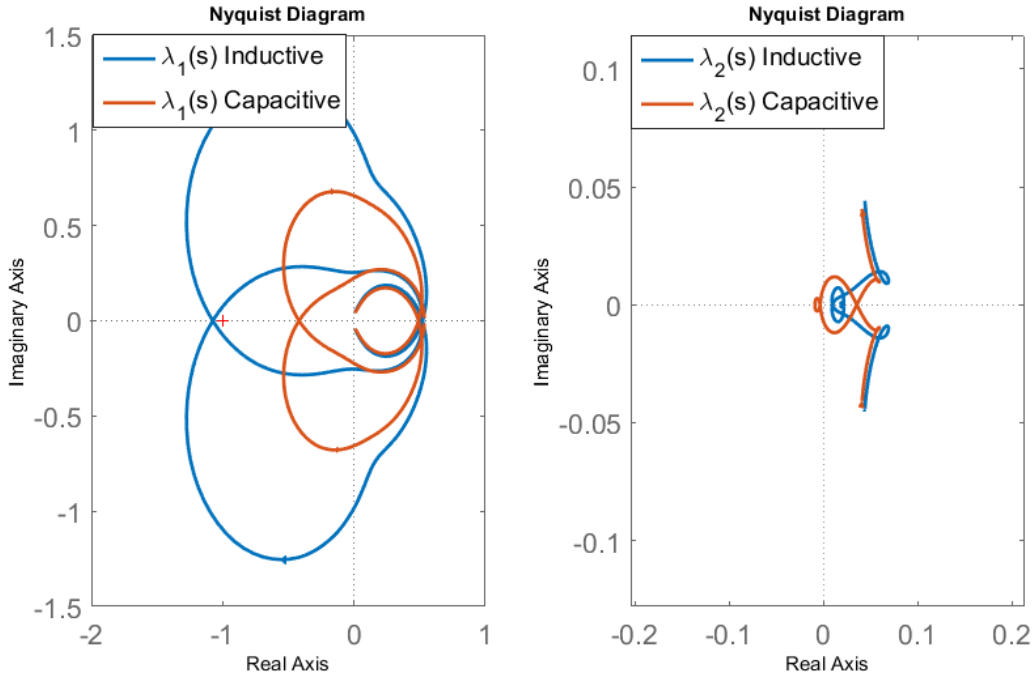

Figure 4-26 Characteristic loci when multiple PVs are at different zones of droop curve

At inductive operation zone, grid and PV impedances have opposite polarity until several hundreds of Hz, while at capacitive zone, grid and PV impedances don't have too much phase difference. So it's more likely to see unstable interconnection when system voltage profile is very high and makes PV inductive in droop mode.

4.3.2 Second PV farm connected to different locations

To compare the interactions of two PV generators at different locations, three cases are compared in which the second PV farm is at bus 56, bus 41 and bus 19 separately. For all three cases, the first PV generator is connected at bus 45, where impedances are measured in *d-q* frames for the grid side and the PV side and shown in Fig.4-27. In Fig.4-27, solid curves are grid impedances and dashed curves are PV impedances. And Fig.4-28 is the Nyquist plots of the two eigenvalues of the return ration matrix.

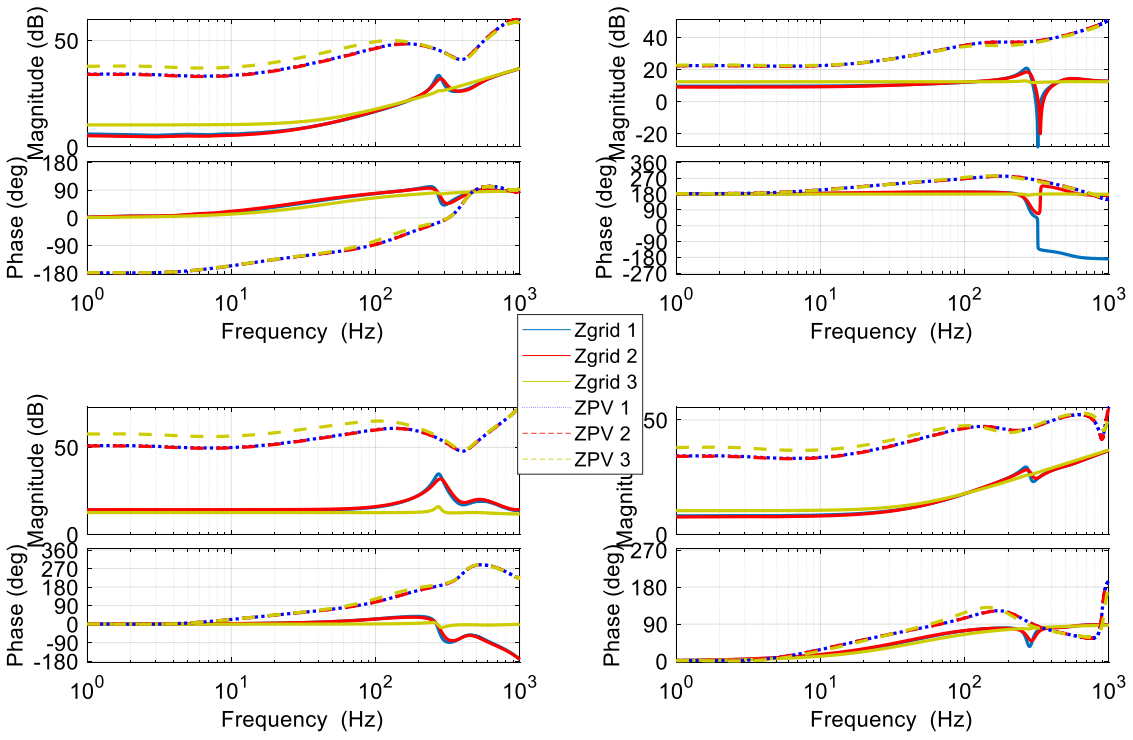

Figure 4-27 PV and grid impedances in *d-q* frame, Case 1: second PV at bus 56, case 2: second PV at bus 41, Case 3: second PV at bus 19.

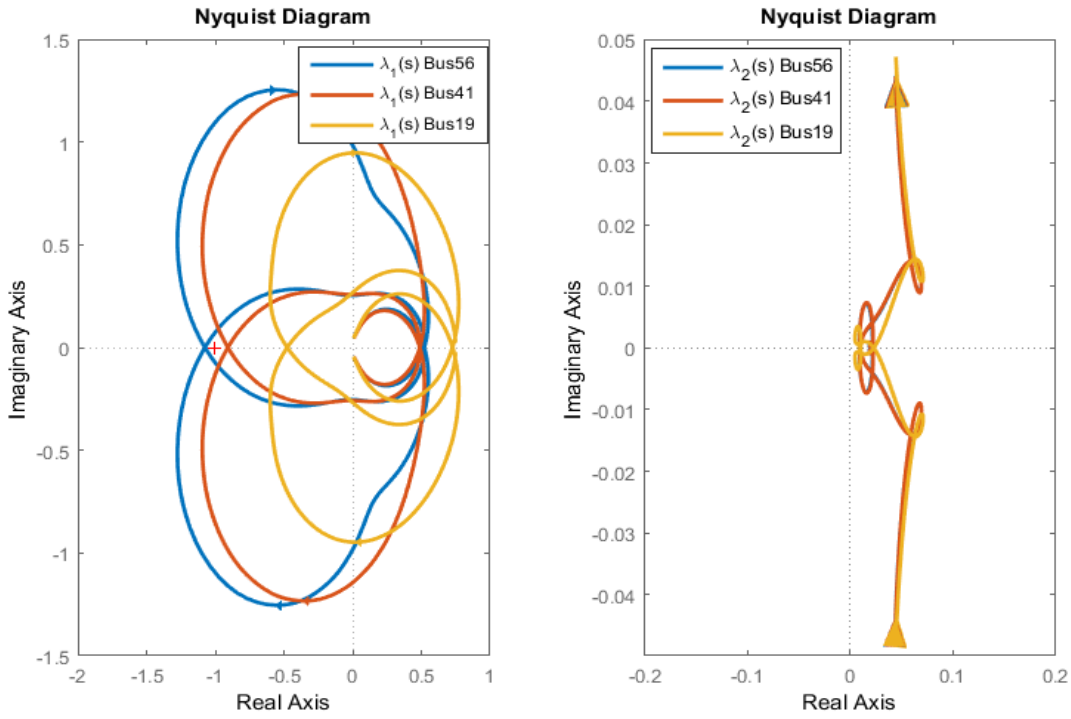

Figure 4-28 Characteristic loci with different allocation for the second PV farm

In case one, Nyquist plot of encircles (-1,0), so the connection is not stable. While in case two and case three, neither eigenvalue loci encircles (-1,0), the operation of second PV farm at bus 41 or bus 19 is stable.

The results of the cases of different locations show that PV generators connected to different branches of the radial system may have interactions and cause instability when they are regulating the AC voltage together, the possibility of interaction decreases if one PV farm move closer to the substation or if the common path of the two buses is shortened.

4.3.3 Different capacities of PV penetration

This section compare the cases when the total capacity of two PV farms changes. Fig.4-29 and Fig.4-30 are comparison of impedances and eigenvalues of 1MW, 2MW

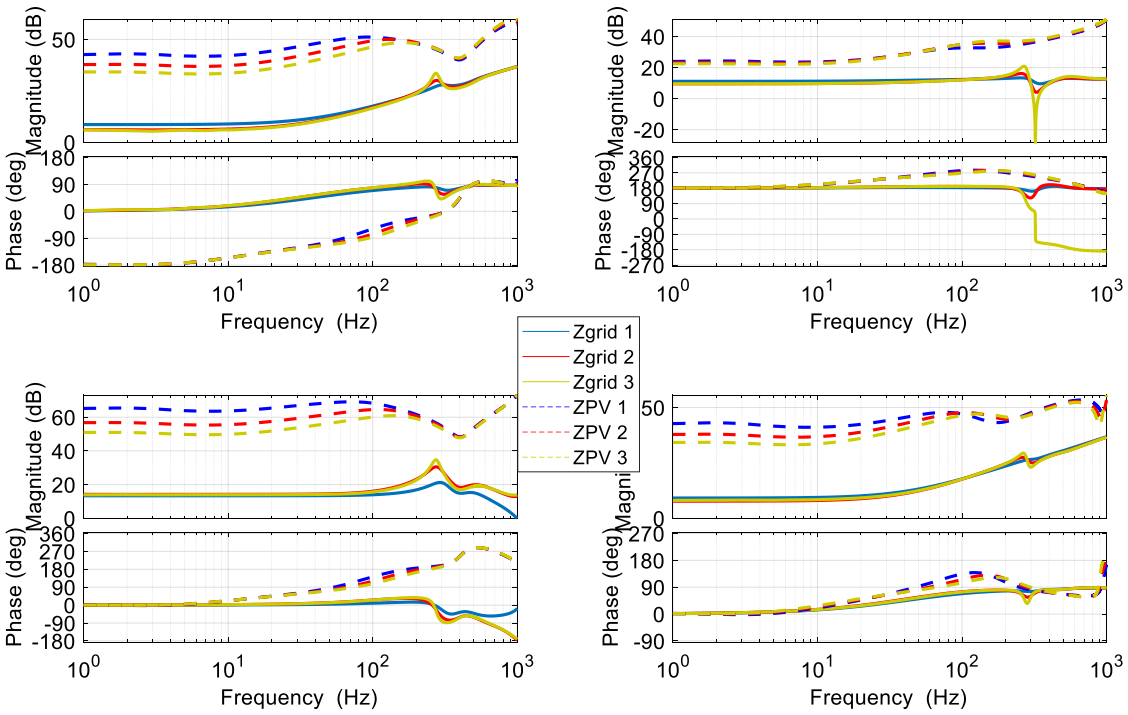

Figure 4-29 PV and grid impedances in *d-q* frame Case 1: 1MW, case 2: 2MW, Case 3: 3MW.

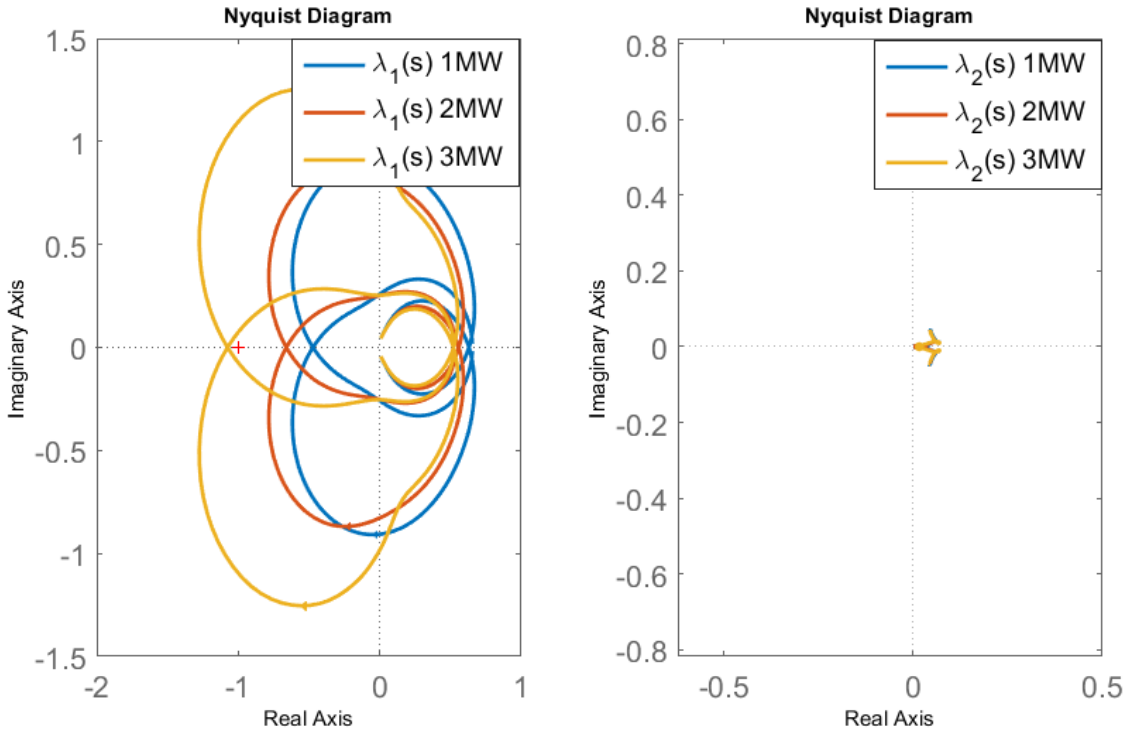

Figure 4-30 Characteristic loci when total PV capacity increases

and 3MW. All PV capacity is split evenly at two physical locations of bus 45 and bus 56. And in all three cases, PV generators are working in inductive zone of droop mode.

The case of 3MW of PV is not stable, as λ_1 encircles (-1,0) two times clockwise. From the changes of eigenvalue loci shown in Fig.4-30, it can be concluded that as PV capacity increases, it's more likely for the PV connection to be unstable.

4.3.4 Different irradiances

This section compares the cases when local irradiance changes for the two PV farms. Fig.4-31 and Fig.4-32 are comparison of impedances and eigenvalues of irradiance of 100%, 80% and 60%.. All PV capacity is split evenly at two physical locations of bus 45 and bus 56. And in all three cases, PV generators are working in volt-var droop mode control.

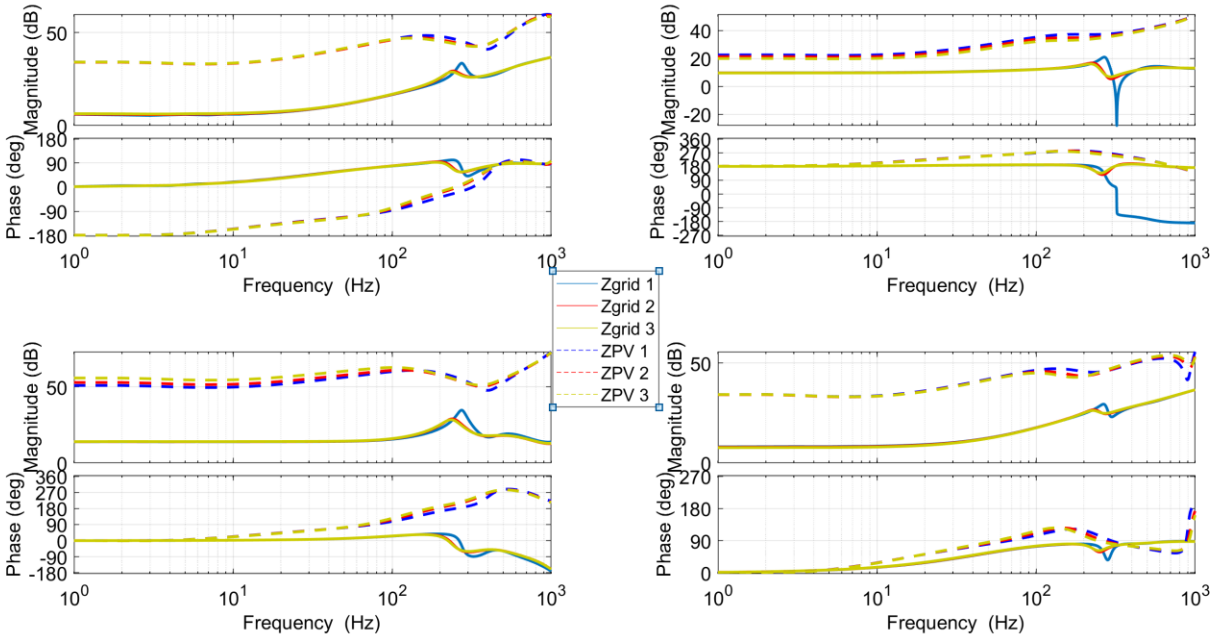

Figure 4-31 PV and grid impedances in *d-q* frame Case 1: 100% iradiance, case 2: 80% irradaince, Case 3: 60% irradiance.

Only the Cases of 100% irradiance is not stable, as λ_1 encircles (-1,0) two times clockwise. From the changes of eigenvalue loci shown in Fig.4-32, it can be concluded that as irradiance increases, it's more likely for the multiple PV farms in the same distribution system to have interactions with each other.

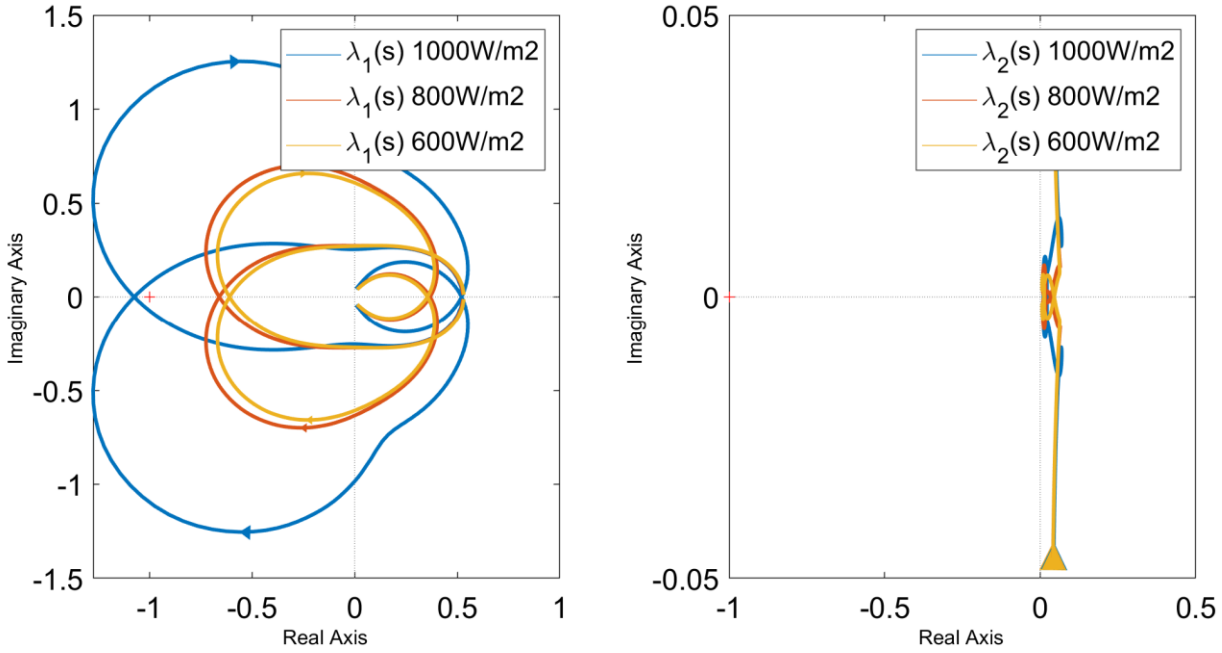

Figure 4-32 Characteristic loci when irradiance changes

4.4Experimental verification on the scaled-down test-bed

4.4.1 One PV Inverter

A hardware experiment is done to measure PV generator and grid impedances in *d-q* frame, based on which GNC is applied to assess connection stability. The hardware circuit is shown in Fig.4-33 with the converter specification the same as Table 3-3. Agilent E4360A PV emulators working as PV array is connected to a DC/AC inverter which is tied to AC source (representing grid) through a line. The line impedance is composed of a resistor of 0.7 and an inductor of 5.7 mH. Impedance measurement unit

(IMU) introduced by [96]-[102] is located between the line and the converter to measure the impedances of the PV inverter and the grid to apply GNC. Fig.4-34 is a photo of all the hardware components.

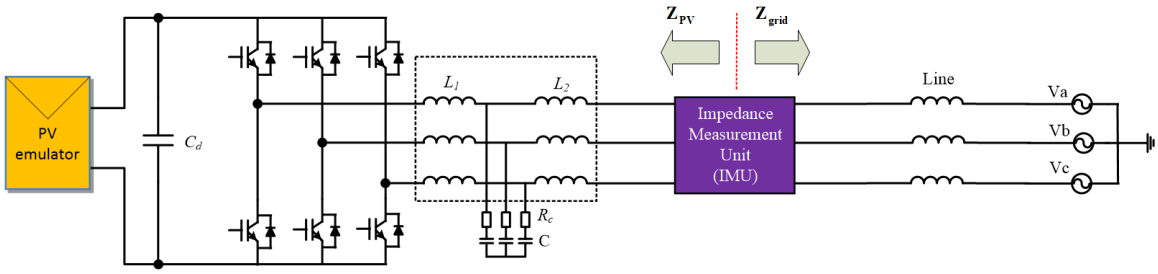

Figure 4-33 Hardware experiment circuit of a single PV inverter case

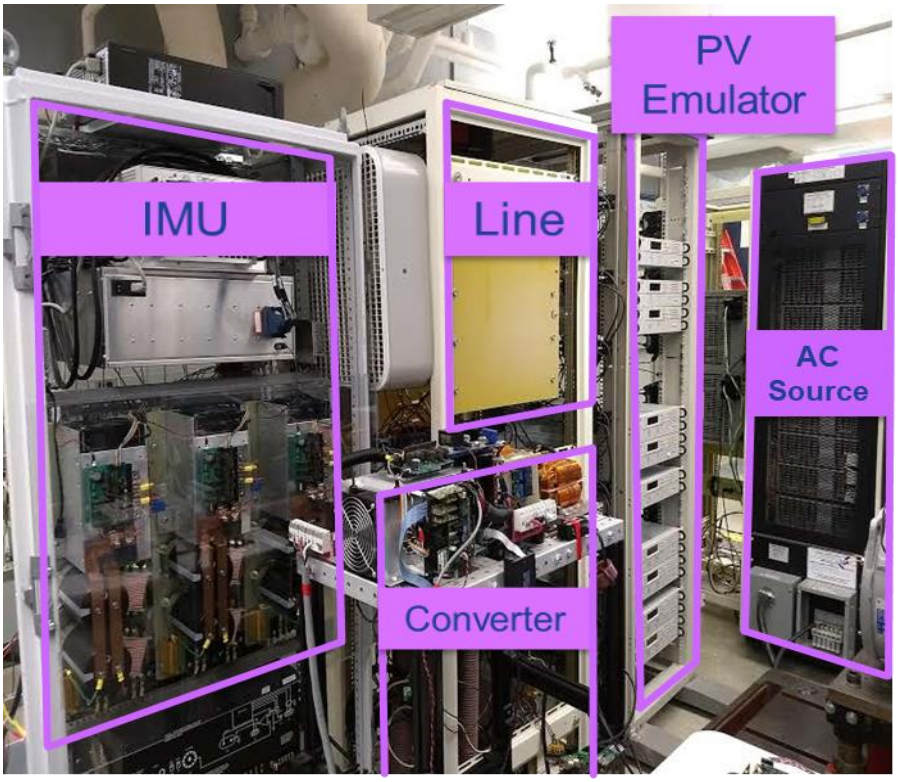

Figure 4-34 Picture of the hardware components

In Fig.4-35, initially PV generator is working under Q control mode with power output of 2640 W and -800 Var. the system is working stably. After Q control mode is shifted to

volt-var control mode Q = - K_v (V-125) and K_v =160, DC voltage starts to oscillate and the AC side voltages and currents become distorted. Fig. 4-36 is a zoomed in view of AC side line-to-line voltage and line current at stable operation state and during the process of going unstable.

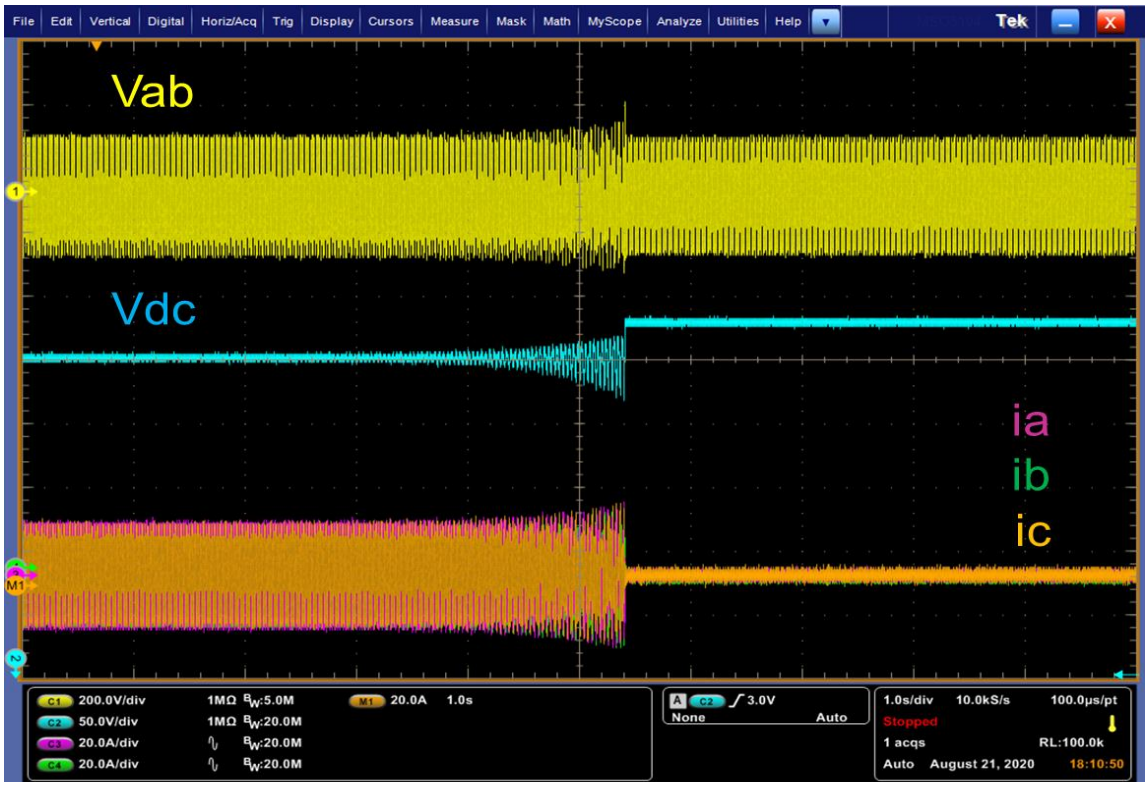

Figure 4-35 Recorded waveform of PV inverter transients on the scope

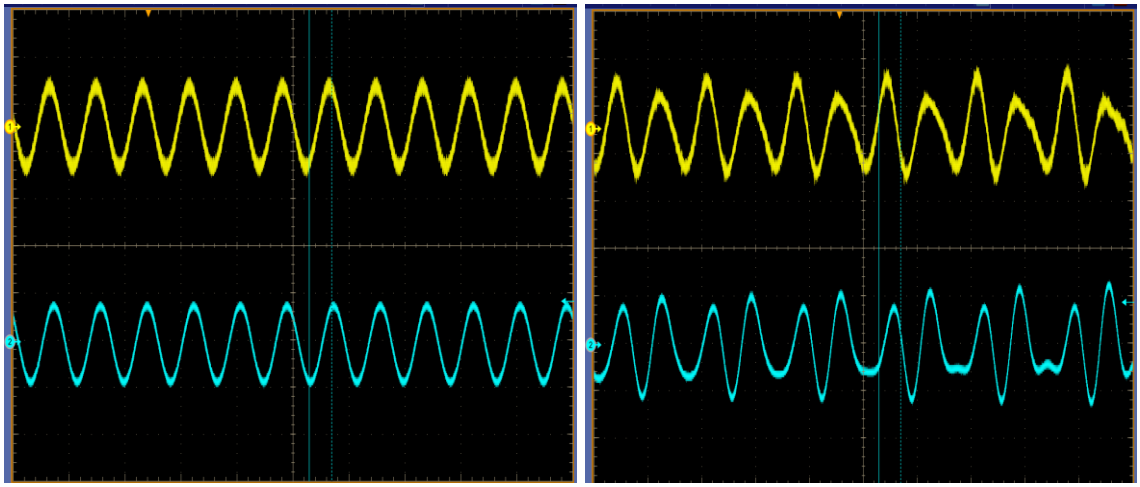

Figure 4-36 PV inverter Vab and Ia waveform on the scope for the stable and unstable cases

Actually all the five reactive power control modes are tested both in steady state waveform and also GNC based on *d-q* frame impedances, which include (1) Unity power factor, (2) Constant reactive power, (3) Constant power factor, (4) Watt-var mode and (5) Volt-var mode. Mode 1, mode 3 and mode 4 can be represented by mode2, so here only the GNC results of mode 2 and mode 5 are shown in Fig.4-37 and Fig. 4-38.

For the stable case of mode 2 constant Q control, GNC is applied on impedances measured of PV generator and the grid. Fig.4-37 is the Nyquist plots of the two eigenvalues. Neither eigenvalues encircles (-1,0), as grid impedance and PV admittance don't have RHP poles, the encirclement condition leads to the conclusion that the connection is stable, proving the results from hardware experiments.

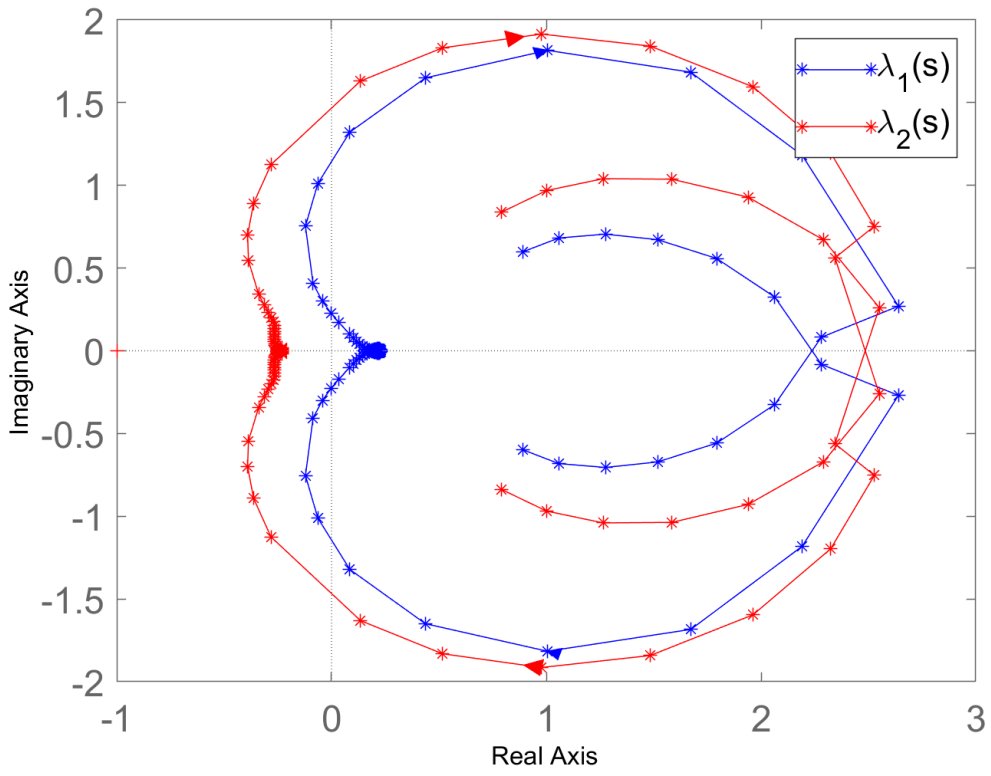

Figure 4-37 Characteristic loci for the Q constant control

For the unstable case of volt-var droop mode control, there's not a stable operation point for impedance measurement on both sides together. So the grid side impedance and PV impedance are measured separately. While grid impedance is being measured, PV reactive controller PI parameters are reduced by half to make the connection stable. And when PV terminal impedance is being measured, the inductance of the line in the grid is reduced from 5.7 mH to 3.3 mH.

Fig.4-38 is the Nyquist plots of the two eigenvalues. The first eigenvalue λ_1 encircles (-1,0) counter-clock twice. While grid impedance and PV admittance don't have RHP poles, the encirclement means the connection is not stable, proving the results from hardware experiments.

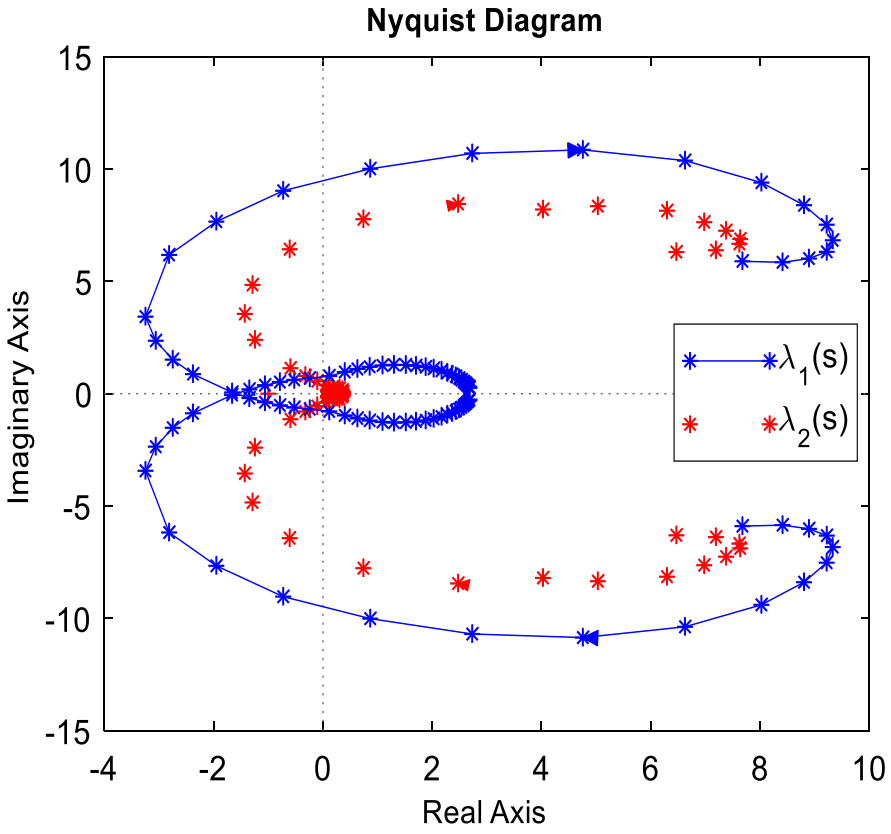

Figure 4-38 Characteristic loci for volt-var droop control

4.4.2 Two PV Inverter

Hardware experiments were also done for the interaction of multiple PV generators in the same distribution system. Fig.4-39 is the main circuit of the two PV generators.

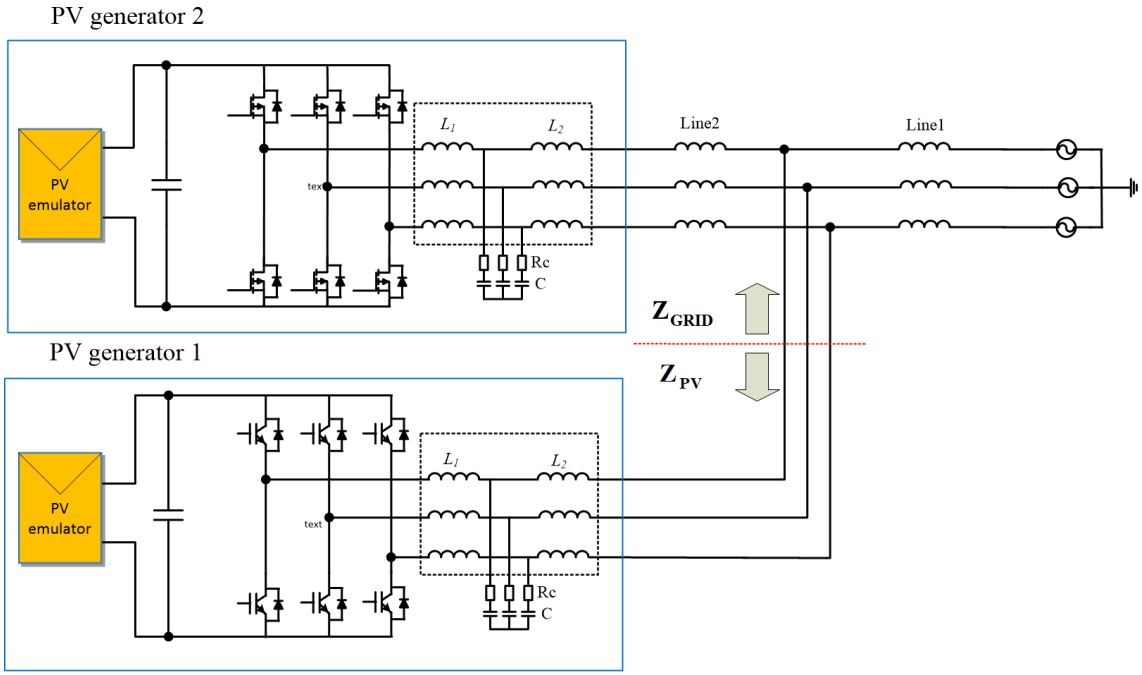

Figure 4-39 Circuit of the two PV inverter hardware experiment

For the first Silicon IGBT converter as in PV generator 1 in the circuit, the operation parameters are changed to Table 4-1 with 5 PV modules in series in the DC side.

Table 4-1 Parameters of the first PV generator

Parameter		**Value**
PV array	V_{oc}	60 V
	V_{mpp}	55 V
	I_{sc}	5.4 A
	I_{mpp}	4.5 A
DC voltage		250 V
DC capacitor		600 μF
LCL filter	L_1	250 μH
	L_2	250 μH
	R_c	1 Ω
	C	35 μF
Switching frequency		20 kHz

A second Silicon-Carbon MOSFET converter is added to work as the second PV generator in Fig.4-39 with the operation parameters of Table 4-2.

Table 4-2 Parameters of the second PV generator

Parameter		**Value**
PV array	V_{oc}	60 V
	V_{mpp}	55 V
	I_{sc}	5.4 A
	I_{mpp}	4.5 A
DC voltage		250 V
DC capacitor		600 μF
LCL filter	L_1	150 μH
	L_2	300 μH
	R_c	1.5 Ω
	C	30 μF
Switching frequency		20 kHz

And the AC side line-to-line rms voltage is 112V and frequency is 60 Hz. Fig.4-34 is a picture of all the components in the circuit. The impedance measurement unit is put at the terminal of PV generator 1, where impedances are measured and GNC is applied.

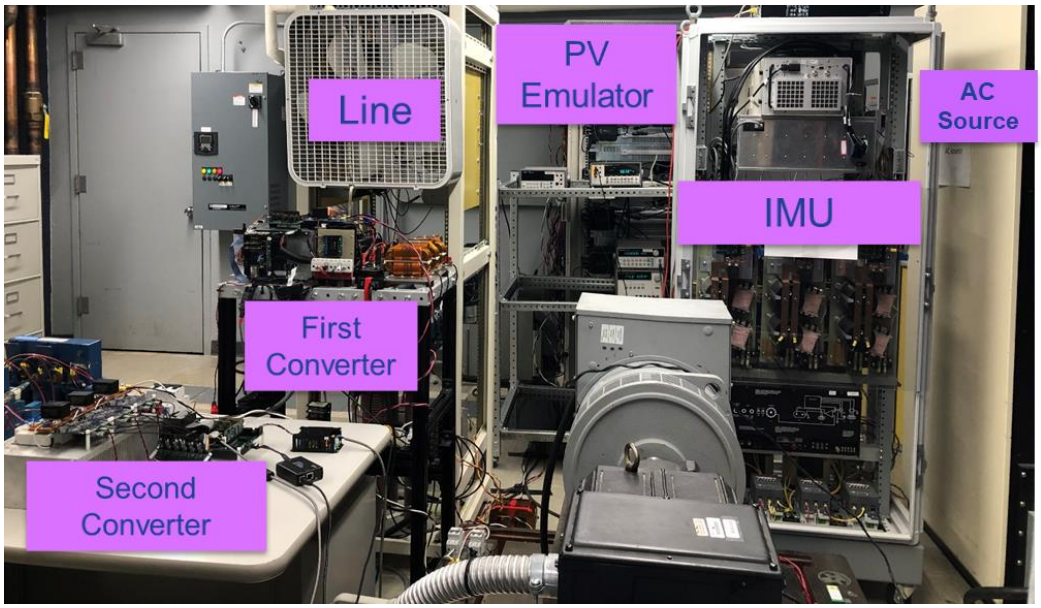

Figure 4-40 Picture of the hardware components of two PV inverter test

In Fig.4-41, initially both PV generators are working under Q control mode, the system is working stably. After Q control mode is shifted to volt-var control mode Q = - K_v (V-105) and K_v =75, DC voltages of both PV generators start to oscillate and the AC side voltages and currents become distorted. The two generators are tripped after the DC voltages are too low.

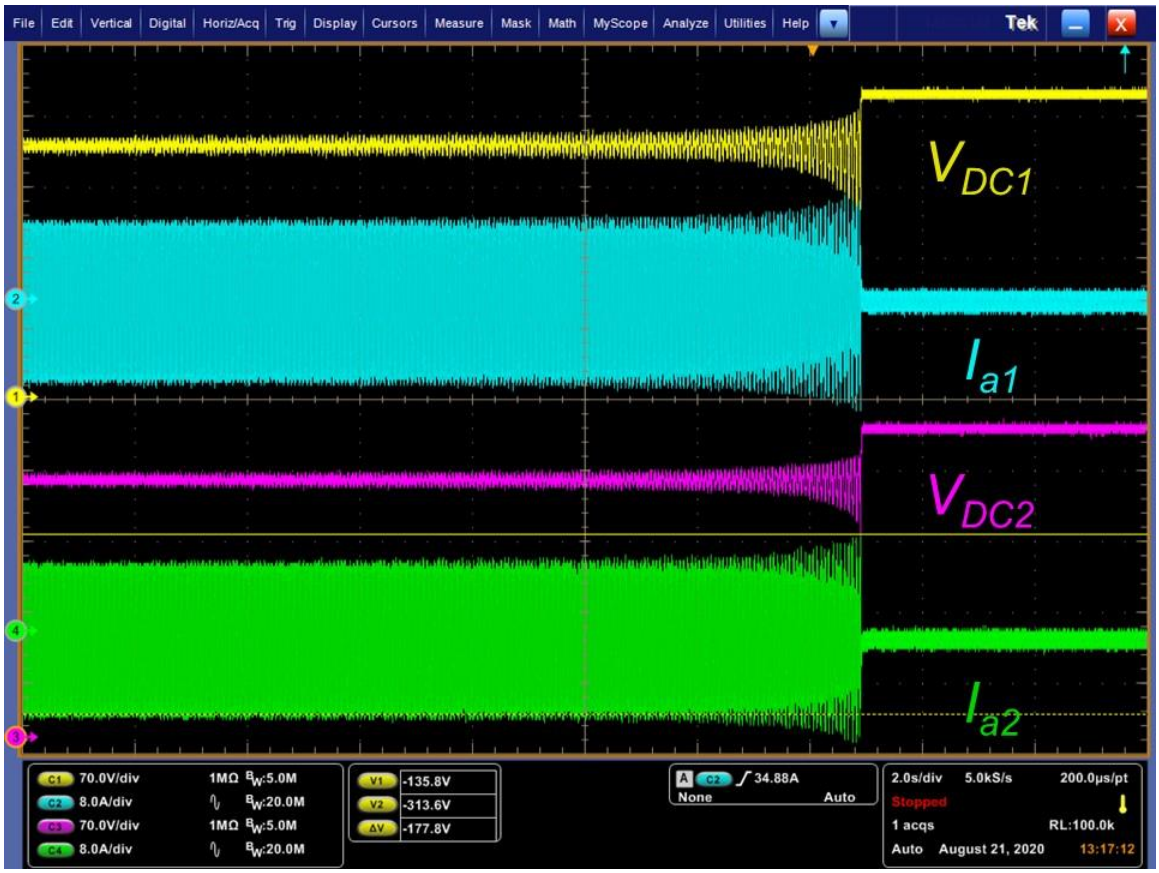

Figure 4-41 Recorded waveform of PV inverter transients on the scope

For the stable case of mode 2 constant Q control, Fig.4-42 is the Nyquist plots of the two eigenvalues. Neither eigenvalues encircles (-1,0), as grid impedance and PV admittance don't have RHP poles, the encirclement condition leads to the conclusion that the connection is stable, proving the results from hardware experiments.

For the unstable case of volt-var droop mode control, Fig.4-42 is the Nyquist plots of the two eigenvalues. The first eigenvalue λ_1 encircles (-1,0) counter-clock twice. While grid impedance and PV admittance don't have RHP poles, the encirclement means the connection is not stable, proving the results from hardware experiments.

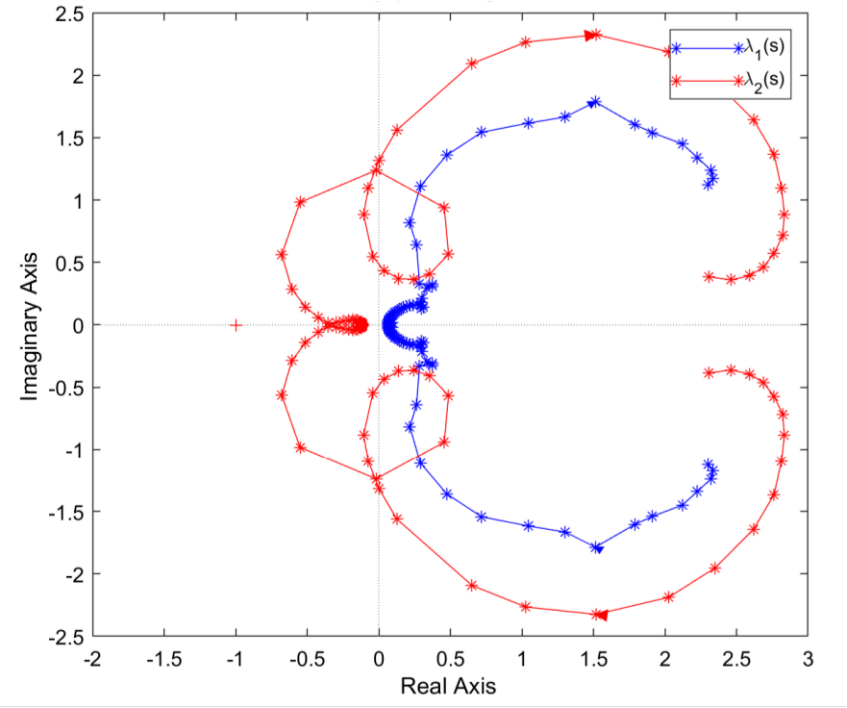

Figure 4-42 Characteristic loci for the stable case of Q constant control

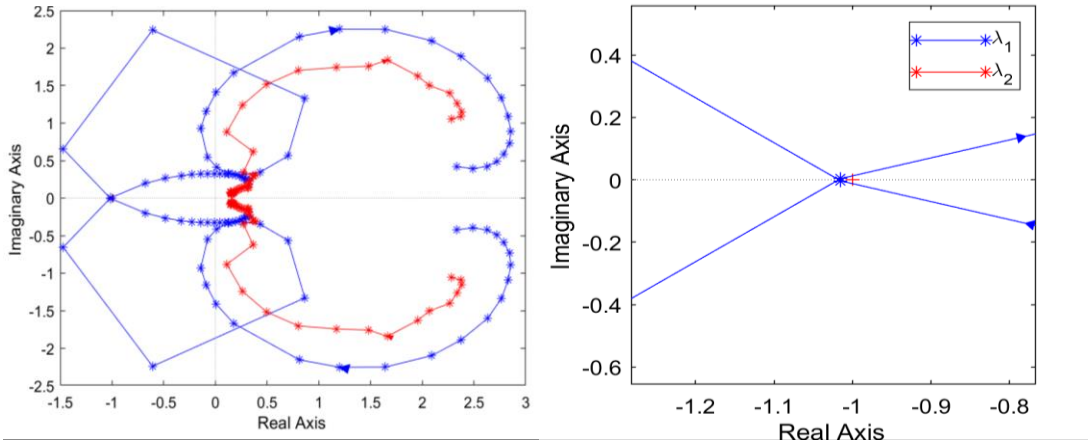

Figure 4-43 Characteristic loci for the unstable case of volt-var control

4.5 Summary and conclusions

A radial medium voltage distribution system is modeled in MATLAB to analyze the impact of PV generator penetration using GNC method based on impedances in *d-q* frames. The increase of number of PV inverters in parallel will also lower the PV impedance and increase the possibility of instability. The reactive power control of volt-var droop mode is the first mode to cause instable connection as the number of PV inverters increases. The discovered instability problem caused by volt-var droop mode control is highly related to the inner current controller, the reactive power loop controller and the digital delay and not quite related to DC voltage controller and PLL block.

Time domain simulation using SIMULINK yields the same conclusion about the stability of the PV connection to the grid under volt-var droop mode. In unstable cases, PV output currents have oscillation in *d-q* frames and have more harmonics in ABC frames. The time domain simulation proves that application of GNC is accurate to predict system stability. The GNC application results are also proved by scale down hardware experiments.

The PV farms connected to different branches of the complicated radial distribution system may have interactions with each other when they are under droop mode control. So the design of control strategy and parameters of PV generator should consider the impact of other PV generators. GNC method based on impedances measurement is feasible accurate for stability assessment of a distribution system with multiple PV farms. The GNC application results of the case of multiple PV farms are also verified by time-domain simulation and hardware experiments.

For the instability problem caused by volt-var droop mode control, comparison is done for different PV allocations, different PV capacities (different number of PV inverters) and different irradiance condition. No matter it's a system with single PV farm or with multiple PV farms, moving any of the PV farm closer to the substation reduces the possibility of instability. Higher capacity of PV penetration makes this stability problem worse and so does higher solar irradiance condition.

Chapter 5. Stability Assessment of Three Phase Unbalanced Distribution System

5.1 Introduction and state of art

For a three-phase balanced system, voltages and currents become DC values in steady state operation after performing the Park transformation. An AC system becomes two coupled dc systems, from which *d-q* frame impedances can be extracted using the traditional linearization method. The aforesaid method is not feasible for three-phase unbalanced system because three-phase variables are no longer DC values in *d-q* frames. Compared to balanced three-phase systems, modeling of unbalanced converter systems is more complicated due to the negative-sequence trajectory that is impressed on the ac system by the unbalanced condition. The first approach that comes out intuitively is to positive-negative-sequence impedance method that takes both positive and negative sequence components and their interaction into account [103]-[107]. But this method assumes that single frequency perturbation on the system only creates the same frequency responses, which is not true even for three-phase balanced system with *d-q* frame asymmetrical control (phase lock loop control or DC voltage loop) [23], needless to say the cases of unbalanced system.

A more accurate impedance model for three-phase unbalanced system is Harmonic State Space (HSS) model based on Linear Time Periodic (LTP) theory [108]-[111]. An unbalanced system is a time-periodic system that is time variant with the line frequency. According to the LTP theory, a frequency of input to this system will induce responses of an infinite vector of frequencies. The vector of frequencies includes the original

perturbation frequency and all frequencies that are shifted from the perturbation frequency by integers of the line frequency, the latter of which is considered as harmonic frequency. The terminal dynamics are represented by harmonic transfer functions (HSF). The order of the HSS model or the HSF is truncated to a certain integer to be applied in practice without sacrificing the accuracy of predicting system stability. Although this method is conceptually clear, its application to the stability analysis of an unbalanced grid-VSC system is still challenging. [112] suggests a much further truncation of the HSF so that it's much easier to be applied in reality. Only the dynamics relevant to the first coupling cycle (FCC) is of most concern and should be modeled in detail. In other words, the inputs of the grid at ±fp+f1 will result in two new responses at ∓fp-f1. The source and load impedance matrices are shrunk to be four-by-four matrices. But [112] assumes that the source side only has passive components but no converters.

This work proposes to use the concept of single-phase *d-q* frame impedance method to measure the terminal dynamics of the unbalanced system and assess system stability by applying Generalized Nyquist Criterion (GNC). It basically creates two virtual circuits from the original three-phase unbalanced system by adding 120 degree of delay and 240 degree of delay. The original system and the virtual two systems are perturbed and analyzed as a whole. As the stability results of two virtual systems are the same as the original system. In addition, a DC operation point can be achieved by applying Park Transformation on the three systems. A new *d-q* frame and new Park transformation is defined using just the phase information of the first circuit. In the new *d-q* frame, the two independent line-to-line voltages and two independent line currents have the same frequency spectrum and the ratios are also constant so that a transfer function can be

derived. The impedance matrices in the new *d-q* frame of the source and load come in the dimension of four by four. And GNC can be applied to assess system stability with four characteristic loci.

Analysis and simulation are done for both three-phase unbalanced systems with converters. The time domain and frequency domain simulation results in Matlab Simulink show that the frequency domain analysis results using this method can predict system dynamics and stability problems accurately for all kinds of three-phase unbalanced systems. Compared with the methods in [112], this approach only needs one Perturbation Injection Unit (PIU) instead of three PIUs which work simultaneously and need complicated cooperation. The method of this work will reduce the cost of the impedance measurement unit for three-phase unbalanced system significantly. In addition, the proposed method is applicable even when the source side has other converters connected.

5.2 D-Q frame impedance modeling of three-phase unbalanced system

The 56 bus system testbed may become three-phase unbalanced. The unbalance may come from the unbalanced three-phase AC voltage source at the substation station at bus 1 or the loads that are connected to the system. This section discusses how to model the impedances each components in the unbalanced system in the *d-q* frame.

5.2.1 Modeling of the three-phase converter in the unbalanced system

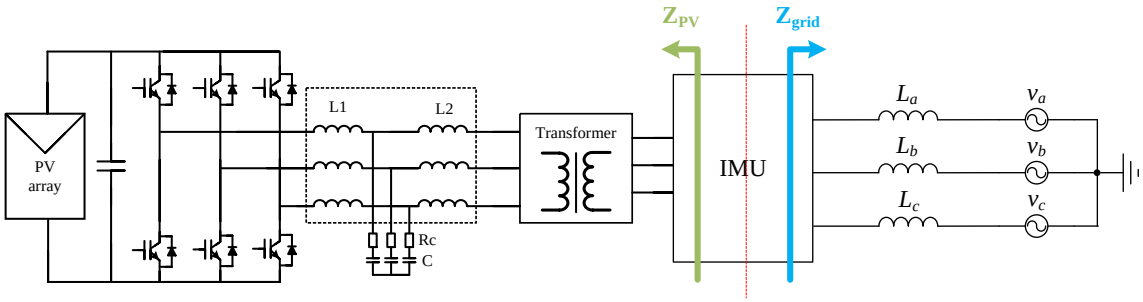

Figure 5-1 Three-phase converter in unbalanced system.

The topology of the three-phase converter in an unbalanced system under analysis is shown in Fig.5-1, in which a PV inverter working under *d-q* frame control is connected to the grid through a line. The power stage of the converter three-phase balanced, but the converter is working in unbalanced condition as its terminal voltages are three-phase unbalanced.

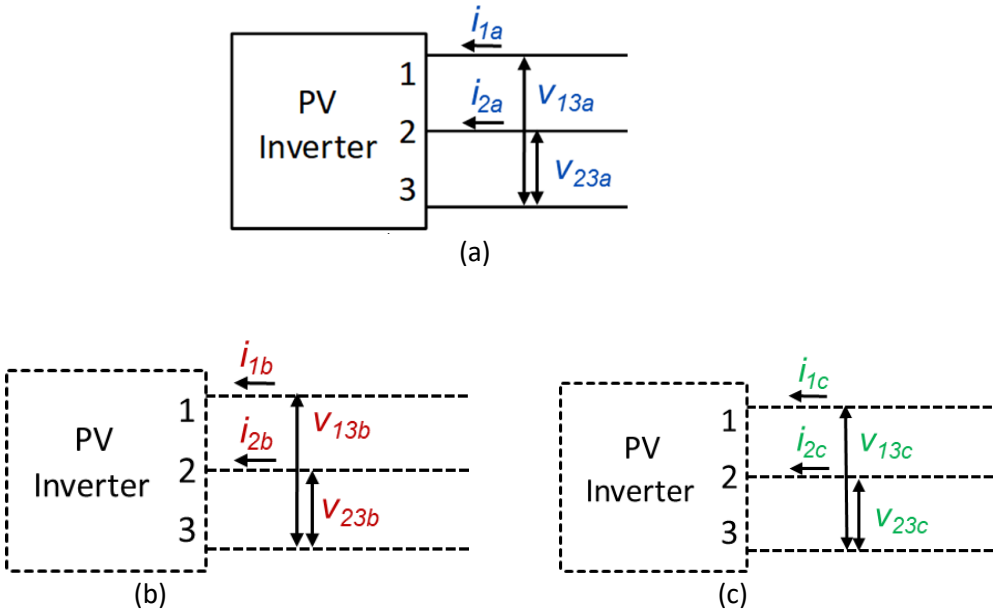

Figure 5-2: The modeling of PV inverter

The original inverter of Fig.5-2 (a) are three-phase unbalanced, the transformation to *d-q* frame will not end up with a LTI system as the components in *d-q* frame are not DC values in steady state. To model the PV inverter in *d-q* frame, the original inverter is

regarded as the phase A circuit with three terminals numbered 1, 2 and 3. And a fictitious phase B and phase C circuit by adding 120 degree of delay and 120 degree of lead in the terminal voltage inputs as shown in Fig.5-2(b) and (c).

$$v_{13b} = v_{13a} \cdot e^{-j120^\circ} \tag{5-1}$$

$$v_{23b} = v_{23a} \cdot e^{-j120^\circ} \tag{5-2}$$

$$i_{1b} = i_{1a} \cdot e^{-j120^\circ} \tag{5-3}$$

$$i_{2b} = i_{2a} \cdot e^{-j120^\circ} \tag{5-4}$$

$$v_{13c} = v_{13b} \cdot e^{-j120^\circ} \tag{5-5}$$

$$v_{23c} = v_{23b} \cdot e^{-j120^\circ} \tag{5-6}$$

$$i_{1c} = i_{1b} \cdot e^{-j120^\circ} \tag{5-7}$$

$$i_{2c} = i_{2b} \cdot e^{-j120^\circ} \tag{5-8}$$

The variables on the same terminal number in the three converters are three-phase balanced. A new abc to *d-q* transformation is defined as

$$\begin{bmatrix} v_{13d1} \\ v_{13q1} \end{bmatrix} = T_{dq1/abc} \begin{bmatrix} v_{13a} \\ v_{13b} \\ v_{13c} \end{bmatrix} \tag{5-9}$$

$$\begin{bmatrix} i_{1d1} \\ i_{1q1} \end{bmatrix} = T_{dq1/abc} \begin{bmatrix} i_{1a} \\ i_{1b} \\ i_{1c} \end{bmatrix} \tag{5-10}$$

$$\begin{bmatrix} v_{23d2} \\ v_{23q2} \end{bmatrix} = T_{dq2/abc} \begin{bmatrix} v_{23a} \\ v_{23b} \\ v_{23c} \end{bmatrix} \tag{5-11}$$

$$\begin{bmatrix} i_{2d2} \\ i_{2q2} \end{bmatrix} = T_{dq2/abc} \begin{bmatrix} i_{2a} \\ i_{2b} \\ i_{2c} \end{bmatrix} \tag{5-12}$$

$$T_{dq1/abc} = T_{dq2/abc} = \begin{bmatrix} \cos(\theta) & \cos(\theta - 120°) & \cos(\theta + 120°) \\ -\sin(\theta) & -\sin(\theta - 120°) & -\sin(\theta + 120°) \end{bmatrix} \quad (5\text{-}13)$$

While the phase θ in the transformation in $T_{dq1/abc}$ and $T_{dq2/abc}$ is the phase of v_{13a}, so basically these two transformations are the same, but just distinguished by the set of variables in transformation. Then the steady state values of v_{13d1}, v_{13q1} , v_{23d2}, v_{23q2}, i_{1d1}, i_{1q1}, i_{2d2}, i_{2q2} are DC values as shown in Fig.5-3

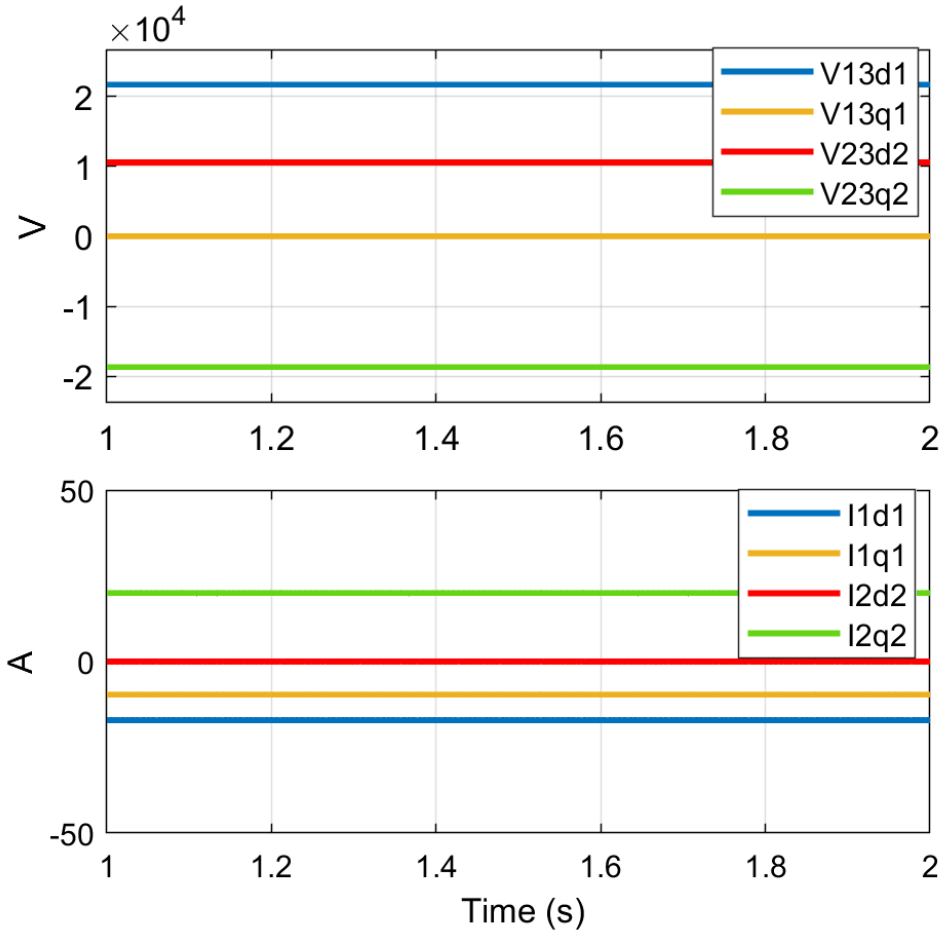

Figure 5-3: The modeling of PV inverter

Assume that there's a perturbation at terminal 1 in all three circuits. v_{pa} , v_{pb} and v_{pc} are three-phase balanced at the frequency of fp+f1.

$$v_{pa} = V_p \cos [2\pi \times (f_1 + f_p)t] \quad (5\text{-}14)$$

$$v_{pb} = V_p \cos [2\pi \times (f_1+f_p)t - 120^o] \quad (5\text{-}15)$$

$$v_{pc} = V_p \cos [2\pi \times (f_1+f_p)t + 120^o] \quad (5\text{-}16)$$

In which f_1 = 60 Hz, f_p = 40 Hz, V_p= 489 V (0.05 p.u.). In the circuit of Fig.5-4(a), a single-phase perturbation is equal to a positive sequence perturbation, a negative sequence perturbation and zero sequence perturbation. Zero sequence perturbation is ignored as the converter is not grounded. It can be proved mathematically using LTP that for the frequencies of interest in the currents responses in Fig.5-4(a), Fig.5-4(b) and Fig.5-4 (c) are three-phase balanced in |±fp+f1| (have 120 degree of phase difference). The magnitude ratio and phase difference between the output current responses and the input voltage perturbations are irrelevant of time. The balanced current responses are also illustrated in Fig.5-4 by small-signal perturbation simulation results of the PV inverter circuit working under unbalanced condition. Terminal 1 voltage is 9% higher than terminal 2 and terminal 3, which is equal to 3% of overall unbalance.

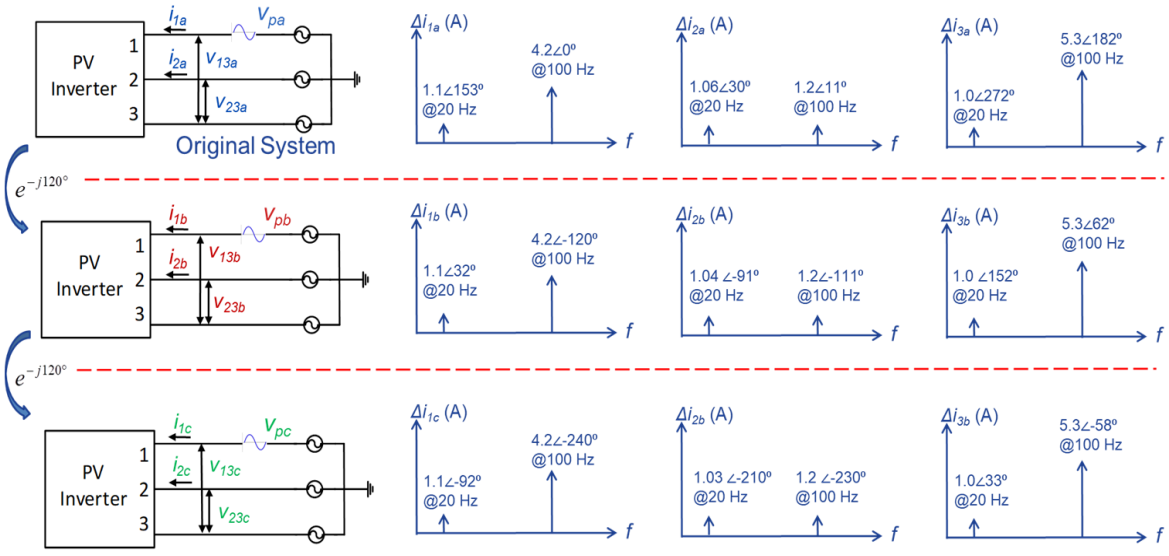

Figure 5-4: The current responses of PV inverter in ABC frame

The current responses of frequencies in concern are shown in Fig.5-4. Only the frequency components of |±fp+f1| are included in the analysis. It can be observed that the current responses of the three terminals (Δi_{1a}, Δi_{2a} , Δi_{3a} as an example) are not balanced. But the current responses of the same terminal (Δi_{1a}, Δi_{1b} , Δi_{1c} as an example) are three-phase balanced at the two frequencies of |±fp+f1|.

The rest of this section takes the PV inverter as an example to demonstrate that if there's a perturbation of frequency f_p on $\Delta \mathbf{v_{13dq1}} = [\Delta v_{13d1}, \Delta v_{13q1}]^T$, the response of the terminal currents $\mathbf{\Delta i_{1dq1}} = [\Delta i_{1d1}, \Delta i_{1q1}]^T$, $\mathbf{\Delta i_{2dq2}} = [\Delta i_{2d}, \Delta i_{2q}]^T$, will only have frequency component of the same frequency f_p. Assume phase of v_{13a} (θ in equation (5-13)) is zero at time zero and the voltage perturbation v_{pa} on the terminal 1 is

$$v_{pa} = V_p \cos(2\pi \times (f_p + f_1)t + \delta) \tag{5-17}$$

V_p is the perturbation magnitude. And δ is the relative angle of v_{pa} over v_{13a}. There are voltage perturbations of vpb and vpc in the virtual phase B and phase C systems too as in (5-18) and (5-19). The perturbations of v_{pa} , v_{pb} and v_{pc} are three-phase balanced.

$$v_{pb} = V_p \cos(2\pi \times (f_p + f_1)t + \delta - 120^o) \tag{5-18}$$

$$v_{pc} = V_p \cos(2\pi \times (f_p + f_1)t + \delta + 120^o) \tag{5-19}$$

Without loss of generality, it is assumed the current response of Δi_{1a}, Δi_{1b} , Δi_{1c} can be written as (5-20)-(5-22).

$$\Delta i_{1a} = I_1 \cos(2\pi \times (-f_p + f_1)t + \delta_1) + I_2 \cos(2\pi \times (f_p + f_1)t + \delta_2) \tag{5-20}$$

$$\Delta i_{1b} = I_1 \cos(2\pi \times (-f_p + f_1)t + \delta_1 - 120^o) + I_2 \cos(2\pi \times (f_p + f_1)t + \delta_2 - 120^o) \tag{5-21}$$

$$\Delta i_{1c} = I_1 \cos(2\pi \times (-f_p + f_1)t + \delta_1 + 120^o) + I_2 \cos(2\pi \times (f_p + f_1)t + \delta_2 + 120^o) \tag{5-22}$$

Park transformation of (5-9)-(5-12) are applied on the voltage perturbations of (5-17)-(5-19) and current responses of (5-20)-(5-22) to get the results of (5-23)-(5-26).

$$\Delta v_{13d1} = \sqrt{\frac{3}{2}}\ V_p \cos(2\pi \times f_p \cdot t + \delta) \tag{5-23}$$

$$\Delta v_{13q1} = \sqrt{\frac{3}{2}}\ V_p \sin(2\pi \times f_p \cdot t + \delta) \tag{5-24}$$

$$\Delta i_{1d1} = \sqrt{\frac{3}{2}}\ I_1 \cos(2\pi \times f_p \cdot t - \delta_1) + \sqrt{\frac{3}{2}}\ I_2 \cos(2\pi \times f_p \cdot t + \delta_2) \tag{5-25}$$

$$\Delta i_{1q1} = -\sqrt{\frac{3}{2}}\ I_1 \sin(2\pi \times f_p \cdot t - \delta_1) + \sqrt{\frac{3}{2}}\ I_2 \sin(2\pi \times f_p \cdot t + \delta_2) \tag{5-26}$$

The same analysis can be done for response on Δi_{2dq2}. The frequency spectrum of $\mathbf{\Delta i_{1dq1}}$, $\mathbf{\Delta i_{2dq2}}$ and $\mathbf{\Delta v_{13dq1}}$ are the same, which only have non-zero magnitude at the frequency of f_p. And the transfer ratio of current responses over voltage perturbation are constant and irrelevant of time. The perturbation can be done at terminal 2 to show when there's only perturbation at $\mathbf{\Delta v_{23dq2}}$, the frequency spectrum of $\mathbf{\Delta v_{23dq2}}$ and $\mathbf{\Delta i_{1dq1}}$ and $\mathbf{\Delta i_{2dq1}}$ are the same.

According to KVL and KCL, in the stationary abc frame or *d-q* frame, the equations (5-27) and (5-28) are all valid

$$-\mathbf{\Delta v_{13}} + \mathbf{\Delta v_{23}} + \mathbf{\Delta v_{12}} = \mathbf{0} \tag{5-27}$$

$$\mathbf{\Delta i_1} + \mathbf{\Delta i_2} + \mathbf{\Delta i_3} = \mathbf{0} \tag{5-28}$$

There are only four independent inputs of voltage perturbations and four independent current responses in the *d-q* frame. In this way, it is proved that the three-phase converters in the unbalanced system can be modelled as (5-29), in which $\mathbf{Y_{dq12}}$ is a four-by-four matrix.

$$\begin{bmatrix} \mathbf{\Delta i_{1dq1}}(s) \\ \mathbf{\Delta i_{2dq2}}(s) \end{bmatrix} = \mathbf{Y_{dq12}} \begin{bmatrix} \mathbf{\Delta v_{13dq1}(s)} \\ \mathbf{\Delta v_{23dq2}(s)} \end{bmatrix} \tag{5-29}$$

5.2.2 Modeling of the unbalanced three-phase lines

The imbalance of the three-phase systems may also come from the asymmetrical impedances of the lines between the source and the load. The asymmetrical lines can be

modeled in the similar way as unbalanced loads in last part. The original system is shown in Fig.5-5 (a) as phase A circuit. Virtual phase B circuit of Fig.5-5(b) is created by adding 120 degree of delay to the circuit of Fig.5-5(a). And virtual phase C circuit of Fig.5-5(c) is created by adding 120 degree of delay to the circuit of Fig.5-5(b). Line 1 in Fig.5-5 (a), Fig.5-5(b) and Fig.5-5(c) forms a three-phase balanced system. So does line 2 and line 3. A three-phase balanced system is constructed from each line separately.

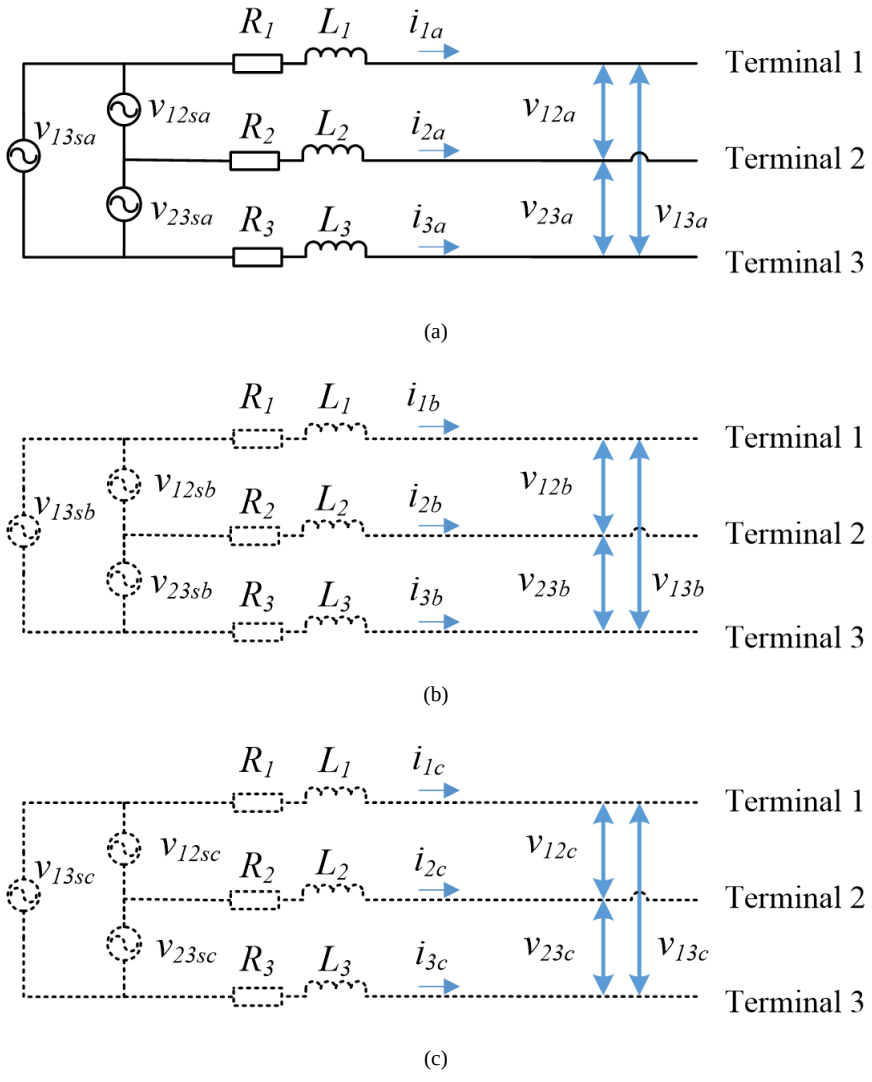

Figure 5-5: Unbalanced lines in ABC frame

After Park transformation of the three-phase balanced circuits in Fig.5-6, a *d-q* frame model can be built for the unbalanced lines as Fig.5-6.

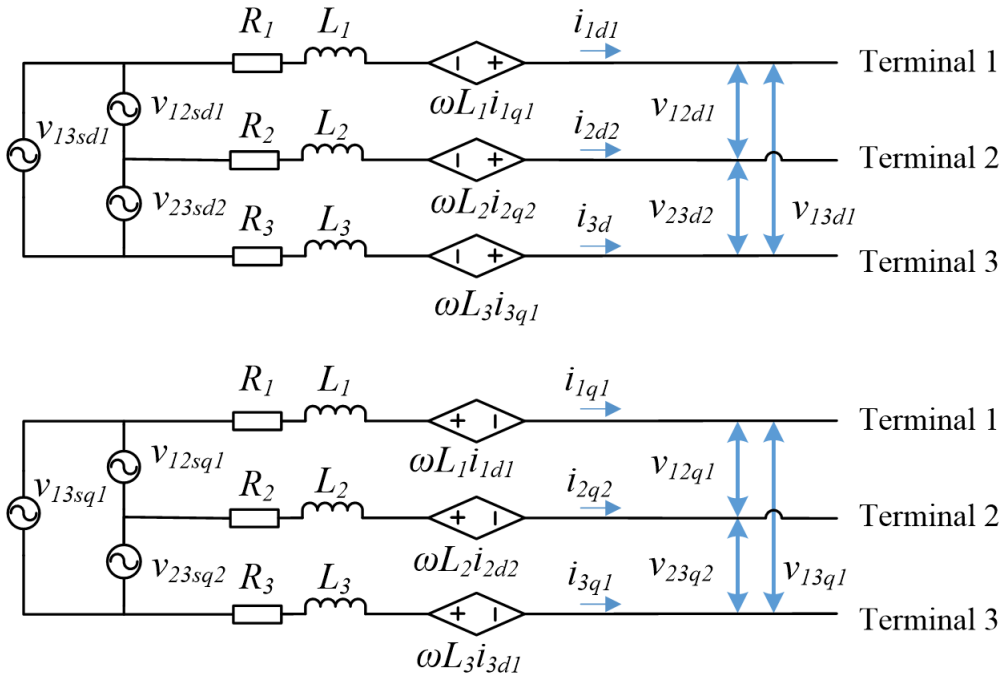

Figure 5-6: D-Q frame model for three-phase unbalanced lines

in which besides the variables of $\mathbf{v_{13dq1}} = [v_{13d1}, v_{13q1}]^T$, $\mathbf{v_{23dq2}} = [v_{23d2}, v_{23q2}]^T$ $\mathbf{i_{1dq1}} = [i_{1d1}, i_{1q1}]^T$ and $\mathbf{i_{2dq2}} = [i_{2d}, i_{2q}]^T$ obtained by (5-9)-(5-12), $\mathbf{v_{12dq1}} = [v_{12d1}, v_{12q1}]^T$ and $\mathbf{i_{3dq1}} = [i_{3d1}, i_{3q1}]^T$ are from equations below

$$\begin{bmatrix} v_{12d1} \\ v_{12q1} \end{bmatrix} = T_{dq1/abc} \begin{bmatrix} v_{12a} \\ v_{12b} \\ v_{12c} \end{bmatrix} \tag{5-30}$$

$$\begin{bmatrix} i_{3d1} \\ i_{3q1} \end{bmatrix} = T_{dq1/abc} \begin{bmatrix} i_{3a} \\ i_{3b} \\ i_{3c} \end{bmatrix} \tag{5-31}$$

Linearization around the DC operation point for the model of Fig.5-6 results in the small-signal impedance matrix as

$$\begin{bmatrix}\mathbf{\Delta v}_{\mathbf{13dq1}}\\ \mathbf{\Delta v}_{\mathbf{23dq2}}\end{bmatrix}=\begin{bmatrix}\mathbf{\Delta v}_{\mathbf{13sdq1}}\\ \mathbf{\Delta v}_{\mathbf{23sdq2}}\end{bmatrix} - \begin{bmatrix} R_1+R_3+s(L_1+L_3) & -\omega(L_1+L_3) & R_3+sL_3 & -\omega L_3 \\ \omega(L_1+L_3) & R_1+R_3+s(L_1+L_3) & \omega L_3 & R_3+sL_3 \\ R_3+sL_3 & -\omega L_3 & R_2+R_3+s(L_2+L_3) & -\omega(L_2+L_3) \\ \omega L_3 & R_3+sL_3 & \omega(L_2+L_3) & R_2+R_3+s(L_2+L_3) \end{bmatrix}\begin{bmatrix}\mathbf{\Delta i}_{\mathbf{1dq1}}\\ \mathbf{\Delta i}_{\mathbf{2dq2}}\end{bmatrix} \quad (5\text{-}32)$$

Define the 4×4 matrix $\mathbf{Z_{dq12}}$ as

$$\mathbf{Z}_{\mathbf{dq12}}=\begin{bmatrix} R_1+R_3+s(L_1+L_3) & -\omega(L_1+L_3) & R_3+sL_3 & -\omega L_3 \\ \omega(L_1+L_3) & R_1+R_3+s(L_1+L_3) & \omega L_3 & R_3+sL_3 \\ R_3+sL_3 & -\omega L_3 & R_2+R_3+s(L_2+L_3) & -\omega(L_2+L_3) \\ \omega L_3 & R_3+sL_3 & \omega(L_2+L_3) & R_2+R_3+s(L_2+L_3) \end{bmatrix} \quad (5\text{-}33)$$

Then the terminal dynamics of the unbalanced load can be represented by

$$\begin{bmatrix}\mathbf{\Delta v}_{\mathbf{13dq1}}\\ \mathbf{\Delta v}_{\mathbf{23dq2}}\end{bmatrix}=\begin{bmatrix}\mathbf{\Delta v}_{\mathbf{13sdq1}}\\ \mathbf{\Delta v}_{\mathbf{23sdq2}}\end{bmatrix}-\mathbf{Z}_{\mathbf{dq12}}\begin{bmatrix}\mathbf{\Delta i}_{\mathbf{1dq1}}\\ \mathbf{\Delta i}_{\mathbf{2dq2}}\end{bmatrix} \quad (5\text{-}34)$$

5.2.3 Modeling of the unbalanced three single-phase loads

The imbalance of the three-phase system mainly comes from the unbalanced line-to-line loads and the asymmetrical impedances of three-phase lines between the source and the load. One example of unbalanced line-to-line loads is the residential distribution system in the power systems. Most residential loads are line-to-line loads that are connected to only two phases. And the imbalance is unavoidable as the loads are fluctuating from time to time.

The unbalanced line-to-line loads are illustrated by Figure 5-7(a). The three loads are connected to the three terminals in delta shape. Similar to the process shown in Fig.5-2, the original circuit is considered as phase A circuit. A virtual phase B circuit in Fig. 5-7(b) is constructed by adding 120 degree of delay on circuit of Fig.5-7 (a). And virtual

phase C circuit in Fig. 5-7(c) is constructed by adding 240 degree of delay on phase A circuit of Figure Fig.5-7 (a). Take load 1 as an example,

$$i_{1b} = i_{1a} \cdot e^{-j \cdot 120°} \tag{5-35}$$

$$i_{1c} = i_{1a} \cdot e^{-j \cdot 240°} \tag{5-36}$$

So i_{1a}, i_{1b} and i_{1c} are three-phase balanced. Load 1 in Figure 5-7(a), Figure 5-7(b) and Figure 5-7(c) forms a three-phase balanced system. So does load 2 and load 3. A three-phase balanced system is constructed from each load separately.

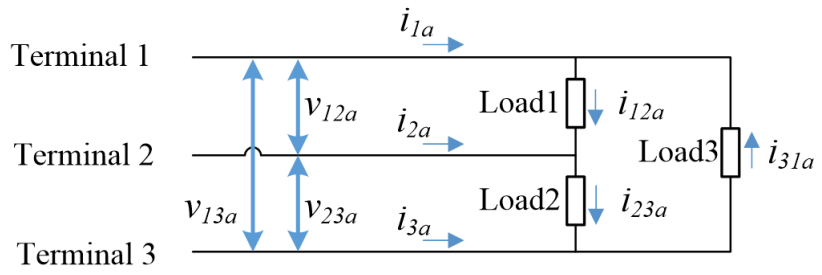

(a)

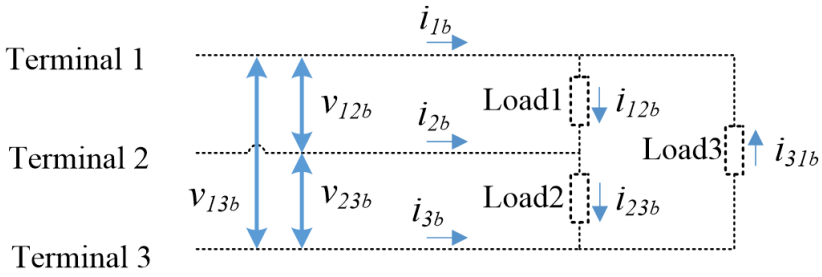

(b)

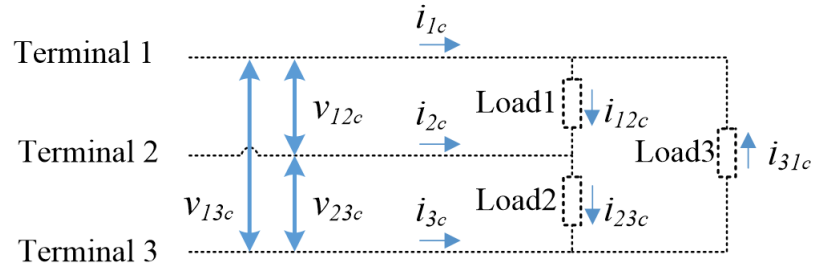

(c)

Figure 5-7: Unbalanced loads in ABC frame

For each load, the three-phase balanced system variables can be transformed to the *d-q* frame by multiplying the matrix of (5-13). Figure 5-8 are the circuits in *d* axis and *q* axis after applying the transformation. All variables in the *d-q* frame become DC values in steady state operation point. A linear time invariant system is created. There may be coupling between *d* axis and *q* axis within each load but not *d-q* coupling between load 1, load 2 and load 3. Figure 5-8 can be simplified to be Figure 5-9 combing d axis and q axis.

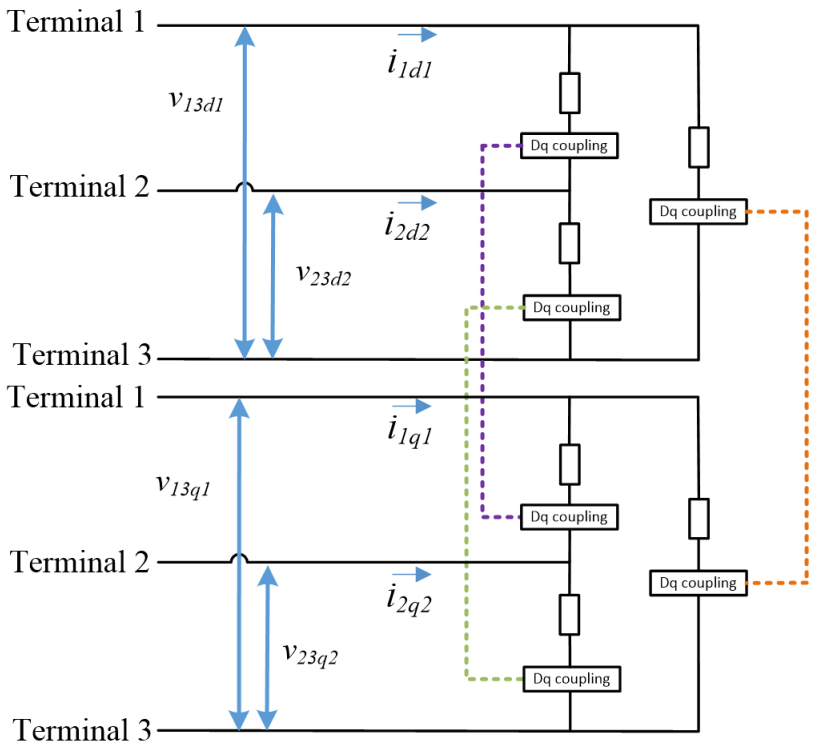

Figure 5-8: Unbalanced loads in *d-q* frame

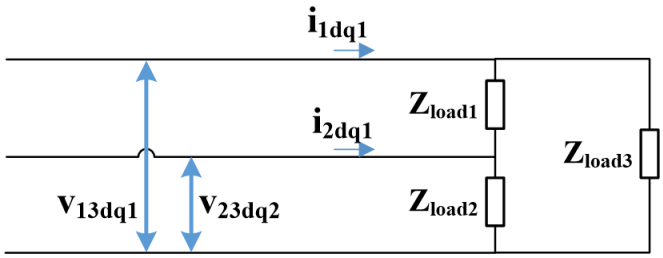

Figure 5-9: Unbalanced loads in *d-q* frame

$\mathbf{Y}_{load1}$, $\mathbf{Y}_{load2}$, $\mathbf{Y}_{load3}$ are the admittance matrices of the three loads in the *d-q* frame separately. It can be derived according to KCL and KVL that

$$\begin{bmatrix} \mathbf{i}_{1dq1} \\ \mathbf{i}_{2dq2} \end{bmatrix} = \begin{bmatrix} \mathbf{Y}_{load1} + \mathbf{Y}_{load3} & -\mathbf{Y}_{load1} \\ -\mathbf{Y}_{load1} & \mathbf{Y}_{load1} + \mathbf{Y}_{load2} \end{bmatrix} \begin{bmatrix} \mathbf{v}_{13dq1} \\ \mathbf{v}_{23dq2} \end{bmatrix} \tag{5-37}$$

Define the 4×4 matrix $\mathbf{Y}_{dq}$ as

$$\mathbf{Y}_{dq12} = \begin{bmatrix} \mathbf{Y}_{load1} + \mathbf{Y}_{load3} & -\mathbf{Y}_{load1} \\ -\mathbf{Y}_{load1} & \mathbf{Y}_{load1} + \mathbf{Y}_{load2} \end{bmatrix} \tag{5-38}$$

Then the terminal dynamics of the unbalanced load can be represented by

$$\begin{bmatrix} \mathbf{i}_{1dq1} \\ \mathbf{i}_{2dq2} \end{bmatrix} = \mathbf{Y}_{dq12} \begin{bmatrix} \mathbf{v}_{13dq1} \\ \mathbf{v}_{23dq2} \end{bmatrix} \tag{5-39}$$

5.3 D-Q frame impedance measurement and application in three-phase unbalanced system

5.3.1 Impedance measurement for the unbalanced system

In a single-phase system, the single-phase *d-q* frame impedance measurement is widely used for stability assessment [67]-[69]. In this kind of approach, a fictitious balanced three-phase is constructed. Single phase sinusoidal variables are regarded as α axis component, on which 90 degree of delay is added to form a fictitious β axis. After α-β to *d-q* transformation, a DC operation point is formed for system steady state, based on which perturbation is introduced and measured to get the *d-q* frame impedances.

The single-phase *d-q* impedances can be obtained via current injection in shunt or voltage injection in series. The measurement procedure is shown in Fig.5-10. For each

desired injection frequency f_p, two injections are needed to form two sets of equations in d axis and q axis to solve for the four unknowns of impedance matrix [69]. The original system sinusoidal voltages and currents is considered to be α axis component, based on which a fictitious β axis is created. Then all variables in $\alpha\beta$ axis are transformed to *d-q* frame. Two kinds of approaches can be used for fabrication of β axis, which are time shift of one fourth of fundamental period and Hilbert transformation. The two approaches are validated by [69]. To reduce the time of perturbation, the time shift of one fourth of fundamental period is chosen to form the fictitious β axis.

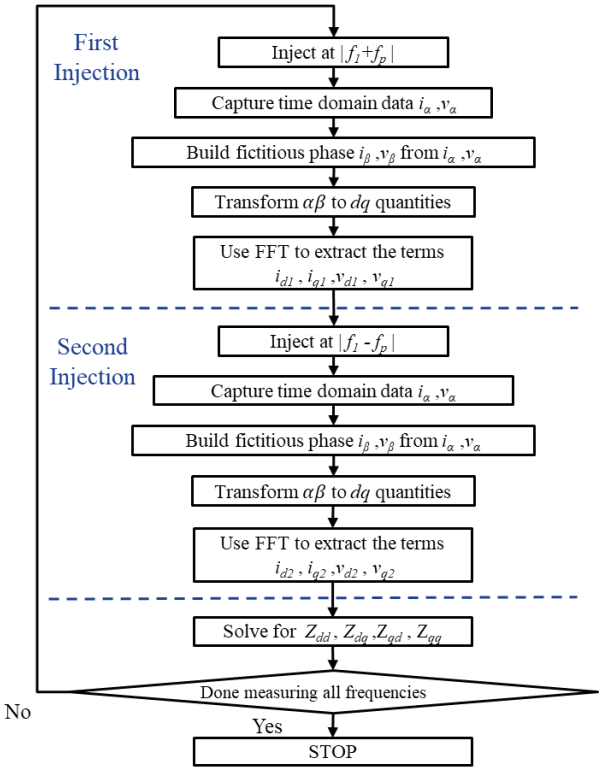

Figure 5-10: Flow chart of single-phase measurement.

Basically speaking, the single-phase impedance measurement method builds a three phase balanced system based on the original system as shown by Fig.5-11. The original

system is the Phase A system, based on which virtual circuits of phase B and phase C are created by adding 120 and 240 degree of delay.

$$v_b = v_a \cdot e^{-j120°} \tag{5-40}$$

$$i_b = i_a \cdot e^{-j120°} \tag{5-41}$$

$$v_c = v_a \cdot e^{j120°} \tag{5-42}$$

$$i_c = i_a \cdot e^{j120°} \tag{5-43}$$

Phase A, Phase B and Phase C circuits form a three phase balanced system. So after applying the transformation of ABC frame to $\alpha\beta\gamma$ frame, the coordinates on γ axis are zero and only the α axis circuit and the β axis circuit are needed.

$$T_{\alpha\beta\gamma/abc} = \sqrt{\frac{2}{3}} \begin{bmatrix} 1 & -\frac{1}{2} & -\frac{1}{2} \\ 0 & \frac{\sqrt{3}}{2} & -\frac{\sqrt{3}}{2} \\ \frac{1}{\sqrt{2}} & \frac{1}{\sqrt{2}} & \frac{1}{\sqrt{2}} \end{bmatrix} \tag{5-44}$$

$$T_{dq/\alpha\beta} = \begin{bmatrix} \cos(\theta) & \sin(\theta) \\ -\sin(\theta) & \cos(\theta) \end{bmatrix}, \theta = \omega \cdot t \tag{5-45}$$

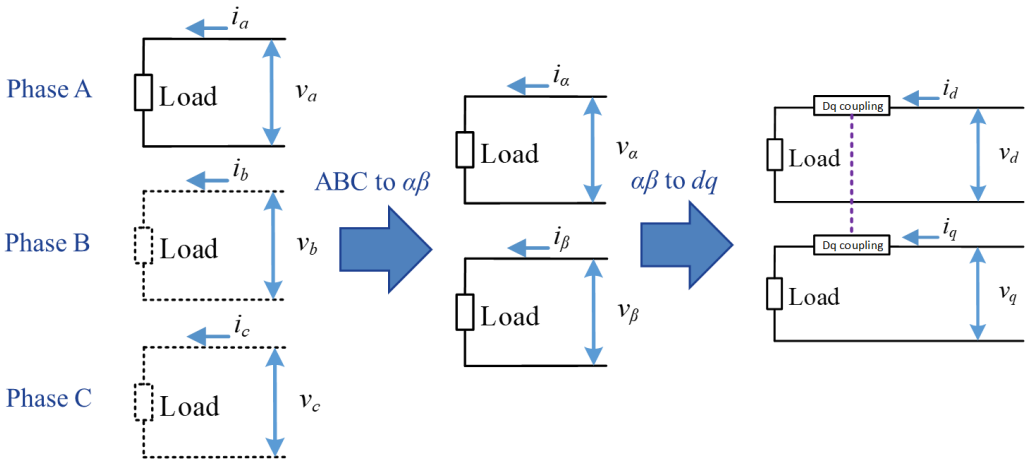

Figure 5-11 Basic algorithm of single-phase measurement method

In addition, the voltage and current in α axis circuit are 3/2 times the original system.

$$v_\alpha = \frac{3}{2} v_a \tag{5-46}$$

$$i_\alpha = \frac{3}{2} i_a \tag{5-47}$$

And the β axis circuit delays the α axis circuit by 90 degree.

$$v_\beta = v_\alpha \cdot e^{-j90^\circ} \tag{5-48}$$

$$i_\beta = i_\alpha \cdot e^{-j90^\circ} \tag{5-49}$$

If the original Phase A circuit is process as virtual α axis circuit as in (5-50) and (5-51)

$$v_\alpha' = v_a \tag{5-50}$$

$$i_\alpha' = i_a \tag{5-51}$$

a virtual β axis coordinate is formed by adding ¼ of line period of delay (90 degree of delay) on α axis coordinate.

$$v_\beta' = e^{-j90^\circ} v_\alpha' \tag{5-52}$$

$$i_\beta' = e^{-j90^\circ} i_\alpha' \tag{5-53}$$

And the *d-q* frame coordinates are obtained through (5-54)

$$\begin{bmatrix} v_d' \\ v_q' \end{bmatrix} = T_{dq/\alpha\beta} \begin{bmatrix} v_\alpha' \\ v_\beta' \end{bmatrix} \tag{5-54}$$

Assume $\mathbf{Z_{dq}}$ is the impedance matrix that needs to be measured for the three-phase balanced systems.

$$\mathbf{v_{dq}} = \mathbf{Z_{dq}} \cdot \mathbf{i_{dq}} \tag{5-55}$$

In which $\mathbf{v_{dq}} = \begin{bmatrix} v_d & v_q \end{bmatrix}^T$, $\mathbf{i_{dq}} = \begin{bmatrix} i_d & i_q \end{bmatrix}^T$,

Then it is proved in [69] that (5-57) is also valid because the ratio and phase shift of $\mathbf{v_{dq}}' = [v_d', v_q']^T$ over $\mathbf{v_{dq}} = [v_d, v_q]^T$ is the same as the ratio and phase shift of $\mathbf{i_{dq}}' = [i_d', i_q']^T$ over $\mathbf{i_{dq}} = [i_d, i_q]^T$.

$$\begin{bmatrix} v_d \\ v_q \end{bmatrix} = \mathbf{Z_{dq}} \begin{bmatrix} i_d \\ i_q \end{bmatrix} \tag{5-56}$$

$$\begin{bmatrix} v_d' \\ v_q' \end{bmatrix} = \mathbf{Z_{dq}} \begin{bmatrix} i_d' \\ i_q' \end{bmatrix} \tag{5-57}$$

According to the modeling analysis of the components in the three-phase unbalanced system in the previous sections, the impedance matrix $\mathbf{Z_{dq}}$ for the load and the source can be measured through single-phase information using single-phase measurement method.

The impedance that needs to be measured is a four-by-four matrix, 16 elements in total. Although in the model for unbalanced single-phase loads or line impedances, there are only 12 unknowns, but for three-phase converters there are 16 unknowns. For each perturbation, four equations can be obtained for solving the unknowns. Without loss of generality, four perturbations are needed to measure the matrix. Either voltage perturbations in series or current perturbations in shunt can be applied according to the impedance characteristic of the device under test (DUT). If DUT is a source with relatively low impedance, the perturbation injection unit should be connected in shunt to the main circuit to inject current perturbations. If DUT is a load with relatively high impedance, voltage perturbation should be the choice instead.

The flow chart of measurement process using voltage perturbation is shown in **Figure 5-12** . Four injections are evenly done on two terminals of the system. On either phase, two frequencies of signals are perturbed leading to the same perturbation frequency in *dq*

frame. For current shunt perturbation, the process is similar except that for the first two perturbations, current is injected between terminal 1 and terminal 3, and for the third and fourth perturbations, current is injected between terminal 2 and terminal 3.

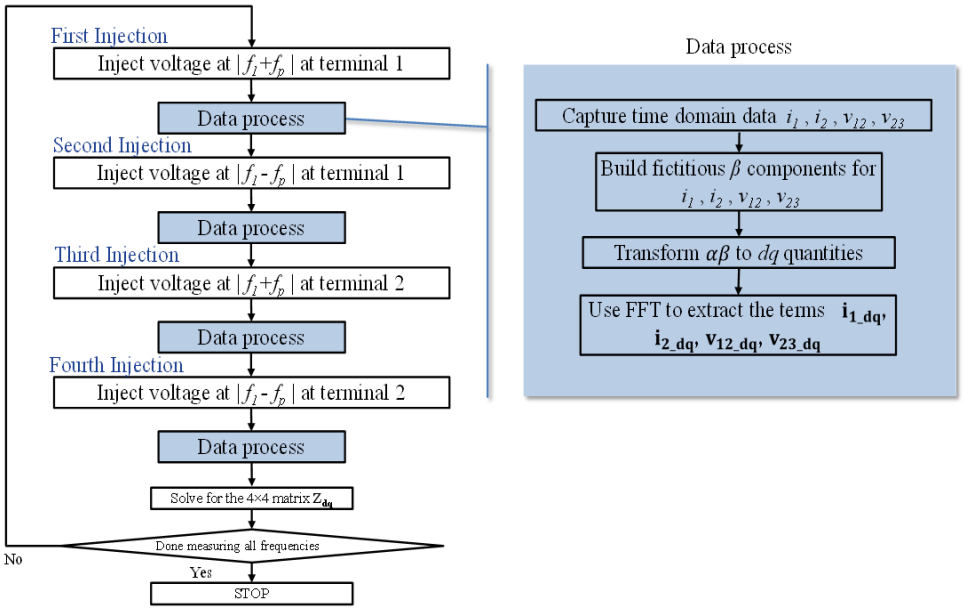

Figure 5-12 Flow char of the impedance measurement for three-phase unbalanced system

5.3.2 GNC application based on the measured *d-q* frame impedances

In the model that has been set forth, the dynamics of the source can be modeled as (5-34), and the dynamics of the load can be represented by (5-29) and (5-39). In other words, the source impedance is $\mathbf{Z_{sdq12}}$ and the load admittance is $\mathbf{Y_{ldq12}}$. For each frequency $s = j\omega$, both $\mathbf{Z_{sdq12}}$ and $\mathbf{Y_{ldq12}}$ are 4×4 matrices.

$$\begin{bmatrix} \Delta\mathbf{v}_{\mathbf{13dq1}}(s) \\ \Delta\mathbf{v}_{\mathbf{23dq2}}(s) \end{bmatrix} = \begin{bmatrix} \Delta\mathbf{v}_{\mathbf{13sdq1}}(s) \\ \Delta\mathbf{v}_{\mathbf{23sdq2}}(s) \end{bmatrix} - \mathbf{Z}_{\mathbf{sdq12}}(s) \cdot \begin{bmatrix} \Delta\mathbf{i}_{\mathbf{1dq1}}(s) \\ \Delta\mathbf{i}_{\mathbf{2dq2}}(s) \end{bmatrix} \tag{5-58}$$

$$\begin{bmatrix} \Delta\mathbf{i}_{\mathbf{1dq1}}(s) \\ \Delta\mathbf{i}_{\mathbf{2dq2}}(s) \end{bmatrix} = \mathbf{Y}_{\mathbf{ldq12}} \begin{bmatrix} \Delta\mathbf{v}_{\mathbf{13dq1}}(s) \\ \Delta\mathbf{v}_{\mathbf{23dq2}}(s) \end{bmatrix} \tag{5-59}$$

A small-signal representation in *d-q* frame can be built as Fig.5-13 for the three-phase unbalanced system based on (5-58) and (5-59), in which

$$\mathbf{v_{load}}(s) = \left[\Delta v_{13d1}(s) \quad \Delta v_{13q1}(s) \quad \Delta v_{23d2}(s) \quad \Delta v_{23q2}(s) \right]^T ,$$

$$\mathbf{v_{source}}(s) = \left[\Delta v_{13sd1}(s) \quad \Delta v_{13sq1}(s) \quad \Delta v_{23sd2}(s) \quad \Delta v_{23sq2}(s) \right]^T$$

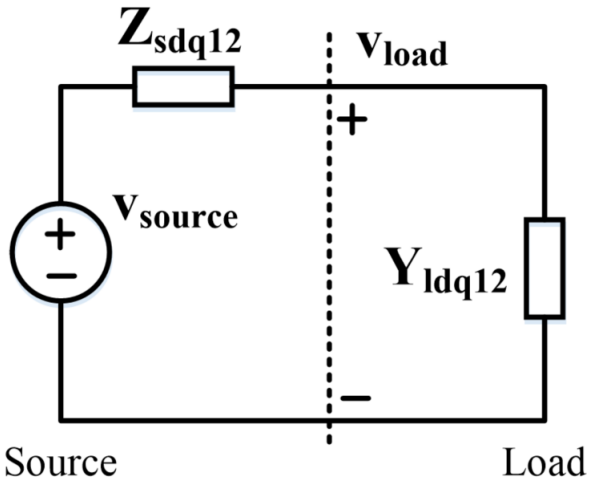

Figure 5-13 Small-signal representation of the three-phase unbalanced system in *d-q* frame

And it can be derived that

$$\mathbf{v_{load}}(s) = [\mathbf{I} + \mathbf{Z_{sdq12}}(s) \cdot \mathbf{Y_{ldq12}}(s)]^{-1} \mathbf{v_{source}}(s) \tag{5-60}$$

Define the return ratio matrix **L(s)** as

$$\mathbf{L}(s) = \mathbf{Z_{sdq12}}(s) \cdot \mathbf{Y_{ldq12}}(s) \tag{5-61}$$

The return ratio matrix **L(s)** is a four-by-four matrix which has four eigenvalues for each frequency $s = j\omega$. Assuming that there's no unobservable right half plane poles for the source and the load, the system stability is assessed by the number of net encirclement of the four characteristic loci around (-1,0) in the Nyquist diagram. If the net encirclement is zero, then the system is stable. If the net encirclement is bigger than zero, then the system is unstable.

5.4 Simulation results of the proposed *d-q* frame impedance based small-signal stability assessment in the unbalanced system

To prove the proposed *d-q* frame impedance model and measurement method, the 56 bus system is utilized to the testbed for small-signal stability assessment under unbalanced operation state. A dynamic model of the system with the PV inverter is built in MATLAB Simulink with PLECS block set. A virtual perturbation injection unit is added to the model to do desired small-signal perturbations. And then the collected waveforms are processed in MATLAB code to extract the *d-q* frame impedances. Fig. 5-14 shows the one-line diagram of the whole system. 3MW of PV inverters (12 inverters each rating 250 kW) are connected at bus 45. Compared to the balanced case, the PLL of PV inverter is added by a second order low pass filter in the frequency loop to be immune to the imbalance. The impedance measurement and GNC application point is at bus 45. The grid impedance and the PV impedance are measured separately.

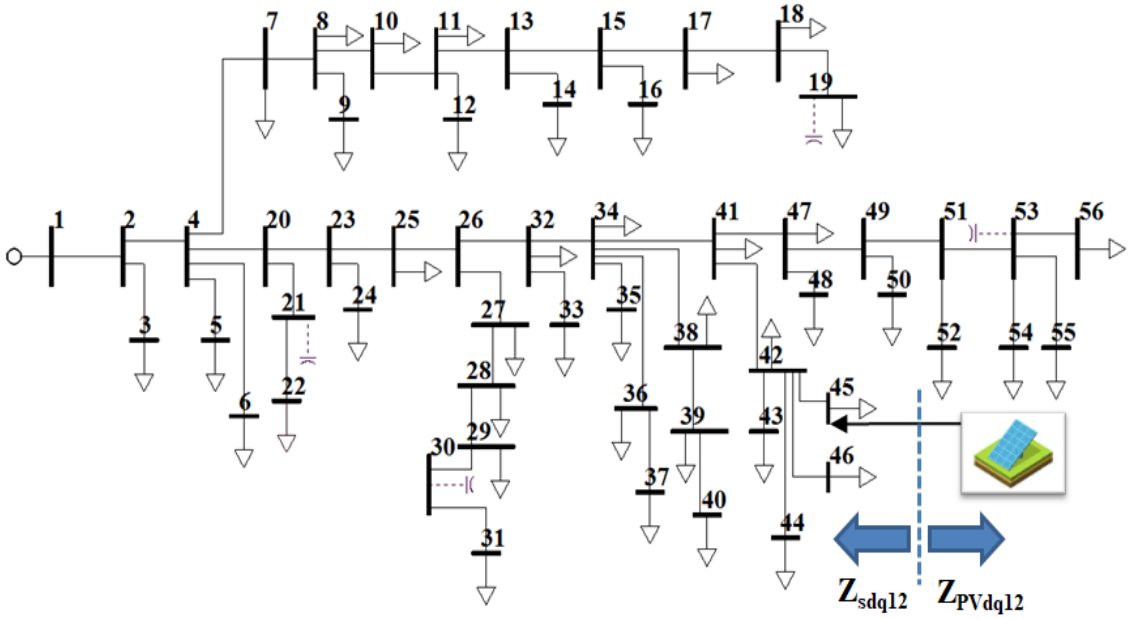

Figure 5-14 Small-signal representation of the three-phase unbalanced system in *d-q* frame

The return ratio matrix for GNC is

$$\mathbf{L}(s) = \mathbf{Z}_{\mathbf{sdq12}}(s) \cdot \mathbf{Y}_{\mathbf{PVdq12}}(s) \tag{5-62}$$

$$\mathbf{Y}_{\mathbf{PVdq12}}(s) = \mathbf{Z}_{\mathbf{PVdq12}}(s)^{-1} \tag{5-63}$$

5.5.1 Unbalance comes from source voltages

In the first case, the unbalance come from the substation voltage, the three phase voltages are 1.04 p.u. , 1.04 p.u. and 0.95 p.u. separately, which causes a 3% unbalance at the substation.

Fig.5-15 is the Nyquist diagram of the four characteristic loci of the measured return ratio matrix of (5-62) when reactive power controller is k_p = 3.3×10^{-5}and k_i = 0.33. None of the eigenvalues of encircles (-1,0). $\mathbf{Z}_{\mathbf{sdq12}}$ and the load admittance $\mathbf{Y}_{\mathbf{PVdq12}}$ don't have

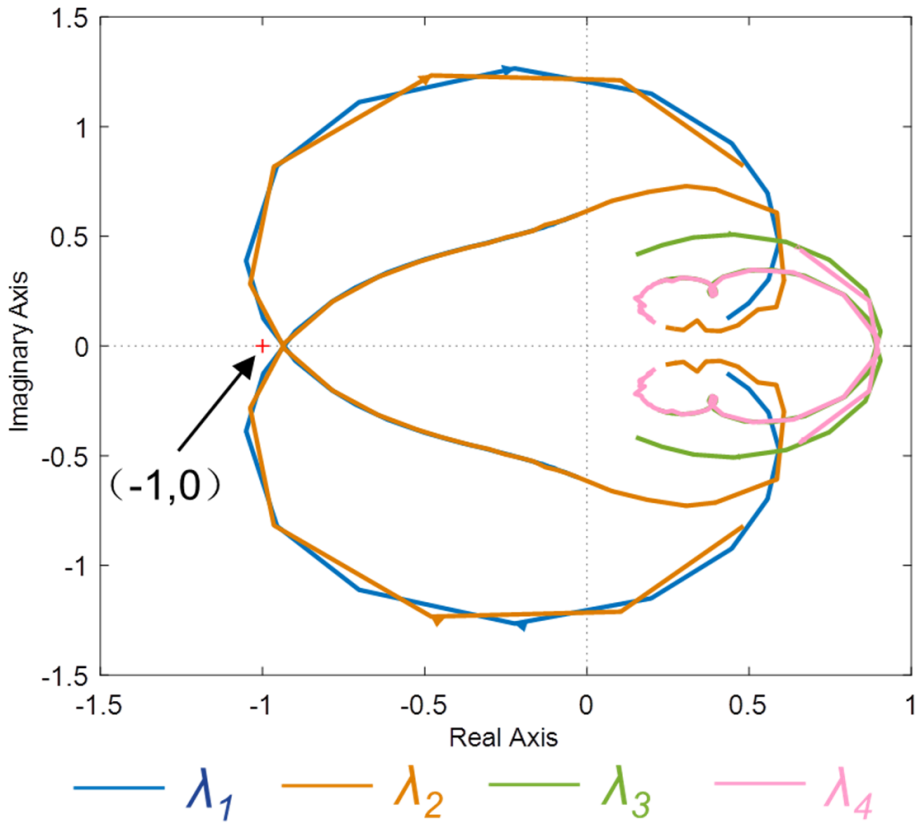

Figure 5-15 Four characteristic loci for the stable case when substation voltage is unbalanced

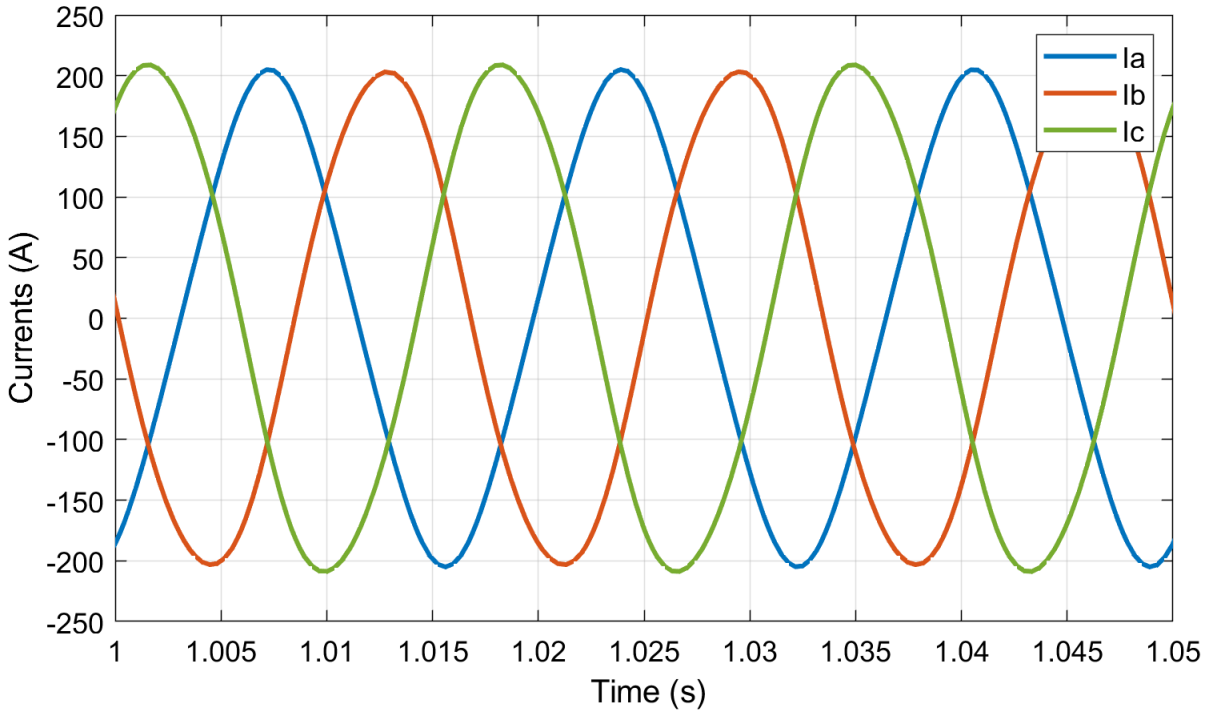

Figure 5-16 PV output currents for the stable case when substation voltage is unbalanced

RHP poles. So the system is stable according to GNC, which is validated by the time domain waveform of PV output currents in Fig. 5-16.

In contrast, Fig.5-17 is the Nyquist diagram of the four characteristic loci of the measured return ratio matrix of (5-62) when reactive power controller is $k_p = 6.6\times10^{-5}$and $k_i = 0.66$. Two of the eigenvalues of encircle (-1,0). λ_1 and λ_2 both encircle (-1,0) twice close wise. So the net clockwise encirclement is 4. $\mathbf{Z_{sdq12}}$ and the load admittance $\mathbf{Y_{PVdq12}}$ don't have RHP poles. According GNC, the system is unstable when PV farm is connected, which is proved by the time domain waveform in Fig. 5-18.

Fig. 5-18 is the waveform of PV output currents in the time domain simulation. There are a lot of harmonics in the current waveform, making it very distorted from the original sinusoidal shape. The unstable simulation waveform doesn't go exponentially increasing because there's still current limiter in the controller.

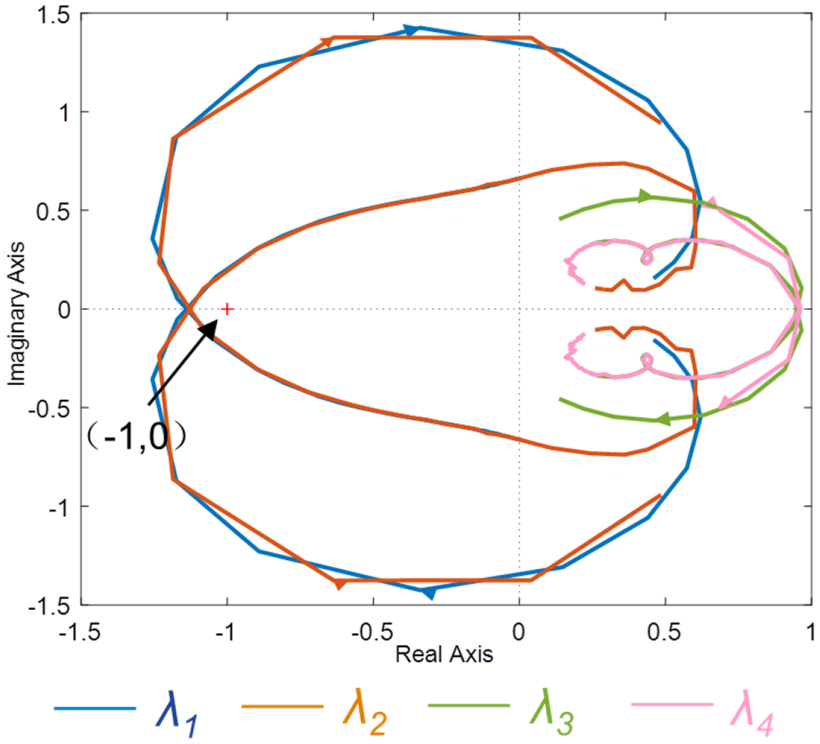

Figure 5-17 Four characteristic loci for the unstable case when substation voltage is unbalanced

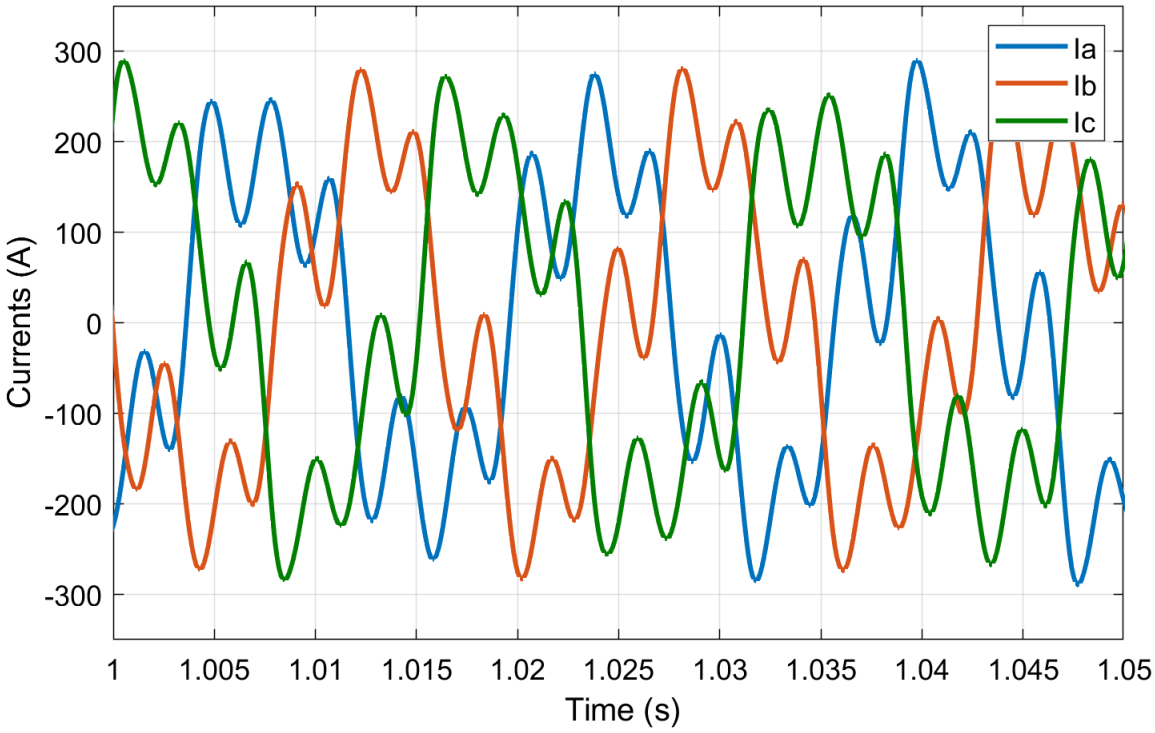

Figure 5-18 PV output currents for the unstable case when substation voltage is unbalanced

If the system unbalance is ignored and the original GNC based on two-by-two matrix *d-q* frame impedance as discussed in chapter 4, the two characteristic loci for the unstable case are shown in Fig. 5-19. It can be observed that neither eigenvalues encircles (-1,0), resulting an assessment result of stable, which is not correct. The comparison of Fig. 5-17 and Fig. 5-19 clearly shows the advantage of the proposed *d-q* frame mode over the original *d-q* frame model.

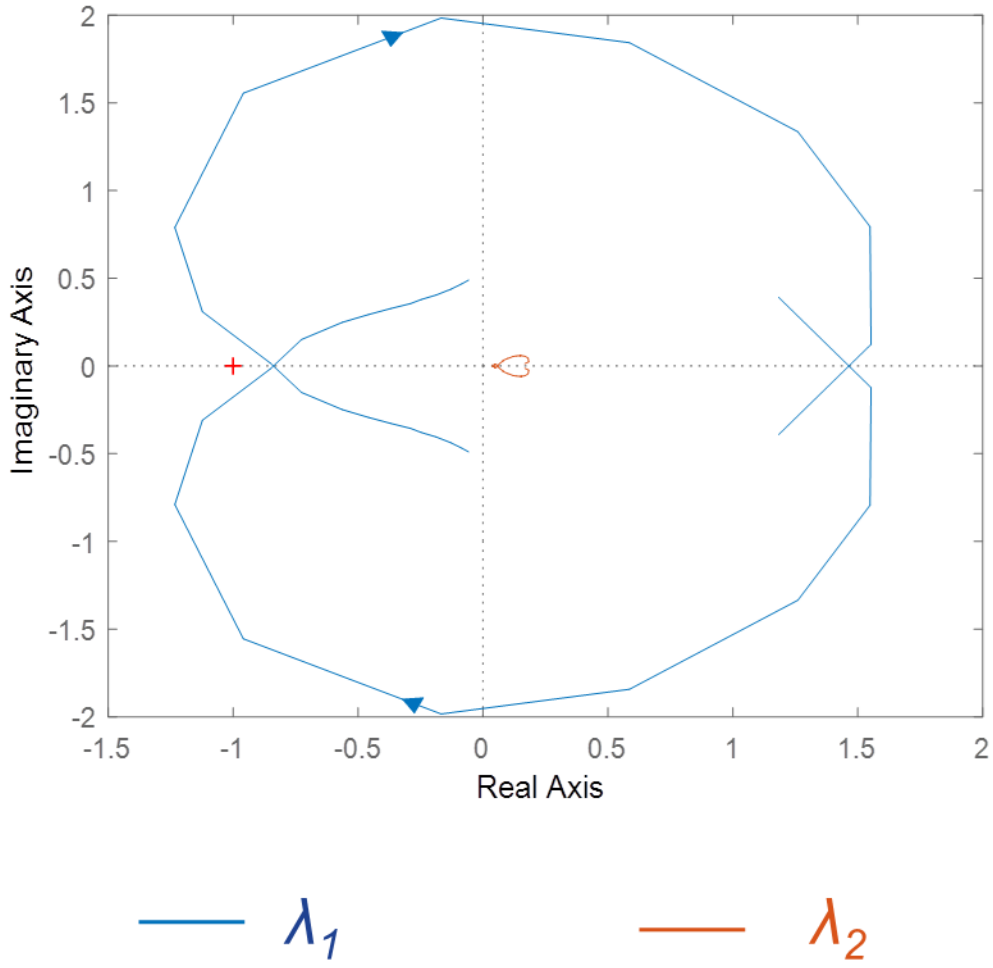

Figure 5-19 Two characteristic loci for the unstable case when substation voltage is unbalanced

5.5.2 Unbalance comes from loads

In a second case, the unbalance comes from the load, 0.7 MW of load are only connected between phase A and phase B . PV terminal voltage unbalance is 1% as the system is very lightly load.

Fig.5-20 is the Nyquist diagram of the four characteristic loci of the measured return ratio matrix of (5-62) when reactive power controller is $k_p = 3.3\times10^{-5}$and $k_i = 0.33$. None of the eigenvalues of encircles (-1,0). $\mathbf{Z_{sdq12}}$ and the load admittance $\mathbf{Y_{PVdq12}}$ don't have RHP poles. So the system is stable according to GNC, which is validated by the time domain waveform of PV output currents in Fig. 5-21.

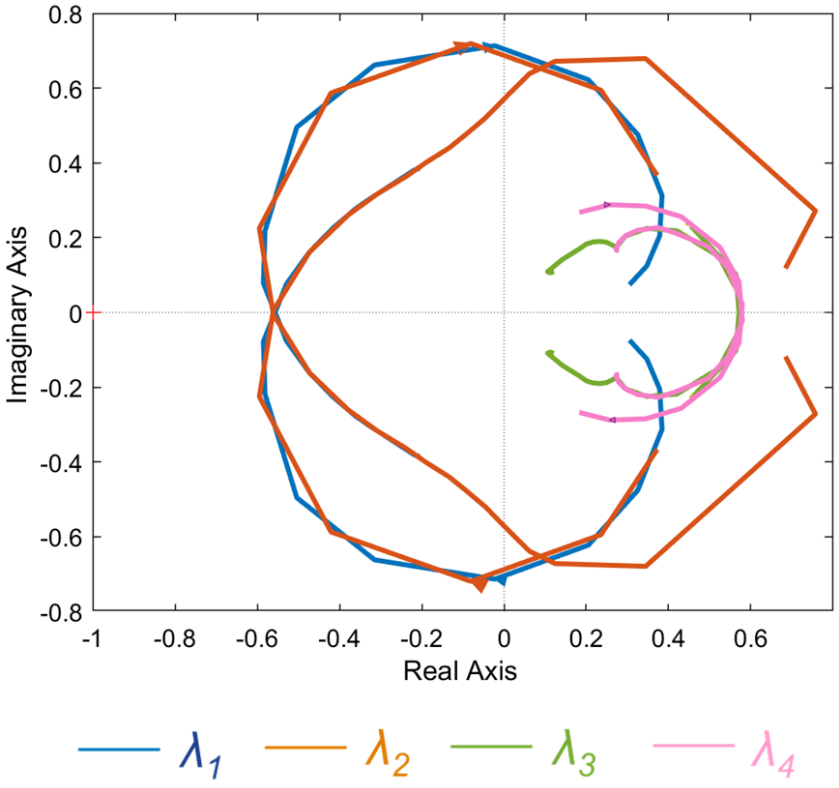

Figure 5-20 Four characteristic loci for the stable case when load is unbalanced

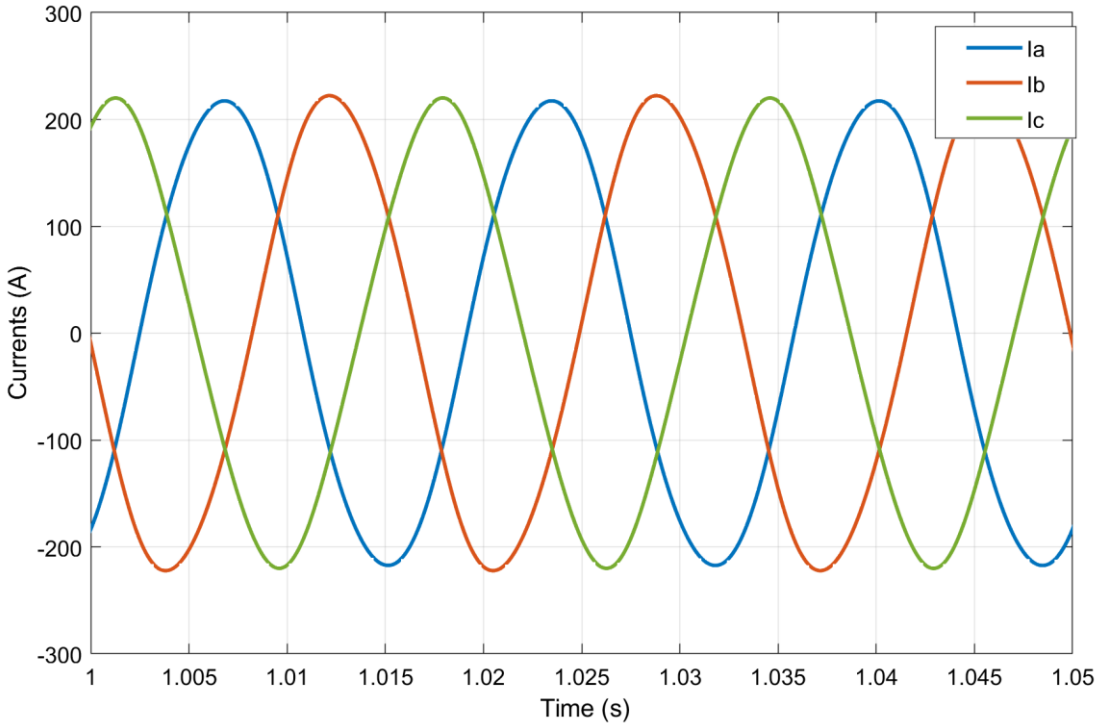

Figure 5-21 PV output currents for the stable case when system load is unbalanced

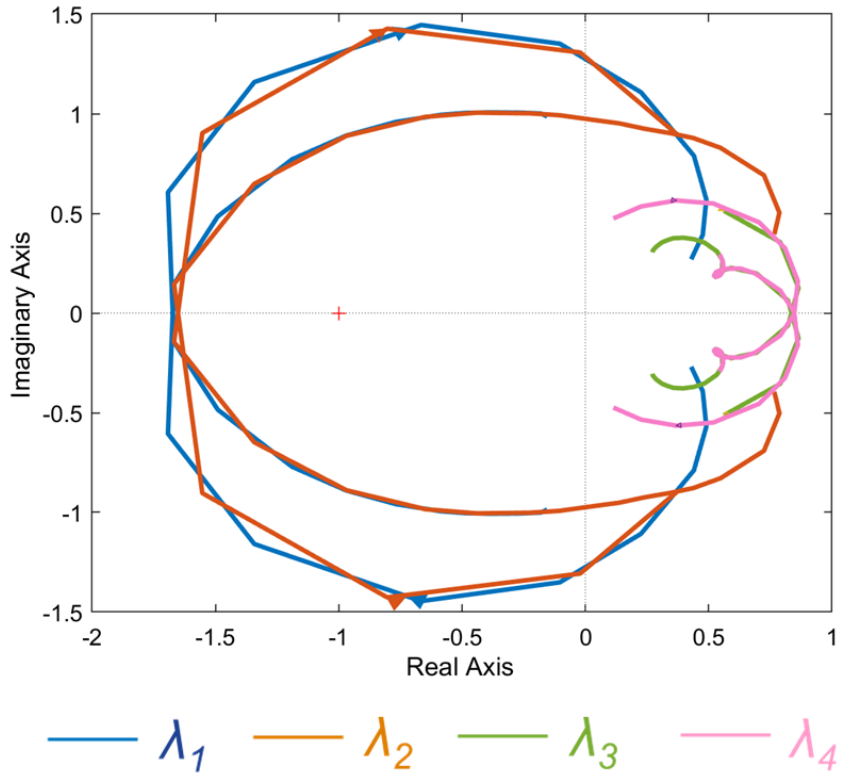

Figure 5-22 Four characteristic loci for the unstable case when load is unbalanced

In contrast, Fig.5-22 is the Nyquist diagram of the four characteristic loci of the measured return ratio matrix of (5-62) when reactive power controller is $k_p = 6.6\times10^{-5}$and $k_i = 0.66$. Two of the eigenvalues of encircle (-1,0). λ_1 and λ_2 both encircle (-1,0) twice close wise. So the net clockwise encirclement is 4. $\mathbf{Z_{sdq12}}$ and the load admittance $\mathbf{Y_{PVdq12}}$ don't have RHP poles. According GNC, the system is unstable when PV farm is connected, which is proved by the time domain waveform in Fig. 5-23.

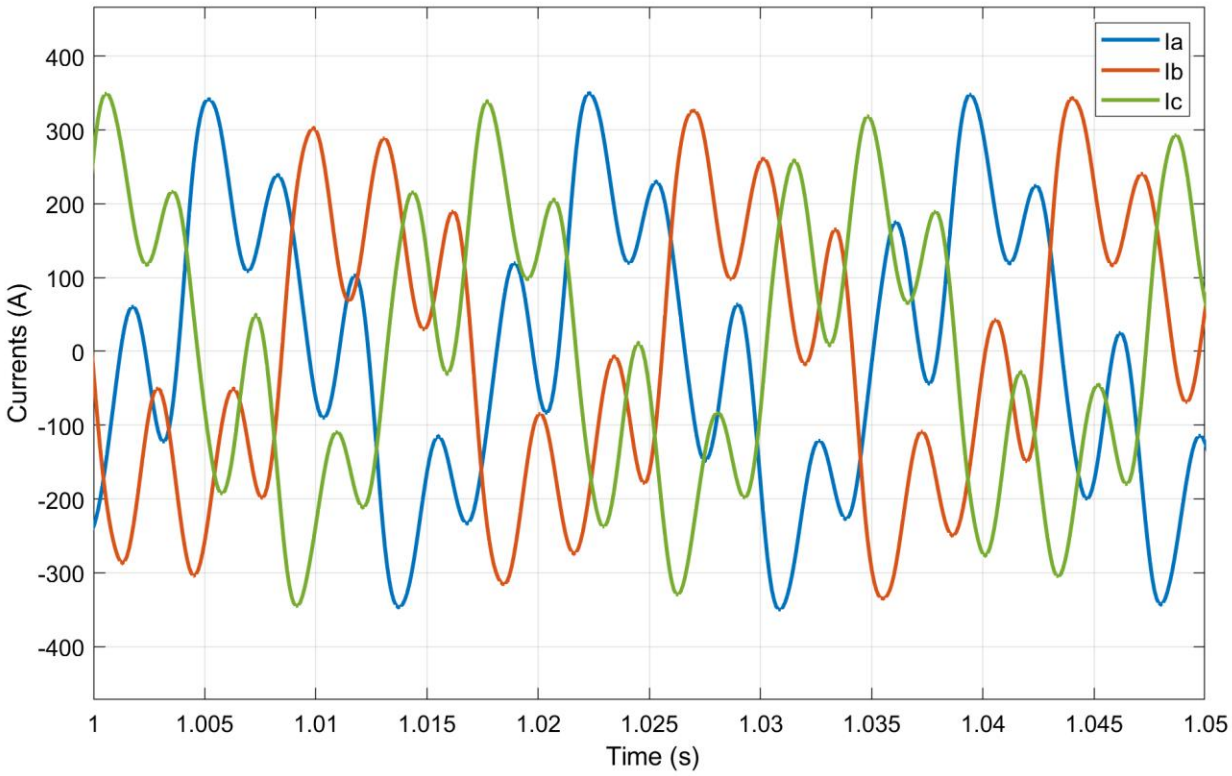

Figure 5-23 PV output currents for the unstable case when system load is unbalanced

5.5 Experimental verification

5.5.1 Unbalance comes from source voltages

A scaled-down hardware experiment was done To test the proposed impedance modeling method and the impedance measurement process. The main circuit is shown below in

Fig.5-24. The impedance measurement unit (IMU) is located between the line and the converter to measure the impedances. And Fig 5-25 is a picture of all the components in the hardware experiments.

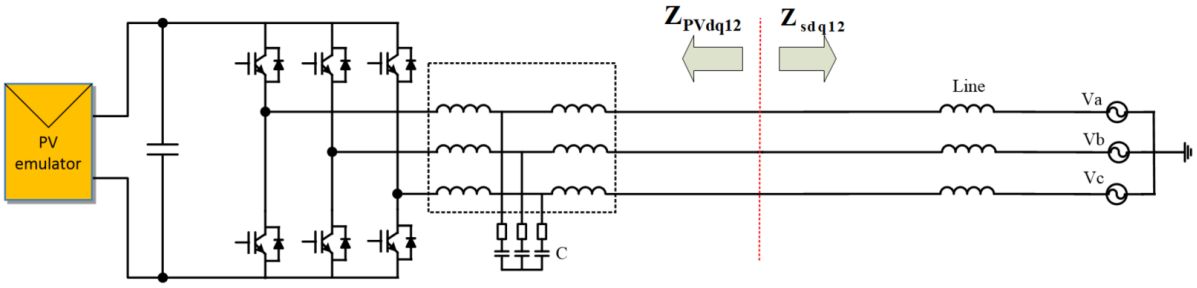

Figure 5-24 Hardware experiment main circuit when the unbalance comes from AC source

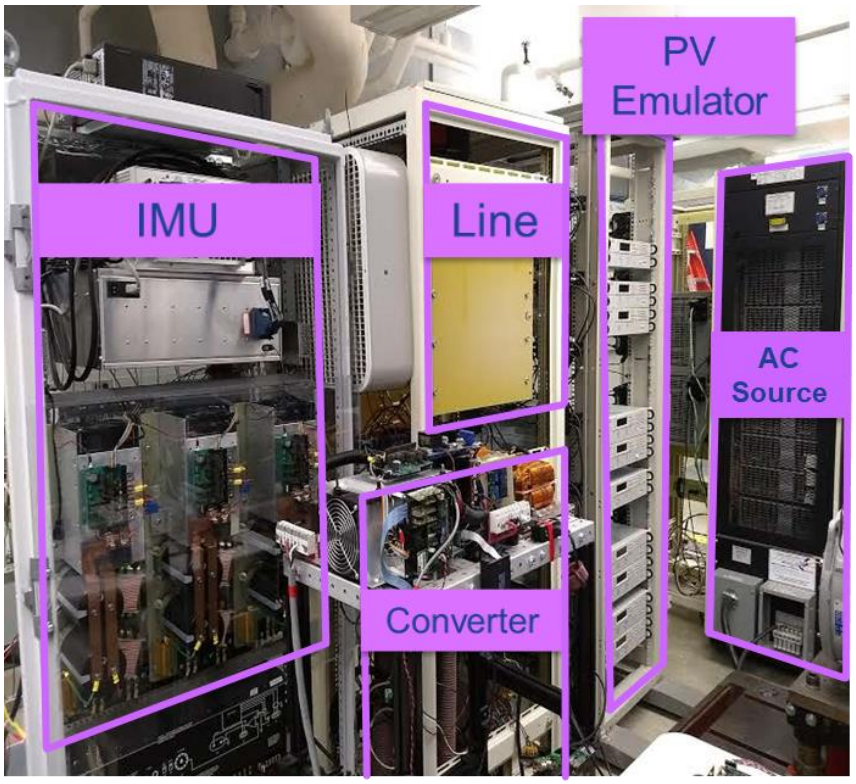

Figure 5-25 Picutre of the hardware circuit

The specifications of the main circuit is shown in Table 5-1 But the AC source is deliberately set to be three-phase unbalanced. The PV emulator is composed of 15 PV

modules which is divided into three strings in parallel. The I-V curve of each module is defined by the parameters of V_{oc} = 55 V, V_{mpp} = 50 V, I_{sc} = 4.5A and I_{mpp} = 3.6A.

Table 5-1 Parameters of the hardware circuits with unbalanced source

Parameter	Value
V_a	71 V
V_b	64 V
V_c	64 V
Line impedance	0.7 Ω + 5.4 mH
AC frequency	60 Hz
Active power output	2.6 kW
DC voltage	250V

The PV is under volt-var droop mode control of $Q = - Kv\ (Vd - 110)$. Fig. 5-26 is the recorded waveform when Kv increases from 30 to 35. The system becomes unstable after

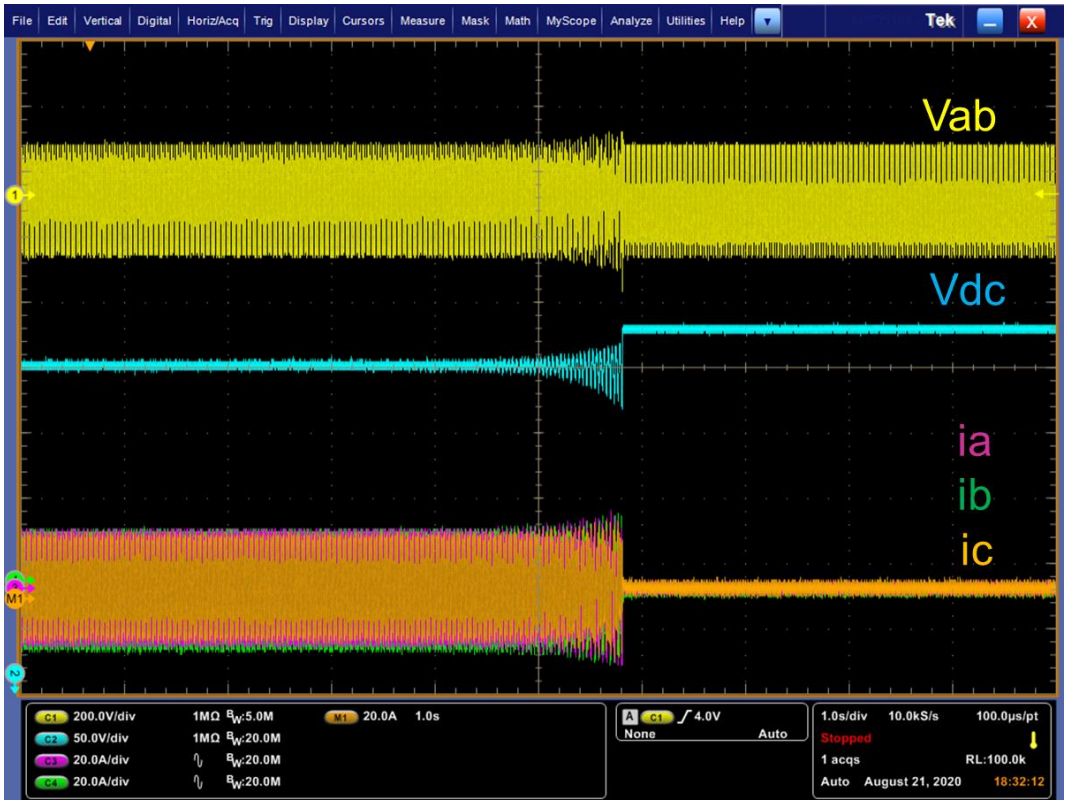

Figure 5-26 Recorded waveform of PV inverter on the scope

the change. The blue curve of DC voltage starts to oscillate until the low DC voltage triggers the controller protection. Fig.5-27 is the characteristic loci of the four by four return ratio matrix when K_v =30. The Nyquist diagram on the right is a zoom in view around (-1,0). The net encirclement is zero, so the system is stable. While Fig.5-28 is the characteristic loci of the return ratio matrix when K_v =35. The net encirclement is four, so the system is unstable. The GNC application results match with hardware test results.

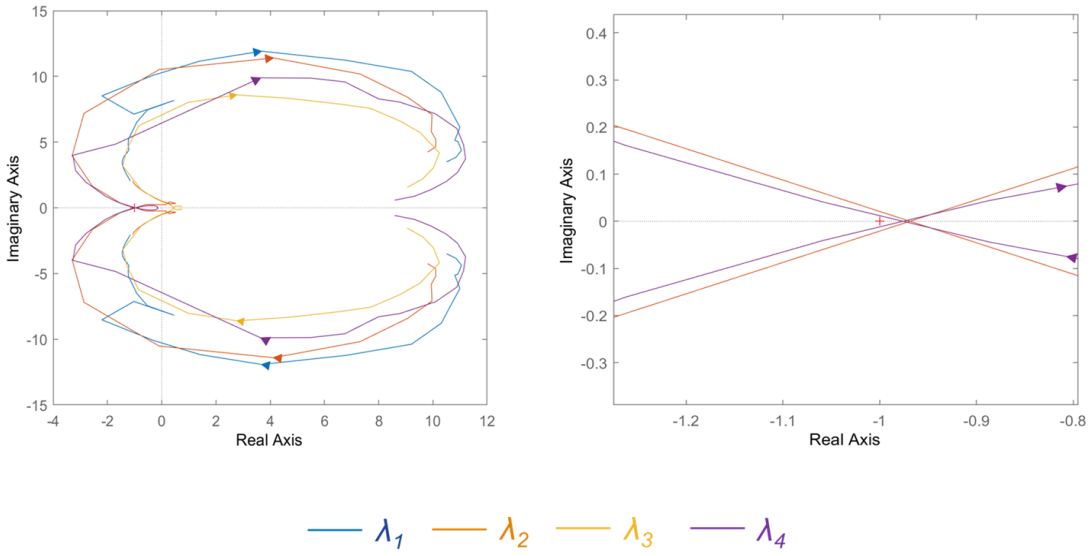

Figure 5-27 Four characteristic loci for the stable case when AC voltage is unbalanced

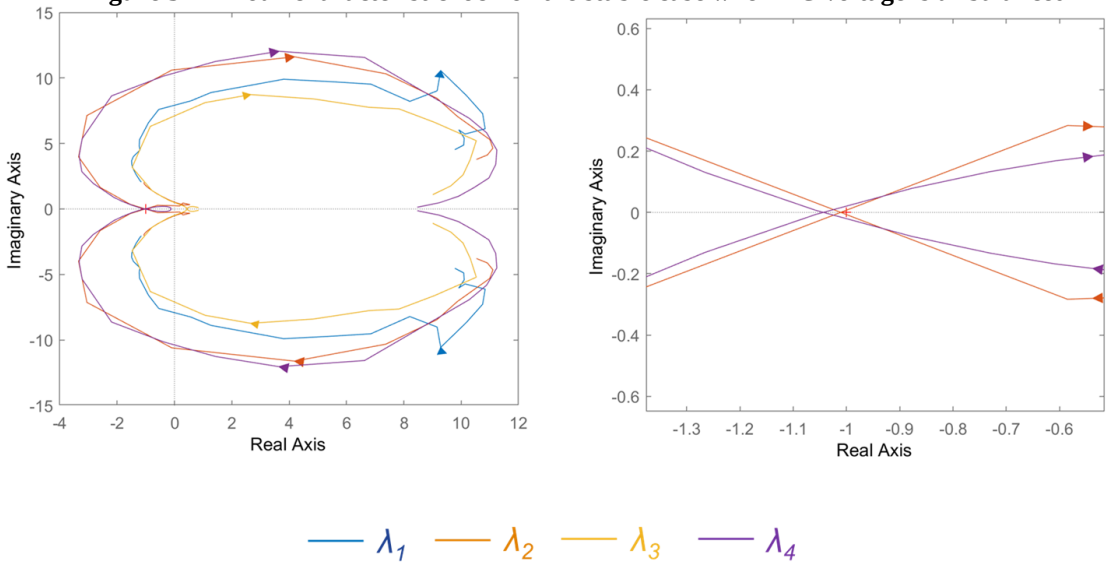

Figure 5-28 Four characteristic loci for the unstable case when AC voltage is unbalanced

5.5.2 Unbalance comes from load

In another case in the hardware experiment, the unbalance comes from the line-to-line loads in between the AC source and the PV inverter. Fig. 5-29 is the main circuit of the experiment. And Table 5-2 lists the parameters of the circuit.

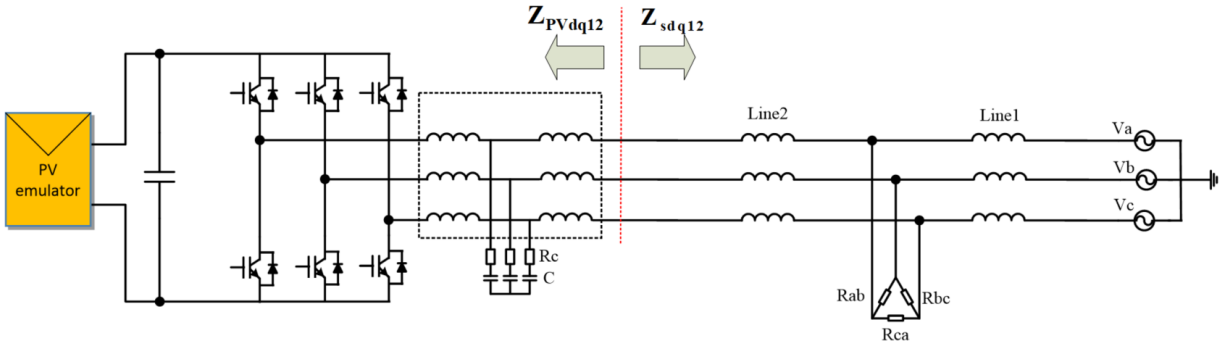

Figure 5-29 Hardware experiment main circuit when the unbalance comes from line-to-line load

Table 5-2 Parameters of the hardware circuits with unbalanced load

Parameter	Value
V_a / V_b/ V_c	64 V
R_{ab}	10 Ω
R_{bc}	15 Ω
R_{ca}	15 Ω
Line 1 impedance	1.2 mH
Line 2 impedance	0.7 Ω + 4.5 mH
AC frequency	60 Hz
Active power output	2.6 kW
DC voltage	250V

The PV is under volt-var droop mode control of $Q = - Kv\ (Vd - 100)$. Fig. 5-30 is the recorded waveform when Kv increases from 25 to 30. The system becomes unstable after the change. The blue curve of DC voltage starts to oscillate until the low DC voltage triggers the controller protection. Fig.5-31 is the characteristic loci of the four by four

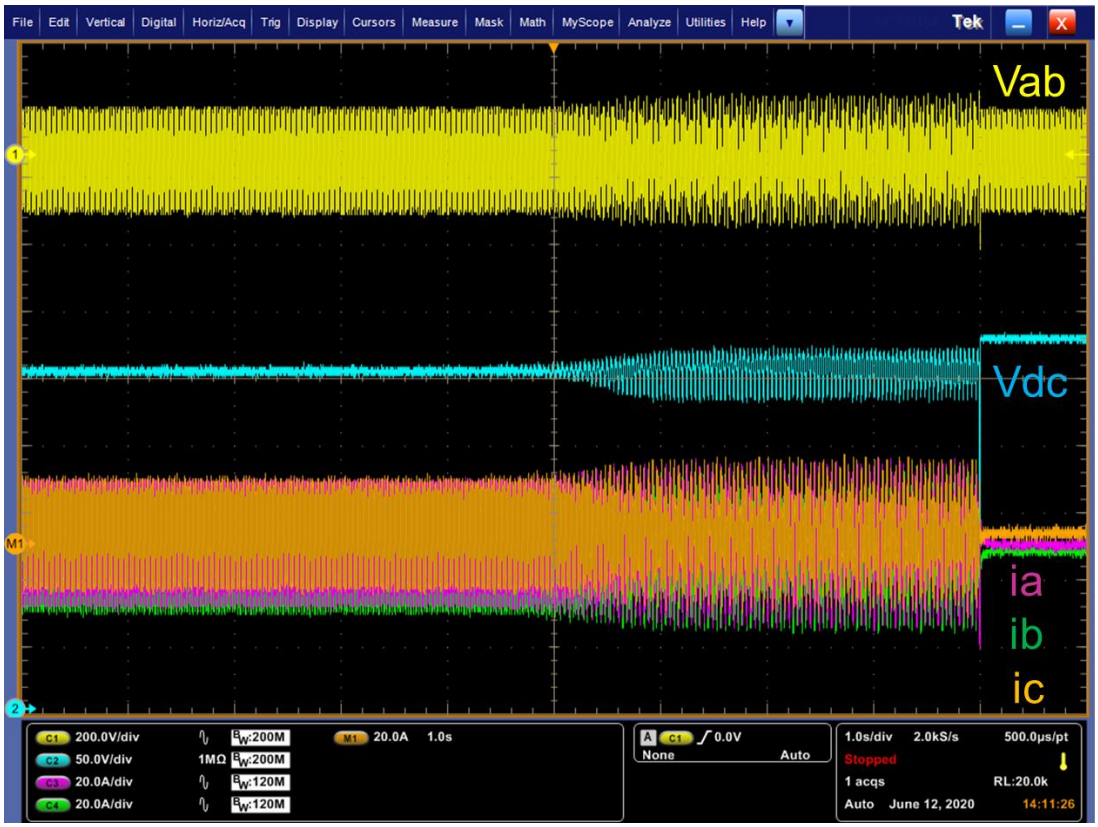

Figure 5-30 Recorded waveform of PV inverter on the scope

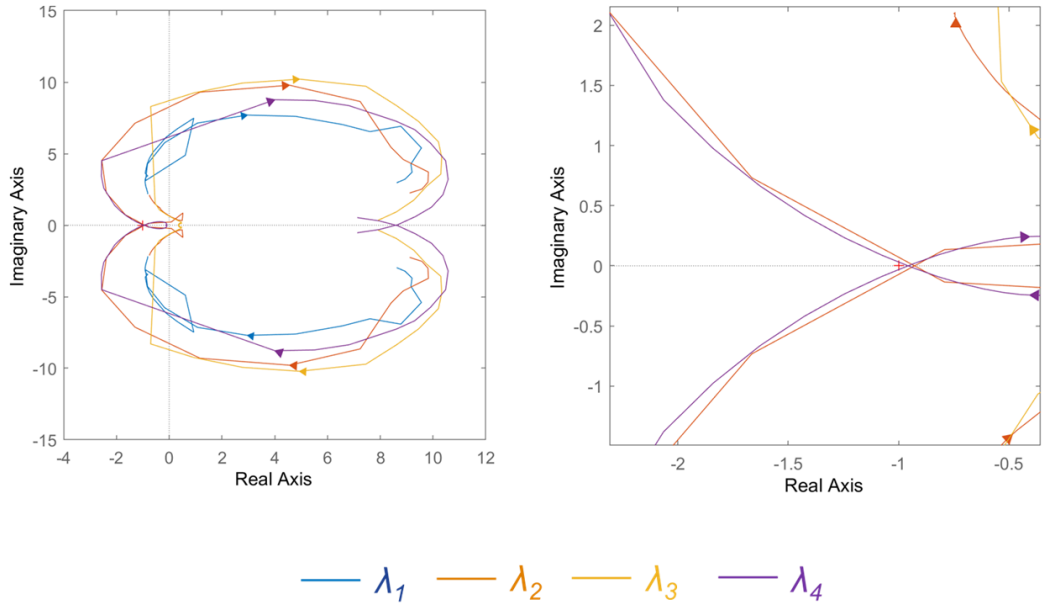

Figure 5-31 Four characteristic loci for the stable case when the loads are unbalanced

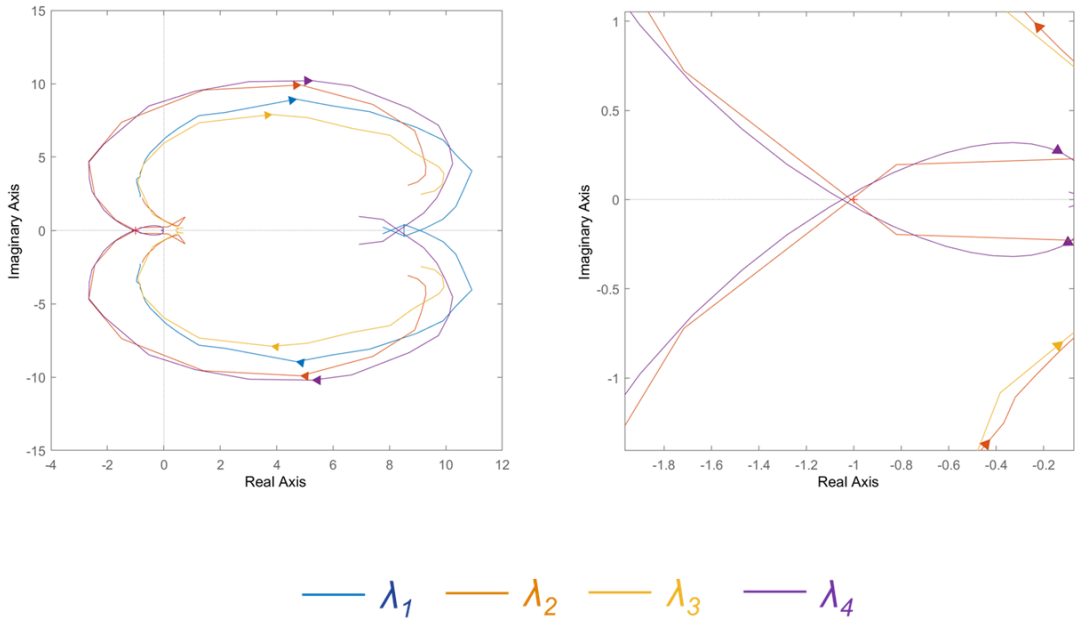

Figure 5-32 Four characteristic loci for the stable case when the loads are unbalanced

return ratio matrix when K_v =30. The Nyquist diagram on the right is a zoom in view around (-1,0). The net encirclement is zero, so the system is stable. While Fig.5-32 is the characteristic loci of the return ratio matrix when K_v =35. The net encirclement is four, so the system is unstable. The GNC application results match with hardware test results.

5.6 Summary and conclusions

Generalized Nyquist Criterion (GNC) based on *d-q* frame two-by-two impedance matrices is widely used on three-phase balanced systems for small-signal stability assessment at the AC interface of power electronics devices, which is not applicable for three-phase unbalanced systems. An algorithm is developed to model the terminal impedance of the source and the load in three-phase unbalanced system at AC interfaces and predict the small-signal stability after the connection based on the measured *d-q* frame four-by-four impedance matrices. This algorithm can be used in all kinds of three-

phase unbalanced systems including distribution systems in utility and three-phase electrical systems on ships and planes. The four-by-four impedance matrix measurement process is designed according to the single-phase *d-q* frame impedance measurement method. Compared to the existing approach of positive-negative sequence impedance, the proposed method is more accurate because the dynamics of *d-q* frame controllers are taken in consideration. And compared to the existing harmonics transfer function method, this model has done some reasonable truncation so that it's feasible to be easily applied in the real system. Time domain simulation and scaled-down experiments have been done to prove the accuracy and feasibility of the proposed method.

A per-phase expanded *d-q* frame impedance model was proposed for the three-phase unbalanced system. In the proposed frame, a DC operating point is obtained, around which linearization can be done to extract terminal impedance matrices. GNC can applied at the connection interface based on the expanded terminal impedance matrices to predict system small-signal stability using the fourth order return ratio matrix. A procedure was developed to measure the 4×4 impedances using single-phase impedance measurement method and verified through simulation. The proposed procedure and stability method was verified through a scaled-down hardware experiment.

Chapter 6. Conclusions and Future Work

With development of renewable energies worldwide, power system is seeing higher penetration of Utility Scale PV farms at distributed level as well as transmission level. This work first does a static analysis of the impact of PV on system voltage profile and power loss in a distribution system. Comparison is done between PV farm of different capacities, different locations and five different reactive power control modes of

(1) Unity power factor mode

(2) Constant reactive power mode

(3) Constant power factor mode

(4) Watt-var mode

(5) Volt-var droop mode.

A known broad statement is that active power injected by PV inverters increases the system voltage. This work contributes to existing knowledge by doing a sensitivity analysis. It is discovered in this work that the impact of active power or reactive power on the voltage magnitude is almost linear, thus the rate by which the voltage increases at different geographical locations can be estimated accurately by the proposed sensitivity matrix, which was shown to be related to the system impedances. The voltage boost because of active power injection will cause a limitation of maximum PV capacity, which can be mitigated by connecting PV to a bus as close to the substation as possible or making use of the reactive power capability of PV. With the assumption of the same reactive power compensation capability, the reactive power control mode of volt-var droop mode is preferred over other modes because it provides voltage regulation service

even when there's no sun, and volt-var droop mode is effective to mitigate overvoltage and under voltage whereas power factor control cannot achieve at the same time. Nonetheless, there will be a PV penetration limit even under reactive power control because PV has limited reactive power control capability at full active power and the high R/X ratio in the distribution system. Furthermore, it was shown that as the capacity of PV inverters increases, the system power loss will find an optimum operating point that will vary both with the physical location of the PV inverter unit and with the amount of power injected, and that the use of reactive power compensation to mitigate the impact on the system voltage profile will detrimentally affect the system power loss, in what is then an operational tradeoff. Accordingly, and in what could be considered a guideline for PV inverter allocation, to reduce the impact on voltage profile PV these units should be connected as close to the substation as possible (electrical distance indicated by sensitivity matrix), where the optimal allocation to reduce network power loss will depend on the distribution of load. Volt-var droop mode is preferred compared to other reactive power control in both aspects.

A major finding of this study is that although volt-var droop mode control is most favorable local reactive power control strategy for voltage regulation and power loss minimization, it may adversely affect system small-signal stability. A radial medium voltage distribution system is modeled in MATLAB to analyze the impact of PV generator penetration using GNC method based on impedances in *d-q* frames. Before applying the GNC methods, a *d-q* frame impedance model is built for Utility PV farm generators to observe how the impedance matrix is shaped by the controllers. The terminal impedances in *d-q* frame are derived of utility-scale PV farm based on small

signal model of the PV generator, which include the dynamics from the PV array, the power stage and the controllers in the synchronous reference frame. The PV terminal impedance matrix model derived from small-signal model is proved by time domain simulation and validated by scaled-down hardware experiments.

A comparison is done among impedances of PV inverters under 5 different reactive power control modes. The terminal *d-q* frame impedance matrix shows least coupling between d axis and q axis at unity power factor control compared to other modes. The sign of Z_{dd} is positive at low frequencies because of constant active power output. The sign of Z_{qq} is negative at low frequencies because of PLL synchronization. And for the impedance matrices of modes of constant reactive power, constant power factor and watt-var modes, the non-diagonal elements become comparatively larger but still much smaller than the diagonal elements. The first four modes have similar *d-q* frame impedances. While the volt-var control mode changes PV terminal impedance signs and magnitudes significantly. There is a stronger *d-q* coupling because reactive power reference which is the source of Q axis current reference is mapped from a droop curve of D axis terminal voltage. The matrix becomes non-diagonal dominant and the negative incremental resistance behavior occurs in D axis instead of Q axis. As the *d-q* frame impedance matrix turn non-diagonal dormant, it's impossible to judge the system stability by purely looking at the impedances of the PV farm and the grid.

For the grid with a single PV farm connection, GNC is applied at PV connection terminal. The increase of number of PV inverters in parallel will also lower the PV impedance and increase the possibility of instability. The reactive power control of volt-var droop mode is the first mode to cause instable connection as the number of PV

inverters increases. The discovered instability problem caused by volt-var droop mode control is highly related to the inner current controller, the reactive power loop controller and the digital delay and not quite related to DC voltage controller and PLL block.

For the distribution system with multiple PV farms, GNC is applied at one of the PV farm connection point. Interestingly, PV farms connected to different branches of the complicated radial distribution system may have interactions with each other when they are under volt-var droop mode control. So the design of control strategy and parameters of PV generator should consider the impact of other PV generators. GNC method based on impedances measurement is feasible accurate for stability assessment of a distribution system with multiple PV farms.

For the instability problem caused by volt-var droop mode control, comparison is done for different PV allocations, different PV capacities (different number of PV inverters) and different irradiance condition. No matter it's a system with single PV farm or with multiple PV farms, moving any of the PV farm closer to the substation reduces the possibility of instability. Higher capacity of PV penetration makes this stability problem worse and so does the higher solar irradiance condition.

The GNC application results of the case of multiple PV farms are also verified by time-domain simulation and hardware experiments. Time domain simulation using SIMULINK yields the same conclusion about the stability of the PV connection to the grid under volt-var droop mode. In unstable cases, PV output currents have oscillation in *d-q* frames and have more harmonics in ABC frames. The time domain simulation proves that application of GNC is accurate to predict system stability. The GNC application results are also proved by scale down hardware experiments.

Generalized Nyquist Criterion (GNC) based on *d-q* frame two-by-two impedance matrices is widely used on three-phase balanced systems for small-signal stability assessment at the AC interface of power electronics devices, which is not applicable for three-phase unbalanced systems. This research provides a band-new view of the unbalanced system by looking at the original circuit as phase A and by adding a fictitious phase B and phase C circuit so that Park transformation to get a DC operation point becomes feasible.

An algorithm is developed to model the terminal impedance of the source and the load in three-phase unbalanced system at AC interfaces and predict the small-signal stability after the connection based on the measured *d-q* frame four-by-four impedance matrices. A per-phase expanded *d-q* frame impedance model was proposed for the three-phase unbalanced system. In the proposed frame, a DC operating point is obtained, around which linearization can be done to extract terminal impedance matrices. GNC can applied at the connection interface based on the expanded terminal impedance matrices to predict system small-signal stability using the fourth order return ratio matrix.

A procedure was developed to measure the 4×4 impedances using single-phase impedance measurement method. Time domain simulation and scaled-down experiments have been done to prove the accuracy and feasibility of the proposed method.

One known limitation of the proposed method for the unbalanced system is that the unbalance is relatively small, as limited by the standard to be below 3%. It is not tested on the highly unbalanced system yet.

This work focuses on the identification of the instability problems of the PV generators based on synchronous reference *d-q* frame in the distribution system,

compares how the instability is influenced by factors including different reactive power control modes, different allocations, different irradiance and so on. The question of how and to what extent does the virtual synchronous generator (VSG) control help with this problem needs to be explored.

In addition, only the reactive power control to support AC voltage profile regulation is applied in the utility PV inverters in this research assuming that peak active power is still achieved all time for maximum energy harvest, it's definitely worthwhile to look into the cases when PV generators also provides grid-support functionality of frequency control, namely the active power – frequency droop curve be executed at the same time as well as reactive power – voltage droop.

As introduced by the first chapter that PV generators are divided into three categories residential PV, commercial PV and Utility PV farms according to the power rating. Only the three-phase Utility PV generators are discussed in this work. But actually the number of commercial PV generators and residential PV generators (three-phase or single-phase on AC side) far exceeds the number of Utility PV farms, and are connected to low voltage parts of the distribution system which have relatively higher per unit impedances than the medium voltage parts as the 12 kV system used in this research. It can be foreseen that if commercial PV generators and residential PV generators are required to provide grid-support functionalities as the Utility PV generators, they are much more vulnerable to this type of instability problems, which should be analyzed before the control of commercial PV generators and residential PV generators is updated to be more complicated.

One more direction for future work is that the connection of only two PV farms is simulated and studied in this research, what if a large number of PV farms are connected to the same distribution system, or like the case of hundreds or thousands of single-phase residential PV inverters in the same feeder? The impedance network may be a good solution for this topic, which needs further investigation and validation.

REFERENCES

[1] Wood Mackenzie, Solar Energy Industries Association (SEIA). "U.S. Solar Market Insight Executive Summary", Dec. 2020, https://www.seia.org/research-resources/solar-market-insight-report-2020-q4.

[2] U.S. Energy Information Administration (EIA), "Most U.S. utility-scale solar photovoltaic power plants are 5 megawatts or smaller", Feb. 2019, https://www.eia.gov/todayinenergy/detail.php?id=38272#.

[3] N. Pogaku, M. Prodanovic, and T. C. Green, "Modeling, analysis and testing of autonomous operation of an inverter-based microgrid,"in *IEEE Trans. Power Electron*., vol. 22, pp. 613-625, Mar. 2007.

[4] J. L. Agorreta, M. Borrega, J. Lopez and L. Marroyo, "Modeling and control of N-paralleled grid-connected inverters with LCL filter coupled due to grid impedance in PV plants," *IEEE Trans. Power Electron*., vol.26, no.3, pp. 770-785, 2011.

[5] W. Du, H. Wang, and L. Xiao, "Power system small-signal stability as affected by grid-connected photovoltaic generation," *Eur. Trans. Elect. Power*, vol. 22, pp. 688–703, Jul. 2012.

[6] Y. Wu, G. Ye and Mohamed Shaaban, "Impact analysis of large PV integration: Case studies in Taiwan.", in *Proc. of IEEE/IAS 52nd Industrial and Commercial Power Systems Technical Conference (ICPS)*, Detroit, MI, USA, 1–5 May 2016.

[7] B. Tamimi, C. Canizares, and K. Bhattacharya, “System stability impact of large-scale and distributed solar photovoltaic generation: The case of Ontario Canada,” *IEEE Trans. Sustain. Energy,* vol. 4, no. 3, pp. 680–688, Jul. 2013.

[8] M. Duckheim, J. Reinschke, P. Gudivada, and W. Dunford, “Voltage and power flow oscillations induced by PV inverters connected to a weak power distribution grid,” in *Proc. IEEE Power Energy Soc. Gen. Meeting Int. Conf.,* 2013, pp. 1–5.

[9] S. Liu, P. X. Liu and X. Wang. “Stability Analysis of Grid-Interfacing Inverter Control in Distribution Systems With Multiple Photovoltaic-Based Distributed Generators”, in *IEEE Transactions on Industrial Electronics*, vol. 63, no. 12, pp 7339 – 7348 , 2016.

[10] Z. Moradi-Shahrbabak and A. Tabesh, “Effects of Front-End Converter and DC-Link of a Utility-Scale PV Energy System on Dynamic Stability of a Power System”, *IEEE Trans. on Industrial Electronics*, vol. 65, no. 1, pp. 403-411 Jan. 2018.

[11] Z. Zhao, P. Yang, Y. Wang, Z. Xu, and J. M. Guerrero, ‘‘Dynamic characteristics analysis and stabilization of PV-based multiple microgrid clusters,’’ in *IEEE Trans. Smart Grid*, vol. 10, no. 1, pp. 805–818, Jan. 2019.

[12] P. Kundur, *Power system stability and control*. New York: McGraw-hill, 1994.

[13] R. D. Middlebrook, “Input filter considerations in design and application of switching regulators,” in *Proc. IEEE Ind. Applicat. Soc. Conf*., Oct. 1976, pp. 94–107.

[14] S. D. Sudhoff, S. F. Glover, P. T. Lamm, D. H. Schmucker, and D. E. Delisle, "Admittance space stability analysis of power electronic systems," *IEEE Trans. Aerosp. Electron. Syst.*, vol. 36, no. 3, pp. 965–973, Jul. 2000.

[15] X. Feng, J. Liu, and F. C. Lee, "Impedance specification for stable dc distributed power systems," *IEEE Trans. Power Electron*., vol. 17, no. 2, pp. 157–162, Mar. 2002.

[16] S. Vesti, T. Suntio, J. A. Oliver, R. Prieto, and J. A. Cobos, "Impedance-based stability and transient-performance assessment applying maximum peak criteria," *IEEE Trans. Power Electron*., vol. 28, no. 5, pp. 2099–2104, May 2013.

[17] M. Belkhayat, "*Stability criteria for ac power systems with regulated loads*," Ph.D. dissertation, Purdue Univ., West Lafayette, IN, Dec. 1997.

[18] A. G. J. MacFarlane and I. Postlethwaite, "The generalized Nyquist stability criterion and multivariable root loci," *Int. J. of Control*, vol. 25, no. 1, pp. 81–127, 1977.

[19] J. Sun, "Small-signal methods for AC distributed power systems—A review," *IEEE Trans. Power Electron*., vol. 24, no. 11, pp. 2545–2554,Nov. 2009.

[20] T. Roinila, M. Vilkko, and J. Sun, "Online grid impedance measurement using discrete-interval binary sequence injection*," IEEE J. Emerg. Sel. Topics Power Electron*., vol. 2, no. 4, pp. 985–993, Dec. 2014.

[21] Z. Bing, "*Three-phase AC-DC converters for more-electric aircraft*," Ph.D. dissertation, Dept. Elect. Eng., Rensselaer Polytech. Inst., Troy, NY, USA, 2010.

[22] X. Wang, F. Blaabjerg, and W. Wu, “Modeling and analysis of harmonic stability in an AC power-electronics-based power system,” *IEEE Trans.Power Electron.*, vol. 29, no. 12, pp. 6421–6432, Dec. 2014.

[23] A. Rygg, M. Molinas, C. Zhang and X. Cai, “A Modified sequence domain impedance definition and its equivalence to the dq-domain impedance definition for the stability analysis of AC power electronic systems,” *IEEE J. Emerg. Sel. Topics Power Electron*., vol. 4, no. 4, pp. 1383–1396, Dec. 2016

[24] Z. Shen, “*Online Measurement of Three-phase AC Power System Impedance in Synchronous Coordinates*,” Ph.D. dissertation, Virginia Tech, Blacksburg, VA, 2013.

[25] M. Kazem Bakhshizadeh et al., "Couplings in Phase Domain Impedance Modeling of Grid-Connected Converters," in *IEEE Transactions on Power Electronics*, vol. 31, no. 10, pp. 6792-6796, Oct. 2016.

[26] X. Wang, L. Harnefors and F. Blaabjerg, "Unified Impedance Model of Grid-Connected Voltage-Source Converters," in *IEEE Transactions on Power Electronics*, vol. 33, no. 2, pp. 1775-1787, Feb. 2018.

[27] B. Wen and P. Mattavelli, "Harmonic current analysis of the active front end system in the presence of grid voltage disturbance," *2018 IEEE Applied Power Electronics Conference and Exposition (APEC)*, San Antonio, TX, 2018, pp. 499-504.

[28] B. Wen, “*Stability Analysis of Three-phase AC Power Systems Based on Measured D-Q Frame Impedances*,” Ph.D. dissertation, Virginia Tech, Blacksburg, VA, 2014.

[29] B. Wen, D. Boroyevich, P. Mattavelli, Z. Shen and R. Burgos, "Influence of phase-locked loop on input admittance of three-phase voltage-source converters," *Twenty-Eighth Annual IEEE Applied Power Electronics Conference and Exposition (APEC*), Long Beach, CA, 2013, pp. 897-904

[30] B. Wen, D. Boroyevich, R. Burgos and P. Mattavelli, "Input impedance of voltage source converter with stationary frame linear current regulators and phase-locked loop," *IEEE Energy Conversion Congress and Exposition*, Denver, CO, 2013, pp. 4207-4213.

[31] B. Wen, D. Boroyevich, P. Mattavelli, R. Burgos and Z. Shen, "Impedance-based analysis of grid-synchronization stability for three-phase paralleled converters," *IEEE Applied Power Electronics Conference and Exposition* - APEC 2014, Fort Worth, TX, 2014, pp. 1233-1239.

[32] B. Wen, D. Boroyevich, P. Mattavelli, R. Burgos and Z. Shen, "Modeling the output impedance negative incremental resistance behavior of grid-tied inverters," 2014 *IEEE Applied Power Electronics Conference and Exposition* - APEC 2014, Fort Worth, TX, 2014, pp. 1799-1806.

[33] B. Wen, D. Boroyevich, R. Burgos and P. Mattavelli, "Modeling the output impedance of three-phase uninterruptible power supply in D-Q frame," 2014 *IEEE Energy Conversion Congress and Exposition (ECCE)*, Pittsburgh, PA, 2014, pp. 163-169.

[34] B. Wen, D. Boroyevich, R. Burgos, P. Mattavelli and Z. Shen, "Small-Signal Stability Analysis of Three-Phase AC Systems in the Presence of Constant Power

Loads Based on Measured D-Q Frame Impedances," in *IEEE Transactions on Power Electronics*, vol. 30, no. 0, pp. 5952-5963, Oct. 2015.

[35] B. Wen, D. Boroyevich, R. Burgos, P. Mattavelli and Z. Shen, "D-Q impedance specification for balanced three-phase AC distributed power system," 2015 *IEEE Applied Power Electronics Conference and Exposition* (APEC), Charlotte, NC, 2015, pp. 2757-2771.

[36] B. Wen, D. Boroyevich, R. Burgos, P. Mattavelli and Z. Shen, "Analysis of D-Q Small-Signal Impedance of Grid-Tied Inverters," in *IEEE Transactions on Power Electronics*, vol. 31, no. 1, pp. 675-687, Jan. 2016.

[37] B. Wen, D. Dong, D. Boroyevich, R. Burgos, P. Mattavelli and Z. Shen, "Impedance-Based Analysis of Grid-Synchronization Stability for Three-Phase Paralleled Converters," *in IEEE Transactions on Power Electronics*, vol. 31, no. 1, pp. 26-38, Jan. 2016, doi: 10.1109/TPEL.2015.2419712.

[38] B. Wen, D. Boroyevich, R. Burgos, P. Mattavelli and Z. Shen, "Inverse Nyquist Stability Criterion for Grid-Tied Inverters," in *IEEE Transactions on Power Electronics*, vol. 32, no. 2, pp. 1548-1556, Feb. 2017, doi: 10.1109/TPEL.2016.2545871.

[39] B. Wen, R. Burgos, D. Boroyevich, P. Mattavelli and Z. Shen, "AC Stability Analysis and d-q Frame Impedance Specifications in Power-Electronics-Based Distributed Power Systems," in *IEEE Journal of Emerging and Selected Topics in Power Electronics*, vol. 5, no. 4, pp. 1455-1465, Dec. 2017, doi: 10.1109/JESTPE.2017.2728640.

[40] H. Yi, X. Wang, F. Blaabjerg and F. Zhuo, "Impedance Analysis of SOGI-FLL-Based Grid Synchronization," in *IEEE Transactions on Power Electronics*, vol. 32, no. 10, pp. 7409-7413, Oct. 2017.

[41] X. Zhang, D. Xia, Z. Fu, G. Wang and D. Xu, "An Improved Feedforward Control Method Considering PLL Dynamics to Improve Weak Grid Stability of Grid-Connected Inverters," in *IEEE Transactions on Industry Applications*, vol. 54, no. 5, pp. 5143-5151, Sept.-Oct. 2018.

[42] C. Li, R. Burgos, Y. Tang and D. Boroyevich, "Impedance-based stability analysis of multiple STATCOMs in proximity," 2016 *IEEE 17th Workshop on Control and Modeling for Power Electronics* (COMPEL), Trondheim, 2016, pp. 1-6.

[43] C. Li, R. Burgos, Y. Tang and D. Boroyevich, "Analysis of small-signal impedance of STATCOMs in D-Q frame," *IECON 2017 - 43rd Annual Conference of the IEEE Industrial Electronics Society*, Beijing, 2017, pp. 870-875, doi: 10.1109/IECON.2017.8216150.

[44] C. Li, R. Burgos, Y. Tang and D. Boroyevich, "Application of D-Q frame impedance-based stability criterion in power systems with multiple STATCOMs in proximity," *IECON 2017 - 43rd Annual Conference of the IEEE Industrial Electronics Society*, Beijing, 2017, pp. 126-131, doi: 10.1109/IECON.2017.8216026.

[45] C. Li, R. Burgos, Y. Tang and D. Boroyevich, "Stability analysis on D-Q frame impedances in power systems with multiple STATCOMs in proximity," *2017*

IEEE Southern Power Electronics Conference (SPEC), Puerto Varas, 2017, pp. 1-6, doi: 10.1109/SPEC.2017.8333639.

[46] C. Li, R. Burgos, B. Wen, Y. Tang and D. Boroyevich, "Stability Analysis of Power Systems With Multiple STATCOMs in Close Proximity," in *IEEE Transactions on Power Electronics*, vol. 35, no. 3, pp. 2268-2283, March 2020, doi: 10.1109/TPEL.2019.2931891.

[47] C. Li, R. Burgos, B. Wen, Y. Tang and D. Boroyevich, "Analysis of STATCOM Small-Signal Impedance in the Synchronous d-q Frame," in *IEEE Journal of Emerging and Selected Topics in Power Electronics*, vol. 8, no. 2, pp. 1894-1910, June 2020, doi: 10.1109/JESTPE.2019.2942332.

[48] C. Li, "*Impedance-Based Stability Analysis in Power Systems with Multiple STATCOMs in Proximity*," Ph.D. dissertation, Virginia Tech, Blacksburg, VA, 2018.

[49] Y. Song and C. Breitholtz, "Nyquist Stability Analysis of an AC-Grid Connected VSC-HVDC System Using a Distributed Parameter DC Cable Model," *IEEE Transactions on Power Delivery*, vol. 31, pp. 898-907, 2016.

[50] M. Amin, A. Rygg and M. Molinas, "Active power flow direction effect on stability in multi-terminal VSC-HVDC transmission system in integrating wind farm," *2016 IEEE 17th Workshop on Control and Modeling for Power Electronics (COMPEL)*, Trondheim, 2016, pp. 1-8.

[51] M. Amin, A. Rygg and M. Molinas, "Impedance-based and eigenvalue based stability assessment compared in VSC-HVDC system," *2016 IEEE Energy Conversion Congress and Exposition (ECCE)*, Milwaukee, WI, 2016.

[52] M. F. M. Arani and Y. A. R. I. Mohamed, "Analysis and Performance Enhancement of Vector-Controlled VSC in HVDC Links Connected to Very Weak Grids," *IEEE Transactions on Power Systems,* vol. 32, pp. 684-693, 2017.

[53] M. Amin, M. Molinas, J. Lyu and X. Cai, "Impact of Power Flow Direction on the Stability of VSC-HVDC Seen From the Impedance Nyquist Plot," *in IEEE Transactions on Power Electronics,* vol. 32, no. 10, pp. 8204-8217, Oct. 2017.

[54] D. Shu, X. Xie, H. Rao, X. Gao, Q. Jiang, and Y. Huang, "Sub- and Super-Synchronous Interactions between STATCOMs and Weak AC/DC Transmissions with Series Compensations," *IEEE Transactions on Power Electronics,* vol. PP, pp. 1-1, 2017.

[55] L. Xu and L. Fan, "Impedance-Based Resonance Analysis in a VSC-HVDC System," *IEEE Transactions on Power Delivery,* vol. 28, pp. 2209-2216, 2013

[56] H. Liu, X. Xie and W. Liu, "An Oscillatory Stability Criterion Based on the Unified dq -Frame Impedance Network Model for Power Systems With High-Penetration Renewables," in *IEEE Transactions on Power Systems,* vol. 33, no. 3, pp. 3472-3485, May 2018.

[57] L. Piyasinghe, Z. Miao, J. Khazaei, and L. Fan, "Impedance Model-Based SSR Analysis for TCSC Compensated Type-3 Wind Energy Delivery Systems," *IEEE Transactions on Sustainable Energy,* vol. 6, pp. 179-187, 2015

[58] [48] J. Lyu, X. Cai, and M. Molinas, "Frequency Domain Stability Analysis of MMC-Based HVdc for Wind Farm Integration," *IEEE Journal of Emerging and Selected Topics in Power Electronics,* vol. 4, pp. 141-151, 2016

[59] M. Amin and M. Molinas, "Understanding the Origin of Oscillatory Phenomena Observed Between Wind Farms and HVdc Systems," *IEEE Journal of Emerging and Selected Topics in Power Electronics*, vol. 5, pp. 378-392, 2017

[60] M. Amin, A. Rygg and M. Molinas, "Self-Synchronization of Wind Farm in an MMC-Based HVDC System: A Stability Investigation," in *IEEE Transactions on Energy Conversion*, vol. 32, no. 2, pp. 458-470, June 2017.

[61] K. M. Alawasa, Y. A. I. Mohamed and W. Xu, "Active Mitigation of Subsynchronous Interactions Between PWM Voltage-Source Converters and Power Networks," in IEEE Transactions on Power Electronics, vol. 29, no. 1, pp. 121-134, Jan. 2014.

[62] X. Chen, Y. Zhang, S. Wang, J. Chen and C. Gong, "Impedance-Phased Dynamic Control Method for Grid-Connected Inverters in a Weak Grid," in *IEEE Transactions on Power Electronics*, vol. 32, no. 1, pp. 274-283, Jan. 2017.

[63] K. M. Alawasa and Y. A. I. Mohamed, "Impedance and Damping Characteristics of Grid-Connected VSCs With Power Synchronization Control Strategy," in *IEEE Transactions on Power Systems*, vol. 30, no. 2, pp. 952-961, March 2015.

[64] D. Lu, X. Wang and F. Blaabjerg, "Impedance-Based Analysis of DC-Link Voltage Dynamics in Voltage-Source Converters," in *IEEE Transactions on Power Electronics*, vol. 34, no. 4, pp. 3973-3985, April 2019.

[65] D. Wang, L. Liang, L. Shi, J. Hu and Y. Hou, "Analysis of Modal Resonance Between PLL and DC-Link Voltage Control in Weak-Grid Tied VSCs," in *IEEE Transactions on Power Systems*, vol. 34, no. 2, pp. 1127-1138, March 2019.

[66] Y. Liao, Z. Liu, G. Zhang and C. Xiang, "Vehicle-Grid System Modeling and Stability Analysis With Forbidden Region-Based Criterion," in *IEEE Transactions on Power Electronics*, vol. 32, no. 5, pp. 3499-3512, May 2017, doi: 10.1109/TPEL.2016.2587726.

[67] Y. Liao, Z. Liu, H. Zhang and B. Wen, "Low-Frequency Stability Analysis of Single-phase System with dq-frame Impedance Approach – Part I: Impedance Modeling and Verification," *IEEE Transactions on Industry Applications*, 2018

[68] J. Sun, M. Xu, M. Cespedes and M. Kauffman, "Low-Frequency Input Impedance Modeling of Single-Phase PFC Converters for Data Center Power System Stability Studies," *2019 IEEE Energy Conversion Congress and Exposition (ECCE)*, Baltimore, MD, USA, 2019, pp. 97-106.

[69] J. Huang, "*AC/DC power system small-signal impedance measurement for stability analysis*," Ph.D. dissertation, Dept. Elect. Eng.,Missouri Univ. Sci. Technol., Rolla, MO, USA, 2009.

[70] S. Lissandron, L. Dalla Santa, P. Mattavelli, and B. Wen, "Experimental validation for impedance-based small-signal stability analysis of single-phase interconnected power systems with grid-feeding inverters," *IEEE J. Emerg. Sel. Topics Power Electron.*, vol. 4, no. 1, pp. 103–115, Mar. 2016.

[71] W. Jewell, R. Rama kumar and S. Hill, "A Study of Dispersed PV Generation on the PSO System," *IEEE Transactions on Energy Conversion*, vol. 3, no. 3, p. 473-478, Sep. 1988.

[72] General Electric Corporate R&D (2003, Aug.), DG Power Quality, Protection and Reliability Case Studies Report, NREL report NRELlSR-560-34635. Niskayuna,

New York, USA. [Online]. Available: http://www.nrel.gov/docs/fy03osti/34635.pdf

[73] H. Kobayashi and M. Takasaki, "Demonstration Study of Autonomous Demand Area Power System," in *Proc. IEEE Power Eng. Soc. Transm. Distrib. Conf. Expo*., Aug. 2006, pp. 548–555.

[74] M. Thomson and D. G. Infield, "Network power-flow analysis for a high penetration of distributed generation," *IEEE Trans. Power Syst*., vol. 22, no. 3, pp. 1157–1162, Aug. 2007.

[75] R. Tonkoski, D. Turcotte, and T. H. M. EL-Fouly, "Impact of high PV penetration on voltage profiles in residential neighborhoods," *IEEE Trans.Sustain. Energy*, vol. 3, no. 3, pp. 518–527, Jul. 2012.

[76] A. Hoke, R. Butler, J. Hambrick, and B. Kroposki, "Steady-state analysis of maximum photovoltaic penetration levels on typical distribution feeders," *IEEE Trans. Sustain. Energy*, vol. 4, no. 2, pp. 350–357, Apr. 2013.

[77] IEEE Standard for Interconnecting Distributed Resources with Electric Power Systems, IEEE Std 1547a™-2018 , 2018.

[78] E. Demirok et al., "Local reactive power control methods for overvoltage prevention of distributed solar inverters in low-voltage grids," *IEEE J. Photovolt*., vol. 1, no. 2, pp. 174–182, Oct. 2011.

[79] I. Kim, R. Harley, R. Regassa and Y. Del Valle, "The effect of the volt/var control of photovoltaic systems on the time-series steady-state analysis of a distribution network," in *Proc. IEEE Power Systems Conference*, Clemson, SC, USA, 2015.

[80] R. Aghatehrani and R. Kavasseri, “Sensitivity-analysis-based sliding mode control for voltage regulation in microgrids,” *IEEE Trans. Sustain.Energy,* vol. 4, no. 1, pp. 50–57, Jan. 2013.

[81] M. Bayat, K. Sheshyekani, and A. Rezazadeh, “A unified framework for participation of responsive end-user devices in voltage and frequency control of the smart grid,” *IEEE Trans. Power Syst.*,vol.30, no.3,pp.1369 -1379, May. 2015.

[82] M. Farivar, L. Chen, and S. Low, “Equilibrium and dynamics of local voltage control in distribution systems,” in Proc. *IEEE Conf. Decision and Control*, Firenze, 2013, pp. 4329–4334.

[83] V. H. M. Quezada, J. R. Abbad, and T. G. S. Roman, “Assessment of energy distribution losses for increasing penetration of distributed generation,” *IEEE Trans. Power Syst.*, vol. 21, no. 2, pp. 533–540, May 2006.

[84] M. A. Cohen and D. S. Callaway, “Modeling the effect of geographically diverse pv generation on California's distribution system”, in Proc. *IEEE International Conference on Smart Grid Communications (SmartGridComm),* Vancouver, BC, 2013, pp. 702-707.

[85] A. M. Al-Sabounchi, J. Gow and M. Al-Akaidi, “Optimal sizing and location of large PV plants on radial distribution feeders for minimum line losses”, in *Proc. Electric Power and Energy Conversion Systems (EPECS),* Sharjah, 2015.

[86] S. Pukhrem, M. Conlon and M. Basu, “Mitigation of over-voltage fluctuation in medium voltage (MV) distribution feeder line with high PV plant penetration”, in *Proc. Universities Power Engineering Conference (UPEC),* Staffordshire University, UK, 2015

[87] A. Agrawal, K. Rahimi, R. P. Broadwater and J. Bank, “Performance of PV Generation Feedback Controllers :Power Factor versus Volt-VAR Control Strategies”, in *Proc. North American Power Symposium (NAPS),* Charlotte, NC, USA, 2015

[88] B. Zhang, A. Lam, A. Domínguez-García, and D. Tse, “An optimal and distributed method for voltage regulation in power distribution systems,” *IEEE Trans. Power Syst.*, vol. 30, no. 4, pp. 1714 - 1726, Jul. 2015

[89] H. Yang and J. Liao, “MF-APSO-Based Multiobjective Optimization for PV System Reactive Power Regulation,” *IEEE Transactions on Sustainable Energy*, vol. 6, no. 4, pp. 346 - 1355, Oct. 2015

[90] F. Olivier, P. Aristidou, D. Ernst and T. Van Custem, "Active management of low-voltage networks for mitigating overvoltage due to photovoltaic units", *IEEE Trans. Smart Grid*, vol. 7, no. 2, pp. 926 – 936, Mar. 2016

[91] M. Farivar, R. Neal, C. Clarke, and S. Low, “Optimal inverter VAR control in distribution systems with high PV penetration”, in *Proc. IEEE Power and Energy Society General Meeting*, San Diego, CA, 2012.

[92] American National Standard For Electric Power Systems and Equipment—Voltage Ratings (60 Hertz), ANSI C84.1-2011, 2011.

[93] D.P. Kothari and I.J. Nagrath, “Load flow studies,” in *Modern Power system analysis*, New York: McGraw-Hill, 2008, pp. 192-194.

[94] E. Demirok et al., “Local reactive power control methods for overvoltage prevention of distributed solar inverters in low-voltage grids,” *IEEE J. Photovolt*., vol. 1, no. 2, pp. 174–182, Oct. 2011.

[95] M. G. Villalva, T. G. de Siqueira, and E. Ruppert, “Voltage regulation of photovoltaic arrays: Small-signal analysis and control design,” *IET Power Electron*., vol. 3, no. 6, pp. 869–880, Dec. 2010.

[96] G. Francis, R. Burgos, D. Boroyevich, F. Wang and K. Karimi, "An algorithm and implementation system for measuring impedance in the D-Q domain," 2011 *IEEE Energy Conversion Congress and Exposition*, Phoenix, AZ, 2011, pp. 3221-3228.

[97] Z. Shen, M. Jaksic, P. Mattavelli, D. Boroyevich, J. Verhulst and M. Belkhayat, "Design and implementation of three-phase AC impedance measurement unit (IMU) with series and shunt injection," 2013 *Twenty-Eighth Annual IEEE Applied Power Electronics Conference and Exposition (APEC),* Long Beach, CA, 2013, pp. 2674-2681.

[98] Z. Shen et al., "Design of a modular and scalable small-signal dq impedance measurement unit for grid applications utilizing 10 kV SiC MOSFETs," *2015 17th European Conference on Power Electronics and Applications (EPE'15 ECCE-Europe)*, Geneva, 2015, pp. 1-9.

[99] Z. Shen, M. Jaksic, I. Cvetkovic, R. Burgos and D. Boroyevich, "Small-signal impedance measurement in medium-voltage dc power systems," *2015 International Conference on Electrical Systems for Aircraft, Railway, Ship Propulsion and Road Vehicles (ESARS)*, Aachen, 2015, pp. 1-5.

[100] M. Jaksic, D. Boroyevich, R. Burgos, Z. Shen, I. Cvetkovic and P. Mattavelli, "Modular interleaved single-phase series voltage injection converter used in

small-signal dq impedance identification," *2014 IEEE Energy Conversion Congress and Exposition (ECCE)*, Pittsburgh, PA, 2014, pp. 3036-3045.

[101] M. Jaksic, Z. Shen, I. Cvetkovic, D. Boroyevich, R. Burgos and P. Mattavelli, "Multi-level single-phase shunt current injection converter used in small-signal dq impedance identification," *2014 IEEE Applied Power Electronics Conference and Exposition - APEC 2014*, Fort Worth, TX, 2014, pp. 2775-2782.

[102] M. Jakšić, Z. Shen, I. Cvetković, D. Boroyevich, R. Burgos, C. DiMarino, et al., "Medium-Voltage Impedance Measurement Unit for Assessing the System Stability of Electric Ships," *IEEE Transactions on Energy Conversion*, vol. 32, no. 2, pp. 829- 841, Jun 2017.

[103] Mauricio Cespedes and Jian Sun, "Methods for Stability Analysis of Unbalanced Three-Phase Systems", P*roceedings of IEEE Energy Conversion Congress and Exposition (ECCE)*, pp. 3090-3097, 2012.

[104] J. Sun, "Small-signal methods for ac distributed power systems–A review," in *Proc. IEEE ESTS*., Baltimore, MD, USA, 2009, pp. 44–52.

[105] M. Cespedes and J. Sun, "Impedance modeling and analysis of gridconnected voltage-source converters," *IEEE Trans. Power Electron*., vol. 29, no. 3, pp. 1254–1261, Mar. 2014.

[106] M. K. Bakhshizadeh et al., "Couplings in phase domain impedance modeling of grid-connected converters," *IEEE Trans. Power Electron*., vol. 31, no. 10, pp. 6792–6796, Oct. 2016.

[107] W. Jin , Y. Li, G. Sun , X. Chen and Y. Gao, "Stability Analysis Method for Three-Phase Multi-Functional Grid-Connected Inverters With Unbalanced Local

Loads Considering the Active Imbalance Compensation", *IEEE access*, 19 September 2018, p. 2169-3536.

[108] V. Salis, A. Costabeber, S. M. Cox, P. Zanchetta, "Stability assessment of power-converter-based AC systems by LTP theory: Eigenvalue analysis and harmonic impedance estimation", *IEEE J. Emerg. Sel. Topics Power Electron*., vol. 5, no. 4, pp. 1513-1525, Dec. 2017.

[109] V. Salis, A. Costabeber, S. M. Cox, P. Zanchetta and A. Formentini, "Stability Boundary Analysis in Single-Phase Grid-Connected Inverters With PLL by LTP Theory," in *IEEE Transactions on Power Electronics*, vol. 33, no. 5, pp. 4023-4036, May 2018.

[110] J. Kwon, X. Wang, F. Blaabjerg, C. L. Bak, V. S. Sularea, and C. Busca, "Harmonic interaction analysis in a grid-connected converter using harmonic state-space (HSS) modeling," *IEEE Trans. Power Electron*., vol. 32, no. 9, pp. 6823–6835, Sep. 2017.

[111] H. Nian, L. Chen, Y. Xu, H. Huang, and J. Ma, "Sequences domain impedance modeling of three-phase grid-connected converter using harmonic transfer matrices," *IEEE Trans. Energy Convers*., vol. 33, no. 2, pp. 627–638, Jun. 2018.

[112] C. Zhang, M. Molinas, A. Rygg, J. Lyu and Xu Cai, "Harmonic Transfer Function-based Impedance Modelling of a Three-phase VSC for Asymmetric AC Grids Stability Analysis", *IEEE Trans. Power Electron*., 2019.